Effect of Doping on Carrier Transport in ZnO Thin Films Grown by Atomic Layer Deposition

By
DEBABRATA SAHA

Enrolment No: PHYS03201004014

Raja Ramanna Centre for Advanced Technology, Indore

A thesis submitted to the

Board of studies in Physical Sciences

In partial fulfilment of requirements

for the Degree of

DOCTOR OF PHILOSOPHY

of

HOMI BHABHA NATIONAL INSTITUTE

August, 2015

STATEMENT BY AUTHOR

This dissertation has been submitted in partial fulfilment of requirements for an advanced degree at Homi Bhabha National Institute (HBNI) and is deposited in the Library to be made available to borrowers under rules of the HBNI.

Brief quotations from this dissertation are allowable without special permission, provided that accurate acknowledgement of source is made. Requests for permission for extended quotation from or reproduction of this manuscript in whole or in part may be granted by the Competent Authority of HBNI when in his or her judgment the proposed use of the material is in the interests of scholarship. In all other instances, however, permission must be obtained from the author.

Debabrata Saha

DECLARATION

I, hereby declare that the investigation presented in the thesis has been carried out by me. The work is original and has not been submitted earlier as a whole or in part for a degree / diploma at this or any other Institution / University.

Debabrata Saha

List of publications included in the thesis

Peer Reviewed Journals:

1. D. Saha, V. K. Sahu, Amit K. Das, R. S. Ajimsha, P. Misra, L. M. Kukreja,"Studies on optical and electrical characteristics of ZnO thin films grown by atomic layer deposition", Phys. Express (2013) 3:9 (available at http://www.cognizure.com/abs/106637273.aspx).

2. D. Saha, Amit. K. Das, R. S. Ajimsha, P. Misra, and L. M. Kukreja, "Effect of disorder on carrier transport in ZnO thin films grown by atomic layer deposition at different temperatures", J. App. Phys. 114, 043703 (2013), (DOI: http://dx.doi.org/10.1063/1.4815941).

3. D. Saha, R.S. Ajimsha, K. Rajiv, C. Mukherjee, M. Gupta, P. Misra, L.M. Kukreja, "Spectroscopic ellipsometry characterization of amorphous and crystallineTiO_2 thin films grown by atomic layer deposition at different temperatures", App. Surf. Sci. 315, 116 (2014), (DOI: http://dx.doi.org/10.1016/j.apsusc.2014.07.098).

4. D. Saha, P. Misra, R. S. Ajimsha, M. P. Joshi, and L. M. Kukreja, "Phase coherent transport in (Zn, Al)O_x thin films grown by atomic layer deposition", App. Phys. Lett. 105, 212102 (2014), (DOI: http://dx.doi.org/10.1063/1.4902513).

5. D. Saha, P. Misra, M. P. Joshi, and L. M. Kukreja, "Observation of dopant-Profile independent electron transport in sub-monolayer TiO_x stacked ZnO thin films grown by atomic layer deposition", Appl. Phys. Lett. 108, 032101 (2016), (DOI: http://dx.doi.org/10.1063/1.4939926).

6. D. Saha, P. Misra, S. Bhartiya, M. Gupta, M. P. Joshi, and L. M. Kukreja, "Dimensional crossover of electron weak localization in ZnO/TiO_x stacked layers grown by atomic layer deposition", Appl. Phys. Lett. 108, 042109 (2016), (DOI: http://dx.doi.org/10.1063/1.4940977).

7. D. Saha, P. Misra, M. P. Joshi, and L. M. Kukreja, "UV light induced insulator-metal transition in ultra-thin ZnO/TiO_x stacked layer grown by atomic layer deposition", (under review).

8. D. Saha, P. Misra, M. P. Joshi, and L. M. Kukreja, "Temperature dependent photoluminescence characteristics of atomic layer deposited (Zn, Ti)O_x thin films above Mott's critical density", (to be submitted)

Conferences and Workshops:

1. "Structural, optical and electrical properties of intrinsic ZnO thin films grown by atomic layer deposition" D. Saha, V. K. Sahu, Amit K. Das, R. S. Ajimsha, P. Misra, L. M. Kukreja, DAE-BRNS 6th National Symposium on Pulsed Laser Deposition of Thin Films and Nanostructured Materials (PLD-2011)", IISc (MRC), Bangalore, November 09-11, 2011.

2. "INUP Familiarization Workshop on Nanofabrication Technologies", Centre for Nanoscience and Engineering, IISc, Bangalore, January 28-30, 2015.

3. "Hands on Training on MOS Capacitor and Micro and Nano Characterization techniques", Centre for Nanoscience and Engineering, IISc, Bangalore, 10-19 March 2015.

4. "Temperature Dependent Electron Transport in Degenerately Doped ZnO Thin Films Grown by Atomic Layer Deposition", D. Saha, P. Misra, M. P. Joshi, and L. M. Kukreja, ICMAT, Singapore, 28th June-3rd July 2015.

5. "Dimensional crossover of electron transport in (Zn, Ti)O_x thin films grown by atomic layer deposition", D. Saha, P. Misra, M. P. Joshi, and L. M. Kukreja, IWPSD, IISc, Bangalore, 7-10 December 2015.

Debabrata Saha

This thesis is dedicated to
my
Adoring Parents & Brothers

Acknowledgements

I would like to express my sincere gratitude to my thesis supervisor Prof. L. M. Kukreja for giving me an exciting opportunity to work with an advanced thin film deposition technique and in a research group that is equipped with state of the art facilities. I will always be indebted to him for his guidance, support and constant encouragement throughout the course of my research study. His expertise in the field, innovative ideas and resourceful suggestions played a very important role in completion of my thesis work in time. I appreciate great degree of freedom he has given to me to carry out my research. I believe the experiences he has shared with me, his advices and constructive criticisms have made me a better researcher.

I am thankful to Dr. P. Misra for fruitful discussions on all the research problems which helped me a lot to solve many critical issues on executing experiments and analysis of experimental results pertinent to my thesis work.

I am also indebted to Dr. Mukesh P. Joshi for many fruitful discussions and his continious support during the tenure of my research work.

Thanks are also due to Dr. R. S. Ajimsha and Mr. A. K. Das for helping me to learn the basics of various thin film deposition and characterization techniques at the very early stage of my research work.

I am thankful to Dr. C. Mukherjee and Mr. K. Rajiv of Mechanical and Optical Support Section at our centre for their extensive help in Spectroscopic Ellipsometry (SE) and Atomic Force Microscopy (AFM) measurements and several fruitful discussions with them. I am also thankful to Dr. R. Rawat, Mr. Sachin Kumar and Dr. M. K. Guptaof UGC-DAE Consortium for Scientific Research, Indore, for their help in temperature dependent magnetoresistance and Secondary ion Mass Spectroscopy measurements respectively. I am highly indebted to BENEQ process engineer Mr. Urmas Jöksi for his constant and very prompt technical support in the entire duration of my research work. I wish to thank Dr. Gurvinderjit Singh of Laser materials Processing Division for his help in X-ray diffraction measurements. I am thankful to Mr. Gangadhar Das and Dr. M. K. Tiwari of Indus Synchrotron Utilisation Division of our centre for their help in Synchrotron based X-ray fluorescence measurements. I wish to thank Mr. M. K. Singh and Ms. Sushmita Bhartiya of our centre for their help in Atomic Force Microscopy measurements. I am thankful to Dr. D. M. Phase and Mr. A. Wadekar of UGC-DAE-CSR, Indore for their helps in XPS measurements. I wish to thank Dr. Arvind Kumar Srivastava of our centre for Transmission Electron Microscopy measurements.

I want to convey my special thanks to the doctoral committee members, Dr. P. K. Gupta, Dr. Arup Banerjee, Dr. S. K. Ray (IIT Kharagpur), Dr. Kaustuv Das, Dr. Rama Chari, Dr. S. B. Roy, Dr. D. K. Palit, Dr. Alok Dubey, and Dr. D. K. Aswal for their constructive comments during my annual presentations which improved my confidence to present research results in open seminars and conferences.

Finally, I would like to convey my deepest regards to my parents and brothers whose enormous encouragement and support have motivated me throughout my research study.

CONTENTS

Page No.

SYNOPSIS

Zinc oxide (ZnO) is a well know semiconductor with a direct band gap of ~ 3.3 eV at room temperature and a large excitonic binding energy of ~ 60 meV. During more than past two decades, extensive research has been carried out on ZnO thin films and nanostructures for potential applications in diverse fields which include UV-blue photonics and optoelectronics (e.g. homo and hetero junction light emitting diodes (LEDs), optically pumped lasers, visible-blind ultra-violet (UV) photo detectors, photovoltaic cells etc.), electronics (e.g. transparent thin film transistors (TTFTs), spintronic devices etc.) and as transparent conducting electrodes (TCEs) for optoelectronic devices. However, the daunting problem to grow stable and reproducible p-type ZnO has impeded the development of ZnO based p-n junction devices.

Intrinsically and/or extrinsically donor doped degenerate ZnO thin films exhibit optical transmittance and electrical conductivity close to that of indium tin oxide (ITO) and therefore, are being considered as cost-effective alternative of ITOs for TCE applications. However, industrial scale manufacturing of high quality and large area ZnO based TCEs for applications in solar cells and flat panel displays require a suitable deposition technique with rapid deposition rate and which can accommodate large area substrates. These requirements can easily be accomplished by employing atomic layer deposition (ALD) technique.

ALD offers a number of industrially and technologically important characteristics which include its large-area deposition capability, pin-hole free conformal coatings, excellent control over film thickness and uniformity, no line-of-sight deposition, high degree of reproducibility in film properties and relatively low deposition temperatures. However, the self-limiting and layer-by-layer growth mechanism of thin films in ALDis ideal for fabricating nanolaminate structures with atomically sharp interfaces and hence, inferior to achieve homogeneous dopant distribution. In our research work, all thin film depositions

were carried out in a flow-type thermal ALD reactor, (Make: Beneq Oy Finland; model: TFS 200) at Laser Materials Processing Division, Raja Ramanna Centre for Advanced Technology (RRCAT), Indore. We found that efficient donor doping of Al and Ti in ZnO thin films could be achieved through a novel sub-monolayer dopant incorporation scheme developed by us which relies on the in-situ sub-saturating exposure of the dopant precursor molecules on the growing ZnO film surface. The resulting films were found to be highly n-type conducting with an average optical transmittance of ~ 80% in the visible spectral range and smooth surface morphologies (RMS surface roughness < 5 nm). Therefore, these films are suitable for TCE applications in liquid crystal displays, LEDs etc. However, the dopant atoms except donating free electrons into the system introduce disorder by statistically occupying the host lattice sites and deteriorating its crystalline quality. The electrical, optical and structural properties of these films were found to be strongly dependent on the dopant concentration. We have carried out a detailed investigation on the effect of dopant induced static-disorder on the temperature dependent carrier transport mechanisms of degenerately n-type doped ZnO thin films grown by ALD. Such studies are important to investigate the underlying carrier scattering mechanisms which control the electron transport properties in these films. The major findings of our research work are presented in the form of thesis composed of following 6 chapters:

Chapter 1 provides an outline of the basic properties of ZnO, which includes its crystal structure, electronic band structure, optical and electrical properties and its prospective applications. An introduction to transparent conducting oxides (TCOs), essential optical and electrical properties of TCOs, plausible sources of electron scattering mechanisms in TCOs have been briefly overviewed. This is followed by a discussion on the potential of degenerately n-type doped polycrystalline ZnO thin films as a prospective TCO material. In these degenerately doped semiconductors, electron transport on the metallic side of the metal

to insulator transition (MIT) is driven by the phenomenon of weak-localization (WL) and diffusion channel electron-electron interactions (EEIs). Therefore, the influence of WL and EEIs on the temperature dependent electrical resistivity and magneto-transport properties has been discussed along with the possible inelastic scattering mechanisms responsible for electron dephasing. Further, a comprehensive literature review on the growth of intrinsic and doped ZnO thin films using ALD and the current state of research is also presented in this chapter.

Chapter 2 deals with the brief introduction of ALD technique, details of ALD equipment, and optimizations of various deposition parameters such as growth temperature, precursor flow rate, pulsing and purging times and various doping schemes. Concise notes on different thin film characterization techniques which includes X-ray diffraction (XRD), Atomic force microscopy (AFM), Transmission electron microscopy (TEM), X-ray photoelectron spectroscopy (XPS), secondary ion mass spectroscopy (SIMS), synchrotron based X-ray fluorescence (XRF), optical transmittance, photoluminescence (PL), electrical resistivity and Hall measurements are presented.

Chapter 3 presents our work on the optimizations of structural, electrical and optical properties of intrinsic ZnO thin films grown by ALD. For this purpose, films were grown on single crystal (0001) sapphire substrates at different substrate temperatures varying from ~ 50-350^{0}C. Diethyl zinc (DEZ) and de ionized water were used as precursors for Zn and oxygen respectively. The ALD window for the self-terminating growth of ZnO was obtained in the temperature range of ~ 140-200^{0}C with a constant growth rate of ~ 0.2 nm/cycle. The XRD and AFM results revealed that ALD-ZnO films were polycrystalline in nature and their crystallinity changed with deposition temperature. All the films were found to be highly transparent in the visible spectral range. Room temperature photoluminescence measurements exhibited near band edge (NBE) excitonic emission for all the films at ~ 380 nm along with

defect level emission (DLE) in the visible spectral range. The films grown at lower substrate temperatures i.e., below ALD window, showed DLE peak centred at ~590 nm (orange) which was attributed to the presence of additional oxygen related defects in ZnO. The position of DLE peak was found to be shifted at ~ 510 nm (green) at higher growth temperatures due to presence of oxygen vacancy related point defects which was confirmed by XPS measurements. The electrical resistivities of the films grown below ALD window were too high to be measured. This was plausibly due to the presence of additional oxygen related point defects in ZnO either in the form of hydroxyl groups and/or oxygen interstitials which act as acceptors for the free carriers and/or compensating the existing n-type carriers. However, these films turned into highly conducting when exposed to UV light (larger than the band gap of ZnO) and retained their conductivity when kept in high vacuum chamber. The highly-conducting state slowly reverted to the initial highly-resistive state when exposed to atmosphere. Such reversible changes in the conductivity clearly implies desorption and adsorption of hydroxyl groups at the surface and at grain boundaries. The films grown within and above ALD window showed stable n-type conductivity plausibly due to more complete reactions between DEZ molecules and the surface hydroxyl groups which resulted in reduced additional oxygen related defects in the as grown films.

In order to investigate the effect of growth temperature on the carrier transport mechanisms of the films, temperature dependent electrical resistivity $\rho(T)$ and Hall measurements were carried out in the temperature range of ~ 5-300 K. The $\rho(T)$ measurements for the films grown below ALD window (i.e., at 50 and 100^0C) were performed after illuminating the samples with UV light for few minutes. However, carrier density in these films could not be measured because of extremely poor Hall mobility. Rest of the films showed carrier density of the order of 10^{19} cm^{-3}. The films grown at 50, 100150, 300 and 350^0C showed semiconductor-like resistivity behaviour i.e., $(d\rho/dT)<0$ in the entire range of the

measurement temperature. This could be attributed to the pronounced crystalline and compositional disorder in these films as revealed by their XRD pattern and room temperature PL spectra. However, a metal to semiconductor transition (MST) at lower temperature was observed for the films grown at ~ 200 and 250^0C. Higher residual resistivity for the sample grown at ~ 250^0C plausibly resulted in its higher MST temperature compared to that grown at ~ 200^0C. The upturn in resistivity below the transition temperature could be well explained by considering quantum corrections to the Boltzmann's conductivity which includes the effect of WL and coulomb EEIs due to the diffusive motion of electrons in presence of disorder.

Chapter 4 presents detail analysis of the temperature dependent carrier transport mechanisms in (Zn, Al)O_x thin films grown by ALD. The deposition temperature was purposely kept at ~200^0C which was found to be the optimum temperature to grow intrinsic ZnO films with desirable structural, optical and electrical properties suitable for TCE applications. Al concentration in the films was varied from ~ 1.6 to 12.4 at% by varying the percentage of Al_2O_3 sub-cycles. All the films up to Al concentration of ~5.5 at% were found to be heavily degenerate with electron density $>10^{20}$ cm^{-3}. A minimum value of resistivity ~ $8.6x10^{-4}$ Ω cm with comparatively good Hall mobility ~18 cm^2/Vs was achieved at ~2.2 at% of Al. With increasing Al incorporation, a crossover from good metallic to barely metallic state was observed at ~5.5 at% of Al. A clear signature of phase-coherent electron transport was observed in temperature dependent electrical resistivity which was further confirmed by magnetoresistance (MR) measurements. The MR data at lower temperatures (T≤ 15K) were analyzed by considering the combined effect of 3-dimensional WL and EEIs. However, at T >15 K, MR data could be well explained by considering only three-dimensional WL contribution. The temperature dependence of phase-coherence length, as extracted from the

MR measurements, indicated inelastic electron-electron scattering as the dominant dephasing mechanism.

Chapter 5 presents the temperature dependent electrical and optical properties of (Zn, Ti)O_x thin films grown by ALD on (0001) sapphire substrates. First, we have optimized the process parameters for TiO_2 deposition to provide sub-saturating exposure of the dopant precursor molecules on the growing ZnO film surface which resulted in sub-monolayer growth of TiO_2 after one complete cycle. Therefore, plenty of surface reactive sites might have remained unoccupied by the $TiCl_4$ molecules. Those unreacted surface sites plausibly occupied by the subsequent exposure of Zn precursor molecules. As a result, diffused dopant distribution was achieved as observed in the SIMS depth profiling spectra and cross sectional TEM measurements.

Ti concentration in the films was varied systematically in a wide range from ~ 0.2 to 10.24 at% by varying the cycle ratio of TiO_x with ZnO. Electron concentration was found to be increased monotonically from ~ 4.2×10^{19} for intrinsic ZnO to ~ 3.8×10^{20} cm^{-3} at ~ 0.78 at% of Ti. With further incorporation of Ti, electron density was found to be decreased. A minimum value of room temperature electrical resistivity ~ 1×10^{-3} Ω cm with comparatively good Hall mobility ~16 cm^2/Vs was achieved for Ti concentration of ~ 0.65 at%. Above this critical Ti concentration resistivity was found to be increased which ultimately reached to a maximum measurable value ~ 38×10^{-3} Ω cm at ~ 6.42 at% of Ti. The films with Ti concentration beyond 6.42 at% were found to be too high resistive to be measured.

Detailed investigation on the electron transport mechanisms of these films were carried out by measuring temperature dependent electrical resistivity $\rho(T)$ and magnetoresistance (MR) measurements in the temperature range of ~ 5-300 K. The $\rho(T)$ curves for all the conducting films showed finite resistivity extrapolated to T→0 K and very low values of relative resistivity ratio ρ(r) = ρ(4.2 K)/ρ(300 K), implying that films were on the metallic side of the

MIT. The (Zn, Ti)O_x films with Ti concentration ~ 0.2-1.7 at% exhibited a smooth transition from 'metal-like' ($d\rho/dT>0$) to 'semiconductor-like' ($d\rho/dT<0$) resistivity behaviour which resulted in a resistivity minimum at T_m (K). Initially, with increasing Ti concentration from 0-0.65 at%, T_m was found to be systematically shifted to the lower temperature and the depth of the resistivity minimum ($\Delta\rho$) was also decreased. Due to these combinatorial effects, 'metal-like' transport behaviour increased up to ~0.65at% of Ti. This was well corroborated with the decrease of room temperature electrical resistivity and increase of the static-disorder parameter $K_F l_e$ (where K_F is the Fermi wave vector and l_e is the elastic mean free path). On the contrary, further incorporation of Ti up to ~ 1.7 at%, resulted in the shifting of the resistivity minimum to the higher temperature with an associated increment in $\Delta\rho$ and eventually above 1.7 at% 'semiconductor-like' behaviour prevailed in the entire range of the measurement temperature i.e., films turned into 'incipient non-metallic'. Such characteristics of $\rho(T)$ curves were analyzed by considering the interplay of screening effect of the impurity potentials and disorder induced WL and EEI phenomena. Temperature dependent MR measurements revealed inelastic electron-electron scattering as the dominant phase-breaking mechanism in the (Zn, Ti)O_x films.

After a detail study on the electron transport, we have carried out optical transmission and photoluminescence characterizations of the (Zn, Ti)O_x films which further confirmed the interplay of screening and disorder. The optical absorption edge was found to be blue shifted with increasing Ti concentration. The increase in optical band gap up to Ti concentration of ~ 0.78at% was found to be in good conformity with the combined effect of Burstein-Moss shift and band gap narrowing effects. The sparsely doped films with Ti concentration up to ~ 0.65 at% exhibited strong and intense near band-edge emission at room temperature. With further incorporation of Ti i.e., at ~ 0.78 at%, emission intensity was found to be significantly deteriorated and completely diminished beyond it. Therefore, we have carried out

temperature dependent (5-300K) photoluminescence measurements for the films (0-0.78 at%) which showed noticeable near band-edge emission at room temperature. Surprisingly enough, the films (0-0.4 at%) even with net electron concentration above the Mott's critical density, exhibited distinct free excitonic (F_x) emission at lower temperatures. In addition to F_x two other well-resolved peaks corresponding to electron-acceptor (e-A) recombination and 1-LO phonon replica of F_x were also observed. However, the spectral features were broadened and merged together for the film with Ti concentration of ~ 0.65 at%. The monotonic blue shift of F_x peak with increase of Ti from 0 to ~ 0.65 at% could be attributed to the screening of F_x binding energy. For the film with ~ 0.78 at% of Ti only momentum non conserving band-to-band transitions prevailed as indicated by their asymmetric spectral line shapes of the low-temperature photoluminescence spectra. The significant reduction in luminescence intensity and associated line broadening were discussed by considering the effects of high degree of carrier compensation, deteriorated crystalline quality and dopant induced potential fluctuations.

Chapter 6 presents the summary of the present research work and discussion on the feasibility of further future works in this direction.

List of Figures

List of Tables

Chapter 1: Introduction

1.1 ZnO: a Versatile Semiconductor

Zinc Oxide (ZnO) is a well known II-VI compound semiconductor which has a direct band-gap of ~ 3.3 eV and a large exciton binding energy of ~ 60 meV at room temperature [1-3]. These characteristics make ZnO a superior candidate over other wide-band gap semiconductors such as GaN for potential applications in short-wavelength optoelectronic devices [4-7]. Moreover, ZnO is chemically rugged, radiation hard, non toxic and biocompatible. The radiation hardness of ZnO is suitable for space applications. Its amenability to wet chemical etching is very useful for various device designing and fabrication. Apart from this, growth of large single crystals, high quality epitaxial thin films and nanostructures (nano wires, nano belts, etc.) of ZnO using various deposition techniques have allowed the research community to realize ZnO-based electronic and optoelectronic devices [3-5]. The epitaxial growth of high quality ZnO on native substrates result in lower extended defect density compared to the GaN thin films grown on sapphire substrates (lattice mismatch ~16%) [3-6, 8]. This is a big advantage of ZnO over GaN for device applications. However, the production of stable and reproducible p-type ZnO has hindered fabrication of bipolar ZnO-based devices [3, 5, 6 and 9]. The basic properties of ZnO including its crystal structure, optical and electrical properties and its applications in diverse fields have been discussed below.

1.1.1 Crystal Structure and Lattice Parameters

Under ambient pressure and temperature the most thermo dynamically stable phase of ZnO is hexagonal wurtzite structure as shown in Fig.1.1 [6, 7]. Such crystal structure consists of two interconnecting sub-lattices of Zn^{2+} and O^{2-} in which each Zn cation is surrounded by four O

anions at the corners of a tetrahedron, and vice-versa. The tetrahedral coordination is typical of sp^3 covalent bonded. However, Zn-O bond also possesses substantial ionic character and thus ZnO lies on the borderline between a covalent and ionic compound semiconductor. The values of the basal plane lattice constant *a* (edge length of the basal plane hexagon) lies in the range of 3.2475 to 3.2501 Å and the axial lattice constant (or height of the unit cell) *c* from 5.2042 to 5.2075 Å [6, 7]. In ZnO, the axial ratio *c/a* is in the range of 1.593-1.603 and the internal parameter *u* (which is a measure of the amount by which each atom is displaced with respect to the next parallel to the *c* axis) which is slightly deviated from the value 1.633 for ideal hexagonal crystal structure [6, 7]. The nearest-neighbour bond lengths along the ***c*** axis (shown as *b* in Fig.1.1) and off *c*-axis (shown as b_1 in Fig. 1.1) and three types of 2nd nearest neighbours b_1', b_2' and b_3' are also shown in Fig.1.1.

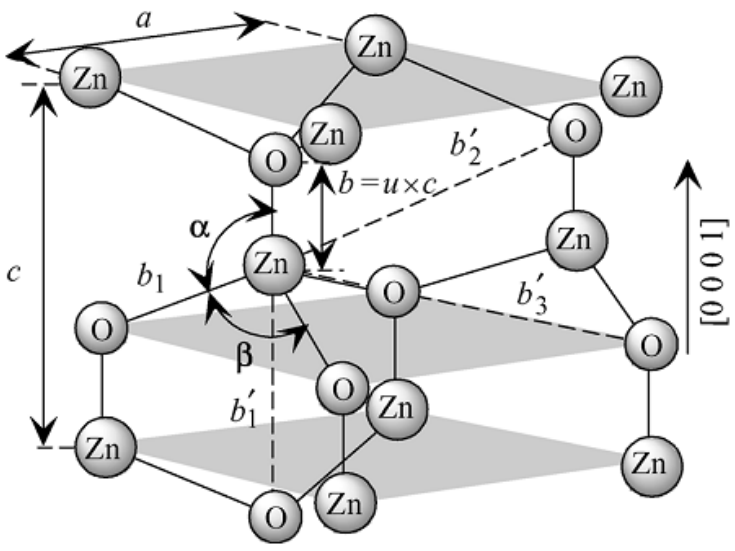

Fig. 1.1 Schematic representation of a wurtzite ZnO structure with lattice constants a in the basal plane and c in the basal direction [Reproduced with permission from: Hadis Morkoç and Ümit Özgür, Zinc Oxide Fundamentals, Materials and Device Technology, Page No.2, Figure 1.2, Publisher: Wiley-VCH Verlag GmbH and Co. KGaA, (2007).]

1.1.2 Electrical Properties

Both the electrical and optical properties of ZnO are found to be strongly dependent on various native point defects which include vacancies (i.e. missing atoms at regular lattice sites), interstitials (i.e. extra atoms occupying interstices in the lattice) and anti sites (i.e. a Zn atom occupying an O lattice site or vice versa) [3, 5 and 9]. Most of the electron paramagnetic resonance (EPR) measurements and density functional theory (DFT) calculations for intrinsic defects in ZnO revealed the presence of oxygen vacancies (V_O), zinc vacancies (V_{Zn}) and zinc interstitials (Zn_i) as the major point defects due to their lower formation energies [5, 9]. The other native defects which include zinc anti sites (Zn_O), oxygen interstitials (O_i) and oxygen anti sites (O_{Zn}) have higher formation energies and therefore, may not have significant role in electrical properties under near-equilibrium conditions [5, 9].

ZnO thin films grown by different deposition techniques are usually found to be n-type conducting [1-7 and 9]. These films are suitable for transparent conducting electrode (TCE) applications. However, growth of stable and reproducible p-type ZnO is highly required for the realization of ZnO based LEDS and laser diodes etc [4]. For this purpose, the background n-type doping in ZnO has to be reduced. Hence, extensive research work has been carried out to control the unintentional n-type conductivity in ZnO [9-12]. However, due to the intricate defect chemistry of ZnO, growth of ZnO thin films with controllable electrical properties is still remained a difficult task [9]. Therefore, no reliable devices based on ZnO p-n homo-junction have been reported so far [3-5].

Fig. 1.2 shows the formation energies of different native defects in ZnO as function of Fermi level position for Zn rich and O rich conditions [9]. As can be seen from Fig. 1.2, V_O has the lowest formation energy among all the native point defects in ZnO. However, DFT calculations have demonstrated that V_O is a deep level defect and therefore, cannot contribute to the observed n-type conductivity in ZnO [29]. With increasing Fermi level (E_F) position,

formation energy of V_O is increased and when E_F reaches near to the conduction band minimum (CBM), V_O assumes the neutral charge state and therefore, never contribute as electron donors.

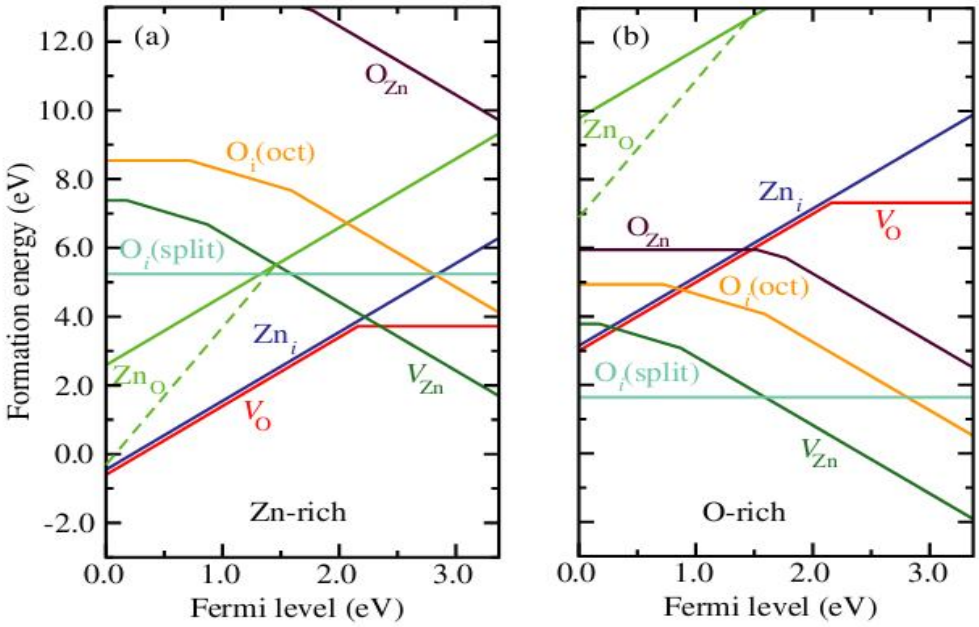

Fig. 1.2 Formation energies as a function of Fermi-level position for native point defects in ZnO for (a) Zn-rich and (b) O-rich conditions. The zero of Fermi level corresponds to the valence-band maximum. [Reproduced with permission from: A. Janotti and C G Van de Walle, Phys. Rev. B 76, 165202 (2007).]

Hall measurements revealed that Zn_i are shallow donors with ionization energy of ~ 50 meV [14]. Therefore, they can contribute to the n-type conductivity in ZnO. However, the formation energy of Zn_i increases with increasing n-type conductivity i.e., for samples with E_F close to the CBM [9]. Therefore, Zn_i are unlikely to be responsible for the unintentional n-type conductivity in ZnO, because they will be present in very low concentrations in n-type ZnO. In contrary, the formation energy of Zn_i is very low for p-type ZnO i.e. E_F close to valance band maximum (VBM) and therefore, they can effectively compensate p-type conductivity [9].

Zinc vacancies (V_{Zn}) act as acceptor type defects in ZnO [9, 15 and 16]. The formation energy of acceptor type defects is decreased with increasing n-type conductivity [9]. As can be seen from Fig. 1.2, the formation energy of V_{Zn} is sufficiently reduced as E_F reaches close to the CBM and therefore, can act as compensating centres for n-type conductivity. Their formation is much favourable in oxygen-rich conditions as shown in Fig.1.2. The other native point defects in ZnO have higher formation energies and therefore, don't have any significant effect in the electrical conductivity under near equilibrium conditions.

Therefore, unintentional n-type conductivity in ZnO cannot be explained by native point defects in ZnO. It is relevant to investigate the possibility for the incorporation of shallow donor impurities during growth of intrinsic ZnO. DFT calculations show that H which is present in almost all growth environments can act as shallow donor impurity in ZnO [17].

The n-type conductivity of ZnO can be dramatically increased by incorporating group III elements like Al, Ga and In [18-21]. These are well known donor dopants in ZnO and each can produce electron density > 10^{20} cm^{-3}. For p-type doping in ZnO either group-I elements (Li, Na and K) for Zn sites [22] or group-V elements such as N, P and As for oxygen sites has been used [23-26]. However, the reproducibility and reliability of p-type conductivity is highly controversial [3, 5]. It has been shown that group-I elements could be better p-type dopant compared to group-V elements in terms of shallowness of the acceptor levels [27]. However, group-I elements tend to occupy the interstitial sites rather than substitutional sites and therefore, act as donor impurities [28].

1.1.3 Optical Properties

Before dealing with the optical properties of ZnO, it is imperative to have a concise discussion on the electronic energy band diagram of this material. The electronic band structure of wurtzite ZnO has been obtained by Vogel *et al.*, using Local Density

Approximation (LDA) and including atomic self-interaction corrected pseudo potentials to correctly consider the Zn 3d electrons [29]. The band gap value determined to be 3.77 eV which is very close to the experimentally obtained value 3.4eV.The valance band maxima and the lowest conduction band minima occur at K=0, implying that ZnO is a direct band gap semiconductor. The valance band of ZnO is splitted into three sub-bands A, B and C by spin-orbit and crystal-field splitting as shown in Fig.1.3 [6]. In addition to these calculations for band structure, photoelectron spectroscopy (PES) and angle resolved photoelectron spectroscopy (ARPES) techniques together with synchrotron radiation excitation have been carried out to experimentally determine bulk and surface electronic band-structure of wurtzite ZnO [30-32].

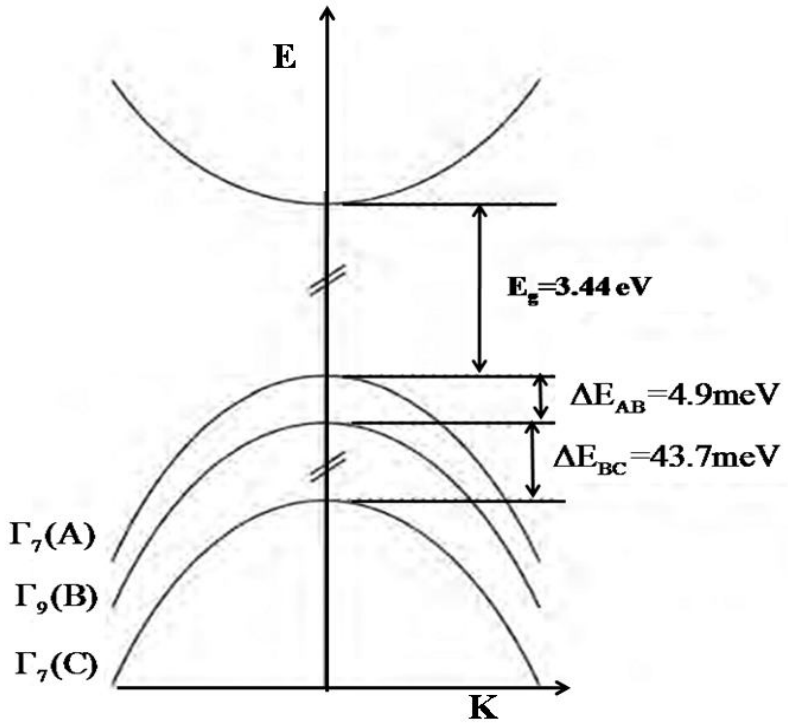

Fig. 1.3 Schematic representation of the crystal field and spin-orbit splitting of the valance band of ZnO into 3 sub-bands A, B and C at 4.2 K.

Optical properties of ZnO thin films have been studied by a variety of experimental techniques such as optical absorption, transmission, reflection, spectroscopic ellipsometry, photoluminescence (optical excitation), cathodeluminescence (electron beam excitation), electroluminescence (excitation by carrier injection) etc [33-38]. Luminescence involves three basic processes. First, a none-equilibrium distribution of electron-hole pairs is created by absorption of incident photons with energy greater than the band gap (E_g). In the second step, the electrons and the holes rapidly thermalize and establish quasi-equilibrium distributions. Finally, the electron-hole pair recombines radiatively by emitting a photon which corresponds to the band gap energy of the material.

In general, ZnO exhibits ultraviolet (UV) near band edge emission (NBE) due to exciton recombination along with a broad visible emission, also called deep level emission (DLE) which is associated with the intrinsic or extrinsic defect levels [3, 39 and 40].

In high quality ZnO crystals and epitaxial thin films the free electrons and holes, generated by the absorption of photons with energy higher than the band gap of ZnO, form excitons due to the Coulomb attractions between the opposite charges [41]. The electron (e) and hole (h) system coupled through Coulombic interaction is known as free exciton. For strong e-h interaction, as observed in ionic crystals, the e and h are tightly bound to each other and the binding distance is of the order of one lattice constant. These excitons are known as Frenkel excitons [41, 42]. If the Coulomb attraction is screened by valance electrons, as in most semiconductors, the e-h pairs are weakly bound and they can spread over several unit cells. These are known as Wannier excitons [41, 42]. The binding energy of free exciton is given by

$$E_x = \frac{1}{4\pi\varepsilon_0}\frac{\mu e^4}{2\hbar^2\varepsilon_0^{\,2}}\frac{1}{n^2} \tag{1.1}$$

where n indicates different excitonic states and μ is the reduced mass of the coupled system as given by

$$\frac{1}{\mu} = \frac{1}{m_e^*} + \frac{1}{m_h^*} \tag{1.2}$$

with m_e^* and m_h^* are the effective masses of electron and hole respectively. The intrinsic transition energy involving a free exciton is given by

$$\hbar\omega = E_g + E_{kin} - E_x \tag{1.3}$$

where E_g is the band gap, E_{kin} is the kinetic energy of the centre of mass motion of the e-h coupled system. Due to the very high binding energy of free exciton in ZnO ~ 60 meV, excitonic recombination persists at room temperature and above.

Apart from free exciton recombination, the NBE emission spectrum of ZnO also consists of bound excitonic luminescence [43, 44]. A free exciton can combine with the impurity or defect sites to form bound exciton complex. The energy position of bound exciton is below the free exciton energy by an amount equal to the binding energy of the bound exciton. Transitions involving bound excitons emit photons with and energy given by

$$\hbar\omega = E_g + E_{kin} - E_x - E_{loc} \tag{1.4}$$

where E_{loc} is the binding energy of the bound exciton. The bound excitonic transitions are characterized by extremely narrow spectral line width and are generally observed at low enough measurement temperatures.

In polar semiconductors like ZnO, one of the channels of excitonic recombination is through mediation of longitudinal optical (LO) phonons [41, 45]. At low temperature, Frölich coupling with the LO phonons is the largest contributor to the exciton-phonon coupling in polar semiconductors with a large ionic character like ZnO and GaN etc [41, 45]. This type of coupling is due to the Coulomb interaction between the exciton and the longitudinal electric field created by the LO-phonons (energy 72 meV) [41]. In photo luminescence spectra this manifests as the appearance of Stokes and anti-Stokes LO-phonon replicas from excitonic

related emission peaks.

Another very common form of luminescence with photon energies lower than those of the excitons, is known as donor-acceptor pair (DAP) recombination emission [46, 47]. The DAP emission appears when an electron on a neutral donor recombines with a hole on a neutral acceptor emitting a photon with corresponding energy. The participating donor and acceptor atoms are left in their ionized positive and negative equilibrium charge states after electron-hole recombination, and possess an attractive Coulomb interaction. The magnitude of this interaction energy depends of the separation distance between the atoms, and this energy is added to the energy of the photon emitted. Photons emitted from closely separated pairs will have higher energy than those emitted from distant atoms. The energy of the emitted photon is then given by [47],

$$\hbar\omega = E_g - (E_D{}^0 + E_A{}^0) + \frac{e^2}{4\pi\varepsilon\varepsilon_0 r_{DA}} \tag{1.5}$$

where r_{DA} is the inter atomic separation. The DAP peak position depends on the excitation level and is found to be shifted to higher energy at higher excitations because of reduced r_{DA} .With increasing temperature, the DAP transitions often disappear as the shallow donor state thermally ionizes. At this condition free electrons from the conduction band will annihilate with holes on the neutral acceptors, giving rise to the so-called free-to-bound (F-B) emission which is generally referred to as (e, A^0) transition [48]. The emitted photon energy is given by

$$\hbar\omega = E_g - E_A{}^0 \tag{1.6}$$

At sufficiently high temperatures the DAP transition is replaced by the (e, A^0) transition. Apart from all these transitions in UV or near UV spectral range, ZnO exhibits broad DLE in the visible region due to defect level emission as stated earlier [3, 39 and 40]. However, the origin of DLE emission is still controversial, and the position and behaviour of DLE in ZnO

is found to be strongly dependent on the growth conditions and growth methods [3]. The commonly observed DLE peaks in ZnO are at ~ 2.5 eV (green) [49, 50] and orange-red at ~ 2.2 eV [51, 52]. The ZnO samples grown in an oxygen deficient atmosphere shows green emission, while the orange-red luminescence is observed in ZnO samples which are grown in oxygen rich environments [39, 40, 51 and 52]. Therefore, the green emission in oxygen deficient ZnO is attributed to the V_O in which transition takes place from conduction band and/or from the Zn_i site to the V_O level [39, 40]. The observation of an orange-red emission may be related to the increase in number of O_i sites [51, 52].

1.1.4 Applications of ZnO

ZnO is an attractive semiconductor which has applications in electronics, UV-blue photonics, acoustics, and sensing etc [1-6]. In electronics, ZnO has potential applications in fabricating transparent thin film transistors (TTFTs) which require all the device components to be transparent. Such TTFTs can be used in wide range of commercial applications where transparency is required. Because of the wide band gap of the channel material, TTFTs will not be degraded on exposure to visible light. The field effect mobility in ZnO based TTFTs is found to be significantly higher compared to the amorphous Si based transistors [4].

Heavily degenerate n-type conducting ZnO thin films are being considered as a cost effective replacement of indium tin oxide (ITO) for transparent conducting electrode (TCE)applications in optoelectronic devices, such as flat panel displays, light emitting diodes (LEDs), solar cells etc [3-6].

ZnO is a promising material for light emitting devices due to its strong and intense UV emission at room temperature. However, daunting problem in the reproducible growth of p-type ZnO has impeded the realization of p-n homojunction based LEDs utilizing ZnO [3-5].

High-quality ZnO thin films grown on Si and Sapphire have been successfully used in thin

film piezoelectric devices such as SAW resonators, filters, sensors, and micro electro mechanical systems (MEMS) etc [3-5].

Nanocrystalline ZnO thin films and nano rods or nanowires based FET sensors, owing to their large surface area, can be used for the detection of a large number of gases including NO_2, NH_3, H_2, H_2S, H_2O etc. The principle of gas sensor devices is based on the modification of nanowire FET channel conductivity. Oxygen vacancies in ZnO act as n-type donors on oxide surfaces which are also chemically active. Upon exposure of charge accepting gas molecules, for example, NO_2 and O_2, electrons are depleted from the conduction band resulting in a reduced n-type conductivity of the oxide. On the other hand, CO and H_2 molecules interact with surface adsorbed oxygen on ZnO and remove it leading to an increase in conductivity [3-5].

1.2 Transparent Conducting Oxides (TCOs)

Transparent conducting oxides (TCOs) are wide band-gap (E_g > 3.0 eV) metal oxides having good optical transparency (>85%) in the visible spectral range and high electrical conductivity. TCO thin films are extensively used as transparent conducting electrodes (TCEs) in optoelectronic devices such as flat panel displays, photovoltaic cells etc [53]. For these applications, commonly used TCO material is tin doped indium oxide (In_2O_3:Sn, abbreviated ITO). However, the scarcity and high price of indium led to the development of cost-effective alternatives of ITOs for industrial applications. Up to now, various binary metal oxide thin films including SnO_2, CdO, ZnO, impurity doped SnO_2 (SnO_2:F), impurity doped ZnO (ZnO:Al, ZnO:Ga) and many ternary compounds (Cd_2SnO_4, Zn_2SnO_4, $CdSb_2O_6$ etc) have been widely investigated for TCO applications [53]. Among these materials, Al and Ga doped ZnO thin films generally exhibit lower electrical resistivity (of the order of 10^{-4} Ω cm) when grown with optimized process parameters and therefore, can be considered as an

excellent choice for the replacement of ITOs [18-20, 54-56].

1.2.1 Electrical and Optical Properties

The requirement of high electrical conductivity in a TCO makes it a heavily degenerate semiconductor. Such high electron density arises due to the intrinsic defects (usually identified as oxygen vacancies and/or metallic interstitials) and/or extrinsic dopants which introduce shallow donor levels (for n-type) just below the conduction band [53, 56]. In order to achieve higher electrical conductivity, electron density has to be increased. However, as mentioned above, besides high electrical conductivity, TCO thin films must have very low absorption in the near UV-VIS-NIR spectral region. The transmission in the near UV is limited by the fundamental optical band-gap of the semiconductor as shown in Fig. 1.4. A second transmission edge comes in the NIR region, mainly due to reflection at the plasma frequency $\omega_p = \sqrt{Ne^2 / m^* \varepsilon_0 \varepsilon_r}$ where m^* is the effective mass of electron and $\varepsilon_r \varepsilon_0$ is the permittivity of the material [53]. Therefore, with increasing electron density IR absorption edge also shifts to the shorter wavelength, thus narrowing the optical transmission window. This creates a fundamental trade-off between the electrical conductivity and long wavelength transmittance in TCOs. However, if highly conducting films are achieved through enhancement of carrier mobility, then certainly there will be no deleterious effect on the optical transmission spectra of the films. Fig. 1.4 shows optical transmission (T), absorption (A) and reflection (R) spectra of a typical TCO thin film in a broad spectral range. The transmission window, fundamental optical adsorption edge and absorption due to plasma oscillations of the free electrons (corresponds to the plasma wavelength λ_p) in the conduction band are also shown in Fig. 1.4.

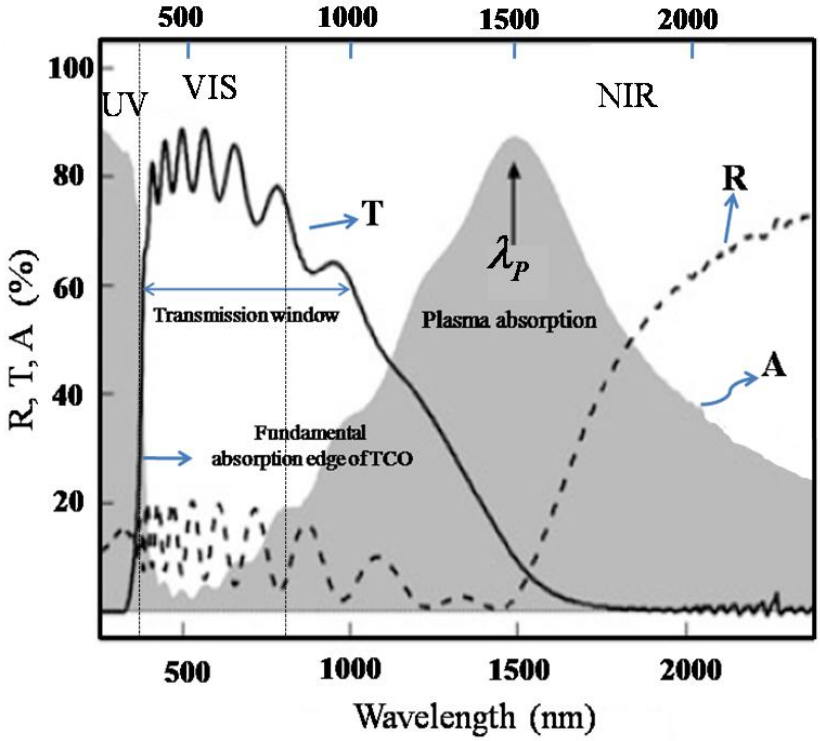

Fig. 1.4 Optical absorption (A), transmission (T) and reflection (R) spectra of a typical TCO thin film.

1.2.2 Other Essential Properties

TCEs are used as carrier collector in most of the optoelectronic devices and therefore, a high work function (~ 5 eV) of the TCE material is required. Surface roughness is another important characteristic, which drastically affect both the optical and electrical properties of the TCE and therefore, the device performance. For applications in organic LEDs, it is required to have extremely smooth TCEs (RMS roughness< 5nm) because, smoother surfaces yield lower contact resistance and also reduced surface scattering effects. However, in amorphous Si:H solar cells hazy or textured surfaces are preferred because, texturing of the TCE surface leads to trapping of the incident light due to enhanced scattering effects [53]. Long term stability of TCO coating is critical for stable performance of the device in open atmosphere. ZnO exhibits poor chemical stability whereas $SnO_2$is the most resistant TCO

material to etch chemically. However, chemical stability and moisture resistance of ZnO improves significantly with addition of dopants (Al, Ga, F, Co) [57]. Moreover, mechanically tough TCO coatings are required to ensure high scratch resistance. The hardness of the known TCO films increases as follows: Ag < ZnO < In_2O_3< SnO_2< TiN. The last but not the least criterion is the lower toxicity of the TCO material which is highly required for large scale manufacturing of TCEs. The toxicity levels of the elements currently used in the TCE industry are as follows: Zn < Sn < In < Cd.

1.2.3 Carrier Scattering Mechanisms in Polycrystalline TCOs

Usually, n-type doped ZnO thin films grown by sputtering, chemical vapor deposition (CVD) and atomic layer deposition (ALD) techniques for commercial scale fabrication of TCOs are polycrystalline in nature [54-56, 58]. Therefore, in this section we have discussed in detail the underlying carrier scattering mechanisms which control the electrical properties in polycrystalline and degenerately n-type doped ZnO thin films suitable for TCO applications.

The main carrier scattering mechanisms in polycrystalline thin films are grain boundary scattering, ionized impurity and neutral impurity scattering and lattice vibration scattering [59-66]. However, as the concentration of neutral donors in n-type doped ZnO thin films is very low and they have lower scattering cross sections, the influence of neutral impurity scattering is quite insignificant [59, 63]. Therefore, according to Matthiesen's rule, the reciprocal mobility is given by [59, 64],

$$\frac{1}{\mu} = \frac{1}{\mu_{gb}} + \frac{1}{\mu_i} + \frac{1}{\mu_{ph}} \tag{1.7}$$

where μ_{gb} , μ_i and μ_{ph} are contributions from grain boundary, ionized impurity and phonon scattering processes respectively. Apart from these fundamental scattering mechanisms, various crystallographic defects such as dislocations and stacking faults also contribute to the

scattering process [63].

(I) Grain boundary scattering

Polycrystalline thin films exhibit huge number of grain boundaries, which introduce electronic defect levels within the band gap of the semiconductor. These defect levels are charged by trapping electrons from the interior of the grains. In an n-type semiconductor depletion zones are generated on both sides of each grain boundary and therefore, creates an energetic barrier of height Φ_{GB} for conduction electrons. Seto *et al.* first introduced the grain boundary scattering model as show in Fig. 1.5 to explain the electrical properties in polycrystalline Si [67]. According to this model, carrier transport across the grain boundaries is possible by classical thermionic emission (TE) as shown in Fig. 1.5.

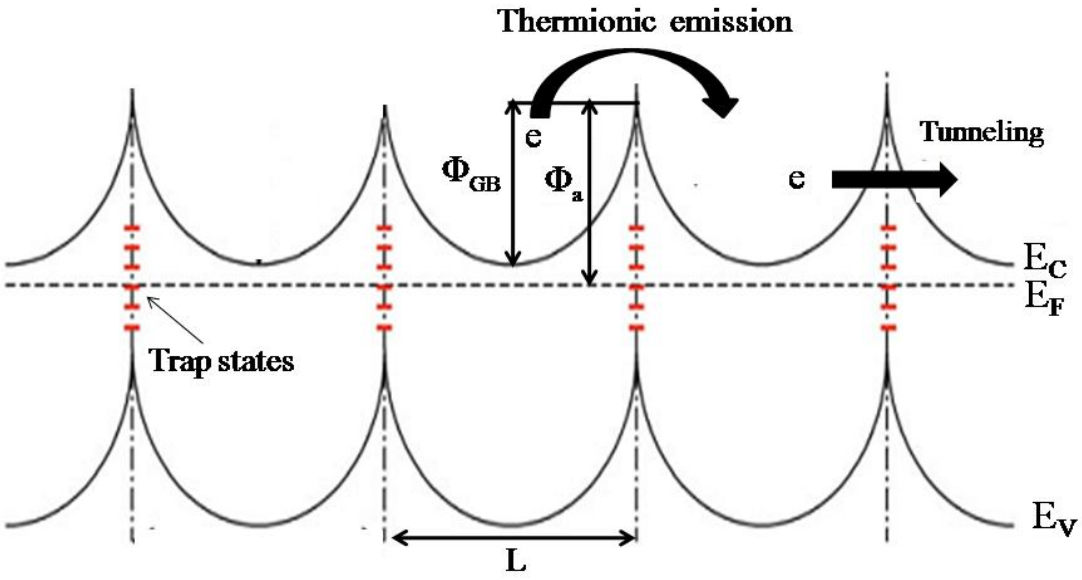

Fig. 1.5 Schematic band diagram of a linear row of grains of identical length L and grain barriers of height Φ_{GB} caused by the electron trap states at grain boundaries. Two different transport paths for electrons (1) Thermionic emission across the barrier, and (2) Tunnelling through the barrier are also shown by arrows.

The effective mobility (μ_{eff}) dominated by TE in case of degenerate semiconductor is given by [59],

$$\mu_{eff} = AT^{-1}\exp(-\Phi_a / k_B T) \tag{1.8}$$

where $\Phi_a=\Phi_{GB}-(E_F-E_c)$is the activation energy and E_F-E_c is the distance between the Fermi level and the bottom of the conduction band in the neutral region, k_B is the Boltzmann constant, T is the sample temperature and A is a constant. For degenerate semiconductors, E_F is within the conduction band and therefore, $\Phi_a< \Phi_{GB}$. In this case, both barrier width and height are sufficiently reduced and therefore, additional electron transport through tunnelling the barriers takes place. The width (d) of the depletion region can be calculated from $d = \sqrt{2\varepsilon_0\varepsilon_r\Phi_{GB}/qn}$ [59]. If we consider electron density n of the order of 10^{20} cm^{-3}, as usually measured in case of ZnO based TCOs; 'd' comes about only few angstroms (i.e. atomic layer thick). Therefore, in these films tunnelling current between grains would be a dominating phenomenon. The tunnel probability is given by [59],

$$T = \exp\left[-\frac{2}{\hbar}\int_{x_1}^{x_2}(2m)^{1/2}\{U(x)-E\}^{1/2}dx\right] \tag{1.9}$$

where $U(x)-E$ is the height of the barriers. Considering a rectangular barrier with height Φ_a and thickness d, the above Eq. 1.9 becomes

$$T = \exp\left[-\frac{2(2me\Phi_a)^{1/2}d}{\hbar}\right]. \tag{1.10}$$

Eq. 1.10 clearly indicates that, for polycrystalline TCOs as Φ_a and d are very small, tunnelling current across grain boundaries will be exceedingly high. Therefore, grain boundary scattering is unimportant in electron transport [59, 66]. Moreover, the mean free path (l_e) of conduction electrons is only few nanometers which is usually much lower than the grain size. This also indicates that intra-grain scattering is dominated over the inter-grain scattering in polycrystalline ZnO based TCOs. Steinhauser *et al.* have carried out an excellent

work in boron-doped ZnO thin films in which they observed a continious transition from grain boundary to intra-grain scattering with increasing electron density [66]. They found that for electron density < $1x10^{20}$ cm^{-3}, Hall mobility is much lower than the optical mobility which clearly indicates significant role of grain boundary scattering in electron transport. However, above this carrier density optical mobility and Hall mobility values are close to each other. This study confirms that at higher carrier density typically above $1x10^{20}$ cm^{-3} grain boundary scattering is not all a dominating factor in polycrystalline ZnO films. However, Ellmer *et al.* proposed that, as ZnO has high density of grain barrier trap states, grain boundaries could limit mobility for electron density as high as $2x10^{20}$ cm^{-3}[61, 65].

(II) Ionized Impurity Scattering

ZnO based TCO films exhibit a large number of ionized impurities including intrinsic defects such as oxygen vacancies, zinc interstitials and as well as extrinsic dopant atoms [56, 61]. These ionized point defects are strong scattering centres for electrons. For a non-degenerate semiconductor, mobility due to ionized impurity scattering shows a temperature dependence of $T^{3/2}$[59]. However, for degenerate semiconductors considering the non-parabolicity of the conduction band, the mobility is given by [63],

$$\mu_i = \frac{3(\varepsilon_r\varepsilon_0)^2 h^3}{Z^2 m^{*2} e^3} \frac{n}{N_i} \frac{1}{F_i^{np}(\xi_d)} \tag{1.11}$$

where $F_i^{np} = \left[1 + \frac{4\xi_{np}}{\xi}\left(1 - \frac{\xi_{np}}{8}\right)\right]\ln(1+\xi) - \frac{\xi}{1+\xi} - 2\xi_{np}\left(1 - \frac{5\xi_{np}}{16}\right)$ and $\xi_d = (3\pi^2)^{1/3}\frac{\varepsilon_r\varepsilon_0 h^2 n^{1/3}}{m^* e^2}$

$\xi_{np} = 1 - \frac{m_0^*}{m^*}$ describes the non-parabolicity of the conduction band, with m_0^* is the effective mass of electron at the conduction band edge. For parabolic band structure $m^* = m_0^*$ i.e. ξ_{np} =0. Therefore, ionized impurity limited mobility in degenerate TCOs is independent of sample temperature. At higher dopant concentration, formation of clusters may lead to even

lower mobilities because, μ_i is inversely proportional with Z^2[63, 64].

(III) Phonon Scattering

The most important scattering process that limits the electrical conductivity in metals or semiconductors is lattice vibration or phonon scattering. At higher temperatures, phonon scattering is always a dominant scattering mechanism in these materials. Ionized impurity scattering as discussed above is purely elastic i.e., $\left|K^i\right| = \left|K^f\right|$. On the contrary, phonon scattering involves absorption or emission of a phonon, i.e., $K^i \pm q = K^f + G$ where, K^i and K^f are the Bloch state wave vectors of incoming and outgoing electron, q is the phonon wave vector and G is the reciprocal lattice vector. Therefore, in phonon scattering a small but finite change in the electron energy takes place i.e., it is inelastic in nature. However, unlike ionized impurity scattering in degenerate semiconductors, phonon scattering is strongly dependent on temperature. The resistivity due to phonon scattering is given by the well known Gruneisen-Bloch (G-B) formula as follows [59]:

$$\rho(T) = \rho(0) + \frac{AT^5}{M\Theta_D}\int_0^{\Theta_D/T} \frac{x^5 dx}{\left(e^x - 1\right)\left(1 - e^{-x}\right)} \tag{1.12}$$

where $\rho(0)$ is the residual resistivity which is independent of temperature, the 2nd term is the G-B equation in which A is a characteristic constant, M is the atomic mass of the atom and is the Θ_D is the Debye temperature of the material. At temperature $T << \Theta_D$, $\rho(T)$ is proportional to T^5 and for $T >> \Theta_D$ it is proportional to T. Therefore, for degenerate TCO films, as carrier density is independent of temperature, Hall mobility μ α 1/T. However, the above formula for phonon scattering is valid for clean metals i.e., in the limit $ql_e = \frac{K_B T}{\hbar \nu_s} >> 1$ where q is the wave number of thermal phonons, ν_s is the sound velocity of acoustic phonons and l_e is the

elastic mean free path conduction electrons [68, 69]. In case of disordered metals $(ql_e << 1)$ in the same temperature limit $T << \Theta_D$, resistivity was found to be proportional to T^2 due to electron-phonon-impurity interference phenomena [70].

1.2.4 ZnO as a Potential TCO Material

We have already discussed the electrical and the optical properties of ZnO in sections 1.1.2and1.1.3, respectively. Here we have summarized the important properties of ZnO thin films which make it a suitable choice for TCE applications.

1. ZnO is non toxic, environment friendly and low cost material.

2. It has a wide optical band-gap of ~ 3.3 eV which lies in the UV spectral range.

3. As grown intrinsic ZnO thin films are usually found to be n-type conducting. Such background n-type conductivity in as grown films is highly advantageous for TCE application. Moreover, extrinsic n-type doping in ZnO can be dramatically increased through incorporation of group III elements like Al, Ga and In etc.

4. Relatively low temperature deposition of highly n-type conducting ZnO thin films on commercially available glass and flexible substrates (polymer, PET etc) is possible.

5. ZnO thin films show preferential growth along the [0001] direction due to the lowest surface energy associated with the (0001) basal plane. Such growth mode results in textured ZnO thin films which are particularly important for solar cell applications. In addition, the hexagonal structure of ZnO provides epitaxial growth on technologically important substrates such as sapphire and therefore, facilitates its integration with the optoelectronic devices.

1.3 Electron Transport in Doped Semiconductors

We have already discussed in the preceding section that degenerate n-type conductivity in TCO films can be achieved through intrinsic and/or extrinsic doping in the host semiconductor lattice. Therefore, it is imperative to briefly discuss the effect of doping on the electrical properties of semiconductors and the evolution of electron transport from band-gap insulating state to metallic to Anderson-localized insulating state with increasing dopant density and dopant induced static-disorder in the films [71-73].

1.3.1 Isolated Shallow Impurities

The band theory of solids with ideal crystal structure i.e., considering movement of electrons in presence of periodic atomic potentials, successfully explains the division of solids into metals and insulators. In metals, Fermi level lies inside the conduction band i.e. in the range of allowed energies. In insulators, Fermi level lies in the range of forbidden gap, with the distance from the Fermi level μ to the nearest edge of the allowed energies E_b

$$\left|E_b - \mu\right| >> K_B T_r \tag{1.13}$$

where T_r~ 300K is the room temperature and K_B is the Boltzmann constant [71]. In metals, as the Fermi level lies in the vicinity of the delocalized states, they show finite conductivity (σ) at T→0 K. On the contrary, for insulators σ→0 as T→0 K because, in the vicinity of Fermi level all states are localized (Anderson-localized insulator) or there are no electronic states (band-gap insulator) [71, 73]. Impurities may create electronic levels E_0 in the forbidden gap. The impurity levels which are close to the conduction band (CB) or valance band (VB) edge may take part in electronic conduction at T > 0 K and are called shallow donors or shallow acceptors, respectively. The presence of donors (n-type) or acceptors (p-type) displaces the Fermi level close to E_b and therefore, electronic conductivity is determined by the impurity

concentration and the ionization energy $|E_b - E_0|$ of the impurities compared to the thermal energy at the measurement temperature. The corresponding electrical conductivity is called impurity conduction in a doped semiconductor [71, 73 and 74]. The materials possessing intrinsic (undoped) or impurity conduction (doped) are called semiconductors. Intrinsic conduction implies conduction due to thermal excitation of carriers across the band-gap between conduction and valence bands of the material. This is called “intrinsic” because it does not require impurity states and therefore, comes into the picture only at higher temperatures. For doped semiconductors, when the temperature is comparable to the activation energy of dopants, decreasing the temperature results in a decrease in conductivity due to carrier “freeze out”, i.e. free carriers become frozen on defect sites and at $T \rightarrow 0$ K conductivity $\sigma \rightarrow 0$ i.e. it becomes an insulator [71, 73 and 74]. Therefore, classifying a material as a semiconductor is rather conditional and in particular depends on the measurement temperature. The conductivity of a semiconductor can be varied from semi-insulating via semi-conducting to semi-metallic regime by varying the dopant concentration. Nearly all of the useful applications of semiconductors are made possible by the ability to selectively introduce particular impurities into the host lattice. Impurities are indeed lifeblood of virtually all semiconductor devices including rectifying p-n junctions, transistors, light emitting diodes, solar cells, photo-detectors etc. Incorporated impurities predominantly occupy substitutional lattice sites into the host semiconductor lattice. However, for compound semiconductors, for example in case of III-V GaAs doped with Si, impurity atom Si can go either on Ga site as an n-type dopant or can substitute As where it act as an acceptor. Which of the two sites (cation or anion site) is preferred by an impurity atom depends on valance electron correlation between impurity and host, the bonding strength of the impurity and the host lattice and the size of the impurity atom. The energy required to ionize the impurity atom is called the ionization energy or the activation energy. For technological applications of

doped semiconductors, shallow impurities, which are completely ionized at room temperature or at device operating temperature, are highly required. The hydrogen atom model can be implemented for obtaining the activation energy and localized state wave functions of the shallow impurities [71, 74]. Such impurities are called 'hydrogenic impurities' because they can be described by the hydrogen atom like potential

$$V(r) = \frac{e}{4\pi\varepsilon r} \tag{1.14}$$

which is identical to the potential of the hydrogen atom except permittivity ε of the host material has been used instead of the free space. The Schrödinger Eq. is written as

$$-\frac{\hbar^2}{2m^*}\Delta\Psi + \frac{e}{4\pi\varepsilon r}\Psi = E\Psi \tag{1.15}$$

The radius of the donor ground state (n=1) is then given by

$$a_H^* = \frac{4\pi\varepsilon\hbar^2}{m^* e^2} = \frac{\varepsilon_r}{m^*/m_0} 0.53\,\text{Å} \tag{1.16}$$

The activation energy is given by

$$E_a = -\frac{m^*/m_0}{\varepsilon_r^{\,2}} 13.6eV \tag{1.17}$$

Therefore from Eqs.1.16 and1.17 we see that effective Bohr radius of donors increased (much larger than the unit cell of the lattice) and activation energy is reduced due to dielectric screening [74].

1.3.2 Mott Transition

So far we have discussed the role of isolated and non-interacting shallow impurities on the electrical conductivity of an insulator ($\sigma \to 0$ at $T \to 0$ K). As the doping concentration increases, the Coulomb potentials of impurities start overlapping. As a result, electrons can transfer more easily from one donor site to another by either tunnelling or by thermal

emission over the barrier. The probability of these processes increases with increasing donor concentration. In other words, the activation energy for electron transport is reduced and eventually vanishes i.e. $\sigma \neq 0$ even at $T \rightarrow 0$ K. Therefore insulator-to-metal transition occurs which is known as Mott transition [71, 73 and 74]. The Mott transition can also be viewed as follows:

Effective screening of impurity potentials at high carrier concentration reduces the activation energy because such potentials are less capable of binding the electrons (considering n-type impurities). The screened Coulomb potential (see Fig. 1.6) also known as Yukawa potential is given by

$$V(r)_{Screened} = (e / 4\pi\varepsilon r)\exp(-r / r_0) \tag{1.18}$$

where r_0 is the Thomas-Fermi screening radius is given by

$$r_0 = \frac{1}{2}\left(a_H^* n^{-1/3}\right)^{1/2} \tag{1.19}$$

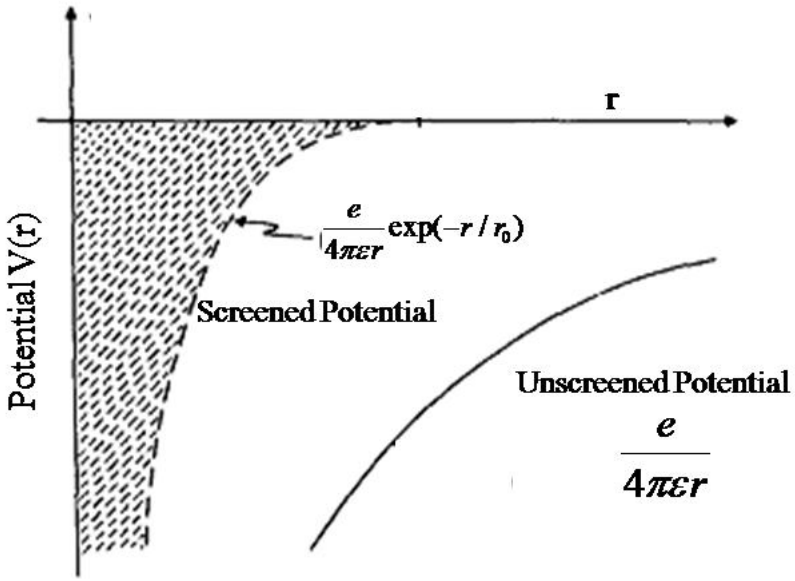

Fig. 1.6 Comparison of screened and unscreened Coulomb potentials of an impurity atom

where $n^{-1/3}$ is the average distance between electrons. If all electrons are localized at their parent atomic sites, the system is described by the length a_H^*. On the contrary if the electrons are itinerant, it is described by the screening length r_e. For low donor density, $r_e > a_H^*$, the screening is inessential, each electron is in the vicinity of its donor atom and the material is an insulator. However, as the donor concentration increases i.e. $n^{-1/3}$ decreases and the inequality is changed to $r_e < a_H^*$, the state of an insulator becomes unstable. If all n electrons abandon their respective donors, they would not be able to return to their parent atom because of the strong screening effect. The ionized donors provide a positive background which compensates the negative charge of electron cloud. Hence, the equality

$$r_e = a_H^*, \text{ i.e., } \frac{1}{2}\left(a_H^* n_c^{-1/3}\right)^{1/2} = a_H^*, \; a_H^* n_c^{1/3} = 0.25 \qquad (1.20)$$

is the condition for the occurrence of the insulator-to-metal transition at the critical carrier density n_c, called Mott critical density [71, 73 and 74]. Peter Phillip Edwards and Michell J. Sienko showed how well Mott criterion is obeyed for a wide range of materials [75]. The above criterion for Mott transition has been derived by considering hydrogen-like impurities. Another somewhat more general explanation can be given in the Hubbard scheme as shown schematically in Fig.1.7 [71]. Let us consider that the energy of an electron at an impurity centre is E_0. According to Pauli Exclusion Principle two electrons with opposite spins can stay at this level. However, if the impurity centre already has one electron, the other electron may be attached to it by overcoming the electrostatic repulsion between the electrons. Therefore, the energy level of the second electron is higher by a value U, the intra-atomic interaction, also called the 'Hubbard U'. If impurity concentration is n, then both levels are spread into mini-bands, each with nV levels (V is the volume) due to the overlap of the wave functions. Since the electron concentration is also n, then for the non-overlapping condition

of the mini-bands, all the nV electronic levels in the lower mini-band are filled (lower Hubbard band, LHB) and all the nV levels in the upper mini-band (upper Hubbard band, UHB) are empty. Therefore, the material is an insulator with a gap at the Fermi level.

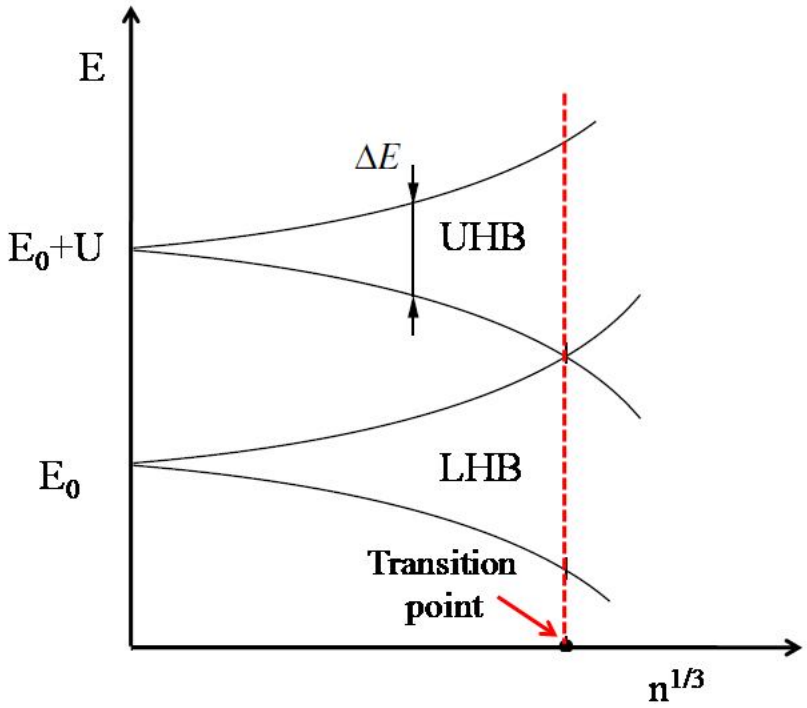

Fig. 1.7 Schematic of Mott transition in Hubbard Scheme.

The mini-band width is given by the transfer integral [71],

$$\Delta E \approx 2J \approx 2\int \psi_i \hat{H} \psi_j d^3r \approx 2E_0 \exp(-r_{ij}/a_H^*) \approx 2E_0 \exp(-1/n^{1/3}a_H^*) \tag{1.21}$$

An increase in concentration results in broadening of the band and eventually they overlap at the critical concentration n_c. At this concentration,

$$\Delta E \approx U \approx 2E_0 \exp(-1/a_H^* n^{1/3}) \tag{1.22}$$

Considering $U \approx E_0$ (both quantities are of the order of atomic energy), the numerical value of the above expression hardly differs from that obtained in Eq.1.20.

The suggested criterion (Eq. 1.20) for the insulator-to-metal transition does not provide any information on the nature of the transition [72]. Mott first proposed that insulator-to-metal

transition in a perfect crystalline material at T=0 K is discontinuous in nature as shown in Fig. 1.8 [72].

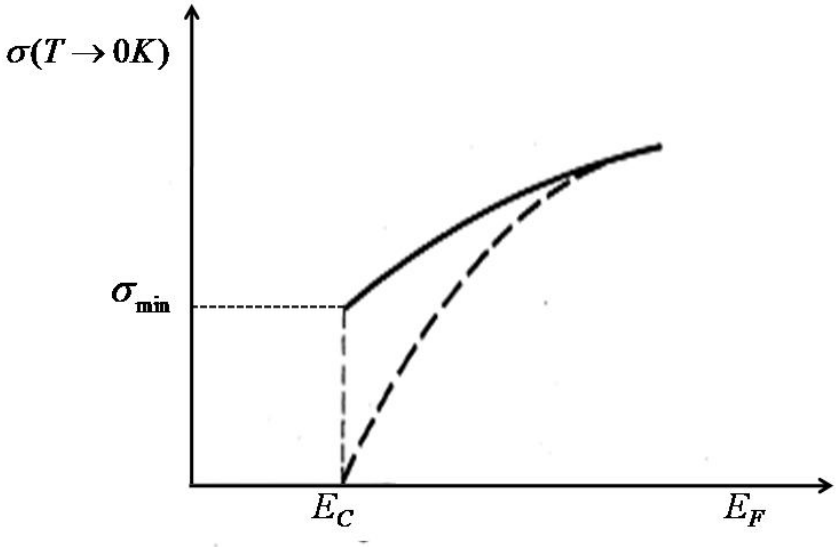

Fig. 1.8 Two possibilities of a continuous or discontinuous transition with σ_{min} are shown. E_C denotes the position of the mobility edge.

He argued that at the transition, there exists a minimum metallic conductivity (σ_{min}), prior to the complete localization of the itinerant electrons [72]. Mott's proposal was based on the Ioffe-Regel (IR) criterion [71] which states that mean free path, l_e, of the itinerant conduction electrons cannot be less than the de Broglie wavelength (approximately K_F^{-1} where K_F is the wave vector at the Fermi surface). Therefore, using the IR criterion $l_e \sim K_F^{-1}$ or $K_F l_e \sim 1$, the expression for 3D Drude conductivity [71],

$$\sigma = \frac{ne^2 l}{\hbar K_F} = (3\pi^2)^{-2/3} \frac{e^2}{\hbar} n^{1/3} (K_F l_e) \tag{1.23}$$

becomes

$$\sigma_{min} = (3\pi^2)^{-2/3} (e^2/\hbar) n^{1/3} \tag{1.24}$$

Mott's concept is that the zero temperature conductivity of the metallic state continuously decreases with decreasing n, and, upon reaching the value σ_{min}, the conductivity drops to zero

i.e., to the insulating state in jumping manner as shown by the solid line in Fig. 1.8 [72]. However, the existence of σ_{min} and the nature of metal-insulator transition were thoroughly investigated by numerous experiments [76-79] which did not confirm the above concept of minimum metallic conductivity and proved that the transition is continious. Abrahams *et al.*[80] on the basis of scaling theory have predicted a continious insulator-metal transition in a non-interacting disordered electronic system.

1.3.3 Anderson Transition

So far we have discussed about Mott transition which is completely driven by electronic correlations, the role of disorder has not been considered. However, in doped semiconductors, dopant atoms not only introduce free carriers into the system, but also create disorder by randomly occupying the host lattice sites. Therefore, the effect of disorder has to be included to analyze electron transport in doped semiconductors [71, 72].

Let us consider, freely moving non interacting electrons in presence of perfect periodic potential V(r) = V(r + a) (where 'a' is the lattice parameter) in an ideal lattice. The single-particle Schrödinger equation is given by

$$\hat{H}\psi(r) = \left(-\frac{\hbar^2}{2m^*}\Delta + V(r) \right)\Psi(r) = E\Psi(r) \tag{1.25}$$

However, in every real solids lattice imperfections and all other kinds of disorder exist and, thus, differs from the ideal model. In order to account this, a disorder potential significantly

The solution of the Eq.1.25 gives Bloch states which are extended throughout the lattice. U(r) has been incorporated in the single-particle Schrödinger equation, the resulting equation is given by

$$\hat{H}\psi(r) = \left(-\frac{\hbar^2}{2m^*}\Delta + V(r) + U(r) \right)\Psi(r) = E\Psi(r) \tag{1.26}$$

Eq. 1.26 provides localized states. It was first pointed out by Anderson that if the disorder strength is sufficiently strong then it can even induce a metal-insulator transition (MIT) [72, 81].In 1958, Anderson in his seminal paper on "The absence of diffusion in certain random lattices" pointed out that if the randomness in electronic-state energies at different lattice sites is large enough, itinerant Bloch wave functions of conduction electrons which are extended throughout the lattice [see Fig.1.9 (a)] become spatially localized [see Fig.1.9 (b)] [81].

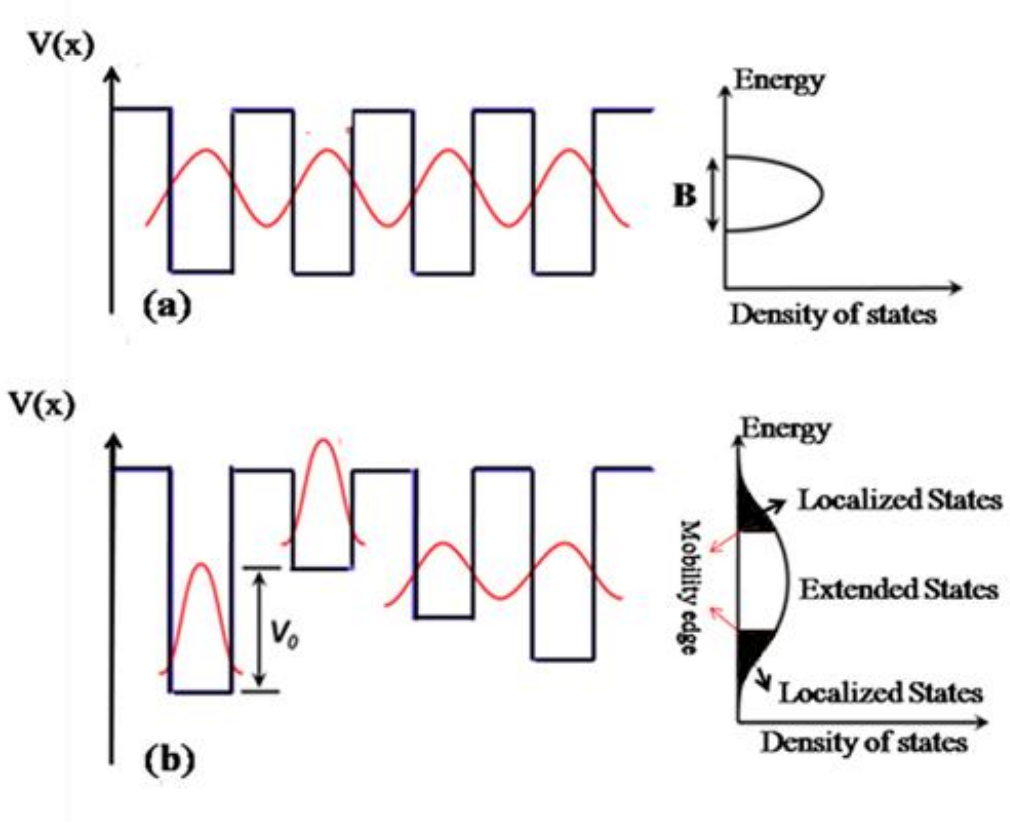

Fig. 1.9 The lattice potential and density of states of (a) an ideal crystal and (b) a disordered crystal are shown. The 'mobility edge' which separates the localized states from that of extended states is also shown with arrows.

The localized wave function as shown in Fig. 1.9 (b) is given by

$$|\psi(r)| \sim \exp\left(|r - r_0| / \xi\right) \tag{1.27}$$

where ξ is the localization length. Anderson used a model of a periodic array of random rectangular potential wells and concentration $N=a^{-d}$, (where 'a' is the lattice parameter and 'd' is the dimension of the lattice) as shown in Fig.1.9 [71]. The depths of the wells lie in the energy interval V_0 which is a measure of the strength of disorder in the system. The tight binding approximation has been used to consider the overlap between wave functions of nearest neighbours. The transfer integral is given by

$$J \approx \int \psi_1 \hat{H} \psi_2 d^3 r \tag{1.28}$$

Ψ_1 and Ψ_2 be the wave functions of electrons at two adjacent sites. The band width due to overlap is given by

$$B = 2ZJ \tag{1.29}$$

where z is the coordination number. For the condition $V_0 >> B$ the states at the Fermi level are localized and the material is called an Anderson insulator. Its structure is different from that of the band insulator. For band insulators, the Fermi level is located in the forbidden gap where the density of states is completely zero. On the contrary, for Anderson insulators, the density of states at the Fermi level is finite. If the parameter V_0 / B is not great enough to give localization throughout the band then states in the band tails would be localized and that energies of localized and extended states would be separated by a sharp energy E_c, known as 'mobility edge' [see Fig.1.9 (b)]. The electrons or holes thermally excited above the mobility edge participate in electrical conduction through diffusion. The carriers below mobility edge participate in the hopping conduction at any finite temperature. Therefore, insulator to metal transition can be triggered by bringing the Fermi level into the coincidence with the mobility edge. This can be done either by varying the parameter V_0 / B or by shifting the Fermi level through carrier incorporation [71].

So far extensive research work on electron transport in various disorder electronic systems

including metallic alloys, doped semiconductors has been carried out which shows that neither Anderson's nor Mott's formalism is sufficient to understand the metal-insulator transition (MIT). Rather, the effect of disorder and interactions between electrons has to be simultaneously considered. Therefore, MIT in these systems is always 'Mott-Anderson type' [71, 72, 78, 82 and 83].

Degenerately doped ZnO thin films which are suitable for TCE applications, always reside on the metallic side of MIT. In this regime, electron transport is strongly influenced by the effects of weak localization (WL) and electron-electron interactions (EEIs) [71, 83]. Therefore, in the following we have briefly discussed these two effects.

1.3.4 Weak Localization

The conventional theory of electron transport in metals is given by Drude formula, according to which free electrons, under the action of an externally applied electric field, are accelerated according to Newton's law of motion until they collide with the ion centres after a time τ, called the relaxation time. The average distance between two successive collisions is given by the mean free path l_e. Due to these independent scattering events the electrical conductivity is given by

$$\sigma_0 = \frac{n_e e^2 \tau}{m} \tag{1.30}$$

where n_e is the electron density and m is the free electron mass. Temperature dependence of metallic conductivity is given by

$$\sigma = \sigma_0 - AT^n \tag{1.31}$$

where the value of n is determined by the inelastic scattering processes such as n=2 (Fermi liquid theory) for electron-electron scattering and in general larger than 2 if electron-phonon scattering dominate. Therefore, the relaxation of electron momentum and the finite value of

the conductivity at T→0 K, (i.e. the residual conductivity σ_0) are due to the imperfections in the lattice. Eq. 1.30 can also be obtained from the evolution of the electron distribution function in presence of an external electric field in semi-classical Boltzmann transport theory. In both Drude and Boltzmann transport theory it is assumed that all electrons are moving along classical trajectories and quantum mechanical interference phenomena are neglected. This description is valid in the limit $K_F l_e >> 1$, i.e. mean free path l_e must be far larger than the wave length λ_F of the electron wave functions to consider them as quasi-particles. However, for higher concentration of defects or in low dimensional electronic systems, the phenomenon of quantum interference becomes important and the Boltzmann transport equation is not applicable. For these dirty metallic systems, the constructive self-interference of electronic waves, as they backscattered from the randomly distributed impurities, gives rise to the weak localization effects as schematically shown in Fig. 1.10 [71, 83-85].

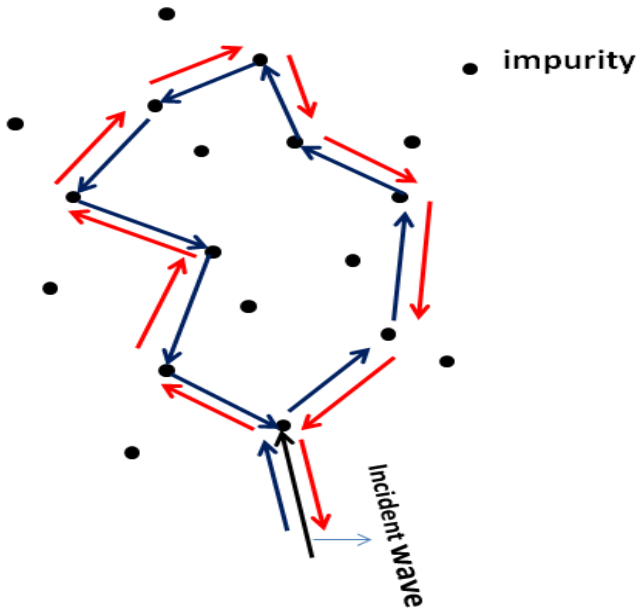

Fig.1.10 Schematic representation of weak localization effect in a disordered electronic system

In 3-dimensional systems, the correction due to WL is given by [71, 83],

$$\frac{\delta\sigma}{\sigma} = -\frac{1}{K_F{}^2 l_e}\left(\frac{1}{l_e} - \frac{1}{L_\varphi}\right) \tag{1.32}$$

where L_φ is the phase-coherence length and is given by

$$L_\varphi = \sqrt{D\tau_\varphi} \approx l_e\sqrt{\tau_\varphi / \tau} >> l_e \qquad (\text{for } \tau_\varphi >> \tau) \tag{1.33}$$

where $D = v_F^2\tau / 3$ is the diffusion constant with $v_F = l_e / \tau$ and τ_φ is the phase-coherence time over which the interfering electrons retain their phase memory. Eq. 1.33 clearly indicates why we need a dirty metallic system to observe WL effects. Temperature dependence of WL (see Eq. 1.32) is completely determined by the term associated with L_φ as follows

$$L_\varphi \propto \tau_\varphi{}^{1/2} \propto T^{-p/2} \tag{1.34}$$

As can be seen from Eq. 1.34, temperature dependence of τ_φ is determined by the temperature dependence of the dominating inelastic scattering rate responsible for electron dephasing. Later in section 1.3.6, we have discussed in detail various inelastic scattering processes in disordered electronic systems which give rise to different values of 'p'. Substituting Eq.1.34 in Eq. 1.32 we obtain the WL term as [71, 72, 83-85]

$$\frac{\delta\sigma}{\sigma} = AT^{p/2} \tag{1.35}$$

This term has to be added with the Boltzmann term in Eq. 1.30 to consider the WL contribution.

1.3.5 Electron-Electron Interactions

In WL correction, the effect of electron-electron interactions (EEIs) has not been considered. However, in a real metal, electrons interact through screened Coulomb potential. In Landau's

Fermi-liquid theory EEIs have been considered for systems without disorder i.e. electrons move like plane waves. Later Altshuler and Aronov showed that long range interactions in disordered Fermi liquids lead to strong singularities near the Fermi level [86]. The correction due to EEIs in 3D conductivity is given by [71-73, 83],

$$\frac{\delta\sigma}{\sigma} = \frac{C}{\pi^3 \hbar D l_e N(E_F)}\left(1 - \frac{l_e}{L_T}\right) \tag{1.36}$$

where $L_T = \left(\hbar D / K_B T\right)^{1/2}$ is the interaction length and $N(E_F)$ is the density of states at the Fermi level. Generally, interaction effects are much enhanced in disordered solids because electrons diffuse rather than freely moving as plane waves. As a result, an electron can stay in a given region of space for much longer time and therefore, can interact with other electrons. From Eq. 1.36 we see that, EEIs result in a temperature dependent correction term $mT^{1/2}$ (m can have either sign) to the Boltzmann conductivity.

1.3.6 Electron-Dephasing

Above we have discussed about WL and EEIs in which coherent electronic wave functions interfere constructively. However, coherence of their wave functions is randomized i.e., dephasing occurs due to various inelastic scattering processes such as, electron-phonon, electron-electron scattering etc [87]. As we have already showed that WL (Eq. 1.32) depends on the temperature dependence of the dominant inelastic scattering rate i.e., the value of the coefficient 'p'. It is experimentally obtained by temperature dependent magnetoresistance measurements [87]. In case of clean metals $(ql_e >> 1)$, the scattering rate $(1/\tau_{ph})$ due to electron-phonon scattering is proportional to T^3 [76-78, 87].This is well established both theoretically and experimentally. However, in case of disordered electronic systems $(ql_e << 1)$, both experimental and theoretical calculations show strong discrepancy [68, 69 and 87]. The

expected T^4 dependence of electron-phonon scattering rate has not been observed experimentally [68, 69 and 87]. J. J. Lin *et al.* have carried out extensive work on electron dephasing in various disordered metallic alloys of varying degree of disorder [68, 69 and 87]. They found that, in most of the cases the value of 'p' lies in between 2-4. In three dimensional strongly disordered systems or close to MIT, electron-electron scattering is found be dominated over the electron-phonon scattering. In dirty metallic systems the inelastic scattering rate due to electron-electron process is given by [87],

$$1/\tau_{e-e} = C(l_e)(K_B T)^{d/2} \tag{1.37}$$

where C depends on the elastic mean free path and d is the dimensionality of the system.

1.4 Atomic Layer Deposition of ZnO: Literature Review

In section1.2.4 we have discussed the potential of n-type doped ZnO thin films for TCE applications in optoelectronic devices. However, industrial scale manufacturing of TCOs requires a suitable thin film deposition technique which at least offers large-area coating and high deposition rate. These requirements can be achieved by employing any one of the following thin film deposition techniques: sputtering, chemical vapor deposition (CVD) or atomic layer deposition (ALD). Among these, ALD possesses a number of industrially and technologically important features which include large area uniformity of the grown films, excellent conformality, easy and precise thickness control down to molecular level, pin-hole free dense films, high degree of reproducibility in various film properties and low growth temperature etc [88-90]. Moreover, thin film deposition cost in ALD can be sufficiently reduced by using cost effective metal halide precursors. Higher deposition rate compared to the single-wafer thermal ALD reactor can also be achieved by employing spatial ALD or roll-to-roll ALD systems [91]. Therefore, ALD is of course a better choice to fabricate ZnO based TCOs for commercial applications.

In recent years, atomic layer deposition (ALD) in which thin film growth proceeds through self-limiting reaction chemistry between the precursor molecules and the growing surface, has emerged as a potential technique to grow ZnO thin films [92-99]. Detail discussions on the principle of ALD, its instrumentation, applications and limitations have been presented in chapter 2.Here we will present a comprehensive overview of the existing literature on the growth of intrinsic and doped ZnO thin films using ALD and the current state of research in this field.

1.4.1 Precursors for ZnO Deposition

ZnO thin films were successfully grown by using variety of Zn and oxygen precursors. Most possibly, the first research article on the growth of ZnO thin films using ALD was reported by Tammenmaa *et al.* using anhydrous zinc acetate ($Zn(CH_3COO)_2$) and H_2O as precursors for Zn and oxygen respectively [100].Wo´jcik*et al.* have also used the same combination of precursors to deposit ZnO films on different substrates in the temperature range of 280-400^0 C [99]. However, there are very few reports in literature, in which $Zn(CH_3COO)_2$ has been used for the growth of ZnO using ALD. The reasons are the followings: (1) $Zn(CH_3COO)_2$is a solid precursor and therefore, it needs to be heated to create sufficient vapor pressure or sometimes carrier gas assisted pulsing has to be used for sufficient precursor dosing into the reactor. (2) The ligand exchange reaction between $Zn(CH_3COO)_2$ and surface –OH groups occurs at relatively higher substrate temperatures to deposit ZnO films. The lowest deposition temperature in this case is 280^{0}C as have been reported by Wo´jcik*et al*. [99]. However, low thermal budget depositions of ZnO thin films for fabricating novel electronic devices on flexible substrates require highly reactive precursors. Unlike CVD, in ALD there is no gas phase reaction between precursor molecules [88-90]. Therefore, highly reactive and volatile precursors can be employed to grow thin films at lower temperatures. Organometallic diethyl

zinc (DEZ) and H_2O have been extensively used for this purpose because the reaction between them is quite exothermic. DEZ is normally kept at ~ 20^0C at which it has a vapor pressure ~ 12.2 Torr (=16.2 mbar) which is sufficient for efficient precursor dosing into the reactor. Typical deposition temperatures of ZnO thin films using DEZ and H_2O are in the range of ~ 80–200^0C [92-98]. However, room temperature growth of polycrystalline ZnO films has also been reported by Jari Malm *et al.* [101]. Dimethyl zinc (DMZ), which is also highly volatile liquid precursor and provides low temperature depositions. Higher growth per cycle (GPC) has been observed using DMZ compared to DEZ. It has been attributed to the less steric hindrance effect due to smaller ligand size of DMZ precursor molecules compared to DEZ [102]. Metal halide $ZnCl_2$ and H_2O have also been used, but it requires heating of the $ZnCl_2$ precursor and exceedingly high deposition temperatures [103]. For oxygen source, apart from de ionized water, several other precursors, including O_2,O_3, mixture of O_2 and O_3, $H_2O_2$and N_2O, have been used with DEZ or DMZ [108, 109]. Moreover, plasma form of oxygen and H_2O has also been used in plasma-enhanced ALD (PEALD) processes [110, 111]. The high reactivity of the plasma species facilitates growth of high quality films with lower defect density (high degree of stoichiometry) at low deposition temperatures.

1.4.2 GPC and ALD Window for ZnO Deposition

Almost in all reports of ALD grown ZnO films, a temperature window also know as ALD window has been observed in which GPC is independent of growth temperature and thin film growth proceeds through self-limiting vapour-solid reactions [88-90, 104-111]. However, the values of GPC and ALD widow are widely scattered in literature [92, 93, 95-99 and 104-111]. This is because; GPC value is determined by the crystal orientation and the incubation or nucleation period of ZnO on the substrate. Moreover, reactor design also plays a crucial role in determining ALD window. In Table 1.1, we have listed the values of GPC and ALD

window for ZnO thin films grown on different substrates using $Zn(C_2H_5)_2$precursor and different co-reactants.

Table 1.1 ALD processes reported for the growth of ZnO thin films with $Zn(C_2H_5)_2$precursor and different co-reactants. The GPC values are within the ALD window.

Precursor/Co-reactant	Substrate	ALD window	GPC	Reference
$Zn(C_2H_5)_2/H_2O$	Au, Glass	130-180 ^{0}C	2.2 Å	104
$Zn(C_2H_5)_2/H_2O$	Sapphire (0001)	130-180 ^{0}C	2.7 Å	105
$Zn(C_2H_5)_2/H_2O$	Glass, Si(100)	100-180 ^{0}C	1.9 Å	106
$Zn(C_2H_5)_2/H_2O$	Si(100)	100-160 ^{0}C	2.3 Å	107
$Zn(C_2H_5)_2/N_2O$	Sapphire (0001)	290-310 ^{0}C	2.6 Å	108
$Zn(C_2H_5)_2/O_3$	SiO_2/Si	230-250 ^{0}C	1.9 Å	109
$Zn(C_2H_5)_2/H_2O$ Plasma	Si(100), Quartz	150-200 ^{0}C	2-2.2 Å	110
$Zn(C_2H_5)_2/O_2$ Plasma	Glass/Si	200-250 ^{0}C	2.8 Å	111

1.4.3 Crystalline Quality of Intrinsic ZnO Thin Films

Although ALD was patented by Suntola in the name of atomic layer epitaxy (ALE), epitaxial growth of high-quality thin films has rarely been reported using this technique till date [112]. In most of the cases, films are polycrystalline or amorphous in nature [88-90]. In literature, usually polycrystalline growth of ZnO thin films has been reported on different substrates in a wide range of deposition temperatures [92-111]. However, preferred orientation of grains can be obtained by varying deposition temperature and other process parameters such as pulsing and purging times, precursor flow rate etc [98, 99, 101, 113 and 114]. At lower growth temperatures, films are generally composed of (10.0), (10.1) and (00.2) oriented grains and

preferred (00.2) orientation is observed at higher temperatures [92, 93, 95, 96, 98, 99 and 106]. Pung *et al.* have given an explanation of the change of growth mode on the basis of the reaction chemistry between DEZ and H_2O [98]. According to them, at relatively higher temperatures (155-220^{0}C), premature dissociation of DEZ molecules provides ethyl group fragments which could adhere on the (00.2) polar surface and therefore, suppressed the c-axis growth of grains. At higher temperatures, i.e. above 220^{0}C, these ethyl groups could be further decomposed into CO, CO_2 and H_2O. Thus, suppression of (00.2) growth mode is no longer possible and ZnO films showed preferred (00.2) orientation at higher temperatures. Wo´jcik*et al.* showed that orientation of grain growth can be controlled by varying the purging time between the precursors [99]. Longer purging time provides not only the complete removal of excess unreacted precursors and reaction by products but also facilitates to prepare a better surface by allowing longer diffusion time for the adsorbed species. Apart from these approaches, suitable substrates namely, (0001) sapphire and GaN have been used to grow high crystalline quality ZnO films [105, 108, 115-117]. Growth of mono crystalline ZnO thin films have been reported by Kopalko *et al.* and Wachnicki *et al.* on GaN/Al_2O_3 using $ZnCl_2$ and DEZ respectively [116, 117]. Ching-Shun Ku *et al.* reported growth of epitaxial ZnO thin films on (0001) sapphire at very low-temperatures (25-160^{0}C) using interrupted flow of precursors DEZ and H_2O [118]. The main motivation of this method was to enhance the duration of reaction between the precursor molecules and the surface states. However, they did not carried out any high resolution X-ray diffraction and TEM measurements to confirm the epitaxial nature of the films. Indeed, films were composed of grains with average size of ~ 50 nm and therefore, films are preferred (00.2) oriented rather than epitaxial in nature. Chen *et al.* obtained high-quality ZnO epi-layers on (0001) sapphire through an RTA treatment of low-temperature grown films [119]. Lee *et al.* reported buffer assisted growth of ZnO thin films on Si (111) substrates in which, initially low-temperature

buffer layer at 180^0C was grown and then the main layer growth was carried out at 270^0C. Significant improvements in the structural, morphological and optical properties were observed in these films. Actually, the crystalline quality of ALD grown films is largely determined by the initial stage growth mode. At higher deposition temperatures, agglomerates can form due to the surface migration of the adsorbed species and therefore results in columnar growths of grains with preferred orientation. On the contrary, at lower deposition temperatures, smooth amorphous or highly polycrystalline films are often observed due to poor surface mobility of the adsorbed species. Baji *et al.* have carried out a detail investigation on the nucleation and growth of ZnO films on different substrates by varying the number of cycles, DEZ pulsing time and deposition temperature [115]. Island-like growth mode of ZnO films was observed on Si substrates even with sufficiently long exposure time of the DEZ precursor. With increasing number of cycles, the number of islands increased and ultimately coalesced together to provide full coverage of the substrate. Therefore, polycrystalline growth of ZnO films on Si substrates has been achieved which was extensively reported in the literature and discussed above. However, layer-by-layer growth of ZnO was observed on GaN substrates at all temperatures. On the contrary, growth mode on sapphire could be tuned from island like (at150^0C) to layer-by-layer mode (at and above 220^0C) by increasing deposition temperature. The XRD results of the film grown at 300^0C in layer-by-layer mode showed (00.2) preferred orientation. This is in good conformity with the results of the available literature as discussed above. Yang *et al.* have carried out micro-structural characterization of ZnO thin films grown on c-plane sapphire and found that basal plane stacking faults as the dominant structural defects in the films [121].

1.4.4 Electrical Properties of Intrinsic ZnO Thin Films

Room temperature electrical properties of ALD grown intrinsic ZnO films have been studied by a number of research groups [92-97, 106 and 122-125]. Films are usually n-type conducting with electron density of the order of $10^{19}cm^{-3}$ and their conductivity strongly depends on the deposition temperature. Moreover, precursors pulsing and purging time, and their flow rates also have significant role in controlling electrical properties. Minimum resistivity value as low as 10^{-4} Ω cm has been achieved typically in the temperature range of ~ 200-220^{0}C, beyond which resistivity starts increasing. In Table 1.2, we have listed minimum values of room temperature electrical resistivity as obtained from the available literature. These highly conducting films can be used for TCE applications. However, in few applications, for example, Schottky rectifying junctions, carrier concentration less than $10^{17}cm^{-3}$ is required. Guziewicz *et al.* showed that extreme control over electron density (N_e) from heavily degenerate level ~ 10^{20} cm^{-3} to as low as ~$10^{15}cm^{-3}$ could be achieved by selecting appropriate precursor for Zn and optimizations of growth temperature and precursor pulse length [93]. They obtained low electron density in low-temperature grown ZnO films due to minimized defect density rather than carrier compensation effect. However, one major problem with the low-temperature growth of ZnO thin films using ALD is their unstable electrical properties following air exposure [126]. Na *et al.* have carried out both in-situ and ex-situ (in open atmosphere at room temperature) electrical conductivity measurements of ZnO thin films and found lower electrical conductivity when measured ex-situ compared to the in-situ measured values [126]. Such decrement in electrical conductivity arises due to the adsorption of oxygen at the surface defect sites and at grain boundaries which extract free electrons from the film and hence reduces its conductivity. This effect is found to be more prominent for the films grown in a flow-type thermal ALD reactor at very low-temperatures using H_2O as co-reactant. In order to investigate the reason, X-ray photoelectron

spectroscopy (XPS) and Fourier transform infrared spectroscopy (FTIR) measurements have been carried out for the ZnO films grown at different substrate temperatures [97, 124 and 127]. For low-temperature grown films, formation of higher defect density and presence of significant number of hydroxyl groups which act as free carrier trapping centres, results in the lower electrical conductivity and instability in the electrical properties when exposed to air. With increasing deposition temperature, the reaction between DEZ molecules and surface –OH groups becomes more complete and the crystalline quality of the films are also improved which results in higher electrical conductivity and quite stable electrical properties [97, 124]. In order to improve the electrical stability and to achieve highly conducting films at lower deposition temperatures in H_2O based thermal ALD process, Yamada *et al.*, and Saito *et al.*, have carried out ZnO thin film deposition in presence of UV light (photo-ALD) [128, 129].Plasma enhanced ALD (PEALD) is a good alternative to avoid –OH group related issues (surface band bending and formation of potential barriers at the grain boundaries) to a great extent and therefore, provides better control on electrical properties. Moreover, due to the high reactivity of the plasma species, PEALD gives reduced defect density and improved film stoichiometry. Kim *et al.* have compared the room-temperature electrical properties of ZnO thin films grown in a thermal ALD reactor with that deposited in a PEALD reactor [130]. They found that low-temperature PEALD grown films were highly resistive (due to carrier compensation effect) compared to the thermal ALD grown films which showed high n-type conductivity [130].

Table 1.2 Reported values of minimum room temperature electrical resistivity and maximum electron density in intrinsic ZnO thin films grown in thermal ALD reactor using DEZ and H_2O as precursor as co-reactant respectively.

Min. ρ (Ω cm) at room temperature	Max. N_e (cm^{-3})	Substrates	Deposition temperatures	References
$3x10^{-3}$	$4.32x10^{19}$	Corning glass	165^0C	122
$2.3x10^{-3}$	$1.67x10^{20}$	Glass	200^0C	123
$1.2x10^{-3}$	$2x10^{20}$	Sapphire	200^0C	92
$3.6x10^{-3}$	$5x10^{19}$	Glass	200^0C	97
$1x10^{-4}$	$1x10^{20}$	SiO_2/Si	200^0C	124
$1.2x10^{-2}$	$3.7x10^{19}$	Glass	200^0C	125
$3.6x10^{-3}$	$5.7x10^{19}$	Sapphire	200^0C	96

As thin film growth in ALD proceeds in cyclic manner through vapour-solid reactions at the growing film surface, it is imperative to study the effect of each precursor pulse on the electrical properties of the growing film. Both Schuisky *et al.* and Na *et al.* have carried out in-situ electrical resistivity measurements in ALD grown ZnO films [126, 131]. They found sharp increment in the resistivity just after the DEZ pulse, plausibly due to the conversion of surface hydroxyl groups into alkyl specie. In the second half reaction i.e. after the water pulse, coverage of surface hydroxyl groups was recovered which resulted in the decrement of resistivity below the value as measured before the ALD cycle. Similar observation has also been reported by Na *et al.* Moreover, through in-situ conductance measurements they showed island-like growth of ZnO thin films at the incubated or initial stage of film growth. They observed that, after few cycle pulse of ZnO, conductance was very low due to the formation of disconnected ZnO islands. However, with increasing number of cycles as the islands coalesced, a sharp increment in the conductance was observed.

1.4.5 Growth of n-type Doped ZnO Thin Films

In order to further improve the electrical conductivity of ALD grown ZnO films, various n-type dopants such as Al, Ga, B, Si, Ti were used [58, 132-139]. Among them, Al doped ZnO thin films have been extensively investigated [58, 132-136 and 139]. The most commonly used precursor for Al is trimethyl aluminium (TMA). So far, a minimum resistivity value $3.8 \times 10^{-4} \Omega$ cm has been reported by Yuan *et al.* using DEZ, TMA and ozone as precursors for Zn, Al and oxygen respectively [136]. In Table 1.3, we have listed commonly used n-type dopants, substrates used for depositions, growth temperatures, minimum values of room-temperature electrical resistivity (ρ) etc. In literature, several pulsing schemes have been used to grow doped ZnO thin films using ALD [132, 136 and 140]. In the most frequently used scheme, 'n' cycles of ZnO are pulsed into the reactor followed by 1 cycle of dopant exposure. The total (n+1) cycles completes 1 'supercycle' which is repeated according to the requirement of film thickness. This pulsing scheme provides localized dopant distribution along film thickness as observed by Lee *et al.* in Al doped ZnO thin films [132]. Although they achieved minimum resistivity value 3.2×10^{-3} Ω cm and very high carrier concentration 2×10^{20} cm^{-3}, doping-efficiency (i.e. no. of conduction electrons per dopant) was found to be only 13% [132]. Such poor doping-efficiency plausibly resulted from the nanolaminate type of growth in which each nano-layer of ZnO and Al_2O_3 were separated by atomically sharp interfaces. In order to maximize doping-efficiency i.e. to increase electronically active dopant density, widely dispersed dopant distribution on the doping plane is required. However, realizing such doping profile in ALD is a difficult task due to its self-limiting and layer-by-layer growth methodology which is ideal for fabricating nanolaminate structures and hence, inferior to achieve homogeneous dopant distribution. In order to alleviate this problem, different doping methodologies have been adopted to grow n-type doped ZnO films using ALD [136, 140]. Yuan *et al.* have achieved homogeneous dopant distribution in Al doped

ZnO thin films using co-injection of DEZ and TMA precursors [136]. These films showed significant improvement in the electrical and optical properties compared to those with layered microstructure [136]. However, in this approach, the simultaneous pulsing of precursors may result in gas phase reaction which is completely undesirable in ALD. In order to eliminate this issue, Na *et al.* have developed a slightly modified multilayer doping scheme [140]. In this method, 'n' cycle of ZnO deposition is followed by '1' pulse of DEZ and TMA exposure. However, DEZ and TMA pulses are separated by an inert gas purging step. Gil *et al.*have developed in-situ surface-functionalization technique in which a surface inhibitor is pulsed into the reactor prior to the dopant exposure to reduce the density of the surface reactive sites on the growing films [141]. Therefore, the subsequent dopant exposure provides widely dispersed dopant distribution on the doping plane. The co-reactant exposure removes the functionalization groups and restores the initial films surface. A significant improvement in the doping-efficiency was obtained for Al doped ZnO thin films using ethanol as a surface inhibitor. Wu *et al.* have achieved significant improvement in the doping-efficiency from 10 to almost 60% by employing larger ligand size precursor molecules (dimethyl aluminum isopropoxide) for Al. Such enhanced doping-efficiency has been attributed to the increased steric-hindrance effect which provides widely dispersed dopant distribution on the doping plane [142].

Table 1.3 Various n-type dopants used in ZnO, deposition temperature, and minimum room-temperature resistivity values as reported in literature.

Dopants	Precursors	Substrates	Min.ρ (Ω cm)	Deposition temperatures	Ref.
Al	$Zn(C_2H_5)_2$, $Al(CH3)_3$, H_2O	Si &Glass	$3.2x10^{-3}$	200^0C	132
Al	$Zn(C_2H_5)_2$, $Al(CH3)_3$, H_2O	Si(100)	$2.5x10^{-3}$	200^0C	133
Al	$Zn(C_2H_5)_2$, $Al(CH3)_3$, H_2O	Soda glass	$9.7x10^{-4}$	200^0C	134
Al	$Zn(C_2H_5)_2$, $Al(CH3)_3$, H_2O	Sapphire, Glass	$6.5x10^{-4}$	200^0C	135
Al	$Zn(C_2H_5)_2$, $Al(CH3)_3$, O_3	Si, SiO_2/Si	$3.8x10^{-4}$	250^0C	136
Ti	$Zn(C_2H_5)_2$, $Ti[OCH(CH_3)_2]_4$, H_2O	Si, Quartz	$8.9x10^{-4}$	200^0C	137
Si	$Zn(C_2H_5)_2$, $[(CH3)_2N]_3SiH$, H_2O_2	Si, Sapphire	$9.2x10^{-4}$	300^0C	138
B	$Zn(C_2H_5)_2$, B_2H_6, H_2O	Borosilicate	$2.0x10^{-4}$	165^0C	128
Ga	$Zn(C_2H_5)_2$, $Ga(C_2H_5)_3$, H_2O	Sapphire	$8.0x10^{-4}$	300^0C	139

So far we have discussed growths of n-type doped ZnO thin films using conventional thermal ALD reactors which are suitable for research studies. For industrial scale manufacturing of ZnO based TCOs, atmospheric pressure spatial ALD system has been used by Illiberi *et al*. [143]. They have obtained a minimum resistivity ~$2x10^{-3}\Omega$ cm for Al doped ZnO thin films. This value is quite large compared to the minimum resistivity values as obtained in thermal ALD based processes. The high deposition rates of thin films in spatial ALD is advantageous for commercial fabrication of ZnO based TCOs.

1.4.6 Applications of ALD Grown ZnO Thin Films

We have already summarized various applications of ZnO thin films and nanostructures in the area of electronics and optoelectronics in section 1.1.4. Here we have particularly discussed the potential applications of ZnO thin films grown by ALD.

1. Low-temperature ALD grown n-type doped ZnO thin films on large area substrates are suitable for TCE applications in thin film electro luminescent (TFEL) displays and solar cells [144].

2. PEALD grown ZnO thin films at very low temperatures exhibit lower defect density and therefore, ideal for channel layer material for thin film transistors (TFTs) [144].

3. As ALD grown films are extremely conformal on high aspect ratio structures, ZnO coatings on silica aerogel and anodic aluminium oxide (AAO) templates can be used to fabricate photo anodes for dye sensitized solar cells (DSSCs) and photo catalytic cells [144, 145-147].

4. As ZnO thin films show change in resistivity in air exposure, it can be used as chemiresistor for gas sensing applications. However, high surface-to-volume ratio is needed for this application. Owing to exclusively surface controlled depositions in ALD, it can be used to fabricate core-shell nanowires and nano-fibers for sensing applications [144].

5. Low thermal budget depositions of highly resistive and non stoichiometric ZnO thin films can be used for resistive random access memory (RRAM) application [148].

Chapter 2: Experimental Techniques

2.1 Atomic layer deposition

Atomic layer deposition (ALD) is a suitable technique to grow thin films of various inorganic materials with monolayer level precession over film thickness and uniformity [88-90]. ALD is basically a modified version of the conventional chemical vapor deposition (CVD) technique. However, unlike CVD, in ALD precursors are sequentially pulsed into reactor and are separated by an inert gas purging step [88, 89]. Although ALD is a relatively new thin film deposition technique in the modern semiconductor industry, the method of ALD, then known as “molecular layering (ML)”, was originally invented more than 40 years ago by the group of Professor Aleskovskii in Soviet-Russia [149]. However, it was first patented under the name “atomic layer epitaxy (ALE)” by Tumo Suntola and co-workers in Finland in the 1970s [112]. The most commonly used name “atomic layer deposition”, started in the early 1990s.

A major breakthrough in the research and development of ALD was observed after the patent filed by Suntola *et al.* in which they demonstrated basic reactor technology and growths of ZnS, GaP and SnO_2thin films [112]. Their rigorous works on ALD coating technology led to the development of thin film electroluminescent displays for commercial application in the 1980s. After that a rapid increase in the number of research publications on ALD was observed and still continuing. Such rapidly growing interest in ALD within the materials research community is due to its numerous potential features including comparatively low-temperature deposition of thin films, high uniformity over large deposition area, easy and accurate control over film thickness, excellent conformality on complex shape geometries, no line-of-sight deposition, pinhole-free films and good reproducibility in film properties [88-90].

In the following we will briefly review principles and basic features of ALD, precursors and reaction mechanisms, instrumentations, applications, limitations and benefits of ALD etc.

2.1.1 Principle of ALD

Thin film growth in ALD takes place in cyclic manner. For the growth of various binary metal oxides (ZnO, SnO_2, Al_2O_3, HfO_2, ZrO_2 etc), metal sulphides (ZnS, CdS etc), metal nitrides (TiN, NbN etc) each growth cycle consists of four sequential steps as shown in Fig. 2.1 [88-90]. The 1st step is the exposure of the substrate surface by the metal precursor 'A' as shown in Fig. 2.1.

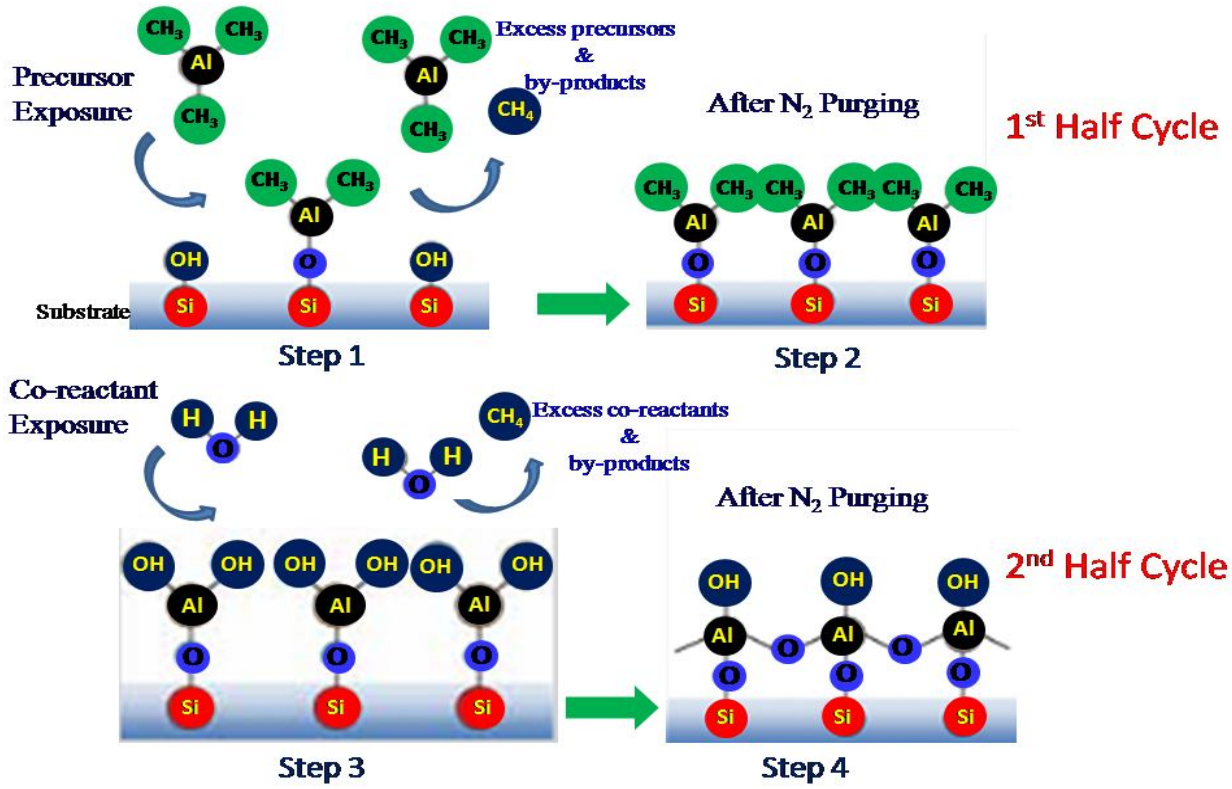

Fig. 2.1 Schematic representation of a typical ALD cycle for Al_2O_3 deposition which consists of four steps in sequence.

In step 2, the reactor is purged by an inert gas flow to remove the unreacted precursor

molecules and the reaction by products. In the 3rd step, the co-reactant 'B' which is usually H_2O/O_3 for metal oxides, H_2S for metal sulphides and NH_3 for metal nitrides is pulsed into the reactor. In the 4th step, the reactor is again flushed by the inert gas flow. These four steps in sequence provides one AB cycle. The growth cycles are repeated in ABABAB.... fashion as many times as necessary to obtain the required film thickness. The reaction steps 1 and 3 are self-limiting in nature. The term 'self-limiting' implies that if the precursor dose 'A' is sufficiently large then no surface sites will be available for further chemisorption reaction of precursor 'B' within the same monolayer of 'A' or vice versa. Therefore, film growth in ALD relies on 'self-limiting' or 'self-terminating' vapor-solid reaction in which the precursor molecules react only at the growing film surface. If the substrate doesn't have surface reactive sites (e.g. graphene, carbon nano-tubes) to chemisorb precursor molecules then surface functionalization of the substrate has to be carried out, otherwise nucleation starts only at defect sites [88, 89]. Because of surface-controlled nature of growth process, ALD grown films are extremely conformal even on high aspect ratio substrates and highly uniform in thickness as schematically shown in Fig. 2.2.

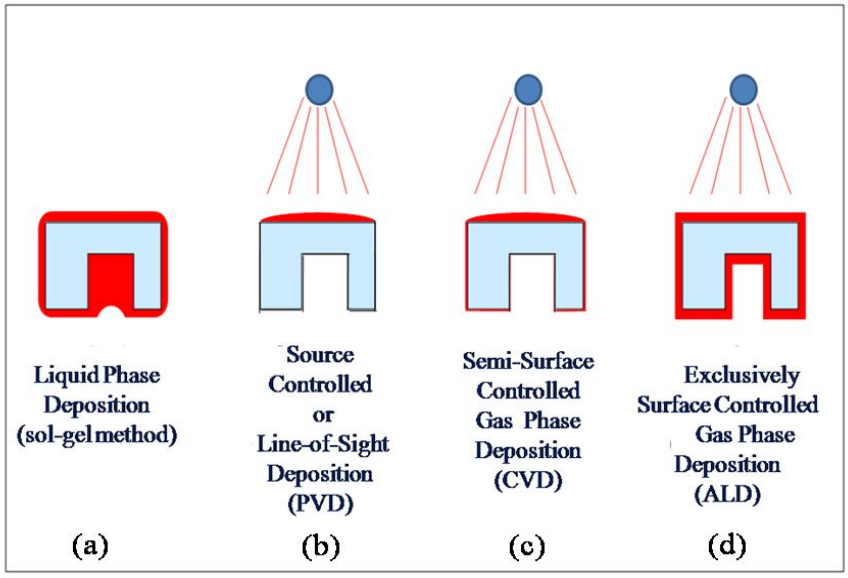

Fig. 2.2 Comparison of step coverage (or conformality) in different thin film deposition techniques: (a) Sol–gel (b) PVD (c) CVD and (d) ALD.

As the precursors are pulsed into the reactor separately, there is no gas phase reaction between the precursor molecules which facilitates the use of highly volatile precursors and consequently thin film growth is possible at relatively low substrate temperatures. Usually, but not always, a temperature range with constant growth rate (see Fig. 2.3), also known as 'ALD window', is observed in the growth of various materials in ALD [88-90].

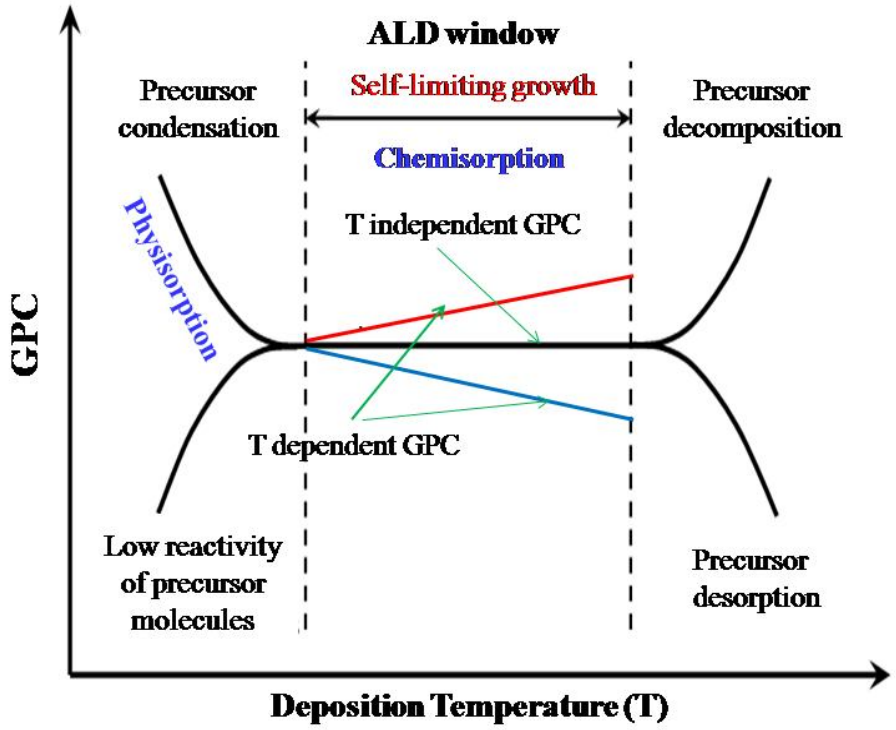

Fig. 2.3 Growth per cycle (GPC) as a function of deposition temperature (T)in a typical ALD growth of a thin film.

This film deposition within ALD window is highly desirable to ensures high degree of reproducibility in various film properties. Especially, for depositing ternary materials, for example (Zn, Al)O_x or (Zn, Ti)O_x thin films, the overlapping ALD windows of the constituent binary materials led to the reproducibility of the electrical properties. As can be seen from Fig. 2.3, GPC in ALD is highly substrate temperature dependent. However, GPC is also found to be dependent on precursor dosing time and the size of the precursor molecules. The

larger ligand size precursor molecules results in steric-hindrance effect in which few surface reactive sites are blocked and therefore, less than one monolayer is deposited in one ALD cycle [142].

2.1.2 Instrumentations for ALD

ALD processes can be realized over a wide range of pressure starting from atmospheric to ultra-high vacuum (UHV) regime. ALD reactors are divided into two major categories: inert gas flow-type reactors operating at pressures higher than 1Torr (similar like CVD reactors), and UHV reactors with molecular flow conditions (similar like molecular beam epitaxy reactors). Due to the self-limiting surface chemistry of ALD, there is no strict requirement of flux homogeneity of precursors. This particular characteristic of ALD offers the use of flow-type reactors in which precursor exposure and purging are rapidly performed compared to UHV reactors. Moreover, in a flow-type reactor, precursor molecules suffer multiple collisions with the substrate surface during transportation through the reactor and therefore, chemisorption probability with the surface states significantly enhanced.

In the present study, all thin film depositions were carried out at Laser Materials Processing Division, Raja Ramanna Centre for Advanced Technology (RRCAT), Indore by using a flow-type thermal ALD reactor (Model: TFS 200, Beneq Oy Finland) with stationary substrate holder (see Fig. 2.4). Below we have briefly discussed the main components of the ALD system.

(I)**Inert gas supply system** for process (carrier gas assisted pulsing of precursors and for inert gas valving) and operating pneumatic valves.

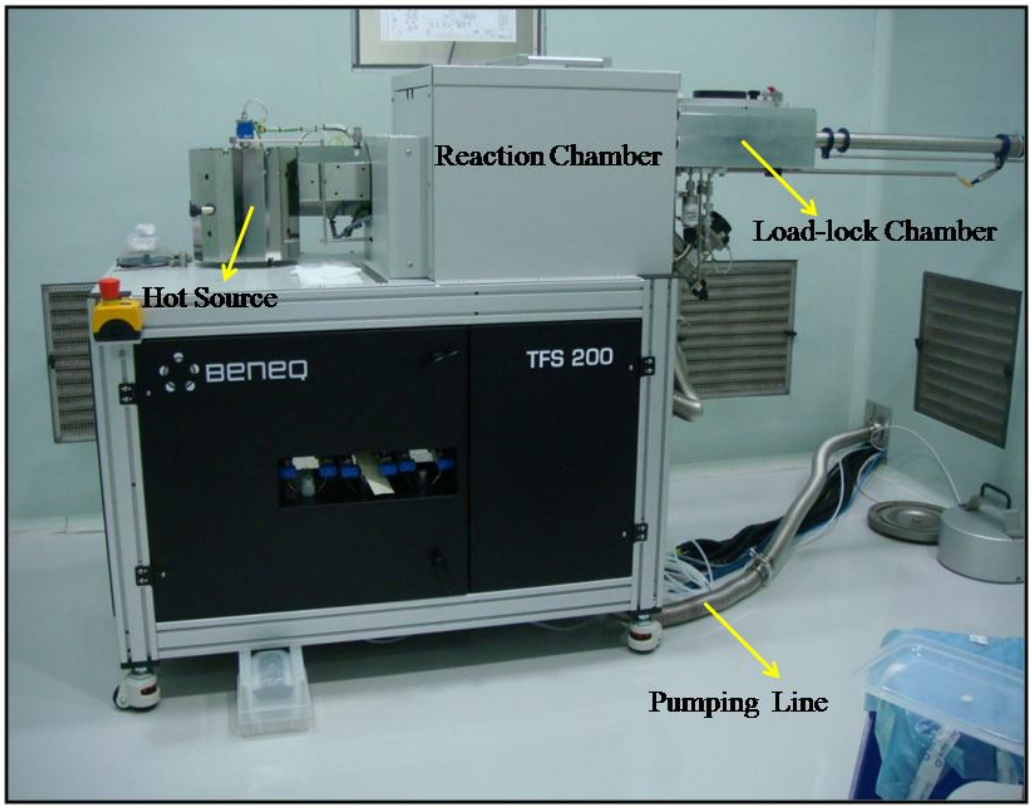

Fig. 2.4 Beneq TFS 200 thermal ALD system in our lab at RRCAT, Indore.

(II) Precursor sources and Pulsing valves: 2 gas lines, 3 stain less steel bubblers for liquid precursors (usually kept at 20^0C) and 1 hot source (HS 200) for low vapor pressure solid precursors which can be heated up to 200^0C (see Fig. 2.5) are connected with the TFS 200 system.

In the present research work, we have used diethyl zinc (DEZ), titanium tetra chloride ($TiCl_4$) and de ionized water as precursors for Zn, Ti and oxygen respectively. All the precursors were kept in liquid source containers at 20^0 C. Solid anhydrous aluminium chloride ($AlCl_3$) was kept inside the hot-source container HS 200 at ~ 190^0C. Unlike liquid source pulsing lines, the precursor pulsing line of HS 200 is heated to avoid precursor clogging effect due to cold spots. Both the liquid and hot source HS 200 can be operated in three different ways, (I) by own vapor pressure. This method is most common for materials with vapor pressure of at

least 10 mbar at source temperature. All the three liquid sources used in this research work were pulsed into the reactor using this method.(II) Carrier gas assisted delivery, when carrier gas valve (DV-ALx) and precursor pulse valve (DV-PLx) are opened simultaneously. (III) Carrier gas assisted booster function, when carrier gas is first loaded into the container by opening the bubbler tube valve DV-BLx (x=1, 2, 3). Therefore, the pressure inside the container is increased. Then precursor pulse valve DV-PLx (x=1, 2, 3) is opened to release the mixture of inert carrier gas and precursor vapor from the container. This is the most efficient way of delivering a low vapor pressure material from the container. As vapor pressure of $AlCl_3$ is quite low compared to the liquid source precursors used, we have used booster option to pulse $AlCl_3$ into the reactor.

In Fig. 2.5 and 2.6 we have shown hot source HS 200 for solid source and three bubblers for volatile liquid precursors respectively.

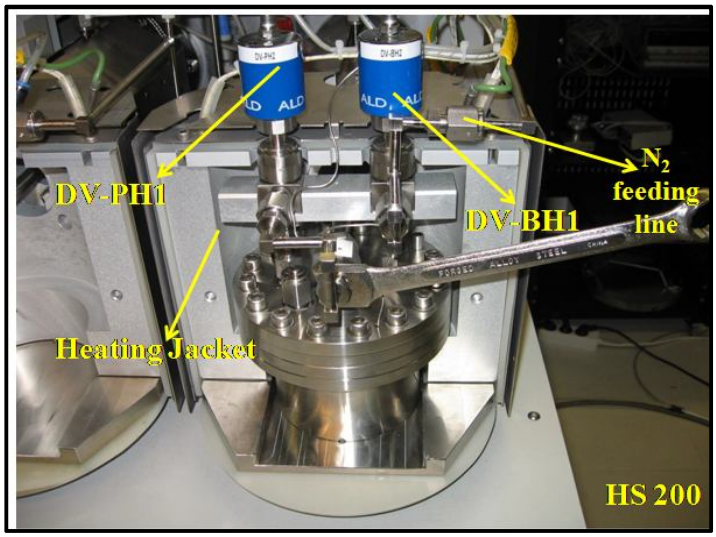

Fig. 2.5 Hot source HS 200 used for anhydrous $AlCl_3$ as Al precursors in BENEQ TFS 200.

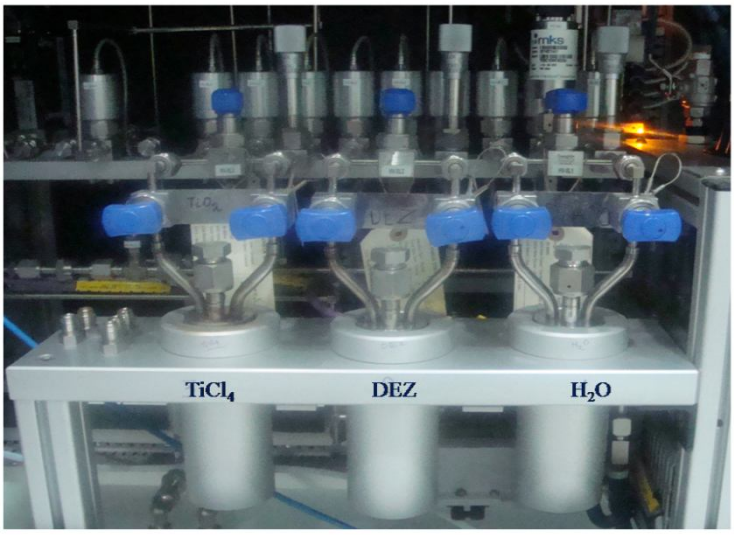

Fig. 2.6 Liquid precursor bubblers for H_2O, DEZ and $TiCl_4$ in BENEQ TFS 200

The TFS 200 HMI valve control window is shown below in Fig. 2.7

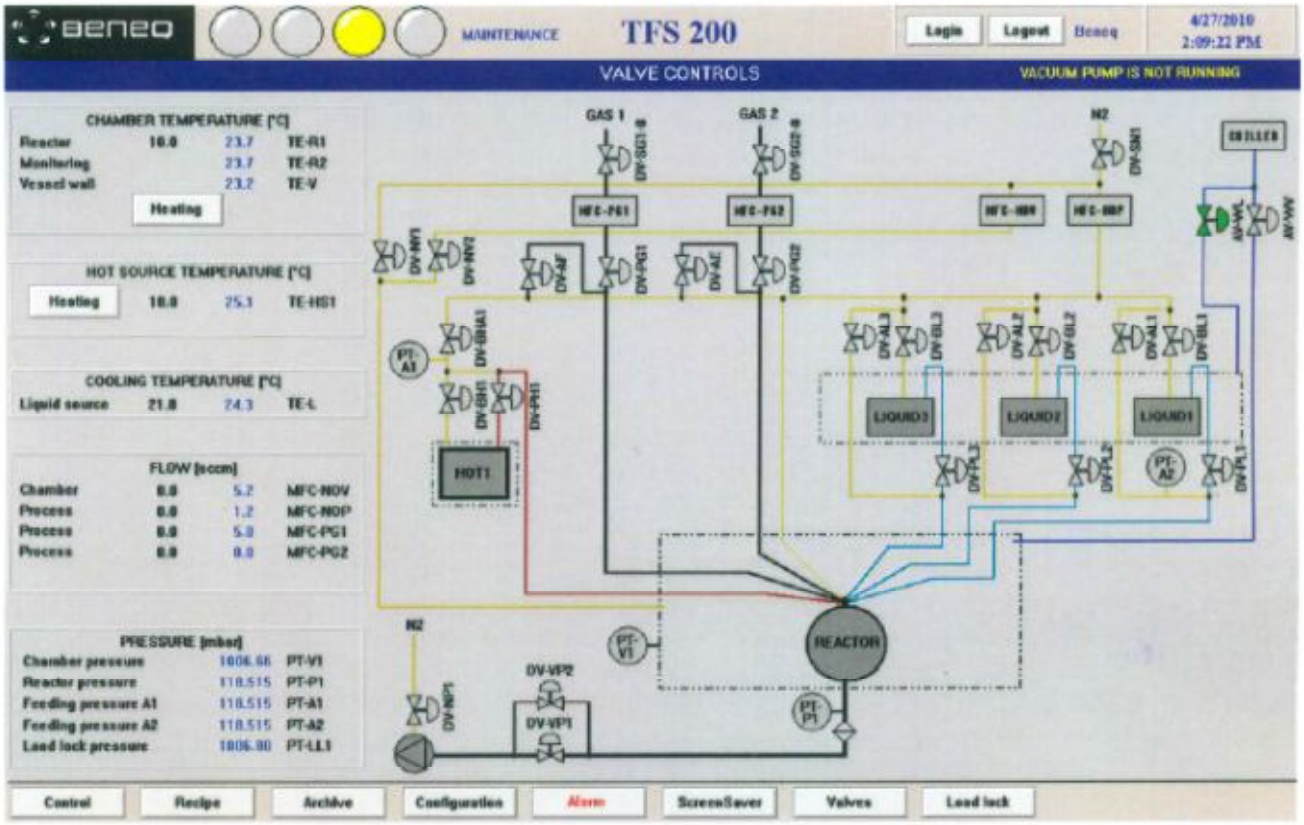

Fig. 2.7 The TFS 200 HMI valve control window (reproduced with permission from BENEQ Oy Finland)

Different pneumatic valves used for precursor pulsing and process gas are listed below:

DV-PL1→Pulsing valve for liquid source 1 (we have used de ionized water)

DV-PL2→Pulsing valve for liquid source 2 (we have used $Zn(C_2H_5)_2$)

DV-PL3→Pulsing valve for liquid source 3 (we have used $TiCl_4$)

DV-BL1→Bubbler tube valve for liquid source 1

DV-BL2→Bubbler tube valve for liquid source 2

DV-BL3→Bubbler tube valve for liquid source 3

DV-AL1→Pulse assist valve for liquid source 1

DV-AL2→Pulse assist valve for liquid source 2

DV-AL3→Pulse assist valve for liquid source 3

NV-PL1→Pulse flow adjusting valve for liquid source 1

NV-PL2→Pulse flow adjusting valve for liquid source 2

NV-PL3→Pulse flow adjusting valve for liquid source 3

DV-PH1→Pulsing valve for hot source

DV-BH1→Bubbler valve for hot source

DV-BHA1→Carrier/purge gas valve for hot source

DV-SN1→Process N_2 valve

Different mass flow controllers are

MFC-NOP→Controls N_2flow, which we kept at 300 sccm, is used as carrier gas and for inert gas valving purpose for each source

MFC-NOV→Controls N_2flow, which we kept at 200 sccm, is used as filler gas to the vacuum chamber. The purpose of this flow is to keep the pressure in the vacuum chamber higher than the pressure in the reaction chamber. This prevents precursors escaping from reaction chamber to vacuum chamber.

MFC-PG1→Controls flow for the gas precursor 1

MFC-PG2→Controls flow for the gas precursor 2

The pressure gauge PT-P1 measures the reactor pressure which lies in the range of 1.5-3 mbar and PT-V1 provides the pressure outside the reaction chamber which was found to be within 8-12 mbar.

(III) Substrate holder which can hold up to 4 inch wafers is located inside the reaction chamber which can be heated up to 500^0C.

(IV) The inert gas valving functions for the liquid sources are built in the mixing unit inside the vacuum chamber and are schematically shown in Fig. 2.8.

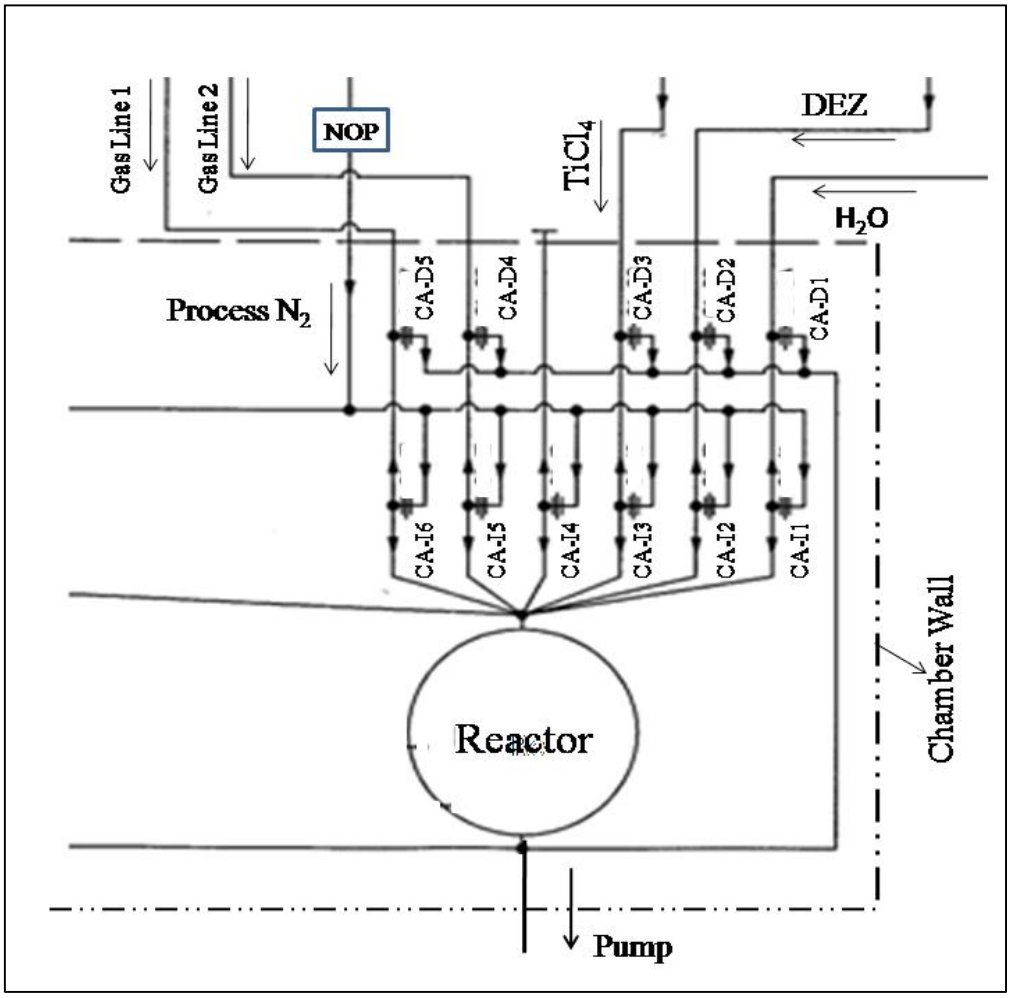

Fig. 2.8 Schematic of inert gas valving system inside the reaction chamber of TFS 200

These flows are controlled by orifices CA-Ix (x=1, 2, 3, 4, 5, 6) and CA-Dx (x=1, 2, 3, 4, 5). During purge stage the nitrogen flow goes through the orifice CA-Ix, and then it is divided into two parts. One part goes through the reaction chamber to the pump line. The other flow goes directly to the drain. These flows will create inert gas valving between reaction chamber and precursor inlets (diffusion barrier to both directions). During precursor pulsing, fraction of the precursor flow is wasted via CA-Dx, but the main flow goes through the reaction chamber. A minor part of the inert gas flow is still going through CA-Ix for preventing precursor flow from going into that line. Similar kind of inert gas valving arrangement has also been constructed for the hot source HS 200 which has not been shown in Fig. 2.8.

(V) Temperature controllers for the solid and liquid sources, reactor and vacuum chambers

(VI) Cooling water circulation from the Unichiller is divided into two circuits. One circuit is for the outer wall of the vacuum chamber and the second one is for liquid sources.

(VI) Dry Pump (Adixen ADP 122P) and related exhaust equipments. A nitrogen purge line and separate cooling water circulation for the dry pump is also arranged.

(VI) Load-lock for loading and unloading substrates as shown in Fig. 2.4.

(VII) Control Unit: process is controlled by PLC (Siemens S7). The user interface is a laptop. There is a flexible recipe system and it has a data logging function for all process parameters. Program codes for growth of ZnO, Al_2O_3, TiO_2, Al doped ZnO and Ti doped ZnO are given in Appendix.

The most common ALD reactor is flow-type single-wafer thermal ALD reactor which we have discussed above. There are other types of ALD systems which include:

(I) Plasma enhanced ALD: In thermal ALD surface chemical reactions for thin film growth are thermally-driven by using a slightly elevated substrate temperature typically in the range of 150-350^0 C. On the contrary, in plasma enhanced ALD (PEALD), the high reactivity of the

plasma species as used in the reactant exposure step, significantly reduces the deposition temperature [150]. The surface reactivity of the plasma species is not only provided by the plasma radicals but is also determined by the kinetic energy of the ions accelerated in the plasma sheath. The PEALD grown films are found to be highly dense with less impurity incorporation, and show improved stoichiometry as compared to the thermal ALD grown films. For the growth of metal oxide thin films using β-diketonate precursors require highly reactive co-reactants as they show low reactivity towards H_2O. In this case, use of PEALD would be a better option. Additionally for the thermal ALD process, the purge after the H_2O pulse needs to be sufficiently longer at low substrate temperatures to avoid parasitic CVD reactions. For PEALD, the purge time after the plasma exposure can be kept relatively short even at room temperature depositions.

(II) Spatial ALD: A major drawback of the conventional ALD system is its low deposition rate. This drawback can be overcome by using spatial ALD technique in which the ALD half-reactions are separated spatially instead in time domain by using inert gas purging steps [91]. This technique allows high deposition rate without compromising with the typical ALD characteristics. A new field of applications of spatial ALD is in flexible electronics which include organic LEDs and organic photovoltaics. For these applications roll-to-roll spatial ALD method is used for coating flexible substrates.

2.1.3 Precursors for ALD

ALD can utilize precursors in solid, gas or in liquid form [88-90]. However, to ensure sufficient mass transportation, the liquid source needs to be sufficiently volatile. All solids and few liquid precursors are usually heated at higher temperature depending upon their melting and boiling points. In some cases, inert gas assisted pulsing is used for low vapor pressure precursors. The strict criterion to achieve self-limiting growth in ALD is that

precursors must not decompose at the deposition temperature. The other requirements of ALD precursors are sufficient reactivity, inert against normal reactor material, intermediate and end products should be inert against film, non-toxic and economical. Typical metal precursors used in ALD are organo-metallic compounds and metal halides, especially chlorides due to their higher vapor pressure and strong reaction with water [88-90]. The non-metal precursors are: water, ozone, hydrogen peroxide, diatomic oxygen, atomic oxygen created through oxygen plasma, and alcohols for oxygen source; hydrogen sulphide for sulphur; ammonia for nitrogen etc [88-90].

2.1.4 Materials Investigated

So far ALD has been successfully used to grow various metal oxides (Al_2O_3, TiO_2, ZrO_2, HfO_2, La_2O_3, Ta_2O_5, Gd_2O_3, NiO, CuO, RuO, ZnO, Ga_2O_3, In_2O_3, SnO_2 etc), sulphides (ZnS, CdS, SrS, In_2S_3 etc), nitrides (GaN, InN, TiN, Zr_3N_4, Si_3N_4 etc), selenides (CdSe, ZnSe), tellurides (ZnTe, CdTe etc) and as well as pure elements (Cu, Ni, Co) [88-90]. Among them, thin films of oxides have been extensively investigated in ALD mainly for high-k dielectric applications. Although ALD is most suited to grow compound materials, pure elements including various transition metals, Ru, Pt have also been deposited. In most of the metal deposition process the metal precursor needs to be reduced in presence of diatomic hydrogen or by using hydrogen plasma.

2.1.5 Benefits and Limitations of ALD

We have summarized below the fundamental characteristics of ALD and related advantages in thin film deposition.

Characteristic of ALD	Inherent implication on thin film deposition	Practical benefits
Self-limiting growth	Film thickness depends only on number of deposition cycles	Accurate and easy thickness control
	No need of precursor flux homogeneity	i)Large area deposition capability ii)Excellent conformality on high aspect ratio structures iii)Large batch capability iv)Good reproducibility in film properties
	Monolayer level precession in material composition	Produces nanolaminate structures with atomically sharp interfaces
Separate precursor dosing	No gas phase reaction between precursor molecules	Use of highly reactive precursors

The major limitation of ALD is its lower growth rate compared to CVD. In most of the cases growth rate lies in the range of 100-300 nm h^{-1}. However, the most promising application of ALD is growing ultra-thin gate dielectric layers for MOSFETs in microelectronic industry

[90]. In such applications, lower growth rate of ALD is not problematic. The lower growth rate in ALD can be effectively compensated through large-area and large-batch depositions. Another limitation is the lack of production-worthy processes for depositing technologically important materials such as Si, Ge, Cu, multi-component oxide superconductors etc [88, 89].

2.1.6 Applications of ALD

The early development of ALD technology was mainly focused on the commercialization of large area thin film electroluminescent (TFEL) displays [88-90]. ALD is successfully used to grow high quality insulator-phosphor-insulator structure, usually the phosphor material is ZnS:Mn and the insulator material is Al_2O_3or Al_2O_3/TiO_2 (ATO). As ALD grown films are dense pinhole free and amorphous at lower growth temperatures, these films are ideal for TFEL applications. ALD grown large area TCO coatings are also useful for flat panel displays, solar cells, smart windows etc. Resistivity value of the order of 10^{-4} Ω cm has been reported in verities of TCO materials which include In_2O_3, SnO_2, SnO_2:F, ZnO:Al, ZnO:Ga etc [151]. However, the main thrust in the commercialization of ALD system is due to its potential applications in microelectronic industry for depositing ultrathin and conformal high-k dielectric layers suitable for memory devices and in CMOS transistors. The continious miniaturization of MOSFETs according to Moore's law requires sub-manometer effective oxide thickness (EOT) for gate dielectric layers which can easily be realized employing ALD [151]. However, commercially the potential of ALD to grow high-k materials for MOSFETs was accepted when processor manufacturing giant Intel announced the use of ALD to grow HfO_2-based high-k materials [151]. Moreover, ALD has also been explored for conformal growth of capacitor dielectrics and metal electrodes on 3D high aspect ratio structures for dynamic random access memories (DRAMs) [151]. Another area of research in microelectronics in which ALD has been successfully implemented to grow materials is non-

volatile memories such as resistive random access memories (RRAMs), ferroelectric RAMs (FeRAMs), phase change memories etc [151].

2.2 X-ray Diffraction

X-ray diffraction (XRD) is one of the most widely used techniques to investigate the structural properties of thin films. In XRD measurement, the sample is illuminated with monochromatic X-ray beam from a Cu-K_α source (0.154 nm). The incoming X-ray photons interact with the electron densities of the atoms and are scattered in all directions. These scattered X-rays interfere with each other constructively or destructively upon reaching the detector. The interference pattern provides crucial informations about the crystal structure of the investigating sample. The diffracted beam interfere constructively at a certain angle θ given by the Bragg's condition: $2d\,\mathrm{Sin}\,\theta = n\lambda$ where n is the order of diffraction, λ is the wavelength of the incident X-ray beam, d is the spacing between planes which contributes to diffraction at an angle θ (angle between the X-ray beam and the crystallographic plane). XRD can be also be used to find the average crystallite size, stress and strain of thin films etc.

2.3 Atomic Force Microscopy

Atomic force microscopy (AFM) is one kind of high resolution scanning probe microscopy (SPM) technique that allows us to image the surface morphology (with lateral resolution ~ 1 nm, vertical ~ 0.1 nm) of the sample under investigation. AFM is routinely used in laboratories to measure average grain size and surface roughness of thin film materials. The advantages of AFM over scanning tunnelling microscopy (STM) are: (a) AFM does not require an UHV environment and conducting sample to image the surface and (b) almost no surface preparation is required for AFM measurement. The AFM instrument uses a sharp tip which is kept in near-contact or in intermittent contact with the sample surface. The tip is

scanned across the sample surface (line by line in a defined grid) and the deflection of the tip is measured by optical lever. The optical lever operates by reflecting a laser beam off the cantilever which strikes a position-sensitive photo-detector. In contact mode operation of AFM, a feedback circuit is used to regulate the force on the sample. The feedback loop consists of a piezo tube scanner that controls the height of the tip from the sample surface, the cantilever and the optical lever. In the present case, AFM measurements were performed by using Agilent Technologies 5420 scanning probe microscope set up.

2.4 Transmission Electron Microscopy

Transmission electron microscopy (TEM) is a high resolution electron microscopy technique which produces a diffraction pattern of an ultrathin specimen of the investigating sample by transmitting a high energy electron (40-200 kV) beam through it. Due to the small de-Broglie wavelength of electrons, the resolution of a TEM is ~ 0.2 nm i.e., typical separation between two atoms in a solid. Unlike scanning electron microscopy (SEM) which is mainly used for surface morphological characterization, TEM image provides detail of crystal structure, microstructural features like grains, dislocations, stacking faults, precipitates etc. However, sample preparation in TEM is very rigorous and thickness of the material needs to be less than 100 nm to transmit electrons, whereas SEM doesn't need special sample preparation step, except for biological or nonconductive samples in which thin metal layer has to be coated. The essential parts of a TEM set up are the followings: (1) Electron source: a tungsten filament. This filament emits electrons when it is heated, (2) Magnetic lenses: used to focus the beam of electrons on the specimen, (3) The sample holder: mechanical arm which holds the specimen, (4) The imaging system: consists of electromagnetic lens system and a screen which has a phosphorescent plate. The plate glows when electrons strike on it after passing through the specimen. The objective aperture is used to select a certain diffraction beam. In

the bright field (BF) imaging mode, only the direct beam is allowed to pass. On the contrary, in the dark field (DF) imaging, the direct beam is blocked by the aperture and one or more diffracted beams are allowed to pass.

2.5 X-ray Photoelectron Spectroscopy

X-ray photoelectron spectroscopy (XPS), also known as electron spectroscopy for chemical analysis (ESCA), is the most widely used technique to detect various elements, their chemical states and relative concentrations of the constituents present in the investigating sample. However, XPS is highly surface sensitive and provides elemental compositions only within 3-10 nm depth from the surface. The principle of operation of XPS is based on photoelectric effect. When the sample surface is irradiated with mono-energetic soft X-ray beam (AlK_α or MgK_α source), the energy of the X-ray photon is adsorbed completely by the core electrons of the atoms. If the photon energy, $h\nu$, is large enough, the core electron will then escape from the atom and emit out of the surface with kinetic energy given by $KE = h\nu - (\Phi_B + \Phi)$ where Φ_B and Φ are the binding energy of the core electron and work function of the sample respectively. Emitted photoelectrons are then focused using the electron optics and sent to the hemispherical energy analyzer to obtain intensity (number of electrons detected) vs. binding energy curve. To obtain relative atomic percentage values and chemical stoichiometry, each raw XPS signal is corrected by dividing its signal intensity by a "relative sensitivity factor" and normalized over all of the elements detected.

In the present study, XPS studies were carried out at a base pressure better than 5×10^{-10} Torr. Al Kα radiation was employed for recording the spectra, with the source operated at an emission current of 10 mA and an anode voltage of 10 kV. A concentric hemispherical energy analyzer with 50 eV pass energy giving an overall resolution of 0.8 eV was used. Au 4f7/2 at 84.7 eV served as an external reference. To correct the shifts in binding energies of core levels due to the charging effect, the graphitic C 1s peak at 284.7 eV was used as an internal

reference. The samples' surfaces were etched using 1 keV Ar ions' beam before performing measurements to remove the air contaminated top layers. The chemical species were identified through the binding energies, which were determined by fitting the spectral line shapes with mixture of Lorentzian and Gaussian functions.

2.6 Secondary Ion Mass Spectroscopy

Secondary ion mass spectrometry (SIMS) is a routinely used technique for quantitative analysis of composition and depth profiling of constituent elements in thin films. SIMS has a detection limit down to concentrations of 1ppm or 1ppb. In SIMS measurement, the sample is sputtered by using a beam of charged particles with energies of few kV. These incoming particles are called primary ions. The charged particles in the sputtered material are known as secondary ions. The mass/charge ratios of these secondary ions are measured with a mass spectrometer to determine the elemental composition of the material. Under typical SIMS conditions the sampling depth is found to be ~1-2 nm. A SIMS set up consists of the following essential parts: (1) a primary beam source, (2) high vacuum chamber (~ 10^{-6} mbar), (3) primary ion column for accelerating and focusing the beam onto the sample, (4) a method of collecting the ejected secondary ions, (5) a mass analyser to isolate the ion of interest and (6) an ion detection system (photographic plate, Faraday cup or a CCD) to record the magnitude of the secondary ion signal.

2.7 Synchrotron X-ray Fluorescence

X-ray fluorescence (XRF) technique is used for elemental identification of a material. When a beam of X-rays with energy higher than ionization energy of the atoms of the material strikes on the sample surface, electrons are ejected from the inner shells of atoms. During this process, vacancies are created at the inner electronic orbitals. These vacancies present an unstable condition for the atom. As a result electrons from the outer shells are transferred to

the inner shells of the atoms. This process emits a characteristic X-ray photon having energy equal the energy difference between the two orbitals involved. As each element in a material has a unique set of energy levels, each element produces a set of X-rays at a unique set of energies, allows us to non-destructively measure the elemental composition of the investigating material. In the present study, we have used synchrotron based X-ray fluorescence technique for the (Zn, Ti)O_x thin films with very low doping concentrations. Ti concentrations in the films were measured at the microfocus XRF beamline (BL-16) of Indus-2 national synchrotron facility at RRCAT, Indore (India). In brief, monochromatic collimated X-rays of energy 12 keV was allowed to excite thin film samples at grazing incidence angles. The fluorescence X-rays (Ti K_α and Zn K_α) emitted from the samples were detected using a Vortex solid state Si drift detector (SII nano, USA) coupled to a digital pulse processor unit (XIA LLC, USA). The observed fluorescence intensities (Ti K_α and Zn K_α) were eventually used to determine concentrations of Ti and Zn elements in the thin film samples.

2.8 Photoluminescence Spectroscopy

Optical properties of materials are studied non-destructively by a variety of experimental techniques such as optical absorption, transmission, reflection, spectroscopic ellipsometry, photoluminescence (optical excitation), cathodoluminescence (electron beam excitation), electroluminescence (excitation by carrier injection) etc. Among these techniques, photoluminescence (PL) is routinely used to characterize semiconducting thin films to obtain valuable informations about the band gap, impurity levels in the sample. Luminescence involves three basic processes. First, a none-equilibrium distribution of electron-hole pairs is created by absorption of incident photons with energy greater than the band-gap (E_g). In the second step, the electrons and the holes rapidly thermalize and establish quasi-equilibrium distributions. Finally, the electron-hole pair recombines radiatively by emitting a

photon which corresponds to the band gap energy of the material. In the present case, a 20 mW He-Cd laser operating at 325 nm was used as an excitation source and luminescence was collected and detected by a spectrometer (Triax 550, Jobin Yvon, France) attached with a UV sensitive CCD detector (Andor, UK). Samples were mounted on the cold finger of a closed cycle He cryostat (Oxford instrument) and was cooled down to 5 K. Temperature of the sample was monitored using a lake Shore temperature controller. Each PL spectrum at a particular measurement temperature was collected when the sample temperature was stabilised and usually it took 15-20 minutes.

2.9 UV-Visible Spectroscopy

In ultraviolet-visible (UV-Vis) spectroscopy one measures the absorption spectrum of a solution or solid in ultraviolet and visible spectral range. In case of thin films, the optical constants, viz., the absorption coefficient (α) and band-gap (E_{go}) of the material, can be determined from the absorption spectrum. Upon shining UV-visible light on thin films, electronic transitions from valence band to conduction band occur for $h\nu \geq E_{go}$ where E_{go} is the fundamental optical absorption edge of the material. As a result, the absorption spectrum of an ideal semiconductor lattice is characterized by a sudden sharp increase in absorption at E_{go}. For direct band-gap semiconductors variation of absorption coefficient is given by $\alpha(h\nu) \propto (h\nu - E_{go})^{1/2} / h\nu$ and for indirect bad-gap semiconductors $\alpha(h\nu) \propto (h\nu - E_{go})^{2} / h\nu$ and the absorption coefficient is obtained from $\alpha = 1/t \ln(I_0 / I) = 1/t \ln(100/T)$ where t is the film thickness. In the present case all optical transmittance measurements were carried out using a UV-visible spectrophotometer (CARY50) in the wave length range 200-1000 nm.

2.10 Spectroscopic Ellipsometry

Spectroscopic ellipsometry (SE) is a non-contact and non-destructive optical technique for measuring thin film thickness, refractive index (n), extinction coefficient (k), surface and interface roughnesses etc. Ellipsometry uses the fact that incident light undergoes some change in the state of polarization when it is reflected off or transmitted through the investigating sample. It measures angles ψ and Δ which are related to the reflectance ratio (ρ) of *p*- and *s*- polarized light by the Eq.2.1

$$\rho = \frac{R_p}{R_s} = \tan(\Psi)\exp(i\Delta), \qquad (2.1)$$

R_p and R_s are Fresnel reflection coefficients for *p*- and *s*-polarized light respectively. Dielectric function (ε) can be obtained by direct inversion of the experimentally measured ρ values for semi-infinite (or opaque) bulk samples without any surface-oxide layer or surface roughness. However, a direct inversion of the experimental data would lead to the pseudo-dielectric function (< ε >) for thin films. Therefore, we followed optical parameterization technique. This method consists of following three steps: (1) a physically possible multilayered optical model for the sample structure is constructed, (2) optical dispersion law is assigned to each layer and (3) optimizing the model parameters to fit the experimentally obtained tan ψ and Cos Δ curves in an iterative procedure. We have constructed a double-layered optical model which consisted of Si (substrate)/ native SiO_2/dense film/ surface roughness. In the present case, SE measurements were carried out using a SOPRA GES-5 (rotating polarizer) system in the wavelength range of 250 – 900 nm at an angle of incidence 70^0.

2.11 Hall and Electrical Resistivity Measurements

(I) Hall Measurement

Let us consider a rectangular shape n-type semiconducting thin film of length '*l*' width '*w*' and thickness '*t*'. If a current 'I' is allowed to flow in the X direction and a magnetic field 'B' is applied in the Z direction, the electrons will experience a Lorentz force perpendicular to the current flow. This Lorentz force results in an accumulation of static positive and negative charges on opposite sides of the sample resulting in a transverse voltage known as the Hall voltage (V_H). Experimentally Hall voltage can be measured by making contacts in van der Pauw geometry as shown in Fig. 2.9. The expression for Hall voltage is given by

$$V_H = \frac{IB}{net} \tag{2.2}$$

Four small Ohmic contacts were made using indium at the four corners of 5mmx5mm square shape samples and a magnetic field of 0.5 T has been used perpendicular to the sample plane. The measurement includes the following steps:

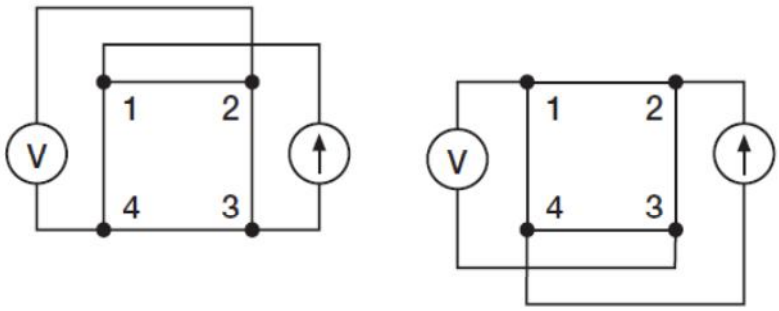

Fig. 2.9 Electrical contacts for Hall measurement in van der Pauw geometry (Source: KEITHLEY Application Note Series)

1. Apply a positive magnetic field B along positive Z axis which is perpendicular to the sample plane.

2. Current I_{13}+ is injected at terminal 1 and taken out at terminal 3 and voltage V_{24}+ is

measured between leads 2 and 4.

3. Current direction is reversed i.e., I_{31}+ to leads 3 and 1 and measure voltage V_{42}+.

4. Likewise, measure V_{13}+ and V_{31}+ with currents I_{42}+ and I_{24}+, respectively.

5. Reverse the magnetic field (negative B).

6. Likewise, measure V_{24}-, V_{42}-, V_{13}-, and V_{31}- with I_{13}-, I_{31}-, I_{42}-, and I_{24}-, respectively.

Now the following values are calculated

$$V_C = (V_{24}+ - V_{24}-),\ V_D = (V_{42}+ - V_{42}-)$$

$$V_E = (V_{13}+ - V_{13}-),\ V_F = (V_{31}+ - V_{31}-)$$

The sample type is determined from the polarity of the voltage sum $V= V_C + V_D + V_E + V_F$. If this sum is positive (negative), the sample is p-type (n-type). The carrier density is calculated from Eq. 2.2. Sheet carrier density is obtained as $n_s=n*t$.

(II) Electrical Resistivity Measurement

The electrical resistivity is measured by following the contact configuration of Fig. 2.10 in van der Pauw geometry.

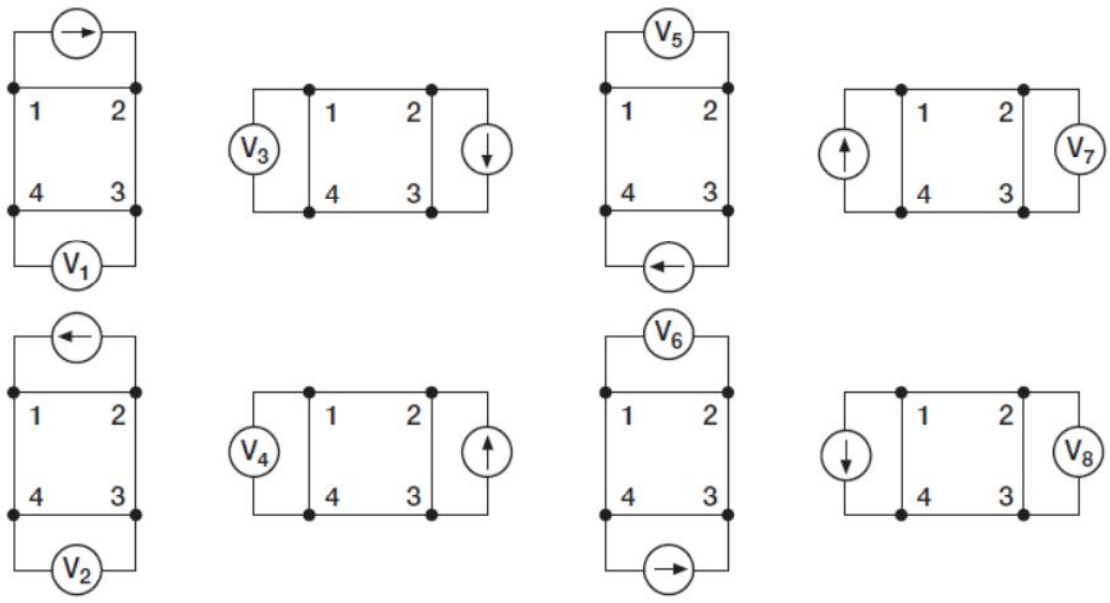

Fig. 2.10 Electrical contacts for resistivity measurement in van der Pauw geometry (Source: KEITHLEY Application Note Series)

The resistivity values are given by

$$\rho_A = \frac{\pi t}{\ln 2}\left(\frac{(V_1 - V_2 + V_3 - V_4)}{4I}\right) \tag{2.3}$$

$$\rho_B = \frac{\pi t}{\ln 2}\left(\frac{(V_5 - V_6 + V_7 - V_8)}{4I}\right) \tag{2.4}$$

where I is the input current. The final resistivity value is given by $\rho = (\rho_A + \rho_B)/2$

Chapter 3: Atomic Layer Deposition of Intrinsic ZnO Thin Films and Studies on Their Electron Transport

3.1 Optimizations of Process Parameters for Intrinsic ZnO Thin Films

As discussed in the experimental section 2.1.1, thin film growth in ALD relies on the complementary and self-terminating gas-solid reactions between the precursor molecules and the surface reactive species. However, to achieve such growth mode, the essential prerequisites are the followings:

1. Choice of a suitable deposition temperature which is sufficient to provide the ligand-exchange energy barrier and safely avoids thermal decomposition of precursors.

2. Precursor pulsing time has to be sufficiently long so that surface saturative growth occurs.

3. Inert gas purging time after each precursor pulsing step has to be sufficiently long to completely eliminate CVD type growth inside the reactor.

Therefore, first we have optimized all the above process parameters to obtain the self-limiting growth of ZnO using ALD. Instead of choosing anhydrous $ZnCl_2$ or $Zn(CH_3COO)_2$which are low vapor pressure solid sources for Zn, we opted for diethyl zinc (DEZ) which is highly volatile (vapor pressure ~ 16 mbar @20^0 C) and has high reactivity to the co-reactant de ionized water (18.2 MΩ).

From literature survey, we found that premature dissociation of DEZ and desorption of surface species significantly affect growth rate and other film properties at substrate temperatures above ~ 200^0C [92, 93, 95, 104-107, 128 and 144]. On the contrary, below ~ 100^0C precursor molecules do not have sufficient energy to react chemically with the surface functional groups to grow high quality ZnO thin films in water based thermal ALD processes. Therefore, initially we preferred a deposition temperature of ~ 185^0 C to grow ZnO thin films

for 1000 cycles on Si (100) (size:10 mm x10 mm) and sapphire (0001) (size: 5 mm x 5 mm) substrates. Substrates were kept at both precursor's inlet and outlet positions. H_2O and DEZ were pulsed into the reactor for 200 ms and the position of the needle valves NVPL1 and NVPL2 were kept at 2.5 turn each. After each precursor's pulsing step the reactor was flushed by high purity (99.999) N_2 to remove the excess precursor molecules and the reaction by-products. Uniform ZnO coating was obtained with growth per cycle (GPC) ~ 0.22 nm which was found to be consistent with the available reported values as listed in Table 1.1. Therefore, precursor and co-reactant feedings were sufficient to provide surface saturative growth. However, to check whether dosing of precursor was excessive or not, we have simultaneously decreased NVPL1 and NVPL2 positions from 2.5 to 0.25 keeping DVPL1 and DVPL2 opening times fixed at 200 ms (see Table 3.1). Different values of film thicknesses as obtained by spectroscopic ellipsometry (SE) measurements are also listed in Table 3.1.

Table 3.1 Optimization of pulsing and purging times for DEZ and co-reactant H_2O for the growth of ZnO thin films on Si substrates at 185^0C.

No. of steps	NVPL1	NVPL2	DVPL1	DVPL2	DEZ Purge	H_2O Purge	Thickness (nm)
1	2.5 turn	2.5 turn	200 ms	200 ms	1s	1s	202
2	1.5 turn	1.5 turn	200 ms	200 ms	1s	1s	196
3	1 turn	1 turn	200 ms	200 ms	1s	1s	190
4	0.50 turn	0.5 turn	200 ms	200 ms	1s	1s	190
5	0.25 turn	0.25 turn	200 ms	200 ms	1s	1s	193
6	0.25 turn	0.25 turn	100 ms	100 ms	1s	1s	180
7	0.25 turn	0.25 turn	50 ms	50 ms	1s	1s	168
8	0.25 turn	0.25 turn	25 ms	25 ms	1s	1s	135

Up to 0.25 turn of needle valves along with 200 ms of pulsing time, no significant change in the films thickness was observed. After reaching at 0.25 turn of needle valves, we decreased pulsing times of both DVPL1 and DVPL2. Film thickness was found to be decreased with decreasing pulsing time and non uniformity in film thickness was also observed. Therefore, we have chosen the process parameters in step no. 5 (highlighted in Table 3.1) to grow ZnO thin film on a 4 inch Si wafer (see Fig. 3.1) for 1000 cycles to check thickness uniformity. We performed standard 9-point thickness measurement of ZnO coating. Thickness variation between any two points on the wafer and between precursor inlet and outlet ports was found to be less than 1%. Therefore, we have considered these process parameters (step no. 5 in Table 3.1) as optimum for the growth of ZnO thin films as far as thickness uniformity and efficient precursor dosing are concerned. Moreover, self-poisoning effect by the reaction by-

products was insignificant; otherwise non-uniform film growth would have been occurred.

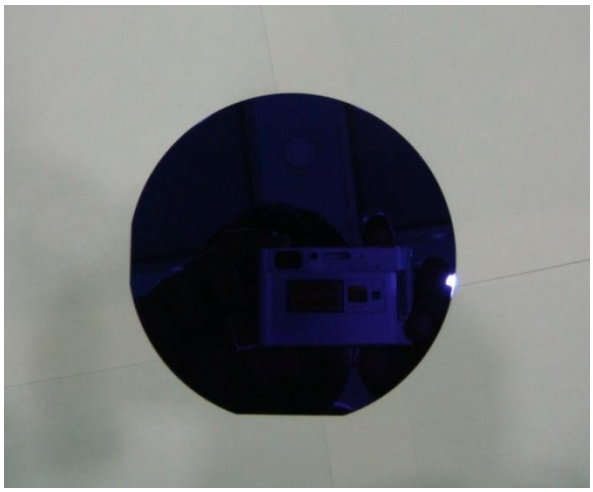

Fig. 3.1 A 4 inch Si wafer coated with ZnO thin film for 1000 cycles at 185^0C with process parameters in step no. 5 of Table 3.1.

In order to check other film properties, we have grown ZnO films on (0001) sapphire substrates with the same deposition parameters. After film growth, we have quickly performed room temperature (RT) photoluminescence (PL) and optical transmittance measurements. All the films were found to be highly transparent with average optical transmittance ~ 80% in the visible spectral range as shown in Fig. 3.2.The band gap value was found to be ~ 3.31 eV as shown in the inset of Fig. 3.2.

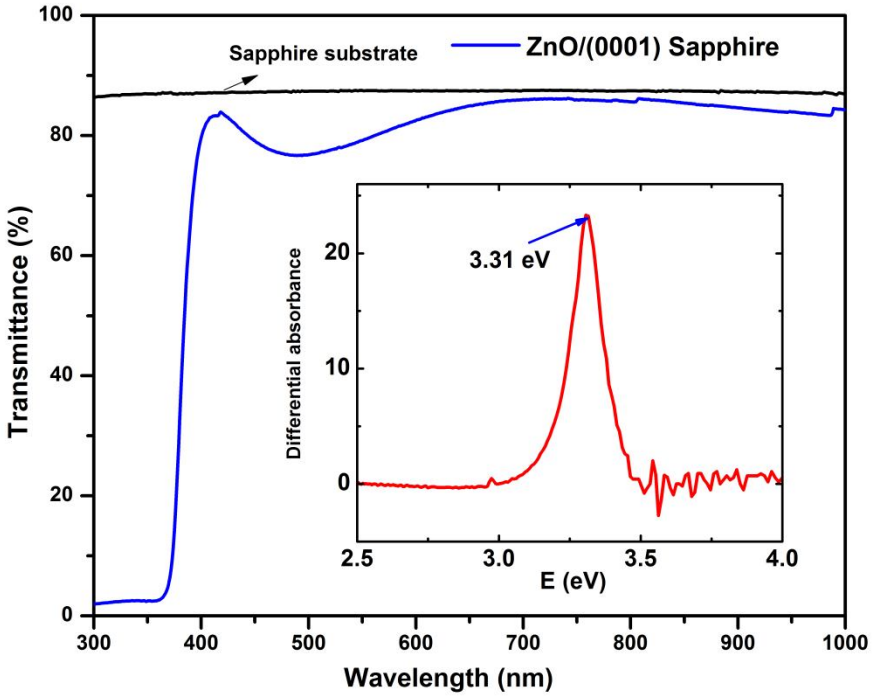

Fig. 3.2 Optical transmittance spectra of ZnO thin film grown with optimized process parameters on (0001) sapphire substrate. Inset shows differential of absorbance as a function of incident photon energy.

The RT PL spectrum (see Fig. 3.3) showed strong and intense near band-edge (NBE) UV emission centred at ~ 380 nm. The PL peak position is slightly red shifted (Stokes shift) with respect to the absorption onset at ~ 374 nm. No defect level emission (DLE) was observed in the visible spectral range of the PL spectrum. The XRD pattern of the film, as shown in the inset of Fig. 3.3, exhibited polycrystalline nature of the film with a preferred (00.2) orientation. Therefore, in addition to the high degree of thickness uniformity, the films grown with the deposition parameters in step no. 5 in Table 3.1 also showed good optical and crystalline quality.

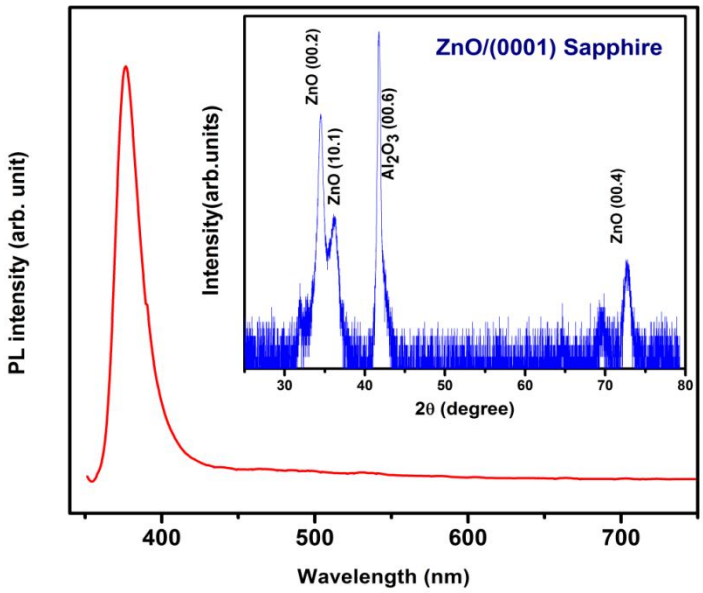

Fig. 3.3 RT PL spectrum of ZnO thin film grown with optimized process parameters (step no. 5 in Table 3.1) at 185^{0}C. Inset shows XRD pattern of the film.

The XPS spectra of the ZnO film as shown in Fig. 3.4 did not exhibit any impurities other than small amount of carbon which clearly implied high chemical purity of the as grown film.

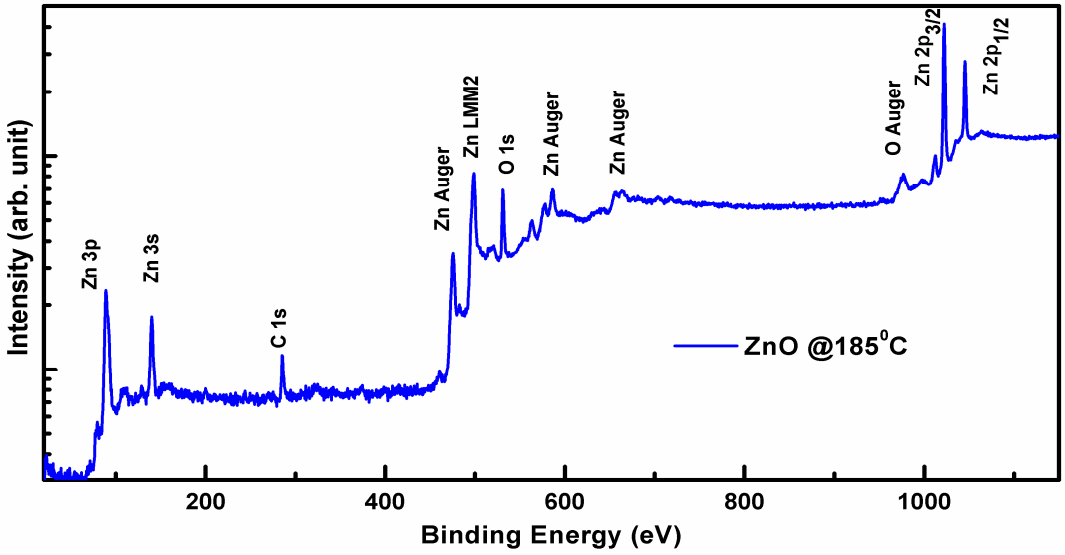

Fig. 3.4 XPS spectrum of ZnO thin film grown at 185^{0}C on (0001) sapphire substrate.

Therefore, N_2 purging time of 1s was sufficient to remove all the reaction by products and precursor's decomposition effect was also negligible. However, optimization of purging time after the water pulse is needed in thermal ALD depositions of ZnO films to control the electrical properties. We have carried out this study which we have discussed in the following section.

3.2 Characteristics of ZnO Thin Films

After some initial optimizations of the process parameters we have carried out ZnO thin film depositions by varying the substrate temperature in the range of ~ 75-275^{0}C. We have studied structural, surface morphological, chemical compositional, RT optical and electrical properties of these films.

3.2.1 Variation of Growth Rate with Temperature

The variation of GPC with growth temperature is shown in Fig. 3.5 GPC was found to be initially increased with increasing growth temperature from 75^{0}C to ~ 140^{0}C, remained nearly constant in the temperature range of ~ 140-200^{0}C, and then decreased gradually with further increase in the growth temperature up to 275^{0}C. So we obtained the typical ALD window in the temperature range of ~ 140-200^{0}C with a constant GPC of ~0.2 nm which is close to the values as reported by other groups [104-111].

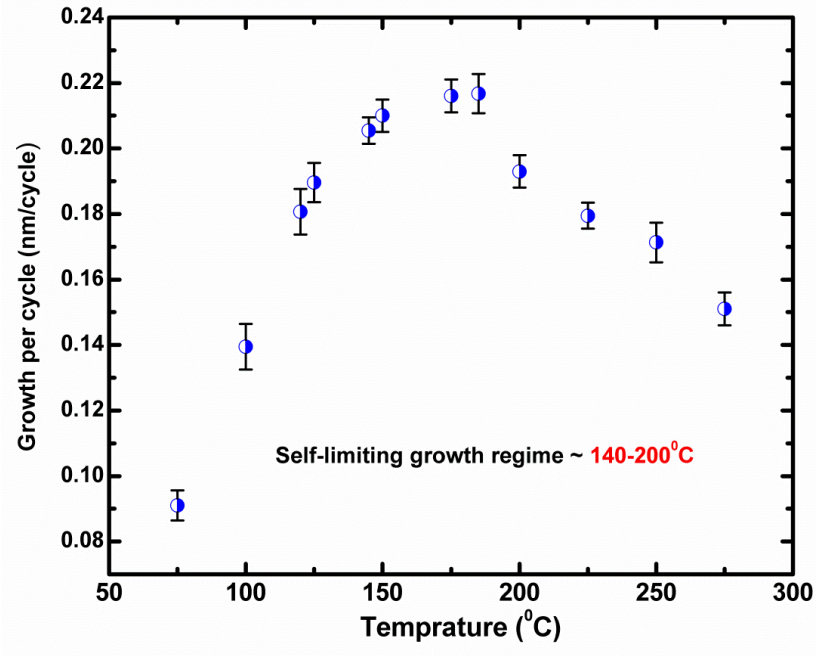

Fig. 3.5 GPC of ALD grown ZnO thin films as a function of substrate temperature in the range of ~ 50 to 275^0 C.

Such dependence of GPC on substrate temperature can be explained as follows: at lower growth temperatures, the reactants don't have sufficient energy to react chemically with the surface functional groups hence lower film growth rate was observed. As the growth temperature increased, the precursor molecules might have obtained sufficient energy to overcome the reaction barrier to react with the surface functional groups available on the growing film surface [95, 97 and 124]. Therefore, GPC was found to be increased with increasing substrate temperature up to ~ 140^{0}C. A nearly constant GPC in the temperature range of ~ 140-200^{0}C could be due to the self-limiting growth of ZnO on Sapphire. The decrease in GPC at higher growth temperatures (i.e. > 200^{0}C) could be due to the enhanced desorption of metal Zn from the growing film surface and/or thermal decomposition of DEZ at high temperatures [95, 97 and 124]. In addition the density of the surface hydroxyl (–OH) groups, which act as chemisorption sites for the DEZ molecules, decreased at higher temperatures resulting in drop off GPC above ALD window [97].

3.2.2 Structural & Morphological Properties

Fig. 3.6 shows the θ-2θ scans of all the ALD-ZnO thin films grown at different substrate temperatures. The XRD results revealed that ALD-ZnO films were polycrystalline in nature and their crystallinity changed with deposition temperature. As can be seen from Fig. 3.6, the films deposited at ~ 200 and 250^0 C of substrate temperatures showed preferred (00.2) oriented growth. However, the FWHM of the (00.2) XRD peak of the film grown at ~ 250^0 C was found to be higher as compared to the film grown at ~ 200^0 C indicating slight deterioration of the crystalline quality of the film grown at ~ 250^0 C. For the films grown at ~ 150, 300 and 350^0 C there was no preferred orientation of the crystallites. In these films diffused and weak XRD peaks were observed corresponding to different crystallographic planes of the hexagonal wurtzite ZnO. The films grown at ~ 150 and 300^0 C were dominated by both (10.1) and (00.2) oriented crystallites. However, a small fraction of crystallites were found to be oriented along the (10.0) direction for the film grown at ~ 350^0C. We have already discussed in section 1.4.3, that preferential growth of ALD-ZnO thin films is strongly dependent on their growth temperatures and other process parameters like precursor's pulsing and purging times, flow rates etc. Pung*et al.* reported that with changing deposition temperature the reaction chemistry between DEZ and H_2O may change due to the premature dissociation of DEZ molecules which result in changing of growth mode with varying crystalline quality [98].

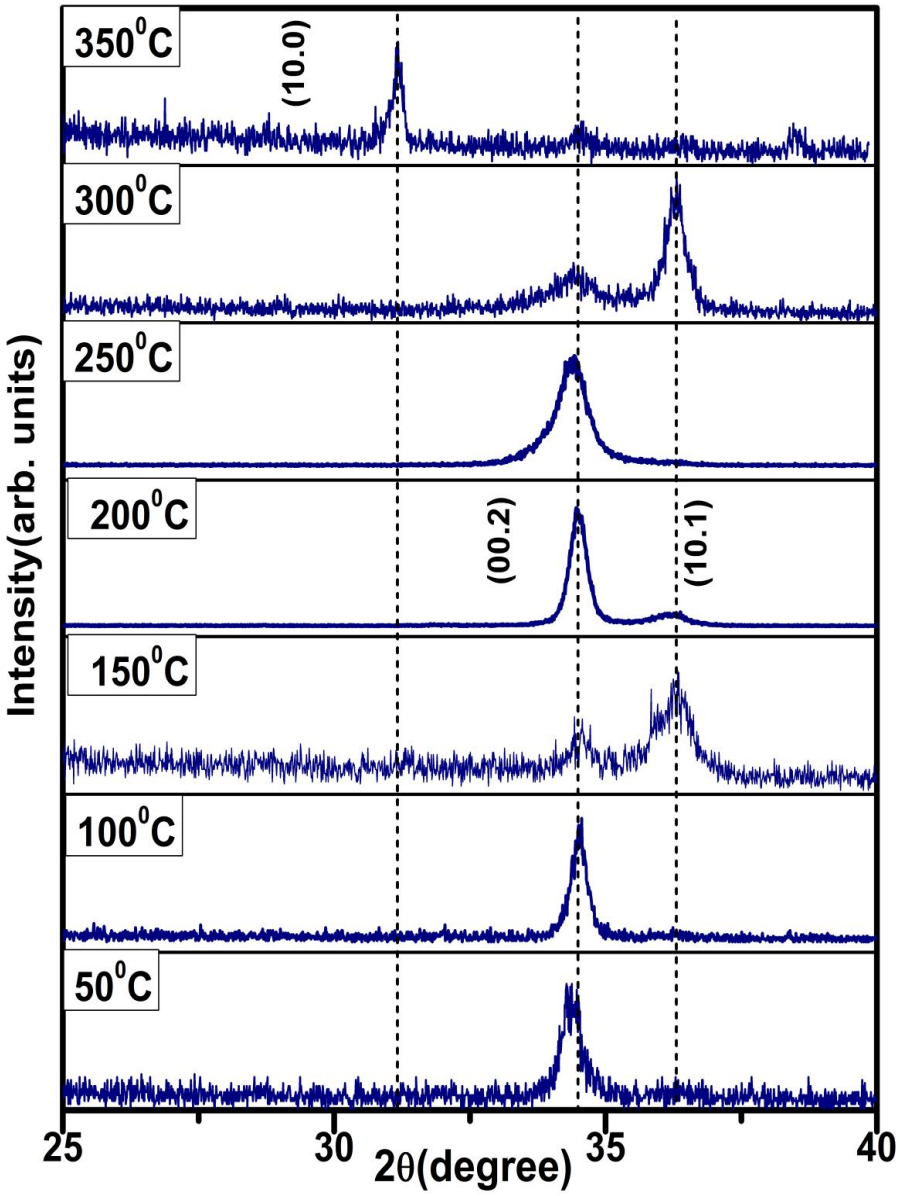

Fig. 3.6 XRD pattern of ALD-ZnO thin films grown on (0001) sapphire substrates at different substrate temperatures.

The surface morphological properties of the films as observed by AFM measurements are shown in Fig. 3.7. All the films were found to be granular and RMS surface roughness was less than 5 nm. As can be seen, the film grown at 200^0 C is composed of densely packed nearly spherical grains whereas the film grown at 100^0 C exhibits nearly triangular shaped grains.

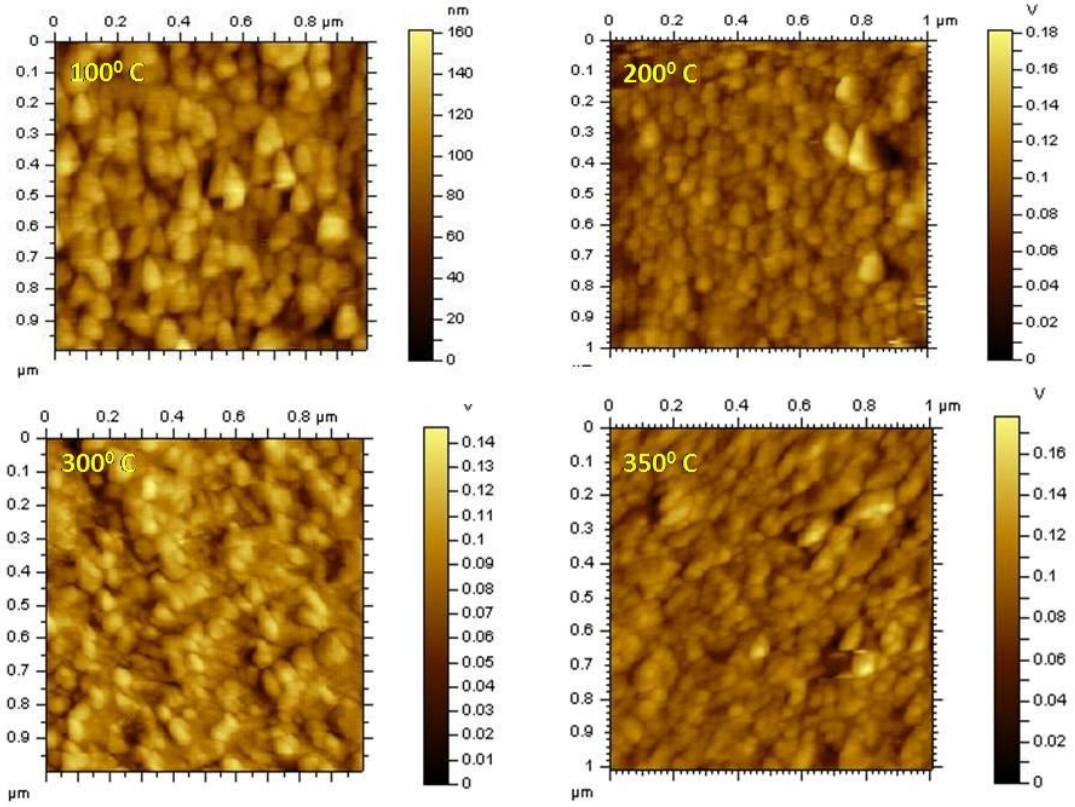

Fig. 3.7 AFM surface morphological images for ZnO thin film grown at 100, 200, 300 and 350^{0}C on sapphire (0001) substrates.

3.2.3 Chemical Compositional Properties

XPS measurements were performed on ZnO thin films grown at 50, 200 and 250^{0}C to detect the presence of native defects and impurities in the films. Sample surfaces were etched using 1 keV Ar ion beam prior to the measurements to remove the air contaminated top layers. The chemical species were identified through their binding energies, which were determined by fitting the spectral line shapes with mixture of Lorentzian and Gaussian functions. The XPS spectra corresponding to the O1s peak for the three films grown at 50, 200 and 250^{0}C are shown in Fig. 3.8. The area under the O1s peak can be deconvoluted into three curves centered at ~530.1 eV, 531.2 eV and 532 eV. The lowest binding energy peak at ~ 530.1 eV is

attributed to O^{2-} ions at regular lattice sites (O_L or Zn-O bonding). The medium binding energy component at ~531.2 eV is associated with O^{2-} ions in the oxygen deficient regions (O_V) within the ZnO matrix. The shoulder at the highest binding energy of ~532 eV corresponds to interstitial oxygen (O_i or O-H bonds). The area under the O-H bonding curve was found to be monotonically decreased with increase in growth temperature. This could be well explained by considering the surface reaction mechanism between DEZ and water which is given by [104-107],

DEZ pulse: surface-OH + C_2H_5-Zn-C_2H_5 → surface-O-Zn-C_2H_5+ C_2H_6↑

H_2O pulse: surface-O-Zn-C_2H_5 + H_2O → O-Zn-OH + C_2H_6↑

At lower deposition temperatures the incomplete chemical reaction between DEZ and surface –OH groups left behind a large number of unreacted –OH groups after completion of each ALD cycle. Moreover, at lower substrate temperatures, complete removal of physisorbed water molecules after the water pulse requires longer purging time [97].These are possibly responsible for the higher –OH group density in films as observed in the XPS measurement. With increase in growth temperature, the chemisorption reaction between DEZ and water becomes more complete which reduces –OH related defects in the films [95, 97 and 124]. These results are in line with the electrical and optical properties of the films as discussed below.

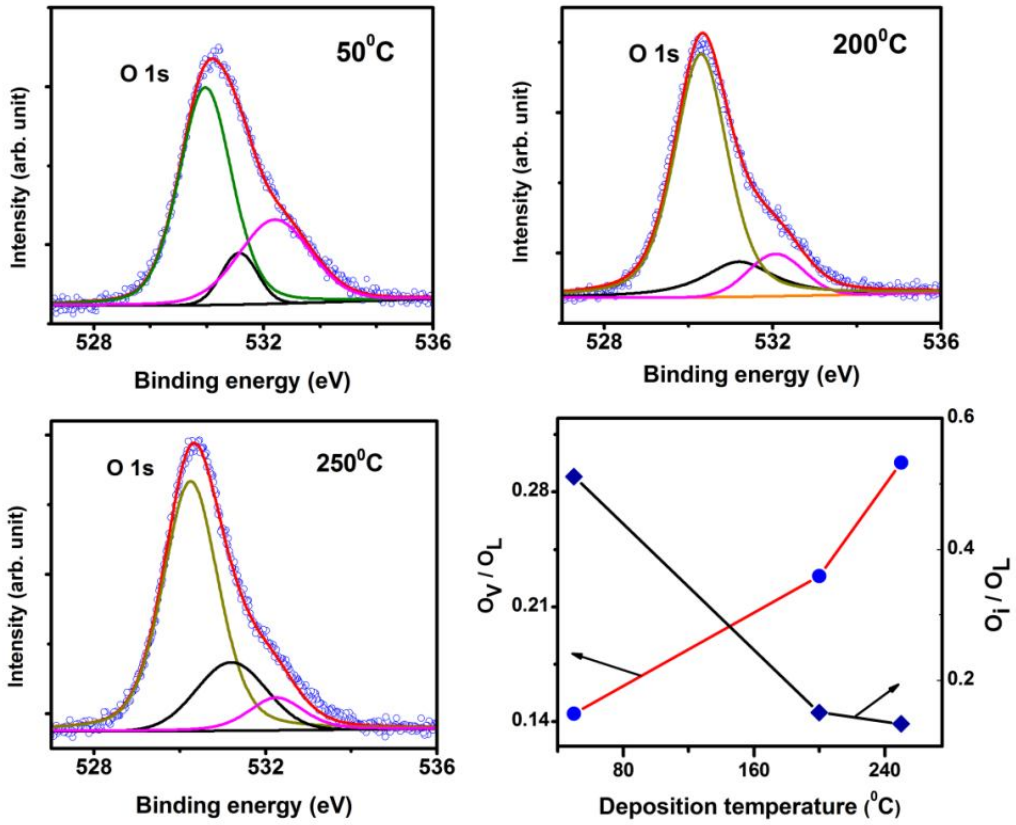

Fig. 3.8 XPS spectra of O1s in as deposited ZnO thin films grown at 50^{0}C, 200^{0}C, 250^{0}C.

3.2.4 Room Temperature Electrical Properties

ZnO films grown below ALD window i.e., at 50 and 100^{0}C were found to be too high resistive to be measured. However, these films turned into highly conducting when exposed to UV light (larger than the band gap of ZnO) and retained their conductivity when kept in high vacuum chamber. The highly-conducting state slowly reverted to the initial highly-resistive state when exposed to atmosphere. Such reversible change in the electrical conductivity could be explained by desorption and adsorption of hydroxyl groups and/ oxygen at the surface and at grain boundaries as schematically shown in Fig. 3.9.

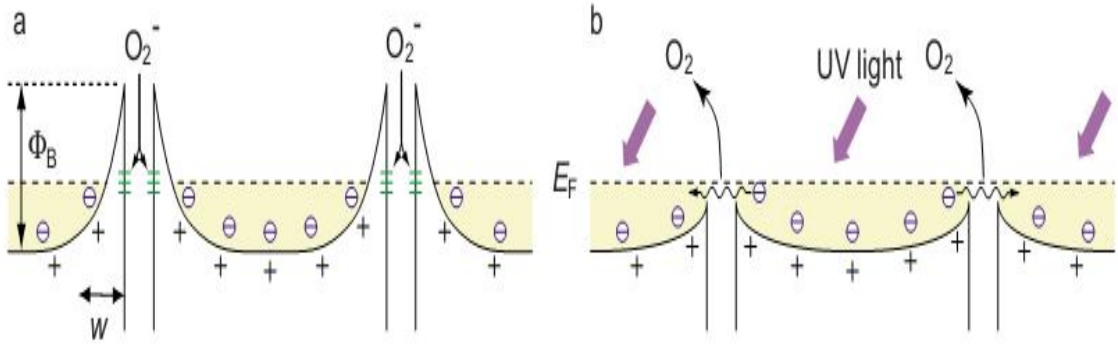

Fig. 3.9 Schematic representation of O_2 adsorption and desorption under UV illumination at grain boundaries in ZnO thin film [Reproduced with permission from: Y. Muraoka, N. Takubo, and Z. Hiroi, J. App. Phys. 105, 103702. Copyright (2009), AIP Publishing LLC].

In low-temperature ALD grown ZnO films, OH groups and/or oxygen get chemisorbed at surface and at grain boundary defect sites by capturing a free electron from the bulk of the film which results in the formation of depletion region and upward band bending at the surface and at grain boundaries [152]. Through absorption of UV photons having energy larger than the band gap of ZnO, electron-hole pairs are created. Due to the potential slope created by the band bending, it is possible that holes migrate to the grain boundary and to the film surface, where they recombine with the adsorbed OH^- and / O_2^- ions. This process causes photo desorption of OH^- and / O_2^- ions which results in increased electrical conductivity due to the available unpaired free electrons in the conduction band. Since there is no oxygen or moisture inside a high vacuum chamber, these films retain their conducting state even after turning off the UV light. After 10 minutes of UV light irradiation, the conductivity values for the films grown at 50 and 100^0 C were found to be ~ $34x10^{-3}$ and $25x10^{-3}\Omega$ cm respectively. Therefore, the highly resistive behaviour for the low-temperature grown ZnO films could be attributed to the presence of additional oxygen related point defects in ZnO either in the form

of –OH groups and/or oxygen interstitials which act as trapping centres for free carriers and/or compensating the back ground n-type conductivity in the films. Such phenomenon of electron trapping and de-trapping is expected to have strong influence on the underlying electron transport of ultrathin ZnO films due to their higher surface to volume ratio. We have observed UV light induced insulator to metal transition in ultrathin ZnO/TiO_x stacked layer. The results of this study have been discussed in chapter 5. Plausible reason for such defect formation has been discussed above in section 3.2.3 by considering the surface reaction between DEZ and water molecules. Moreover, the presence of such defects has also been verified by XPS measurements. As stated earlier, at lower deposition temperatures, complete removal of physisorbed water molecules requires longer purging time in thermal ALD reactors [97]. Therefore, we have carried out ZnO thin film growth at 100^0 C with sufficiently long purging time of 10 sec after the water pulse. However, these films were also found to be highly resistive similar to those grown with 1 sec purging time. This problem arises mainly due to the use of thermal ALD reactor and water as a co-reactant. In order to avoid the –OH group related issues, plasma enhanced ALD (PEALD) or O_3 based ALD would be a better option. Yamamoto *et al.* carried out growth of B doped ZnO thin films by photo-atomic layer deposition (photo-ALD) technique in which UV light was irradiated onto the substrate during film depositions [129]. By following this technique, they were able to minimize the chemical disorder by decreasing the number of dangling bonds in the films which resulted in highly stable ZnO thin films with lower electrical resistivity.

The films grown within and above ALD window showed stable n-type conductivity. Although the RT resistivity values of these films as measured immediately after their depositions were found to be slightly lower compared to the values measured after exposing them in open atmosphere during 30 days. This observation clearly indicates that the effect of free carrier trapping was not significant for these films. This was plausibly due to more

complete reaction between DEZ molecules and the surface functional groups which resulted in reduced –OH group density in the films as confirmed by XPS measurements. Fig. 3.10 shows the variation of RT resistivity (ρ), carrier density (n) and mobility (μ) of the films as a function of growth temperature. As can be seen from Fig. 3.10(a), RT resistivity of the films initially decreased from ~ $24x10^{-3}$ Ω cm to ~ $3.6x10^{-3}$ Ω cm with increase in growth temperature from 150 to 200^0C. With further increment of growth temperature, resistivity was found to be increased up to ~ $16x10^{-3}$ Ω cm at 350^0C. The higher value of RT resistivity for the films grown at ~ 150, 300 and 350^0C plausibly resulted from the intensified disorder and poor crystalline quality of these films as observed in their XRD pattern and RT PL spectra (discussed later). Fig. 3.10(b) shows that electron concentration in the films first increased from ~ $1.6x10^{19}$ cm^{-3} to the maximum ~ $5.7x10^{19}$ cm^{-3} as the growth temperature was increased from 150 to 200^0C and then decreased up to ~ $2.1x10^{19}$ cm^{-3} with additional increment in growth temperature. Such high level of unintentional electron density in ALD grown ZnO films has been extensively reported in the literature and is attributed to the various intrinsic and/or extrinsic point defects such as zinc interstitials, oxygen vacancies, and/or hydrogen as discussed in section 1.1.2. These point defects introduce shallow donor levels below the conduction band minimum and are the sources of high level of electron doping in the ALD-ZnO films. The variation of Hall mobility with growth temperature as depicted in Figure 3.10(c) was found to be consistent with the above explanation of the resistivity behaviour (Figure 3.10(a)). The film grown at 200^0C showed highest Hall mobility ~30 cm^2/V s which could be due to the improved crystalline quality and reduced defects in the film. However, Hall mobility decreased significantly for the films grown at substrate temperatures of ~ 150, 300 and 350^0C presumably due to the strengthened disorder in these films.

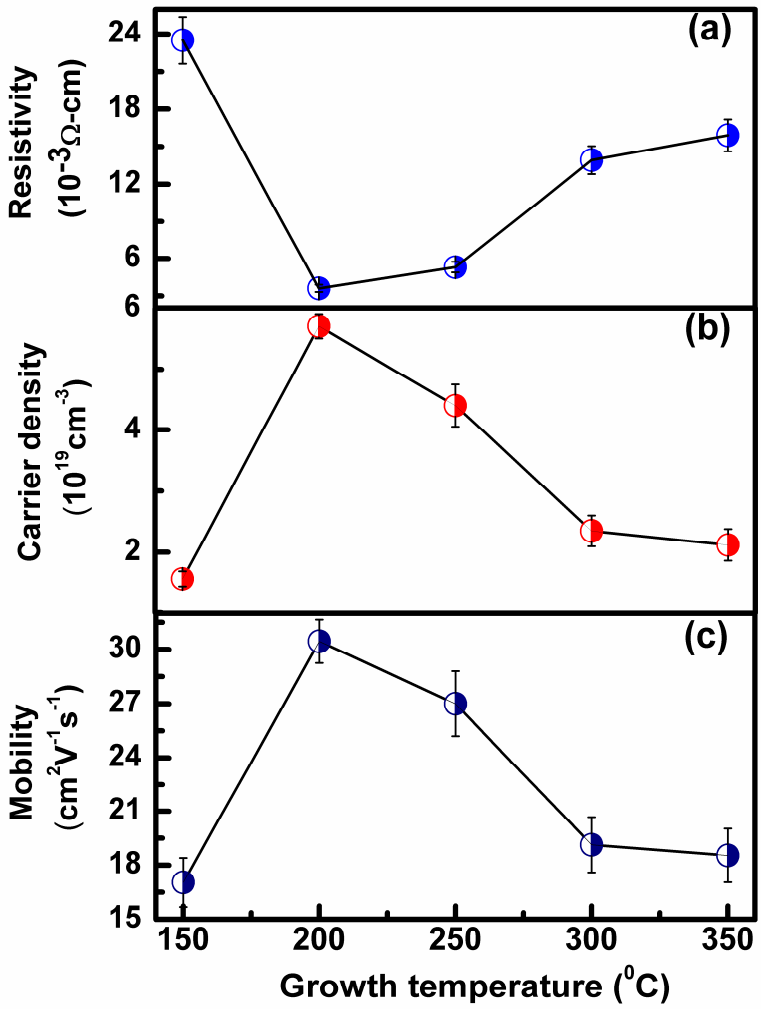

Fig. 3.10 Variation of RT (a) resistivity (b) carrier concentration and (c) Hall mobility of ALD-ZnO thin films with growth temperature. The solid lines connecting the data points are guide to the eye.

3.2.5 Room Temperature Optical Properties

The Optical transmittance measurements were carried out using a UV-Visible spectrophotometer. All the films were found to be shiny and highly transparent to the naked eyes. Optical transmittance spectra of ZnO films recorded at room temperature in the spectral range from 300 to 600 nm are shown in Fig. 3.11. All the ZnO films are ~80 % transparent in the visible spectral range with a sharp cut off at ~ 380 nm which corresponds to the fundamental optical absorption edge of ZnO. The variation of optical band-gap with growth

temperatures is shown in the inset of Fig. 3.11. The higher optical band-gap for the film grown at 200^0C could be attributed to the Burstein-Moss effect [153]. Surprisingly, optical band-gap values for the highly resistive films grown at 50 and 100^0C were found to be higher compared to all the conducting films except that grown at 200^0 C. Such blue-shift in the optical absorption edge could be due to their poor crystallinity as observed in the XRD pattern. These films had significant fraction of amorphous ZnO phase which possesses only short range periodicity. Such high degree of disorder in the films plausibly results in the formation of mobility edge, which localizes a fraction of extended states in the conduction and valance bands [154]. Therefore, effectively optical band-gap value is increased. One more possibility is the distortion in the band structure of ZnO lattice due to thermal mismatch and lattice mismatch strains [155].

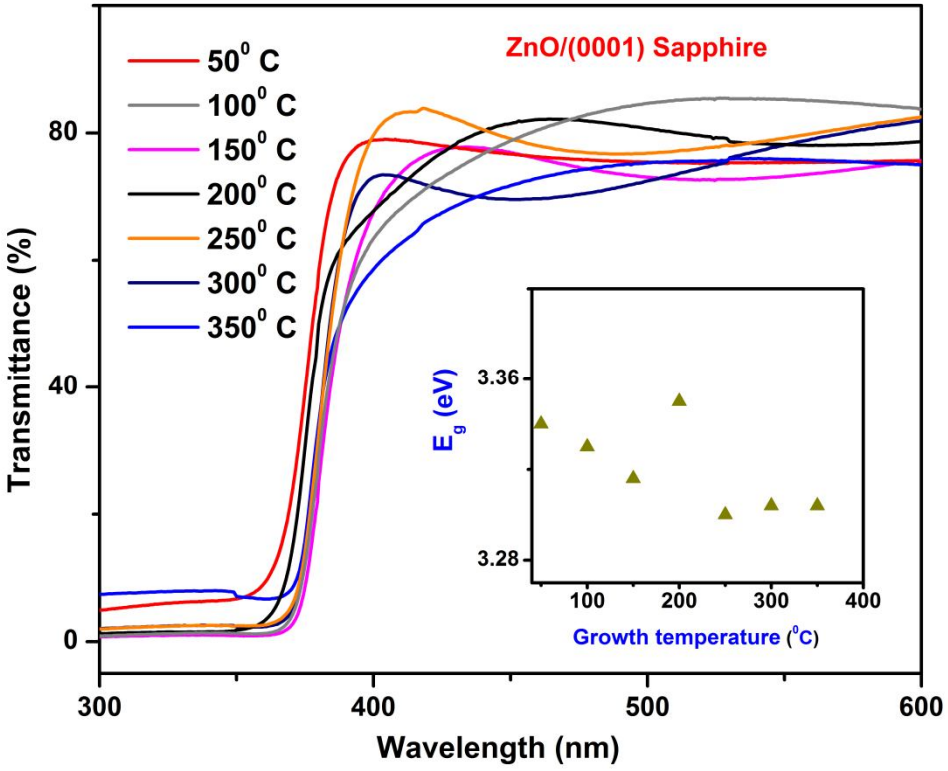

Fig. 3.11 Optical transmittances of ALD ZnO thin films grown on sapphire at different substrate temperatures. The inset illustrates the variation of band gap of ZnO thin films with deposition temperature.

Fig. 3.12 shows the RT PL spectra for all the ZnO thin films grown at different substrate temperatures. All the films exhibited excitonic near band edge emission (NBE) at ~375 nm corresponding to the optical band-gap of ZnO (~ 3.30 eV). NBE peak position in each case was found to be red shifted (Stokes shift) compared to the optical absorption edge of the corresponding film. The shift in NBE peak positions with respect to each other could be due to the effect of strain in the films [155].

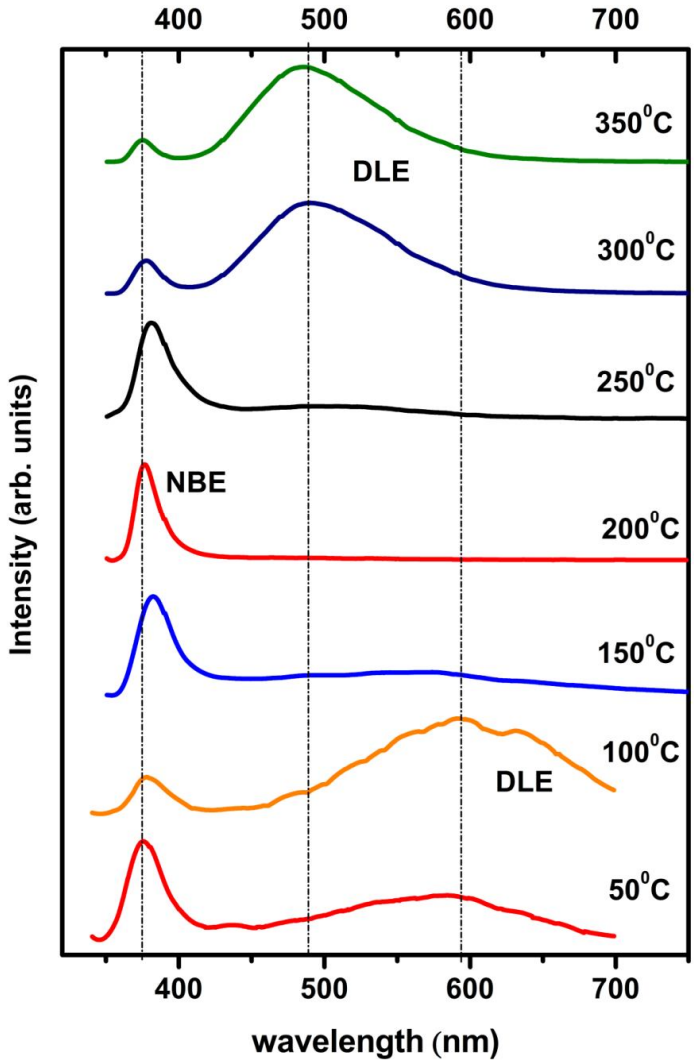

Fig. 3.12 Room temperature photoluminescence spectra of ALD ZnO thin films grown on sapphire substrate at different substrate temperatures.

NBE PL peak intensity was found to be considerably enhanced with increasing growth temperature up to 200^0C and then decreased with further increment in temperature as shown in Figure 3.13. The full width at half maximum (FWHM) or sharpness of the NBE PL was found to be decreased monotonically with increasing growth temperature, reaching a minimum value at 200^0C (see Fig. 3.13) and then increased with further increment in growth temperature. Therefore, ZnO thin films with optimum optical quality were obtained at 200^0C. Apart from the NBE PL in the UV spectral range, a broad PL in the visible spectral range known as defect level emission (DLE) was also observed for the films grown on either side of 200^0C as shown in Fig. 3.12. The films grown at 50 and 100^0 C i.e., below ALD window exhibited strong DLE peak centered at ~ 595 nm (orange). As the growth temperature was increased up to 150^0C, the intensity of this DLE peak was found to be significantly reduced and eventually diminished in the films grown at and beyond 200^0C. However at250^0C, a faint and broad PL peak appeared at ~ 490 nm (green). The intensity of this DLE peak was found to be drastically increased with further increment in growth temperature up to 350^0C. The origin of DLE emission in ZnO is still controversial and its position and behaviour strongly depends on growth methods and conditions. The orange PL in undoped ZnO has been attributed to the presence of excess oxygen or oxygen interstitials in ZnO lattice, while green PL has been attributed to the presence of oxygen vacancies as has been discussed in section 1.1.3.Vanheusden *et al.* proposed that the green PL at 510 nm in ZnO is originated due to the recombination of electrons in singly ionized oxygen vacancies (O_V^+) with photo excited holes in the valence band [39, 40].Studenikin and Cocivera suggested that the green luminescence in ZnO is due to an electron-hole recombination process involving a donor-acceptor complex, which most likely consists of an oxygen vacancy and a zinc vacancy [50]. Electron paramagnetic-resonance analysis showed that the green emission consists of two transitions, with electron-hole re-combinations from conduction band to V_O level and from Zn_i to V_O

level [3, 4].Green emission is commonly observed in oxygen deficient ZnO films whereas orange luminescence is seen in oxygen-rich films as discussed in section 1.1.3. Presence of such native point defects in ALD grown ZnO films has already been verified by XPS measurements. The XPS spectra for the ZnO films grown below ALD window showed presence of significant amount of oxygen interstitials. This might be the reason that orange PL was predominantly observed in these films. However, oxygen vacancy related point defects were found to be increased with increasing growth temperature which plausibly resulted in green luminescence in the films grown at 300 and 350^0 C.

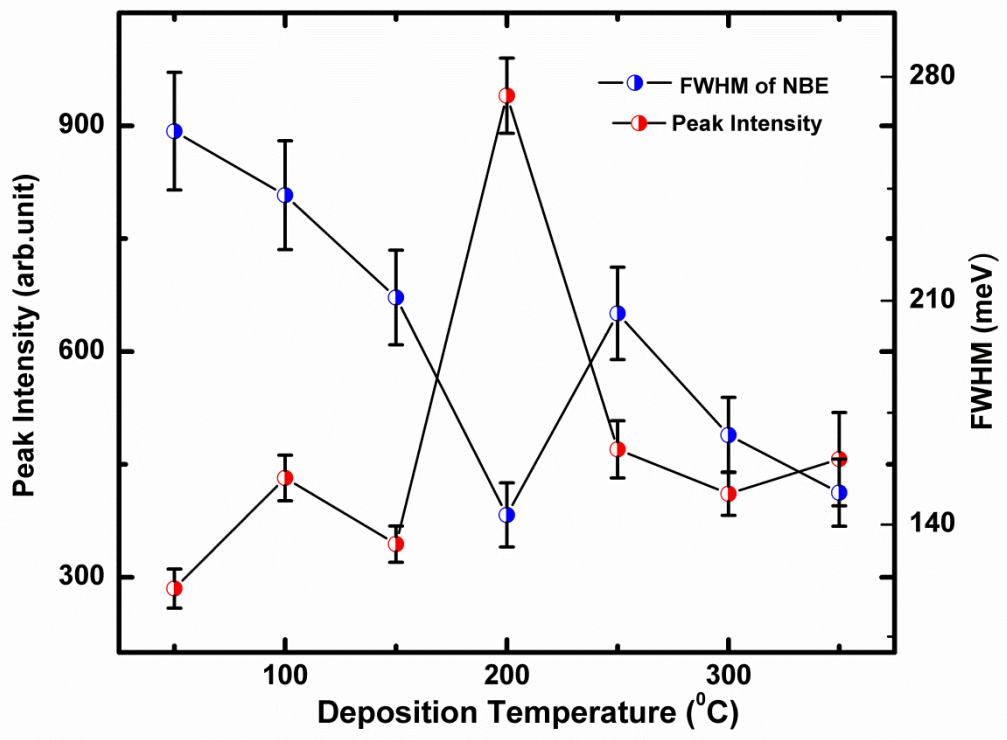

Fig. 3.13 FWHM and NBE peak intensity of ZnO thin films as a function of substrate temperature.

3.3 Temperature Dependent Electron Transport Studies

So far we have discussed our results on structural, RT optical and electrical properties of intrinsic ZnO thin films grown by ALD at different substrate temperatures. In order to efficiently use these films in electronic devices and in TCE applications, it is imperative to investigate the underlying carrier scattering mechanisms which control the electrical

properties in these films. For this purpose, we have carried out temperature dependent electrical resistivity and Hall measurements in the temperature range of ~ 5 to 300 K. The results of these studies are discussed below.

3.3.1 Temperature Dependent Electrical Resistivity and Hall Measurements

Fig. 3.14 shows results of the temperature dependent electrical resistivity ρ (T) measurements for the films grown at different substrate temperatures. The ρ (T) measurements for the highly resistive films grown at ~ 50 and 100^0 C were carried out in UHV chamber after illuminating the samples with UV light for 10 minutes. The ρ (T) curve for the film grown at 100^0 C (see Fig. 3.14 (a)) exhibited a 'semiconductor-like' resistivity behaviour i.e., $(d\rho / dT) < 0$ in the entire range of the measurement temperature with a finite value of resistivity at T→0 K. Therefore, this film was on the metallic side of the metal to insulator transition (MIT). Similar resistivity behaviour was also observed for the film grown at 50^0 C which has not been shown in Fig. 3.14. The ρ (T) curves for the films grown at ~ 150, 300 and 350^0 C (Fig. 3.14 (b), (e) and (f)) also showed 'semiconductor-like' resistivity behaviour in the entire range of the measurement temperature. However, as these films showed stable n-type conductivity, ρ (T) measurements were carried out without any UV light pre-treatment. The films grown at ~ 200 and 250^0 C showed a transition from 'metal-like' to 'semiconductor-like' resistivity behaviour at lower temperatures (see Fig. 3.14 (c) and (d)).

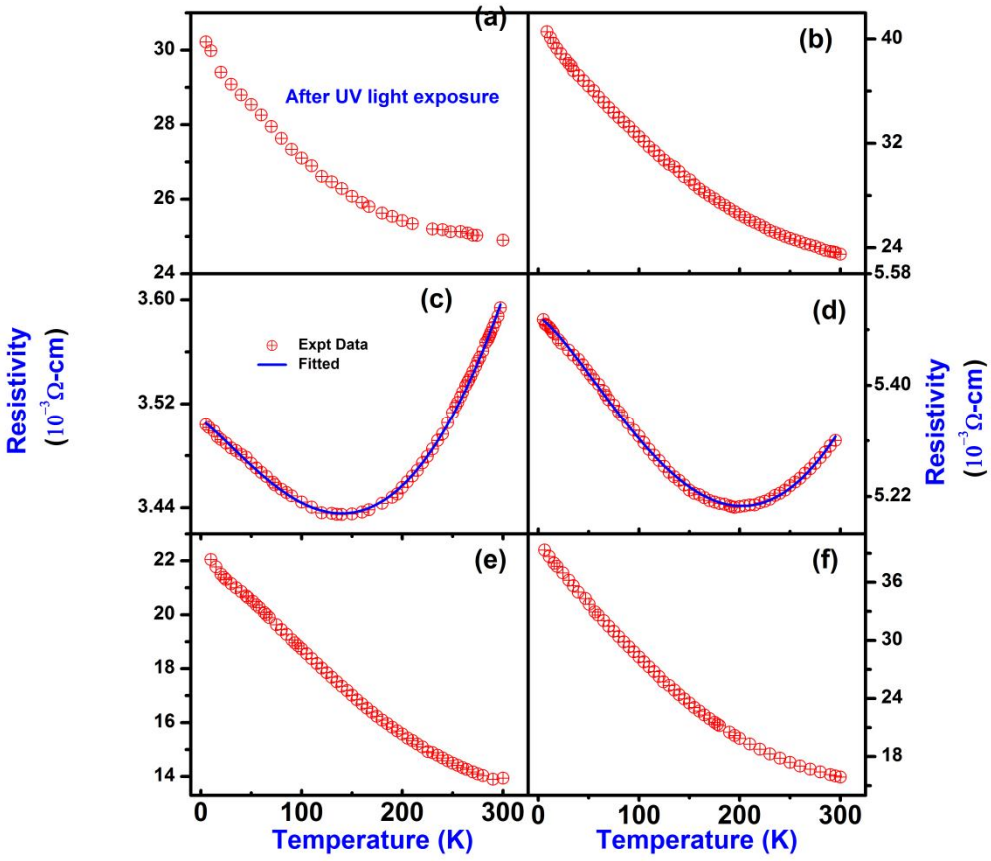

Fig. 3.14 Variation of resistivity with temperature for ALD-ZnO thin films grown at (a) 100, (b) 150, (c) 200, (d) 250, (e) 300 and (f) 350^{0}C on sapphire substrates.

The observed 'semiconductor-like' behaviour in all the ρ (T) curves could not be fitted by classical Arrhenius equation. This suggests that carrier transport in these films was not due to the simple thermal activation of carriers as commonly observed in semiconductors. The above observation is expected because the carrier concentrations in these films were quite high and they were heavily degenerate in nature. Fig. 3.15 shows the temperature dependent Hall measurement data for all stable n-type conducting films. As can be seen, carrier concentration was nearly independent of temperature over the entire measurement temperature range, a characteristic of a degenerate electronic system.

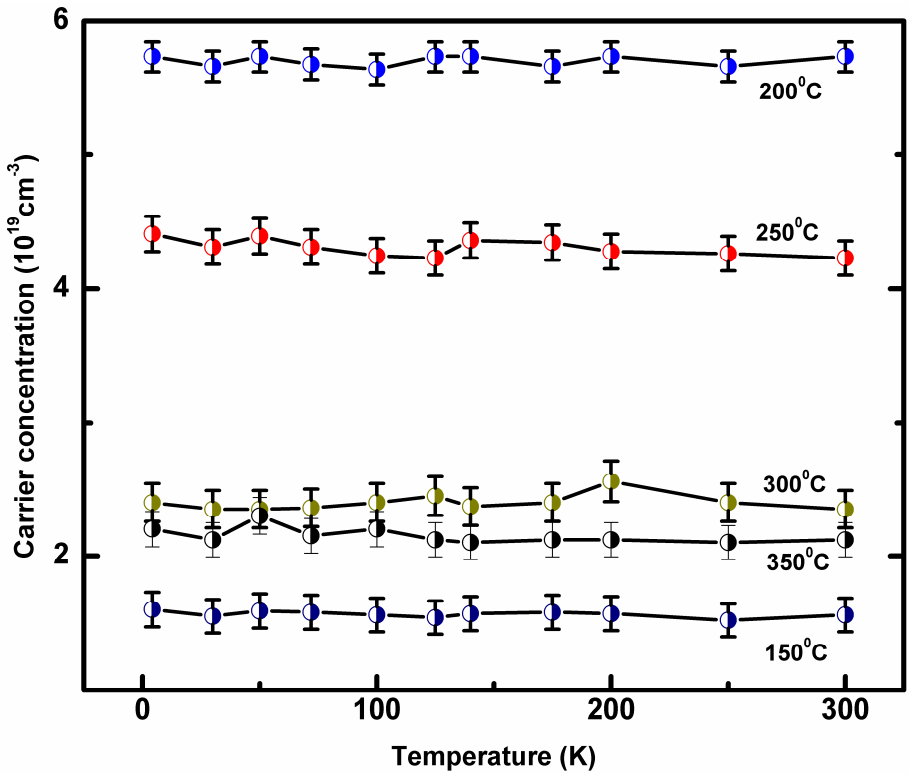

Fig. 3.15 Variation of carrier concentration with measurement temperature for ZnO thin films grown at different substrate temperatures on (0001) sapphire substrates. Solid lines connecting the data points are guides for eye.

For doped semiconductors MIT occurs due to the formation of a degenerate band as suggested by Mott [73]. As can be seen from Fig. 3.15, the measured carrier concentrations for all the ZnO films exceed the Mott's critical carrier concentration (n_c) required to create a metallic state for ZnO ($n_c \approx 1.01\text{x}10^{19}/\text{cm}^3$). In these heavily doped ZnO thin films Fermi level moves into the conduction band. However, despite their highly degenerate nature, 'semiconductor-like' behaviour ($d\rho/dT < 0$) was observed plausibly due to the disorder induced localization of carriers which impeded the metallic transport in these films [82, 96]. The native donor type point defects, which were responsible for high electron density in the films, statistically occupied the host lattice and/or interstitial sites and thus introduced disorder in the films leading to the weak-localization (WL) effect (see section 1.3.4). Tiwari

et al. showed a transition from the band-gap insulating state to the Anderson localized insulating state in oxygen deficit ZnO thin films due to the random distribution of oxygen vacancies which introduced disorder and hence localization of free carriers in the films [156].Therefore, aspects of both Mott (electron correlation) and Anderson (disorder-induced localization) effects are present in intrinsically doped ZnO thin films [82]. The presence of native defects and micro-structural disorder in ALD grown ZnO thin films could be confirmed from their XRD pattern and RT PL spectra as discussed earlier. For a more comprehensive insight into the carrier transport mechanisms in these films we divided our samples into two categories. The first category includes the films grown at 200 and 250^0 C which were inside and slightly above the self-limiting growth window of ZnO. These films exhibited a resistivity minimum at lower temperatures. The second category consists of the films grown at 150, 300 and 350^0 C which were just inside and far above the self-limiting growth window. These films showed only 'semiconductor-like' behaviour in the entire range of measurement temperature.

The observed 'semiconductor-like' resistivity behaviour at lower temperatures for the films belonging to the first category (Fig. 3.14(c) and (d)) could be well explained by considering quantum corrections to the Boltzmann conductivity [95]. Such an approach can be implemented when the Fermi wavelength $\lambda_F(2\pi/(3\pi^2 n_e)^{1/3})$ becomes comparable to the elastic mean free path $l_e(h/\rho n_e e^2\ \lambda_F)$ of conduction electrons, where n_e is the carrier density, ρ is the resistivity and e is the electronic charge. For ZnO thin films grown at 200 and 250^0 C we obtained $l_e < \lambda_F$; hence, quantum corrections could be taken into account to interpret the transport mechanisms in these films. Quantum corrections include the effect of weak localization (WL) and electron-electron interactions (EEIs) which we have discussed in detail in sections 1.3.4 and 1.3.5. Including these two corrections, temperature dependent electrical resistivity for a disordered electronic system is be given by [95],

$$\rho(T) = \frac{1}{\left(\sigma_0 + mT^{1/2} + aT^{p/2}\right)} + bT^2 \qquad (3.1)$$

where σ_0 is the residual conductivity (conductivity value at T→0 K) which was included due to the presence of usual temperature independent elastic scattering of electrons from defects, the term $aT^{p/2}$ corresponds to WL due to the self-interference of coherent electron wave functions as the electrons are backscattered from impurities, temperature dependence of this term can be determined from the temperature dependence of the scattering rate ($\tau_\varphi^{-1} \approx T^p$) of the dominant dephasing mechanism (p = 2 for inelastic electron-electron collisions and 3 for electron-phonon scattering) and the term $mT^{1/2}$ comes due to the coulomb EEIs due to the diffusive motion of conduction electrons. In addition to these two corrections, a term bT^2 is included in order to account the high temperature inelastic scattering contribution. The resistivity curves in Fig. 3.14(c) and (d) showed a decent fit to Eq. 3.1. The corresponding values of the fitting parameters are given in Table 3.2. The best fit (solid lines) was obtained for p = 3 which means that electron-phonon scattering plays a dominating role in the carrier transport mechanism.

Table 3.2 Values of the fitting parameters of Eq. (3.1) for ZnO thin films grown at 200 and 250^{0}C on (0001) sapphire substrates.

Growth temperature (^{0}C)	σ_0 (Ω^{-1}cm^{-1})	m (Ω^{-1}cm^{-1}K$^{-1/2}$)	a (Ω^{-1}cm^{-1}K$^{-3/2}$)	b (Ω cm K^{-2})
200	(285.3±0.1)	(3.26±0.87)x10^{-2}	(1.08±0.01)x10^{-2}	(7.8±0.05)x10^{-9}
250	(181.4±0.1)	(5.83±0.62)x10^{-2}	(1.15±0.01)x10^{-2}	(1.2±0.01)x10^{-8}

The above theory of quantum corrections to the conductivity is considered to be valid at

lower temperatures provided that the sum of the correction terms ($\delta\sigma$) is much smaller than the Boltzmann conductivity, i.e.,

$$\delta\sigma = aT^{p/2} + mT^{1/2} << \sigma_0 \qquad (3.2)$$

In the studied interval of temperatures (4.2 K < T < T_m) the values of $\delta\sigma/\sigma_0$ as calculated from the fitting parameters listed in Table 3.2 for the ALD-ZnO films grown at 200 and 250^0 C were found to be 0.06 and 0.16 respectively, i.e., quantum corrections were indeed very small as compared to the Boltzmann conductivity, so we can reliably use Eq. 3.1.

Within the context of this discussion, it is worthy to mention that residual resistivity ρ_0, as obtained by fitting the ρ (T) curves using Eq.3.1, gives a measure of degree of disorder in the films. Higher value of ρ_0 indicates higher static-disorder in the film. The RT PL and XRD measurements showed that the micro-structural disorder in the film grown at 250^0 C was higher compared to that grown at 200^0C. This is well corroborated with the higher ρ_0 value of the film grown at 250^0 C compared to that grown at 200^0C. The resistivity minimum for the film grown at 250^0 C was found to be shifted to the higher temperature (T_m ~ 195 K) compared to the film grown at 200^0 C (T_m ~ 150 K). This could be explained by considering the degree of disorder in the films. The condition for electron interference which resulted in the resistivity minimum is given by $L_\varphi > l_e$ as discussed in section 1.3.4. The value of L_φ is decreased with increasing temperature (Eq. 1.34 in section 1.3.4) due to inelastic scattering processes. Therefore, as the film grown at 250^0 C had lower value of l_e compared to the film grown at 200^0 C, the condition for interference could be satisfied at higher temperatures for the film 250^0 C compared to that grown at 200^0 C. These critical observations revealed the significant role of disorder in the low-temperature electron transport in ALD grown ZnO thin films. In the second category which consists of the films grown at ~ 150, 300 and 350^0C, all the ρ (T) curves showed only 'semiconductor-like' resistivity behaviour plausibly due to

pronounced disorder formation in these films. The strengthened disorder in these films was verified by XRD pattern and RT PL spectra of the films as discussed above. Moreover, the increased value of their RT resistivity and decreased mobility as compared to the films grown at ~ 200 and 250^0C clearly implied the increased disorder strength in these films. Electrical conduction in these highly disordered films might be expected to be due to the Mott's 3D variable-range hopping (VRH) mechanism of electrons among localized defect states. Generally, carrier transport in the films having carrier concentration $n < n_c$ i.e., on the insulating side of the MIT is expected to proceed through VRH mechanism. However, Siegrist *et al.* observed VRH mechanism in $GeSb_2Te_4$films with carrier concentration $n > n_c$ [82]. They attributed the pronounced increment in resistivity at lower temperatures to the disorder induced Anderson localization effect. Therefore, as the films in the 2nd category were highly disordered, we have tried to fit the resistivity data using VRH Eq. However, the observed 'semiconductor-like' behaviour could not be fitted by the VRH formula, implying that carriers were not strongly localized in these films. The above observation was not surprising because all these films had finite value of σ_o and a very weak temperature dependence of resistivity with relative resistivity ratio $\rho_r = \rho$ (4.2K)/ ρ (300K) values 1.6-2.5 implying that these films were on the metallic side of the MIT. These observations suggests that although these films exhibited only 'semiconductor-like' behaviour due to the presence of pronounced disorder, the degree of static disorder was not strong enough to turn them into Anderson localized insulators.

3.4 Conclusions

We have successfully grown ZnO thin films on Si and Sapphire substrates using a thermal ALD reactor by varying substrate temperature from 50-350^0 C. The ALD window for the self-limiting growth of ZnO was obtained in the temperature range of ~ 140-200^{0}Cwith a constant growth rate of ~ 0.2 nm/cycle.XRD, RT PL spectra and XPS measurements of the films showed that crystalline and compositional native defects were strongly dependent on the substrate temperature. RT Hall measurement showed that all the films were degenerate with carrier concentration exceeding the Mott's critical density n_c required for metallic conduction. The effect of disorder on the underlying electron transport mechanisms of these films were analyzed by low temperature electrical resistivity and Hall measurement. To investigate the effect of disorder on the underlying charge transport mechanisms in these films, the electrical resistivity was measured in the temperature range of ~ 4.2 to 300 K. The films grown at ~ 150, 300 and 350^0 C were found to be semiconducting in the entire range of the measurement temperature due to the intensified disorder which impeded the metallic transport in these films. However, the films grown at ~ 200 and 250^0 C showed a transition from metallic to semiconducting transport behaviour at lower temperatures due to the reduced defects and improved crystalline quality of these films. The observed semiconducting behaviour below the transition temperature for these films could be well explained by considering quantum corrections to the Boltzmann conductivity which includes the effect of disorder induced weak localization and coulomb electron-electron interactions. The optimum structural and optical quality ZnO film was obtained at 200^{0}C which also showed minimum RT resistivity value of ~ 3.6x10^{-3}Ω cm and considerably good Hall mobility of ~ 30cm^2/Vs. These films are good candidate for TCE applications. However, further decrement in the electrical resistivity can be achieved by extrinsically doping these films using n-type impurities. In the next 2 chapters we have discussed n-type doping in ALD grown ZnO films.

Chapter 4: Electron Transport in Al Doped ZnO Thin Films Grown by ALD

4.1 Growth of Al Doped ZnO Thin Films

(Zn, Al)O_x thin films of thickness ~ 220 nm were grown on epi polished (0001) sapphire substrates at 200^0C of reactor temperature using ALD. The deposition temperature was purposely kept fixed at 200^0C which was found to be the optimum temperature to grow intrinsic ZnO thin films suitable for TCE applications. Anhydrous aluminium chloride ($AlCl_3$), diethylzinc ($Zn(C_2H_5)_2$) and deionised water (H_2O) were used as precursors for Al, Zn and Oxygen respectively. $Zn(C_2H_5)_2$ and H_2O were kept in stainless steel bubblers at ~ 20^0C and pulsed into the reactor for 200 ms. $AlCl_3$ was kept in a hot-source container at ~ 190^0C to create sufficient vapor pressure and pulsed into the reactor by using high purity N_2 gas assisted booster option. In order to incorporate sub-monolayer of Al_2O_3 on the growing ZnO film surface, pulsing time of $AlCl_3$ for Al_2O_3deposition has been optimized at 200^0C. We have increased pulsing time of $AlCl_3$ from 25 to 500 ms keeping all the other process parameters fixed. GPC was found to be increased from ~ 0.02 nm for 25 ms to ~ 0.15 nm for 200 ms and then become constant with further increment in pulsing time. Such variation of GPC clearly indicates that with increasing pulsing time more and more $AlCl_3$ molecules get chemisorbed up to 200 ms and at this value plausibly all available surface reactive sites on the film surface occupied by the $AlCl_3$molecules. Thus constant GPC was achieved at and above 200 ms of pulsing time. As Al_2O_3shows amorphous nature up to a very high deposition temperature of 800^0 C, further optimization for the growth temperature is not needed at least for doing purpose. We have pulsed $AlCl_3$for 25 ms (well below the saturation value) which presumably resulted in sub-monolayer growth due to incomplete surface coverage by the precursor molecules. A schematic of the typical pulsing and purging scheme is shown in

Fig.4.1. Al concentration in the films (obtained via energy dispersive X-ray analysis) was varied by varying the percentage of Al_2O_3 cycles [R_{dopant} (%) = {1/(1+n)}x100%] as listed in Table 4.1.

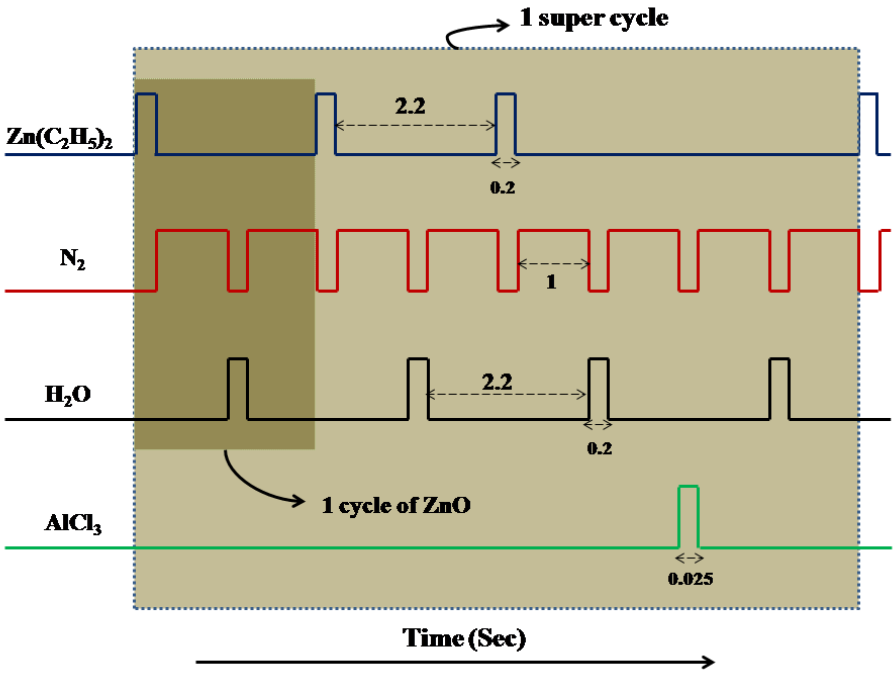

Fig. 4.1 Schematic of pulsing and purging sequence for the growth of (Zn, Al)O_x thin films in ALD. A typical super cycle consists of 3 ZnO cycles and 1 Al_2O_3 cycle is shown.

The various (Zn, Al)O_x films with different Al concentrations were named as S (n, 1: s) where n denotes number of ZnO cycles, followed by 1 cycle of Al_2O_3, making one complete supercycle, and s represents total number of supercycles. A schematic representation of (Zn, Al)O_x thin films grown in ALD is shown in Fig. 4.2.

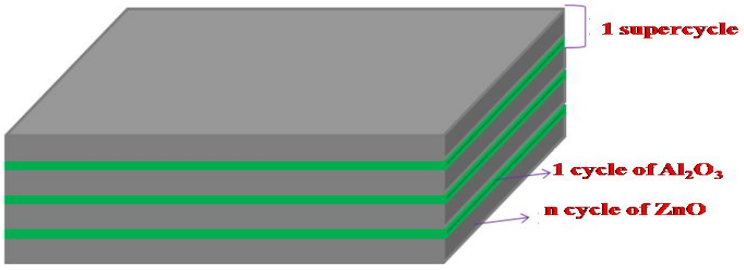

Fig. 4.2 Schematic diagram of the (Zn, Al)O_x thin film grown by ALD.

Table 4.1 List of the values of R_{dopant} (%), Al(at.%), electron density (N_e), RT electrical resistivity (ρ) and mobility (μ) of (Zn, Al)O_x thin films. The values of Burstein Moss (BM) and band gap narrowing (BGN) effects are also calculated for the samples considering the band gap of bulk ZnO as 3.37 eV.

Sample name S (1, n: m)	R_{dopant} (%)	Al (at.%)	N_e (x10^{20} cm^{-3})	ρ (10^{-3}Ω cm)	μ (cm^2/Vs)	ζ (%)	E_g (eV)	ΔE_{BM} (eV)	ΔE_{BGN} (eV)
S1 (70, 1:14)	1.4	1.6	2.2	1.7	17	25	3.45	0.62	-0.54
S2 (50, 1: 20)	1.9	2.2	4.1	0.86	18	39	3.57	0.94	-0.74
S3 (30, 1:33)	3.2	3.8	4.7	0.94	14	26	3.74	1.03	-0.66
S4 (20, 1: 48)	4.7	5.5	2.0	10.4	3	6	3.72	--	--
S5 (10, 1: 91)	9.1	12.4	--	--	--	--	5.6	--	--

4.2 Structural and Optical Properties

The θ-2θ XRD patterns for all the (Zn, Al)O_x thin films with varying Al concentrations are shown in Fig. 4.3.All the films were found to be polycrystalline with a dominant (00.2) peak up to sample S3, although other orientations corresponding to (10.1) and (10.0) were also observed. Such XRD patterns are similar to the previous results as reported for Al doped ZnO thin films grown by ALD [58, 132-136 and 143]. The (00.2) peak position of the intrinsic ZnO film ($2\theta = 34.46^0$) was found to be shifted to higher value compared to the bulk ZnO ($2\theta = 34.40^0$). This could be due to the lattice mismatch and thermal mismatch strains between ZnO and sapphire which induced residual compressive strain in the as grown film [58, 132-136 and 143]. Al^{3+} has an ionic radius of 0.54Å which is smaller than the Zn^{2+} cation (0.74 Å). Therefore, crystalline quality of host ZnO lattice would be distorted due to the substitutional incorporation of Al^{3+}. However, we observed that with initial incorporation of Al up to film S3, the position of the (00.2) diffraction peak was shifted to the lower 2θ values i.e., ZnO lattice relaxes its residual compressive strain through Al incorporation. The (00.2)

peak intensity was found to be reduced with increasing doping concentration and was almost diminished for the film S4. The (00.2) and (10.1) peaks were found to be diffused and broadened for the film S4. With further incorporation of Al i.e., the film S5 was found to be X-ray amorphous [143].This could be attributed to the lower values of ZnO cycles (n =10) which is close to the incubation period of ZnO ($\tau \sim 6$ as reported by Banerjee *et al.*) on the AlO_x terminated surface [58]. Therefore, nucleation of ZnO was strongly inhibited which lead to the amorphous nature of the film [143].

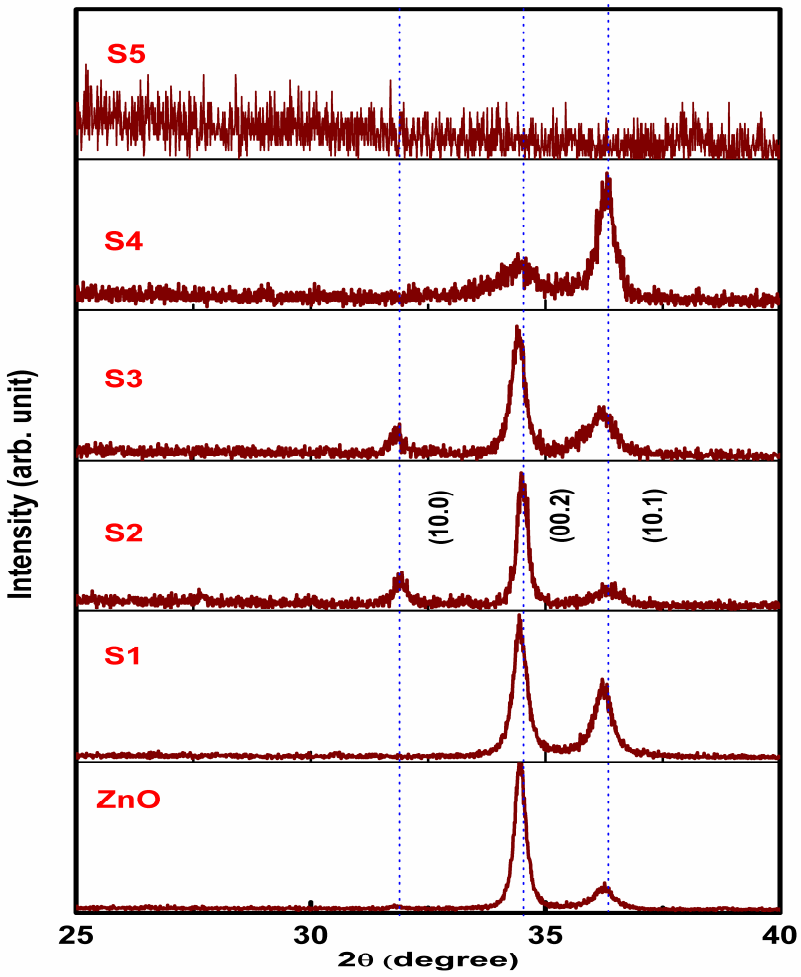

Fig. 4.3 XRD pattern of (Zn, Al)O_x thin films grown on (0001) sapphire substrates with different Al concentrations.

The optical transmittance spectra for all the films with varying Al concentrations are shown in Fig.4.4. All the films showed average optical transmittance ~ 85% in the visible spectral range. The absorption edge was found to be slowly blue shifted with increasing Al concentration up to 5.5 at%. However, with further incorporation of Al, absorption edge exhibited a drastic shift to the higher energy. The optical band-gap values are listed in Table – 4.1. The increase in band-gap energy with increasing electron density up to Al concentration of ~ 3.8 at% i.e., for the films S1-S3, could be due to the combined effect of Burstein-Moss (BM) band filling (arising due to the degenerate nature of the films) and band-gap narrowing (BGN) (arising due to many body interactions above Mott's critical density) [157]. We have discussed these effects on the optical absorption spectra of degenerate semiconductors in chapter 5 (section 5.8). The film S4, with lower electron density compared to the film S3, showed higher optical band-gap. However, the sharpness of the fundamental optical absorption edge was also found to be deteriorated due to increased structural disorder in the film as evident from its XRD pattern. Therefore, the increased band-gap value for the film S4 could not be entirely due to the BM and BGN effects. The significant modification in the band structure of ZnO due to strengthened structural disorder has to be taken into account [158]. With further incorporation of Al, i.e., sample S5 with the highest Al concentration, did not show any signature of the wurtzite host ZnO lattice and was found to be completely X-ray amorphous. This sample did not exhibit the fundamental optical absorption edge corresponding to ZnO lattice. Similar results were also reported by Lu *et al.* in Al doped ZnO thin films grown by magnetron sputtering [158]. The plausible reason behind such deteriorated optical and structural properties could be due to the formation of insulating α-Al_2O_3 and/or $ZnAl_2O_4$ phases in the films [158]. Formation of such phases in S5 is highly plausible because for this film the value of n (=10) was very close to τ (=6) as discussed earlier.

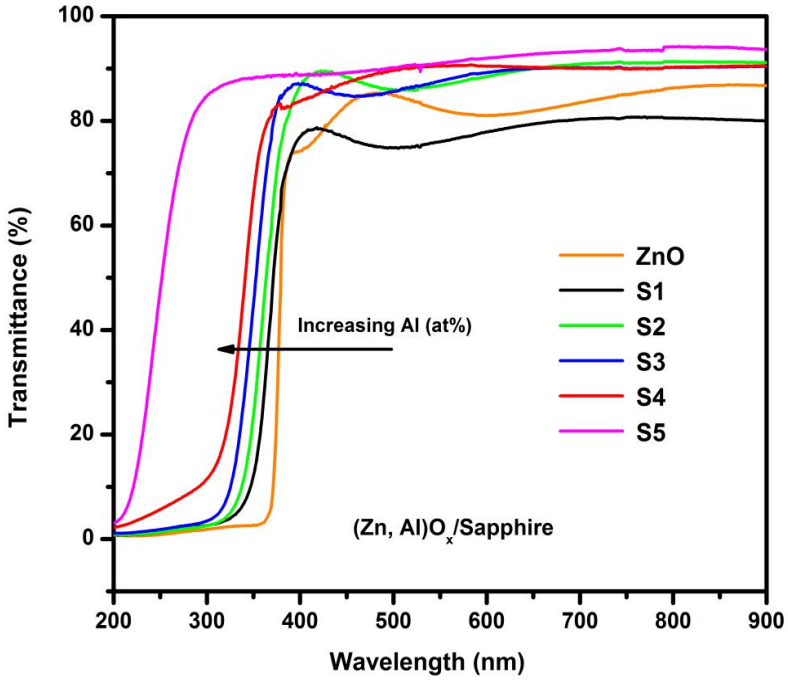

Fig. 4.4 Optical transmittance spectra (Zn, Al)O_x thin films with different Al concentrations.

4.3 Room Temperature Electrical Properties

The variation of room temperature electrical resistivity (ρ), electron density (N_e), and Hall mobility (μ) with Al concentration (at.%) could be seen from Table 4.1. The measured electron density for the film S1 with the minimum Al concentration of ~1.6 at% was found to be ~ 2.2x10^{20} cm^{-3}. This value was significantly higher compared to the electron density of intrinsic ZnO film, which indicates that despite the periodic incorporation of insulating Al_2O_3sub-monolayer during deposition, Al atoms acted as efficient electron donors. The doping efficiency of Al impurities can be obtained by using the following equation

$$\zeta(\%) = [(N_e - N_0) / \{Al(\%) N_A (\sigma / M_{mol})\}] \times 100\% \qquad (4.1)$$

where N_e and N_0 are the carrier densities of the AZO and intrinsic ZnO films respectively, σ and M_{mol} are the bulk density and molar mass of ZnO respectively, N_A is the Avogadro's

number. The values of doping efficiencies at different dopant concentration are listed in Table 4.1. The increase in electron density showed a concomitant decrease in resistivity up to ~2.2 at% of Al. Further incorporation of Al resulted in increased electrical resistivity which reached to a value ~10.4x10^{-3}Ω-cm at ~5.5at% of Al. The resistivity of the film S5 having Al concentration of ~12.4 at% was too high to be measured at room temperature. The sharp rise in the electrical resistivity for the film S4 compared to S3 was due to the combinatorial effect of poor Hall mobility (~3 cm^2/V s) and decreased electron density. The decrease in electron density at higher Al concentration plausibly resulted from the formation of compensative intrinsic defects and defect complexes. As the number of ZnO cycles for the films S4 (n=20) and S5(n=10) are close to the incubation period (τ=6) of ZnO on AlO_x terminated surface, the possibility of the formation of separate insulating α-Al_2O_3 and/or $ZnAl_2O_4$ phases into the conducting ZnO matrix could not be completely ruled out [158]. Moreover, the XRD and RT PL spectra for the film S4 were found to be significantly deteriorated compared to the intrinsic ZnO film. The excessive Al incorporation for the film S5 strongly perturbed the polycrystalline host ZnO lattice, and transformed it to an X-ray amorphous structure. The band edge UV photoluminescence for this film was found to be completely diminished. All these factors suggested that incorporated Al atoms introduced pronounced crystalline and compositional disorder in the films S4 and S5, which lead to the tremendous electron scattering and consequently poor Hall mobility for the film S4. Strengthened carrier scattering could also lead to the strong-localization of charge carriers which inhibits electron diffusion. Therefore, it can be concluded that interplay of carrier-injection and disorder-incorporation by the Al dopants drive the RT electrical properties of the (Zn, Al)O_x films.

4.4 Temperature Dependent Electrical Resistivity Measurements

In order to further investigate the influence of degree of static-disorder defined by the dimensionless parameter $K_F l_e$ ($K_F l_e = (3\pi^2)^{2/3}(\hbar\sigma_{RT} / e^2 N_e^{1/3})$ where, K_F is the Fermi wave number, σ_{RT} is the room temperature conductivity and l_e is the elastic mean free path of free electrons) and electron density on the transport phenomena, temperature dependent electrical resistivity ρ (T) and MR measurements were carried out. Fig. 4.5 shows the ρ (T) curves for the all the conducting (Zn, Al)O_x thin films (S1-S4).

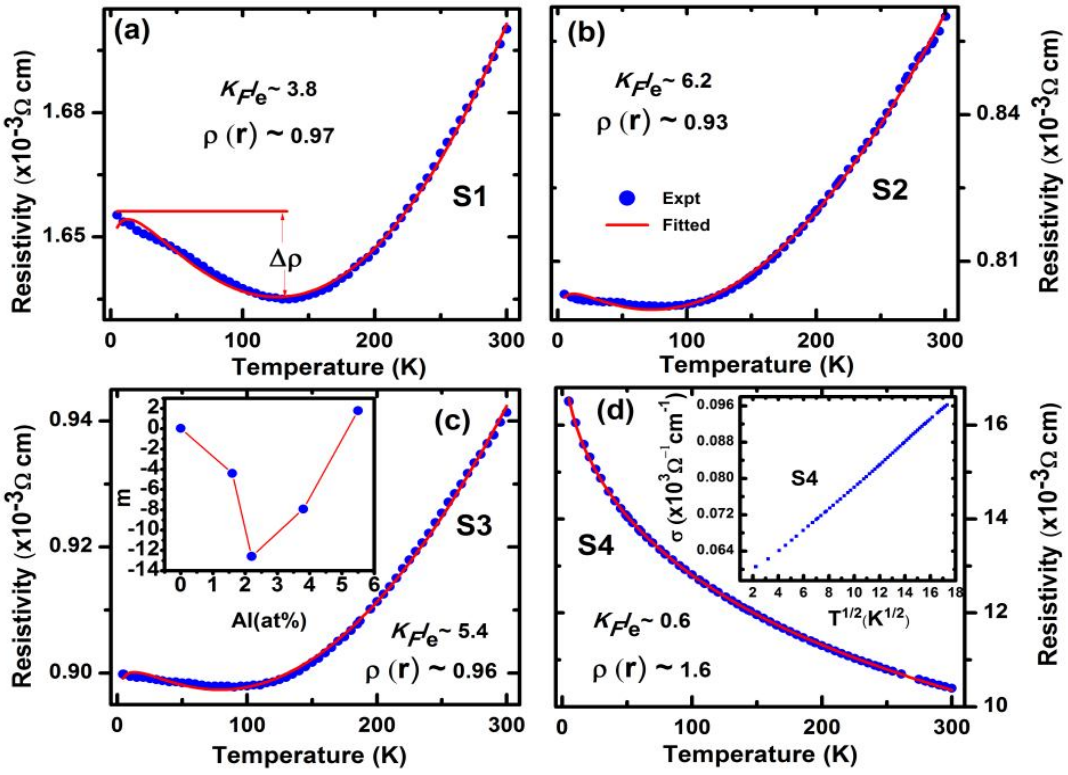

Fig. 4.5 Temperature dependent (5-300K) electrical resistivity of the (Zn, Al)O_x thin films S1, S2, S3 and S4. The solid lines show the fittings of experimental data with Eq. 4.2.The inset of Fig. 4.5(c) shows the variation of the fitting parameter 'm' used in Eq. 4.2 with Al concentration. The inset of Fig. 4.5(d) shows linear relationship between σ (T) and $T^{1/2}$.

For the film S1, a resistivity minimum was observed at T_m ~135 K, which was lower compared to the intrinsic ZnO film (T_m ~150 K) grown by ALD with similar process parameters. For the film S2, T_m was found to be shifted more to the lower temperature (T_m~90 K) and the degree of the resistivity upturn $\Delta\rho = (\rho_{4.2K} - \rho_{T_mK}) / \rho_{T_mK}$ was also found to be decreased. The ρ (T) curve for the film S3, was found to be almost similar to that of S2. This is probably due to their very close RT resistivity and mobility values. The films S1-S3 which were 'comparatively clean with $K_F l_e$>1, exhibited enhanced good metallic (dρ/dT>0) behaviour. These films with Al concentrations in the range of ~1.6-3.8 at% were situated deep into the metallic side of the metal-insulator transition (MIT). However, further incorporation of Al moved the film S4 ($K_F l_e$<1) towards MIT which showed barely metallic resistivity behaviour (dρ/dT<0 with ρ(T→0K)≠0) in the entire range of the measurement temperature.

In disordered electronic systems such as doped semiconductors, low-temperature electrical resistivity curves are often analyzed within the framework of quantum corrections to conductivity (QCC). QCC considers the following two quantum-interference effects (QIE's): WL and IEI (also known as electron-electron interactions (EEI's)) as discussed above. QCC is applicable on the metallic side of the MIT. In the present case, the (Zn, Al)O_x films (S1-S4) with N_e far above the Mott critical density (n_c), showed very weak temperature dependence of electrical resistivity with ρ(r)=0.93-1.6 and non zero ρ at T→0K. Therefore, these films are on the metallic side of the MIT, and the following QCC Eq. could be reliably employed [159]

$$\rho(T) = \left\{1/\left(\sigma_0 + aT^{p/2} + mT^{1/2}\right)\right\} + bT^{\alpha} \qquad (4.2)$$

In Eq. 4.2, σ_0 is the residual conductivity at T→0 K, $aT^{p/2}$ corresponds to WL and $m(n)T^{1/2}$ comes from the EEI's effect. In addition to these two quantum corrections, a term bT^{α} is included in order to consider the high temperature scattering contributions and p is the exponent of temperature for the dominant inelastic scattering rate $(1/\tau_{in})$. The values of all the fitting parameters used in Eq. 4.2 are listed in Table 4.2.

Table 4.2 Values of the parameters used in Eq. 4.2 to fit the experimental resistivity curves for the films S1, S2, S3 and S4 in Fig. 4.5.

Sample	σ_0 ($\Omega^{-1}cm^{-1}$)	m ($\Omega^{-1}cm^{-1}K^{-1/2}$)	a ($\Omega^{-1}cm^{-1}K^{-3/4}$)	b ($\Omega^{-1}cm^{-1}K^{-\alpha}$)	α
S1	609.4±0.61	-4.4±0.6	1.6±0.2	$(7.2\pm3.0)\times10^{-10}$	2.2±0.1
S2	1258±2.94	-12.58±2.6	4.93±0.9	$(15\pm9.6)\times10^{-9}$	1.6±0.1
S3	1120±1.89	-7.92±1.58	2.98±0.59	$(6.6\pm4.5)\times10^{-9}$	1.7±0.1
S4	56±0.1	1.79±0.27	0.13±.006	0	0

The linear relationship between σ (T) (=1/ρ(T)) and $T^{1/2}$ (i. e., $\sigma(T)=\sigma(0)+AT^{1/2}$) for the film S4 in the entire range of the measurement temperature (see inset of Fig. 4.5(d)) implied enhanced influence of EEI's on the transport mechanisms. This is expected because the motion of free electrons in the film S4 turns out to be more diffusive due to the strengthened static-disorder ($K_F l_e<1$) in the film, as discussed earlier. Therefore, the electron screening cloud could not follow the motion of free electrons as easily as it was possible for the 'comparatively clean' films S1-S3 ($K_F l_e>1$). The reduced screening resulted in enhanced EEI's effect for the film S4. The variation of the fitting parameter 'm' with Al concentration as shown in the inset of Fig. 4.5(c), also supports our above observations. As could be seen, with increasing Al concentration up to ~ 2.2 at%, the value of 'm' was decreased, which implied increased screening of EEI's phenomena. Beyond 2.2 at%, the value of 'm' was found to be increased due to the progressive loss of screening with increasing static-disorder as discussed earlier.

4.5 Temperature Dependent Magnetoresistance Measurements

In order to further elucidate the role of QIE's on the phase-coherent electron transport for the films S1-S4 we have carried out MR measurements (see Fig. 4.6) at different temperatures as

a function of applied magnetic field (B). Small negative MR was observed for all the (Zn, Al)O_x films in the entire range of the measurement temperature (5-200K) and magnetic field (0-8T).

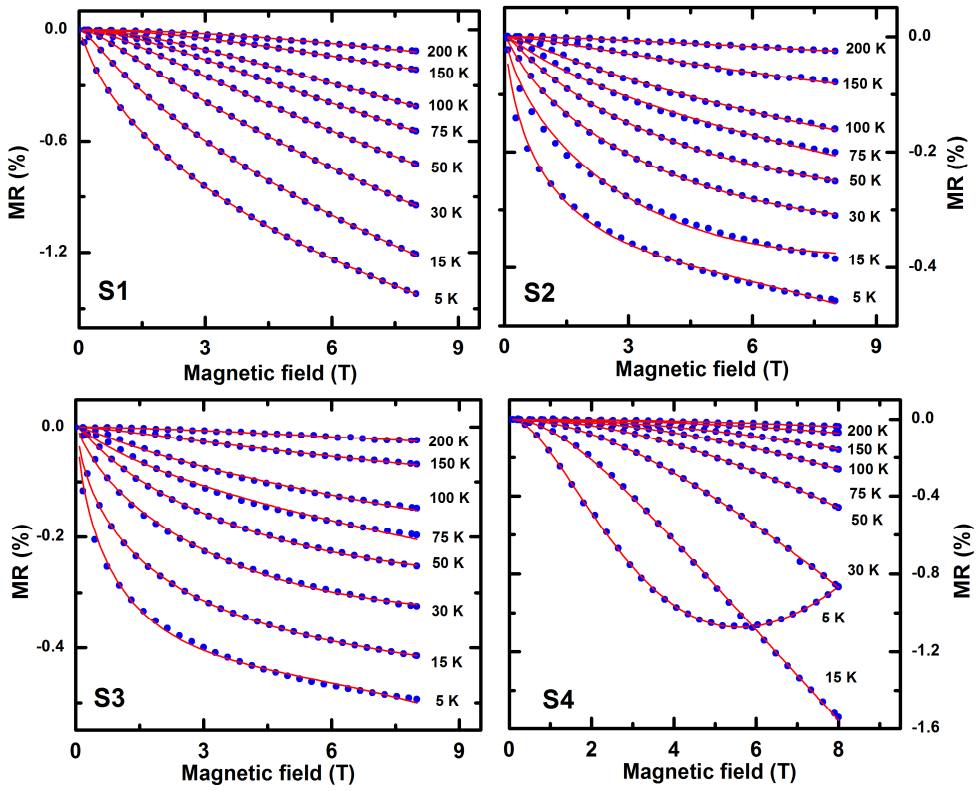

Fig. 4.6 Magnetic field dependent (0-8 T) MR of all the (Zn, Al)O_x thin films S1-S4 at different temperatures in the range of 5-200K. The solid lines show the fitting of the experimental data with Eq. 4.7.

In a disordered metallic system, the phase-coherence of the two time-reversed electronic wave functions, responsible for WL, can be destroyed by a weak magnetic field. Therefore, the small negative MR for the conducting (Zn, Al)O_x thin films plausibly arises from the magnetic field suppressed WL effect. The decrease of negative MR with increasing temperature was due to the progressive loss of WL by the relevant inelastic phase-breaking mechanisms. For three-dimensional WL regime, the expression for negative MR as derived by Kawabata is given by [160],

$$\left(\frac{\Delta\rho}{\rho(0,T)^2}\right)_{WL} = -\frac{e^2}{2\pi^2\hbar}\sqrt{\frac{eB}{\hbar}}f_3(\delta) \tag{4.3}$$

where we have considered $\rho(H,T) \approx \rho(0,T)$ due to the small magnitude of MR, $\delta = \hbar/\left(4eBl_\phi^2\right) = \hbar/\left(4eBD\tau_\phi\right)$ considering phase-coherence length $l_\phi = \sqrt{D\tau_\phi}$ where τ_ϕ is the electron dephasing time, $D = \mu KT/e$ is the electron diffusion constant and μ is the electron mobility. The function $f_3(\delta)$ used in Eq. 4.3 is given by

$$f_3(\delta) = \sum_{N=0}^{\infty}\left[2\left(\sqrt{N+1+\delta} - \sqrt{N+\delta}\right) - \frac{1}{\sqrt{N+1/2+\delta}}\right]. \tag{4.4}$$

However, in the present case, the low-temperature negative MR data were found to be significantly deviated from Eq. 4.3. This could be due to the presence of EEI's which has already been considered to analyze the temperature dependent electrical resistivity curves [72, 78 and 159]. The diffusion channel EEI's in which the dominant effect comes from the splitting of the spin states by magnetic field (or Zeeman contribution) manifests itself in positive MR. The presence of positive MR at lower temperatures is indeed reflected by the upturn in negative MR for the film S4 at 5K. Therefore, we have considered both three-dimensional WL and Zeeman splitting contributions to analyze the MR results for the (Zn, Al)O_x films at lower temperatures (T ≤ 15 K). The expression for positive MR due to 3D EEI's effect as derived by Lee and Ramakrishnan is given by [72],

$$\left(\frac{\Delta\rho}{\rho(0,T)^2}\right)_{EEI} = \frac{e^2}{\hbar}\frac{F_\sigma}{4\pi^2}\sqrt{\frac{KT}{2\hbar D}}g_3(h) \tag{4.5}$$

with $h = g\mu_B B/KT$ where g is Lande factor, μ_B is the Bohr magneton and F_σ is the Coulomb interaction parameter. The function $g_3(h)$ can be written as [72],

$$g_3(h) = \int_0^\infty d\Omega\,\frac{d^2}{d\Omega^2}\left[\Omega N(\Omega)\right]\left(\sqrt{\Omega+h} + \sqrt{|\Omega-h|} - 2\sqrt{\Omega}\right) \tag{4.6}$$

with $N(\Omega) = \left[\exp(\Omega)-1\right]^{-1}$. The solid lines in Fig. 4.6 show the theoretical fittings of the

experimental negative MR data for all the films using the following Eq.

$$MR(\%) = \frac{\rho(H,T) - \rho(0,T)}{\rho(0,T)} \times 100(\%) = \rho(0,T)\left[\left(\frac{\Delta\rho}{\rho(0,T)^2}\right)_{WL} + \left(\frac{\Delta\rho}{\rho(0,T)^2}\right)_{EEI}\right] \times 100(\%) \quad (4.7)$$

where we have considered the superposition of both WL (Eq. 4.3) and EEI's (Eq. 4.5). However, at higher temperatures (T >15K), the contribution of positive MR from EEI's would be negligible and therefore, fitting was performed using WL contribution (Eq. 4.3) only. The values of l_ϕ at different temperatures were obtained from the least-squares fitting of the negative MR data. For all the temperatures, l_ϕ was found to less than the thickness (d ~ 220 nm) of the (Zn, Al)O_x films. Therefore, the films were effectively three dimensional (3D), as far as phase-coherence is concerned. In order to obtain phase-coherent electron transport along the entire film thickness l_ϕ has to be greater than d. This could be achieved by tuning the strength of static-disorder through controlled Al incorporation into the ZnO matrix and scaling down the film thickness with atomic level precision using ALD. As can be seen in Fig. 4.7, l_ϕ was decreased with increasing temperature due to the strengthening of the relevant inelastic scattering mechanism (see section 1.3.6). Therefore, the temperature dependence of l_ϕ is entirely controlled by the temperature dependence of the inelastic scattering length l_{in}. The relation between τ_ϕ and τ_{in} (inelastic scattering time) is given by [87],

$$\frac{1}{\tau_\phi(T,l_e)} = \frac{1}{\tau_{in}(T,l_e)} + \frac{1}{\tau_\phi{}^0(l_e)} = A_{in}(l_e)T^p + \frac{1}{\tau_\phi{}^0(l_e)} \quad (4.8)$$

where the strength of the inelastic scattering $A_{in}(l_e)$ depends on l_e i.e. degree of static-disorder, $\tau_\phi^0(l_e) \equiv \tau_\phi(T \to 0)$ is the dephasing time at very low temperatures and p is already defined in section 1.3.4 in chapter 1. From Eq. 4.8 it follows that $l_\phi \propto T^{-p/2}$ using $l_\phi = \sqrt{D\tau_\phi}$.

In Fig. 4.7 the linear portion of all the $\log l_\phi$ vs logT plots were straight line fitted to extract the value of p.

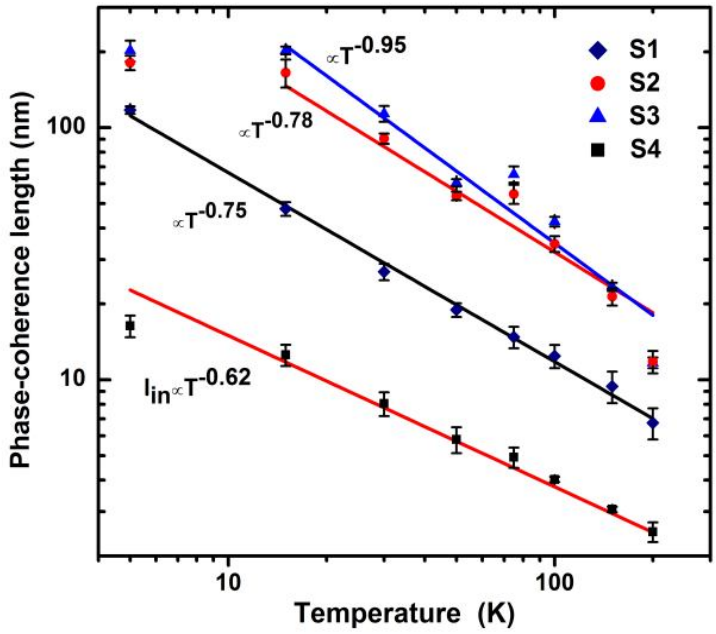

Fig. 4.7 Variation of phase-coherence length with temperature for all the (Zn, Al)O_x thin films S1, S2, S3 and S4. The solid lines show straight line fitting of the linear portion of the curves.

The temperature dependence of l_ϕ was found to be closely $\propto T^{-3/4}$ for all the films. Therefore, the temperature exponent comes out to be p = 3/2 which implied that the dominant mechanism responsible for phase-breaking was the inelastic electron-electron scattering (see section 1.3.6).

4.6 Conclusions

In conclusion, the temperature-dependent electron transport mechanisms in (Zn, Al)O_x thin films have been investigated on the metallic side of the MIT. Due to the fine tuning of disorder by controlled Al incorporation, a crossover from good metallic to barely metallic resistivity behaviour was observed at ~5.5 at.% of Al. The barely metallic film with the highest static disorder ($K_F l_e$~0.6) showed enhanced EEI's due to reduced screening effect which plausibly manifested itself in the upturn in negative MR at 5 K. It was observed that instead of periodic incorporation of insulating Al_2O_3sub-monolayer into the conducting ZnO matrix, the electron transport in these films was effectively three-dimensional. The persistence of quantum-interference over a wide range of temperature strongly recommends ALD grown (Zn, Al)O_x thin films as a prospective disordered n-type semiconductor for the development of futuristic ZnO based electronic devices utilizing phase-coherent transport.

Chapter 5: Electron Transport in Ti Doped ZnO Thin Films Grown by ALD

In the present chapter, we have discussed growth and temperature dependent electron transport in atomic layer deposited Ti doped ZnO thin films. There are very few reports in which Ti has been used as an n-type dopant in ZnO [137]. So far, Al and Ga doped ZnO thin films have been extensively studied for this purpose and are being considered as a superior alternative for TCO applications [132-136, 139]. However, in the present study we found significantly enhanced doping-efficiency in (Zn, Ti)O_x thin films compared to Al doped ZnO films grown by ALD. We have already discussed growth and carrier transport in Al doped ZnO thin films in the previous chapter. As Al_2O_3 shows amorphous nature up to deposition temperature as high as ~ 800^0C, we did not optimize growth parameters of Al_2O_3 thin film for doping purpose. We simply kept the pulsing time of $AlCl_3$ very low to provide sub-saturating exposure of the dopant precursor on the growing ZnO film surface. However, as TiO_2 shows a phase transformation from amorphous to crystalline anatase at higher deposition temperature and significant change in surface morphology, it is imperative to optimize process parameters of TiO_2 deposition for efficient doping in ZnO [161]. Moreover, for the growth of multi-component materials in ALD with good reproducibility in various film properties, it is always required to choose a deposition temperature which lies within the self-limiting ALD window of both the materials [151]. Therefore, in this chapter, first we have discussed deposition of TiO_2 thin films in ALD followed by the discussion on growth and temperature dependent electron transport in (Zn, Ti)O_x thin films.

5.1 Growth of TiO_2 Thin Films Using ALD

TiO_2 thin films were grown on Si (100) and sapphire (0001) substrates by varying the substrate temperature in the range of ~ 50 to 400^0C. Titanium tetrachloride ($TiCl_4$) and deionised water (H_2O) were used as precursors for titanium and oxygen respectively. One TiO_2 growth cycle includes the following four steps in sequence (1) 500ms of $TiCl_4$ exposure, (2) 1s of N_2 purge, (3) 500 ms of H_2O exposure, and (4) 1s of N_2 purge. The growth of TiO_2 in ALD proceeds according to the following irreversible exchange reactions [151, 161 and 162],

$$n(\text{-OH})(s)+TiCl_4(g) \rightarrow (\text{-O-})_nTiCl_{4-n}(s)+nHCl(g) \quad (5.1)$$

$$(\text{-O-})_nTiCl_{4-n}(s)+(4-n)H_2O(g) \rightarrow (\text{-O-})Ti(OH)_{4-n}(s) + (4-n)\ HCl(g) \quad (5.2)$$

where n = 1-3.The number of ALD cycles was kept fixed at 2500 for each TiO_2thin film deposition. We have carried out detailed investigation on structural and surface morphological properties of these films using XRD and AFM measurements. We have divided the entire range of deposition temperatures ($50^0C \leq T_s \leq 400^0C$) into three different temperature zones, namely zone-I ($T_s \leq 150^0C$), zone-II ($150^0C < T_s \leq 250^0C$) and zone-III ($250^0 < T_s \leq 400^0C$). The θ-2θ XRD patterns for all the films grown on Si (100) substrates at three different temperature zones are shown in Fig. 5.1. The films deposited in zone-I did not show any XRD peak of TiO_2 indicating that films were amorphous in nature. The films deposited in zone-II were found to exhibit an anatase (101) peak at $2\theta = 25.4^0$ [162-164]. The intensity of the anatase (101) peak was found to be increased with increasing growth temperature from 200 to 250^0C as shown in Fig. 5.2. However, above 250^0C i.e. in zone-III the anatase (101) peak intensity dropped sharply and the film grown at 400^0C showed rutile (110) peak at $2\theta = 27.5^0$ in addition to the anatase (101).

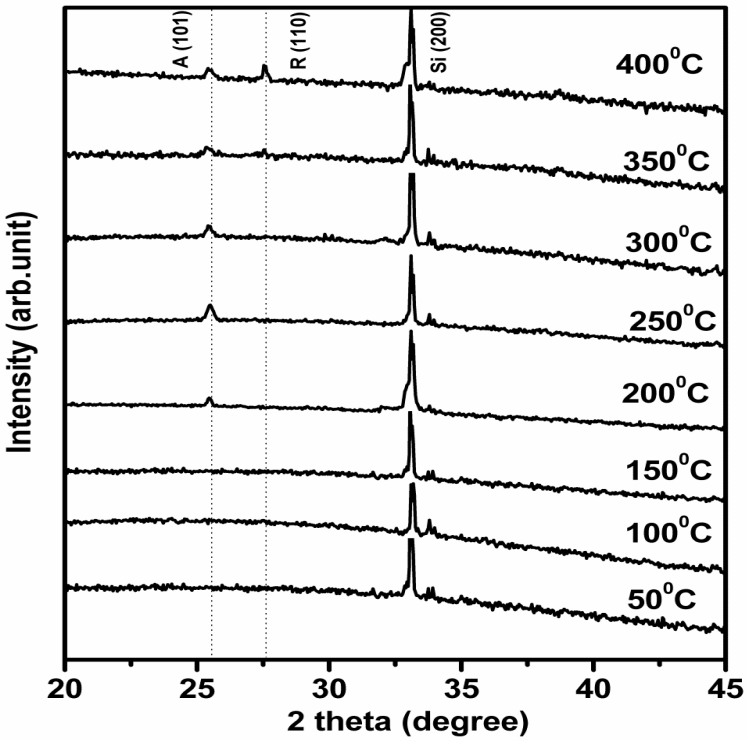

Fig. 5.1 XRD patterns of TiO_2 thin films grown on Si (100) substrates at different temperatures

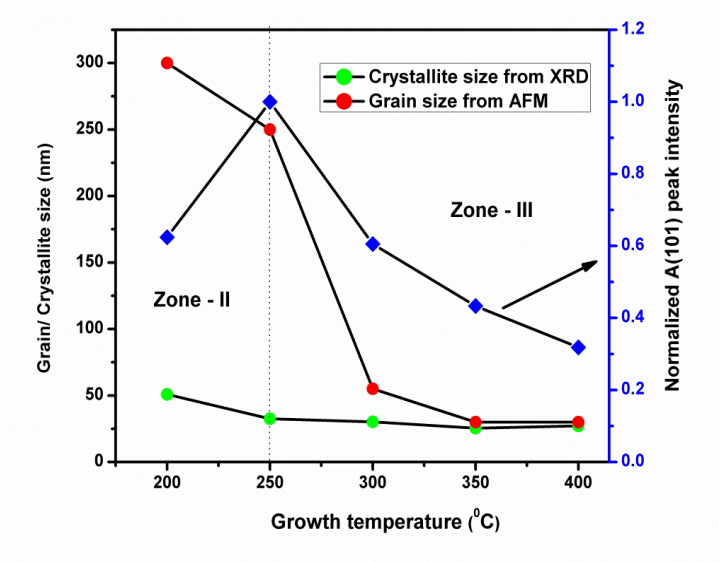

Fig. 5.2 AFM grain size, crystallite size corresponding to the A (1 0 1) peak and normalized A (101) peak intensity at different substrate temperatures in zone-II and III. The normalization of the A (101) peak intensity was performed with respect to the maximum A (101) peak intensity observed for the film grown at 250^0C.

Fig.5.3 shows both the 3D and 2D AFM micrographs (scanning area 5 μm x 5 μm) for all the ALD grown TiO_2 films.

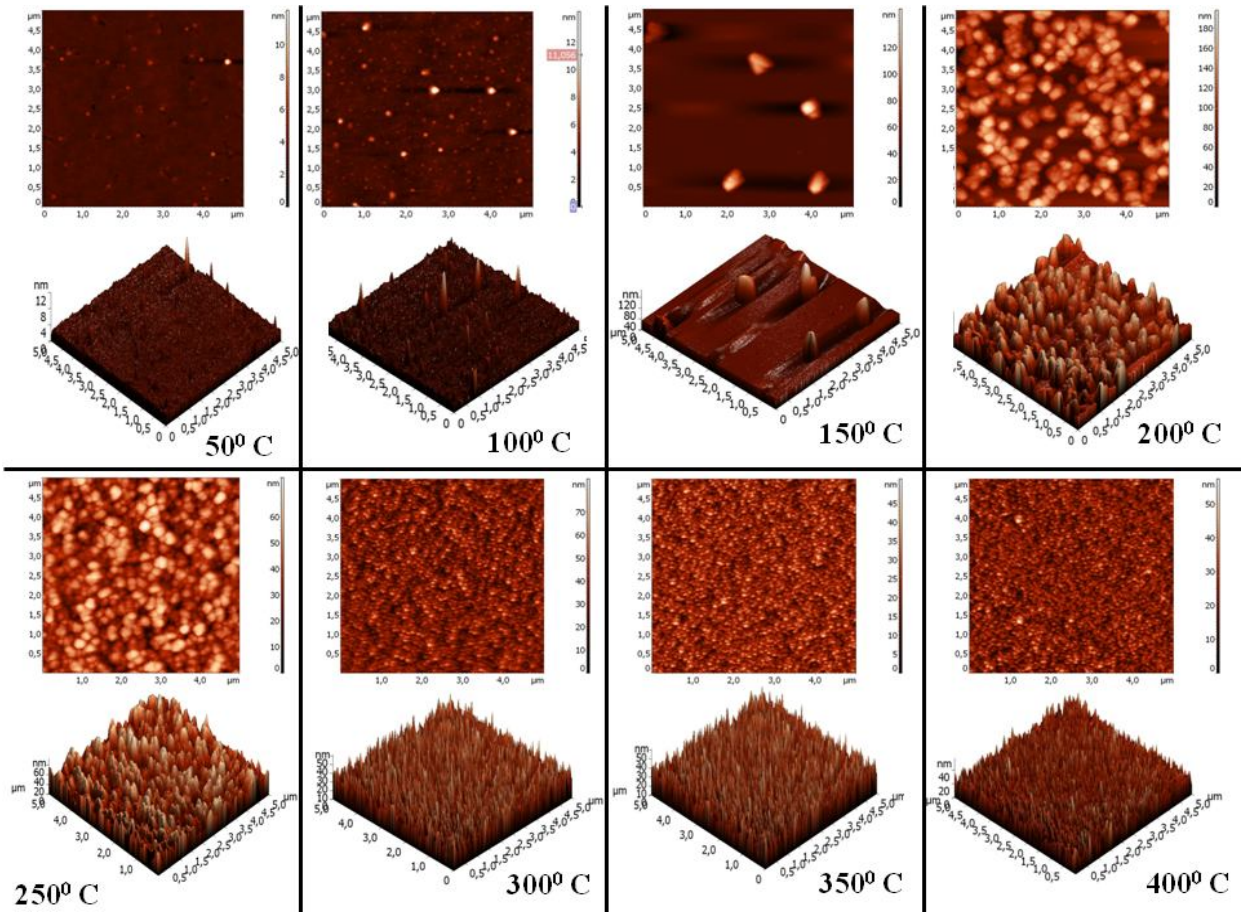

Fig. 5.3 2D and 3D AFM micrographs (5 μm × 5 μm) of all the TiO_2 thin films deposited on Si (1 0 0) substrates. Amorphous (grown at 50, 100, 150^{0}C), large-grained anatase (grown at 200, 250^{0}C) and nanocrystalline films (grown at 300, 350 and 400^{0}C).

As can be seen, no crystalline grains were observed in the amorphous films (Zone-I) deposited at 50 and 100^{0}C. These films showed quite smooth surface morphologies with RMS surface roughness values ~ 0.2 nm (at 50^{0}C) and ~ 0.4 nm (at100^{0}C), comparable to the roughness of the bare substrates. However, an increased RMS surface roughness of ~ 12 nm

(see Fig. 5.4) was observed for the amorphous film grown at 150^{0}C. This is attributed to the formation of few hillocks (mean size ~ 500 nm) on the smooth amorphous background as observed in the AFM micrograph. However, the crystalline volume fraction of these hillocks was so small that they could not be detected by lab source XRD system. The RMS surface roughness of the film without considering these hillocks was found to be comparable to the values obtained for the films grown at 50 and 100^{0}C. The film grown at 200^{0}C was composed of large-size, loosely-packed crystalline grains (average size~ 300 nm), oriented parallel to the anatase (101) direction and separated by micron size voids. The film grown at 250^{0}C was found to have densely-packed and comparatively lower-size grains (average size ~ 250 nm) which increased the crystalline volume fraction and resulted in more intense anatase (101) peak compared to the film grown at 200^{0}C (see Fig. 5.2).

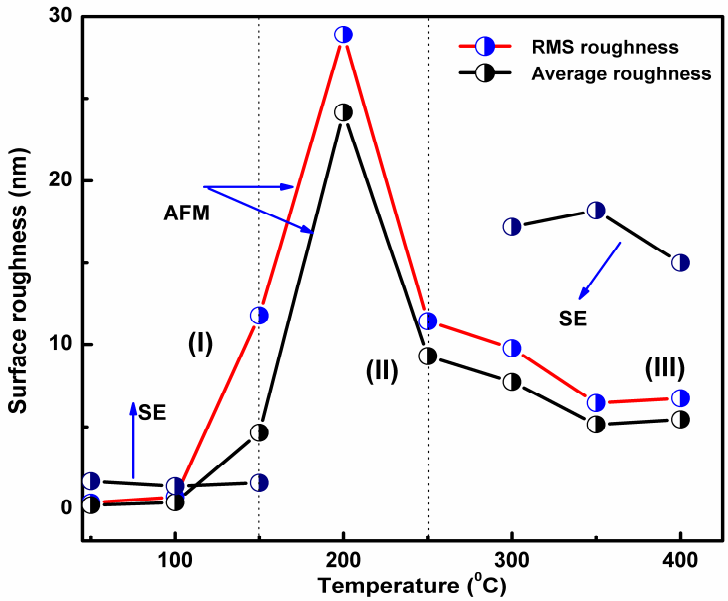

Fig. 5.4 Variation of RMS and average surface roughness as obtained from the AFM measurements with growth temperature for all the films grown in the substrate temperature range of ~ 50-400^{0}C.The vertical dashed lines separate different temperature zones (I, II, III). The solid lines connecting the data points at different temperatures are guides to the eye. The thicknesses of the top porous layer (t_s) as obtained from the spectroscopic ellipsometry (SE) measurements are also shown.

The highest RMS surface roughness of~ 29 nm was measured at the amorphous to crystalline-anatase phase transformation temperature of 200^0C. In zone-III, the significant decrease in surface roughness was due to the formation of densely-packed nanocrystalline grains. The observed higher values of surface roughness for the crystalline films in zone-II and III compared to the amorphous films in zone-I indicate that ideal two-dimensional layer-by-layer ALD growth did not take place for the crystalline films on Si (100) substrates [165]. The surface roughness could be correlated with the morphological development of the films by analyzing their 3D AFM micrographs at different substrate temperatures. The AFM micrographs of TiO_2 films grown at and above 200^0C clearly indicated that growth mode was essentially columnar. However, their lateral size and packing density was found to be strongly dependent on the substrate temperature. The high film-substrate interface energy could be the driving force to form three-dimensional agglomerates at the initial stage of film growth. As the number of deposition cycles increased, these agglomerates grew both laterally and vertically, resulted in columnar grains. The other possible mechanism for the low temperature crystallization could be due to the formation of volatile surface intermediate species $Ti(OH)_nCl_{4-n}$ by dissociative adsorption of by-product HCl (see reactions (5.1) and (5.2)) onto the growing film surface [165]. The gas-phase migration process of these intermediate species enabled them to easily migrate to the minimum free energy position to initiate crystallization. The phenomenon of agglomeration could also be verified from Fig. 5.2 where we have shown the AFM grain size and crystallite size corresponding to anatase (101) XRD peak for the films grown in zone-II and III. The crystallite size which is defined as the mean size of a coherent scattering domain having perfect arrangement of unit cells was obtained from Scherrer Eq. The AFM grain size was found to be considerably higher compared to the crystallite size in zone-II. This difference arises because AFM micrograph provides the size of the agglomerated or coalesced crystallites (domain of crystallites). As can be seen from

Figure 5.3, for the films grown above 250^{0}C, the crystalline nuclei covered the substrate more uniformly at the initial stage of film growth and reduced the grain size. The very high nucleation density for the films grown in zone-III resulted in nanocrystalline densely-packed grains. The values of crystallite size and AFM grain size were found to be almost matched in zone-III (Fig. 5.2) which indicated the absence of any agglomeration process during film growth.

The variation of GPC (GPC= total thickness/total no. of cycles) with growth temperature is shown in Fig. 5.5. As can be seen, with increasing growth temperature in zone-I, GPC is decreased. This could be due to the decrease in ligand release from the adsorbed chloride molecules.

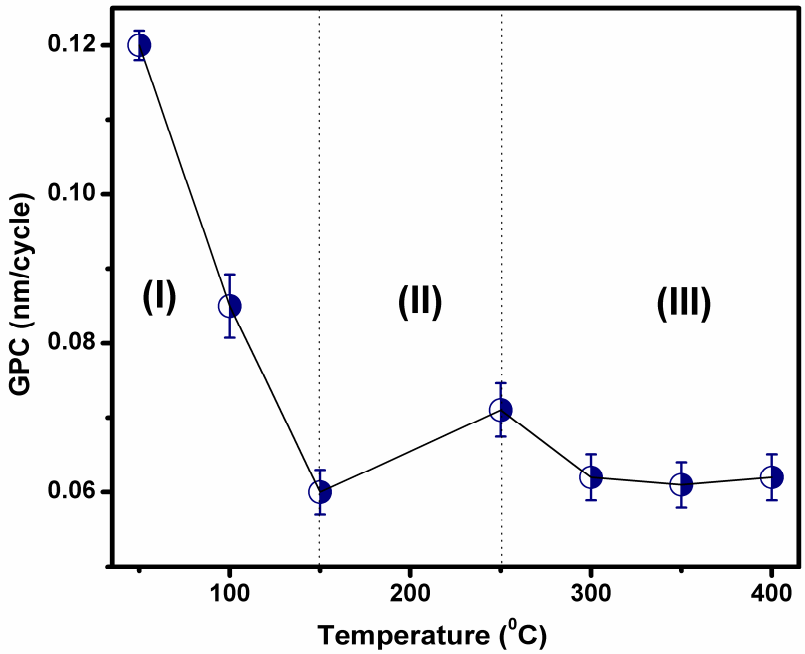

Fig. 5.5 Variation of GPC of TiO_2 thin films as a function of growth temperature. The solid line connecting the data points is the guide for eye.

In zone-II, i.e., for the films grown at 200 and 250^{0}C, the measured spectroscopic ellipsometry (SE) data could not be fitted by using the same optical model and dispersion relation used in zone-I and III. The film grown at 200^{0}C showed very high RMS surface

roughnesses which scattered a significant fraction of light out of the collection cone of the ellipsometer analyser and might also depolarize the light beam. This could be the reason that no interference fringes were observed in the experimentally measured tan ψ and Cos Δ spectra for this film. Therefore, we could not even able to fit the SE data in the visible spectral range. However, quite reliable fitting was obtained for the films 250^0C in the visible spectral range using Cauchy dispersion relation. The thickness was found to be ~ 177 nm. The abrupt increase in film surface area due to the discrete growths of columnar grains facilitated larger amount of precursors to get chemisorbed in each ALD cycle and thus increased the GPC of the film. In zone-III i.e., for the nanocrystalline films, the GPC was found to be almost independent of the substrate temperature. The constancy in GPC in this temperature zone might be due to the chemically stabilized surface states and no significant change in the surface morphology as observed in AFM measurements. Aarik *et al.* using in-situ quartz crystal microbalance (QCM) technique showed that self-limiting growth window for depositing TiO_2 in ALD lies within the temperature range of 150-350^0C [162-164]. This is contrary to the ZnO thin film deposition which showed constant GPC over the self-limiting growth window. Such difference plausibly arises due to the drastic change in the surface morphology of TiO_2 thin film grown at the amorphous to crystalline phase transformation temperature.

Fig. 5.6 shows XPS spectra of Ti 2p and O1s of TiO_2 thin films grown at 100 and 200^0 C. Line shape fittings of the peaks were performed after the subtraction of a Shirley type background. Ti 2p split into two peaks, one at binding energy 458.8 (Ti $2p_{3/2}$) and another at 464.4 (Ti $2p_{1/2}$) due to spin-orbit splitting. The O1s peak with binding energy 530.4 eV originates from the lattice O^{2-} (O–Ti–O). The shoulder at 532.0 eV corresponds to the surface hydroxyl group (Ti–OH). The TiO_x surface for both the films grown at 100 and 200^0 C were found to be non-stoichiometric. However, the film grown at 200^0 C (anatase) showed

improved stoichiometry (Ti: O =1: 1.92) compared to the film grown at 100^0 C (amorphous) (Ti: O =1: 1.81).

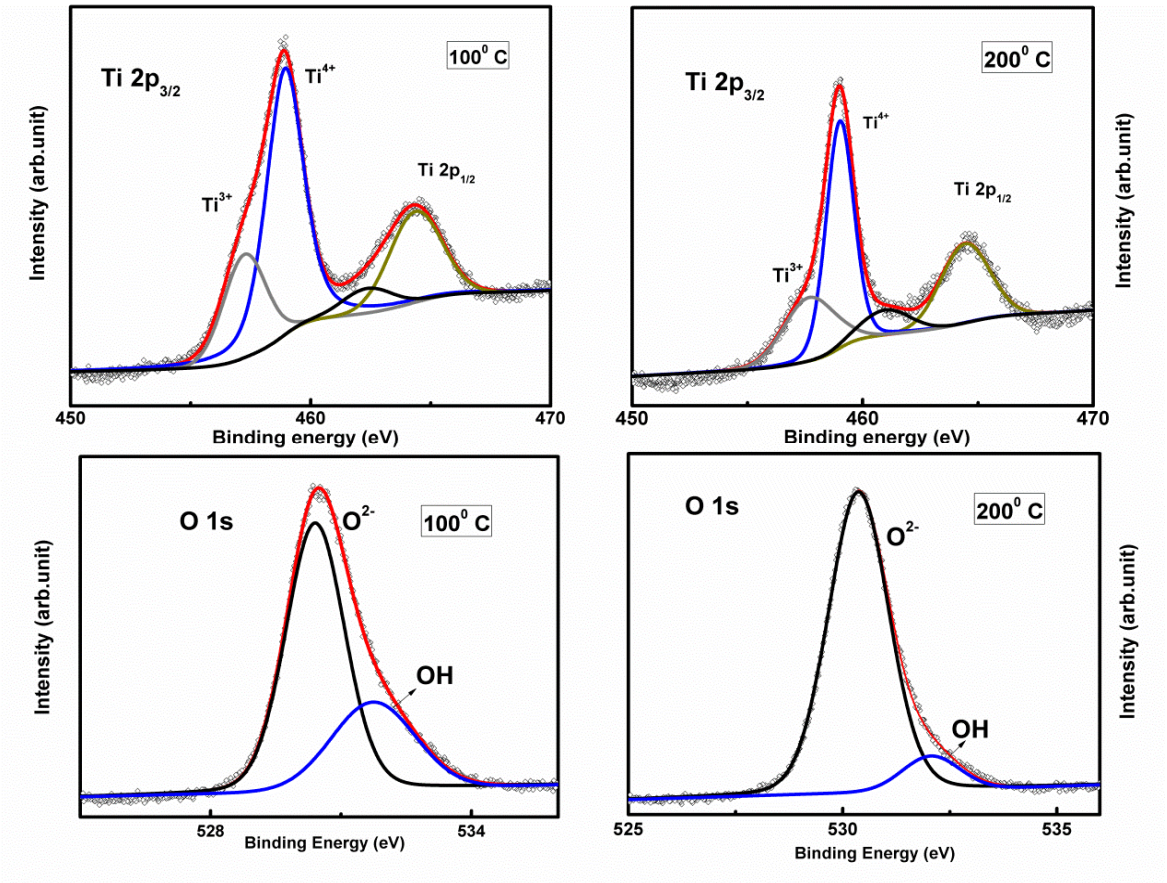

Fig. 5.6 XPS spectra of Ti 2p and O1s of TiO_2 thin films grown at 100 and 200^0 C.

5.2 Incorporation of Sub-Monolayer of TiO_x in ZnO

During thin film deposition in ALD, dopant atoms are uniformly distributed within a strictly two-dimensional monolayer through chemisorption of precursor molecules on the growing film surface [88, 89]. The comparatively low-temperature deposition of thin films in ALD also reduces the diffusion of dopant atoms out of the doping plane. Consequently, extremely narrow doping profile with high peak concentration of dopants can be achieved in ALD. Such well-defined and spatially localized dopant distribution along the vertical direction of the host semiconductor lattice is known as δ-doping or spike-doping [166]. δ-doped semiconductors

with low sheet resistance are indispensable to realize ultra-shallow junctions in the foreseeable future of low-dimensional electronic devices. However, due to the very high dopant density in a δ-doped layer, a significant fraction of the dopant atoms introduces static-disorder without donating free carriers into the system. Therefore, widely dispersed dopant distribution on the doping plane is crucial to enhance doping-efficiency. Realizing such doping profile in ALD is a difficult task due to its self-limiting and layer-by-layer growth methodology which is ideal for fabricating nanolaminate structures with atomically sharp interfaces [151]. Hence, ALD is an inferior technique to achieve higher doping-efficiency. In order to alleviate this problem, different methods have been adopted for ALD grown n-type doped ZnO films which include, pulsing a surface inhibitor prior to the dopant exposure, exploiting larger ligand size precursor molecules for the dopant to promote steric hindrance effects and employing different pulsing schemes of precursor and co-reactant [136, 140 and 142]. In all these methods, the main motivation was to achieve spatially dispersed dopant distribution on the doping plane. In the present case, we kept pulsing time of $TiCl_4$ ~ 25 ms which is well below the surface saturative exposure of $TiCl_4$ precursor on the hydroxyl terminated TiO_2 surface. The deposition temperature of ~ 200^0C is highly useful because at this temperature host ZnO thin film showed highest electrical conductivity with optimum structural and optical properties as discussed earlier. Moreover, amorphous to crystalline phase transformation temperature of TiO_2 was also found to be ~ 200^0C. At this temperature growth of TiO_2 was deviated from the ideal layer-by-layer growth of ALD and formed discrete 3-dimensional agglomerates after few deposition cycles. Therefore, a single pulse of TiO_2 will give a sub-monolayer growth so that plenty of surface reactive sites will remain unoccupied by the $TiCl_4$ precursor. Those unreacted surface sites will possibly be occupied by the subsequent growth of ZnO on TiO_2 layer. Therefore, the higher interfacial diffusion between ZnO and TiOx was obtained which produced uniform Ti distribution along film

thickness for the films (for S4-S10) rather than forming a nano-laminated structure of ZnO and TiO_x. The significant interfacial diffusion could also be confirmed from the higher FWHM of the Ti peak in the SIMS depth profiling spectra for the films S1-S3 as discussed in the next section 5.3.

5.3 Growth of (Zn, Ti)O_x Thin Films and Their Doping-Profiles

Sub-monolayer TiO_x incorporated ZnO [(Zn, Ti)O_x)] thin films were grown on epi-polished single crystal (0001) sapphire substrates at 200^0C. Ti concentration in the films was measured using synchrotron XRF measurements. A representative XRF spectrum for the (Zn, Ti)O_x films is shown in Fig. 5.7. The presence of small amount of Cl in the film as observed in the XRF spectrum is plausibly coming due to the use of $TiCl_4$ precursor. No other impurity peak other than Cl was observed in the samples. The Ar and Fe peaks in the XRF spectrum are coming from the background.

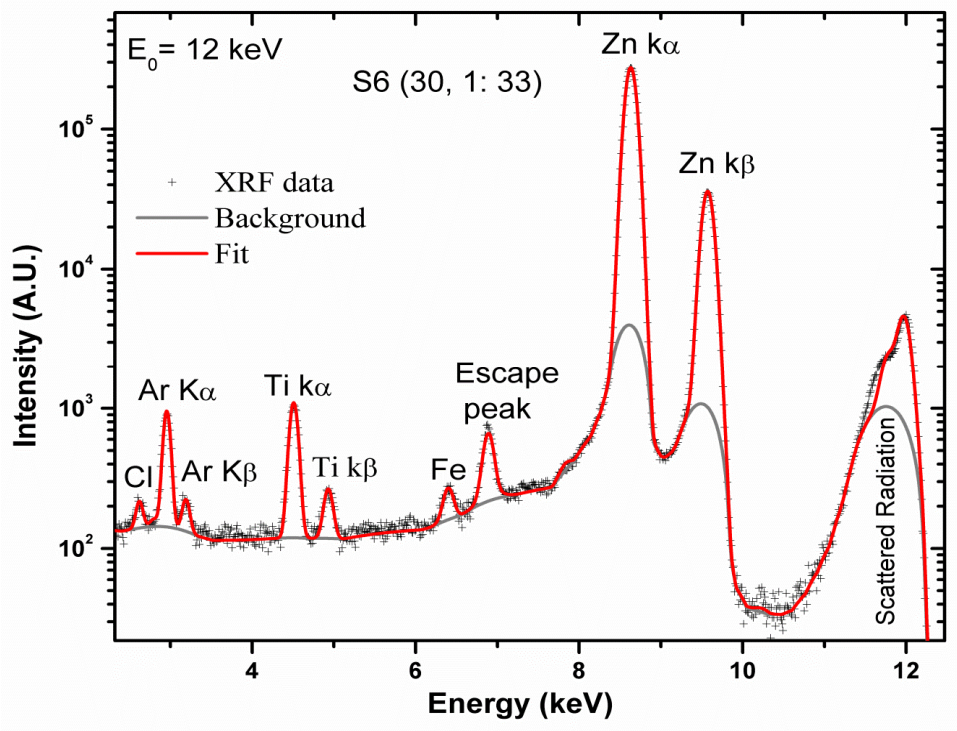

Fig. 5.7 A representative synchrotron XRF spectrum (samples S6) for the (Zn, Ti)O_x films.

Ti concentration was varied systematically in a wide range from ~ 0.2 to 10.4 at. % by varying percentage of TiO_x cycle R_{Ti} (%) = {1/(1+n)}x100%] where 'n' is the number of ZnO cycles in a supercycle (Table 5.1). The (Zn, Ti)O_x films were named as S (n, 1: s) where '1' cycle of TiO_x exposure after 'n' cycles of ZnO makes one complete super-cycle, and 's' represents total number of super-cycles [58]. The thickness of the (Zn, Ti)O_x films as measured by spectroscopic ellipsometry technique was found to be in the range of ~ 180-220 nm.

Table 5.1 List of all (Zn, Ti)O_x thin films with different R_{Ti} (%). The values of static-disorder parameter $K_F l_e$, relative resistivity ratio $\rho(r)$, temperature of resistivity minimum (T_m), zero temperature conductivity (σ_0), diffusion constant (D) and screening parameter γF_σ are also listed in the table.

Sample name S (n,1: s)	R_{Ti} (%)	$K_F l_e$	$\rho(r)$	T_m (K)	σ_0 ($\Omega^{-1}cm^{-1}$)	D (cm^2s^{-1})	γF_σ
S1 (250, 1:4)	0.4	4.2	0.97	130	542.94	5.8	1.40
S2 (150, 1: 7)	0.7	4.6	0.95	120	705.52	6.5	1.28
S3 (100, 1:10)	1.0	5.0	0.95	115	812.05	6.8	1.36
S4 (60, 1: 16)	1.6	5.3	0.96	100	945.81	7.3	1.39
S5 (50, 1: 20)	2.0	4.2	0.98	125	789.77	5.9	1.57
S6 (30, 1: 33)	3.2	2.7	1.03	190	441.51	3.8	1.16
S7 (20, 1: 48)	4.8	1.6	1.06	--	240.29	2.3	1.08
S8 (15, 1: 63)	6.3	0.9	1.13	--	116.36	1.3	0.91
S9 (10, 1: 100)	9.1	0.2	1.58	--	16.98	0.31	0.90
S10 (5, 1: 167)	16.7	--	--	--	--	--	--

First we have concisely discussed the growth of (Zn, Ti)O_x films in ALD and variation of its doping profile with 'n'.

Fig. 5.8 shows Ti concentration (at.%) in the films as a function of 'n'.

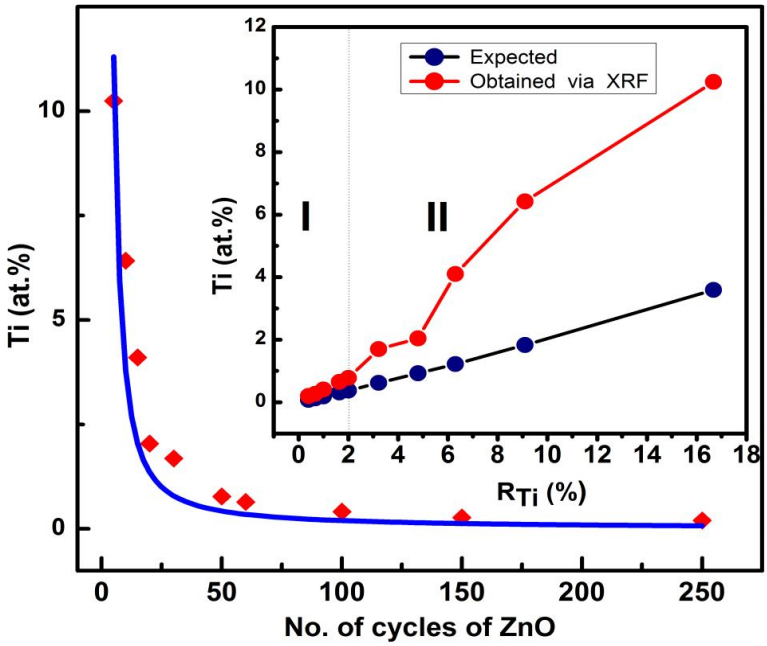

Fig. 5.8 Ti concentration (at.%)as a function of number of ZnO cycles 'n'.The solid blue line shows fitting with Eq. 5.4. The inset shows variation of expected (Eq. 5.3) and experimentally obtained Ti concentrations with R_{Ti} (%).

As can be seen, at lower values of n (≤30) Ti concentration increased abruptly and was found to be almost constant for n ≥50. Such variation in Ti (at.%) could be attributed to the incubated growth of ZnO on TiO_x terminated surface [58]. We have calculated expected values of Ti (at.%) from rule of mixture formula [132, 167],

$$Ti(at.\%) = \frac{\rho_{Ti}^{0}}{\rho_{Ti}^{0} + n\rho_{Zn}^{0}} X100\% \qquad (5.3)$$

As can be seen, expected and experimentally obtained Ti concentrations showed significant deviation for n≤30 (See inset of Fig. 5.8) which further confirmed retarded chemisorption of $Zn(C_2H_5)_2$ molecules subsequent to TiO_X exposure. Therefore, we have used following phenomenological model (Eq. 5.4) to fit the experimental data in Fig. 5.8

$$Ti(at\%) = 100/[1 + (\rho_{Zn}^{0}/\rho_{Ti}^{0})[n - \tau + \tau\exp\{-(n/\tau)\}]] \qquad (5.4)$$

where τ is the cycle number of ZnO at which it reaches 63.2% of ρ^0_{Zn}, ρ^0_{Zn} (8.2×10^{14} cm^{-2})and ρ^0_{Ti} (1.53×10^{14} cm^{-2}) are areal densities of Ti and Zn atoms deposited during each ALD cycle of pure TiO_2 and ZnO films, respectively. The least square fitting was obtained for τ = 7. This is an important result which will later be correlated with the degree of static-disorder in the films. Fig. 5.9 shows SIMS depth profiling spectra for few selected (Zn, Ti)O_x films. The films S1-S3 showed spatially localised or inhomogeneous Ti distribution along film thickness.

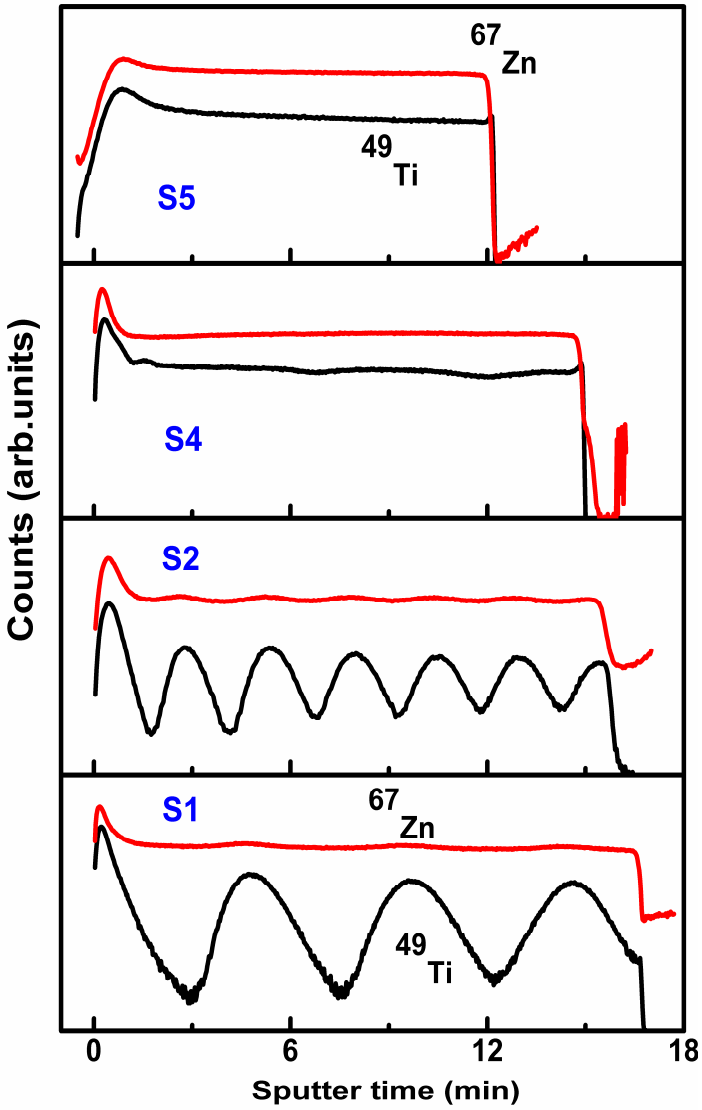

Fig. 5.9 SIMS depth profiling spectra for (Zn, Ti)O_x thin films

The periodic oscillations in Ti counts were found to be closely matched with the period of TiO_x incorporation in the host ZnO lattice. This is expected because 'n' for these films was sufficiently higher to overcome the impeded growth of ZnO which resulted in well separated vertically stacked multiple TiO_x sub-monolayers in the ZnO matrix. However, the higher FWHM of the doping profile implied significant interfacial diffusion between ZnO layer and TiO_x sub-monolayer. Thus, the spatially localized dopant distributions in these films were not δ-like. The rest of the films (S4-S10) showed homogeneous Ti distribution because of reduced spacer layer thickness of ZnO. Such doping profiles for the films (S1-S10) are in contrary to the above discussion where we emphasized that ALD is a suitable technique for fabricating nanolaminate structures and δ-doped semiconductors. We have purposefully obtained such anomalous dopant distributions through sub-saturating exposure of $TiCl_4$ precursor on the growing film surface. Moreover, at 200^0C, TiO_2 transforms its phase from ultra-smooth amorphous to quite-rough crystalline anatase. At this temperature growth of TiO_2 was found to be deviated from the ideal layer-by-layer deposition of ALD which resulted in discrete 3-dimensional agglomerates after few deposition cycles. Therefore, in the present case, a single cycle of TiO_2providedsub-monolayer growth, so that plenty of surface reactive sites remained unoccupied by the $TiCl_4$molecules. Those unreacted surface sites plausibly occupied by the subsequent exposure of $Zn(C_2H_5)_2$ molecules and resulted in diffused dopant distributions as observed in the SIMS depth profiling spectra. Such doping profile is indeed very crucial for higher dopant activation as discussed earlier [136, 140 and 142].

5.4 Structural Properties

XRD spectra of (Zn, Ti)O_x thin films are shown in Fig. 5.10. All the films were found to be polycrystalline with a dominant (00.2) peak, although other orientations corresponding to

(10.1) and (10.0) were also observed similar to (Zn, Al)O_x thin films. Such XRD patterns are in line with the previous results obtained for Al and Ti doped ZnO thin films grown by ALD [58, 143, 167 and 168]. Ti^{4+} has an ionic radius of which is very different from the Zn^{2+} cation (0.74 Å). Therefore, crystalline quality of host ZnO lattice would be distorted due to the substitutional incorporation of Ti^{4+} similar to the Al doped ZnO thin films. However, in zone-I, i.e., for the samples S1-S5, no significant deterioration in the crystalline quality of the host lattice was observed as indicated by their XRD patterns. This was plausibly due to the very small amount of dopant incorporation in ZnO through sub-monolayer TiO_x insertion. A significant decrement in the (00.2) peak intensity and increment in the FWHM of both the (00.2) and (10.1) peak were observed for the film S6 with Ti concentration of ~ 1.68 at. %. With further incorporation of Ti i.e., the films with Ti concentrations at and above ~ 2 at.% were found to be X-ray amorphous [143]. This could be attributed to the lower values of ZnO cycles ($n \leq 20$) which is close to the incubation period of ZnO ($\tau \sim 7$) on the TiO_x terminated surface. Therefore, nucleation of ZnO was strongly inhibited which lead to the amorphous nature of the films [143].

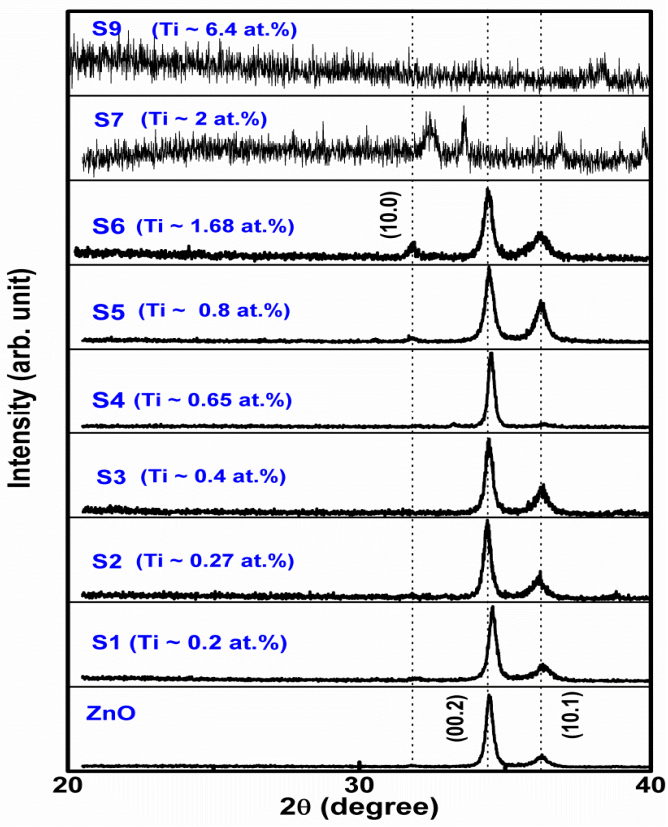

Fig. 5.10 XRD pattern of (Zn, Ti)O_x thin films grown on (0001) sapphire substrates with different Ti concentration.

5.5 Room Temperature Electrical Properties

Fig. 5.11 shows variation of room temperature electron density and electrical resistivity with Ti concentration. Initially with increasing Ti incorporation from ~ 0 to 0.77 at% (zone-I: S1-S5) electron density was increased monotonically from ~5.2x$10^{19}$to 3.8x10^{20} cm^{-3} and then decreased with further insertion of Ti (zone-II: S6-S10). Increase of electron density in zone-I indicates that incorporated Ti atoms serve as efficient electron donors in ZnO. This was plausibly due to the effective screening of Ti impurity potentials by the free electrons of the sufficiently thick (n>>τ) degenerate ZnO spacer layers. The screened impurity potentials (or Yukawa potential given by $V(r) = (e/4\pi\varepsilon r)\exp(-r/r_s)$ where ε is the permittivity of ZnO

and r_s is the screening radius) are less capable of binding the valance electrons and consequently, ionization energy decreases (see section 1.3.2). Temperature dependent electrical resistivity of the films, as discussed later, did not show any carrier activation behaviour i.e. ionization energy was completely vanished. Thus, films were metallic in nature (see section 1.3.2).

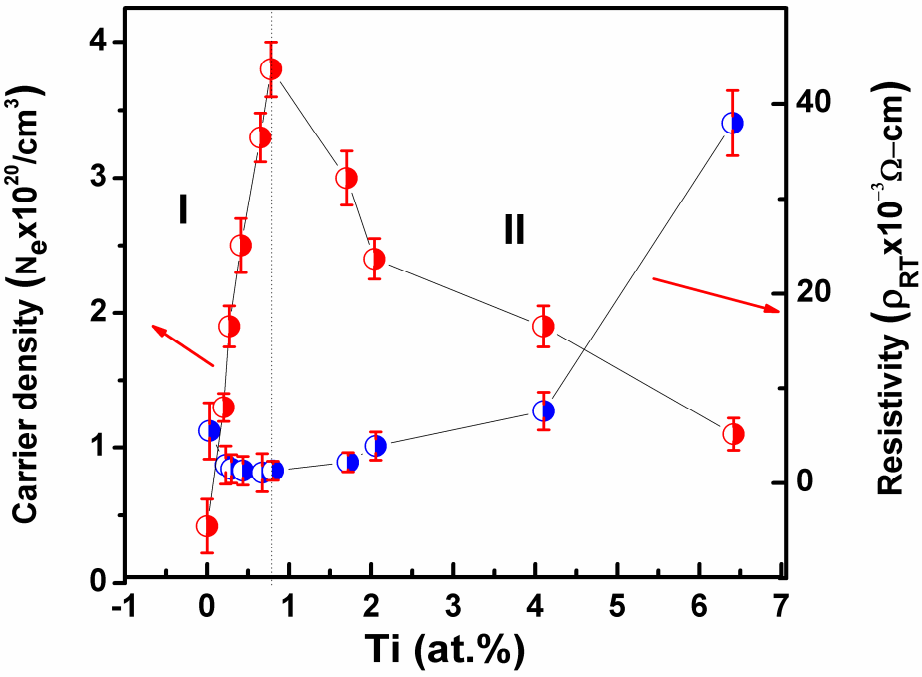

Fig. 5.11 Variation of carrier density and room temperature electrical resistivity of (Zn, Ti)O_x thin films with Ti concentration in the range of 0 (ZnO) to ~ 6.42 at.% (S9).

The decrease of electron density in zone-II indicates inefficient screening of incorporated Ti impurities due to sufficiently reduced ZnO spacer layer thickness (n>τ) and thus, a significant fraction of impurities remained electrically inactive. However, carrier compensation effect due to the formation of intrinsic defects and defect complexes cannot be completely ruled out [169, 170]. The variation of room temperature electrical resistivity (ρ) with Ti at.(%) is shown in Fig. 5.11. Initially, resistivity was found to be decreased from ~ 4.3x10^{-3} Ω cm for intrinsic ZnO to ~1x10^{-3} Ω cm at ~0.65 at.% of Ti. As could be seen, the decrease of

resistivity was quite slow compared to the sharp increment of electron density in zone-I. This was due to the increased ionized impurity scattering which lowered electron Hall mobility with increasing Ti concentration as shown in Fig. 5.12.

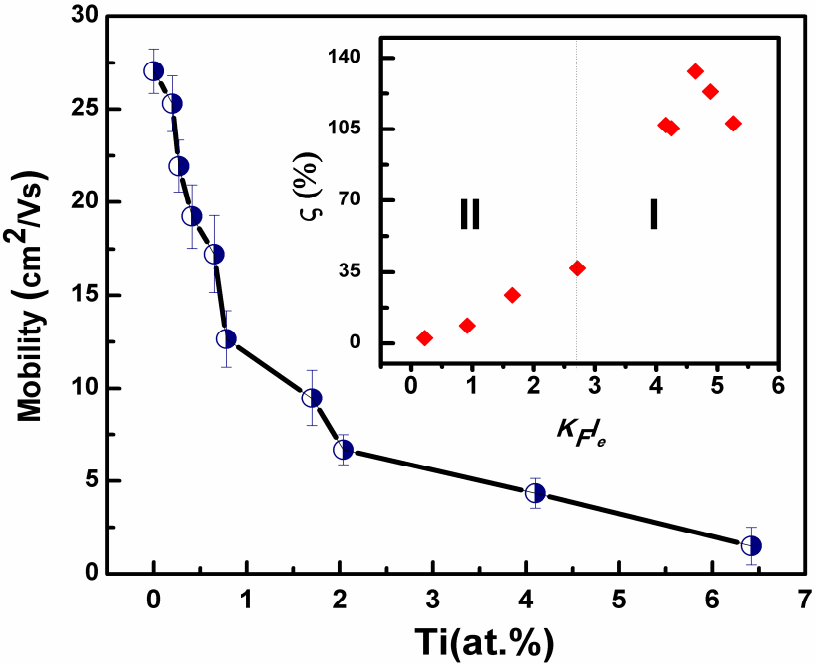

Fig. 5.12 Variation of Hall mobility in (Zn, Ti)O_x thin films with Ti concentration. Inset shows doping-efficiency as a function of static-disorder parameter $K_F l_e$

Above 0.65 at.% of Ti, resistivity was found to be increased and ultimately reached to a maximum measureable value ~ 38x10^{-3} Ω cm at ~ 6.42 at.%. The resistivity of the film S10 with Ti concentration of ~10.24 at.% was too high to be measured and thus, was not included in Fig. 5.11. The relatively sharp increment of resistivity in zone-II resulted from the decrease of both electron density and Hall mobility. The poor electron Hall mobility for the films at higher Ti at.% plausibly resulted from the tremendous electron scattering due to strengthened structural and compositional disorder in the films [82]. As a measure of static-disorder, we have calculated the values of the dimensionless parameter $K_F l_e$ (see Table 5.1) where K_F is the Fermi wave number and l_e is the elastic mean-free path of conduction electrons [71]. For

$K_F l_e > 1$, i.e., $l_e > \lambda_F (= 2\pi / K_F)$ implies scattering of electrons are weak enough and metallic transport (finite conductivity at T→0 K) through Bloch extended states is possible [71, 82]. On the other hand, in the strong scattering regime $K_F l_e < 1$ i.e., $l_e < \lambda_f$, insulating (vanishing conductivity at T→0 K)behaviour prevails due to the localization of electronic states [71]. The inset of Fig. 5.12 shows doping-efficiency ζ(%) as a function of $K_F l_e$. The films in zone-I with n>>τ were in the lower disorder limit ($K_F l_e$ ~ 4.2-5.4) which showed enhanced doping-efficiencies for both inhomogeneous (S1-S3) and homogeneous (S4 & S5) dopant-profiles. However, as the strength of disorder is increased in zone-II $(K_F l_e \sim 0.5 - 2.7)$ with n ~ τ, electrons become less mobile and, most plausibly, cannot screen the impurity potentials as efficiently as in zone-I. Therefore, a major fraction of incorporated Ti atoms remained electronically inactive which resulted in sharp fall of doping-efficiency in transition from zone-I to zone-II. In order to further elucidate the interplay of screening and disorder on electron transport, temperature dependent electrical resistivity (ρ(T)) was measured for all the films in the temperature range of 5-300K.

5.6 Temperature Dependent Electron Transport

The ρ(T) curves for few selected (Zn, Ti)O_X films are shown in Fig. 5.13. All the conducting films (S1-S9) showed finite resistivity at T→0 K and very low relative resistivity ratio ρ(r) = ρ(4.2 K)/ρ(300 K) (see Table-5.1) values which implied that films are on the metallic side of the metal-insulator transition (MIT) [76-79].

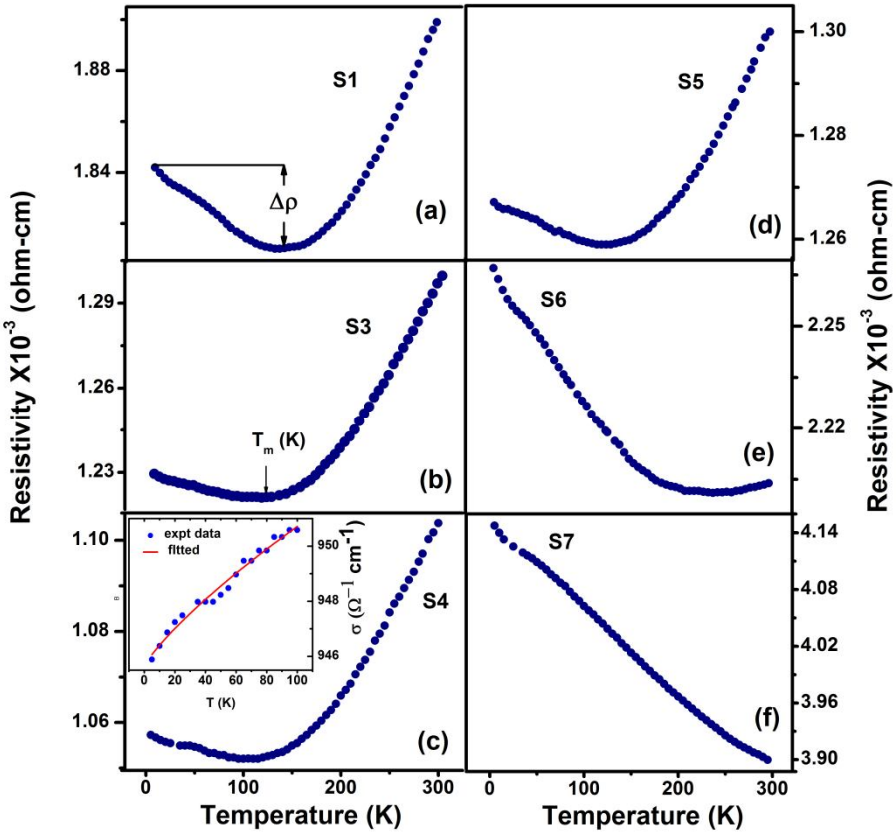

Fig. 5.13 Temperature dependent (5-300K) electrical resistivity of few selected (Zn, Ti)O_x thin films. The inset of (c) shows fitting of the conductivity curve below T_m (K) using quantum corrections to conductivity Eq. 5.6.

In Fig. 5.14 we have plotted the reduced activation energy W [171],

$$W = -T\{d \ln \rho(T) / dT\} \tag{5.5}$$

as a function of measurement temperature for the samples S7, S8 and S9. As can be seen, W has a positive temperature coefficient for all the films. This observation clearly implied that these films which showed semiconducting behaviour in the entire temperature range of the measurement temperature were also on the metallic side of the MIT [171].

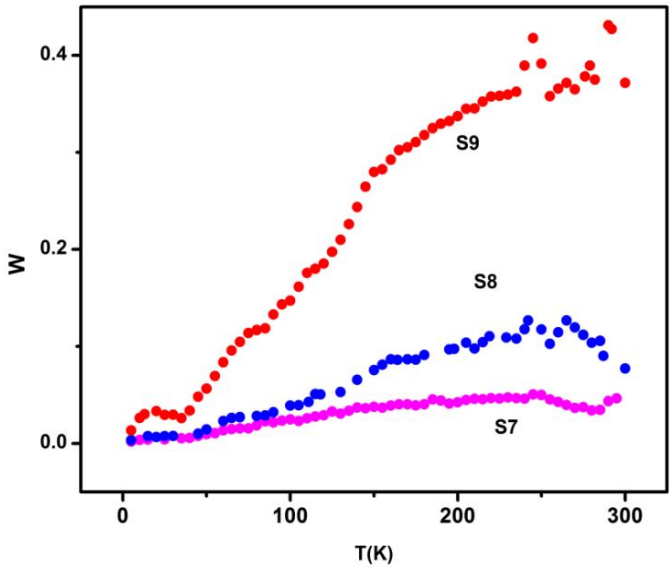

Fig. 5.14 Reduced activation energy W for samples S7, S8 and S9 as a function of temperature.

The films S1-S6exhibiteda smooth transition from 'metal-like' (dρ/dT>0) to 'semiconductor-like' (dρ/dT<0) behaviour with decreasing temperature which resulted in a resistivity minimum at T_m (K). The 'semiconductor-like' resistivity behaviour below T_m(K) plausibly arises due to disorder induced electron weak localization (WL) and electron-electron interactions (EEIs) [84, 85]. Initially with increasing Ti concentration from 0-0.65 at.%, T_m was found to be shifted to the lower temperature and the depth of the resistivity minimum ($\Delta\rho$) was also found to be decreased. These two observations clearly indicate enhancement of 'metal-like' transport behaviour due to the dominance of screening effect over disorder induced WL and EEI phenomena. This is well corroborated with the increase of $K_F l_e$ and decrease of room temperature resistivity up to ~0.65at.% as discussed earlier. However, with further incorporation of Ti, $K_F l_e$ was found to be decreased and the resistivity minimum started shifting to the higher temperatures (for S5 and S6) with a concomitant increase in Δρ. Eventually, for the films S7-S9'semiconductor-like' resistivity behaviour prevailed in the

entire range of the measurement temperature i.e., the films turned into 'incipient non-metallic' in nature [71].The appearance of pronounced 'semiconductor-like' resistivity behaviour for the films in zone-II (i.e., S6, S7, S8 and S9) is quite surprising because these films were heavily degenerate having electron concentration far above the Mott critical density, similar to those grown in zone-I. Thus, strengthened electron scattering due to higher static-disorder plausibly resulted in such anomalous resistivity behaviour in zone-II [82]. The temperature dependent electrical resistivity data for all the films were found to be consistent with the theoretical predictions of quantum corrections to conductivity (QCC) as has been used for (Zn, Al)O_x thin films. However, in that case the degree of static-disorder could not be varied systematically due to the low vapor pressure of anhydrous $AlCl_3$ precursor. In the present case, the high volatility of $TiCl_4$ and the controlled dopant incorporation capability of ALD enabled us to realize extreme level of tunability in the position of the resistivity minimum as shown in Fig. 5.13. Such outstanding experimental results make possible to explore the influence of screening and disorder on electron transport of (Zn, Ti)O_x films. The 3D QCC Eq. considering the corrections due to WL and EEI's is given by [72, 76-79],

$$\sigma(T) = \sigma_0 + \left(\frac{e^2}{2\pi^2\hbar}\right)\left(\frac{c}{D}\right)^{1/2} T^{p/2} + \left(\frac{1.3e^2}{4\pi^2\hbar}\right)\left(\frac{k_B}{2\hbar D}\right)^{1/2}\left[\frac{4}{3} - \frac{3}{2}\gamma F_\sigma\right] T^{1/2} \qquad (5.6)$$

where $D = v_F^2\tau/3$ is the diffusion coefficient, $\gamma F_\sigma > 0$ is the Coulomb interaction parameter and the value of the constant c can be obtained from $\tau_\phi^{-1} = cT^p$ where τ_ϕ^{-1} is the scattering rate of the dominant dephasing mechanism. A representative fitting of ρ(T) curve below T_m (K) using Eq. 5.6 is shown in the inset of Fig. 5.13(c). The value of γF_σ was found to be decreased for the films in zone-II (see Table 5.1) which clearly imply reduced screening of the Coulomb EEIs due to the enhanced diffusive nature of conduction electrons (lower values of D) in presence of strengthened static-disorder. In order to get a more insight into the

transport properties we have carried out temperature dependent magnetoresistance measurements as shown in Fig. 5.15.

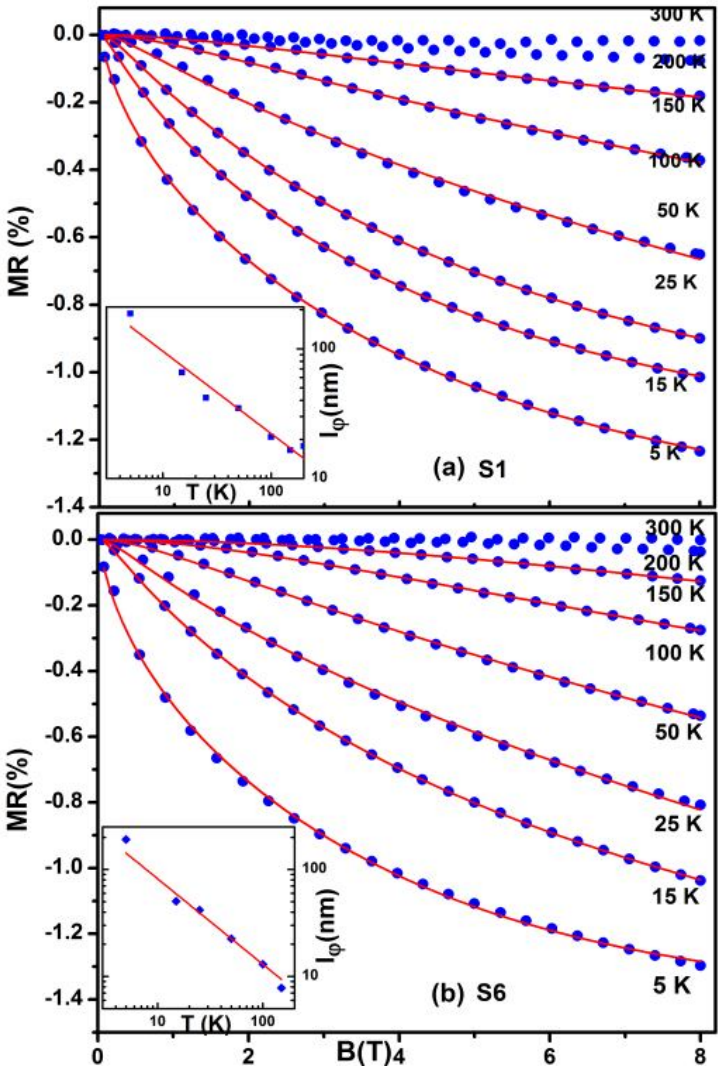

Fig. 5.15 Magnetic field dependent (0-8 T) MR for the films S1 and S6 at different temperatures in the range of 5-300K. The solid lines show the theoretical fitting of the experimental data. Inset shows variation of phase coherence length with temperature.

The magnetoresistance data were analysed by following the same procedure as has been used for (Zn, Al)O_x thin films (see section 4.5 in chapter 4). At T≤15 K, Eq. 4.7 was used which

considers contributions of both WL and EEI's. However, at higher temperatures (T >15K), only WL contribution from Eq. 4.3 was found to be sufficient [172-175]. The value of the phase coherence (see inset of Fig. 5.15) length $l_\phi = (D\tau_\phi)^{1/2}$ was found to be smaller than the film thickness even at 5 K which justifies the use of 3D transport equations for both homogeneous and inhomogeneous dopant profiles. Such results are completely different from that obtained in multiple stacked Ge:P δ-doped layers which showed strongly confined two-dimensional electron gases and associated 2D WL and EEIs [176]. Such difference in electron transport arises due to the degenerate nature of host ZnO lattice which facilitates to detach conduction electrons from the doping plane through screening effect and results in 3D electron transport. Therefore, unlike Ge:P δ-doped layers, spatial localization of dopants in inhomogeneously doped (Zn, Ti)O_x films are not mirror-imaged by the conduction electrons.

5.7 Effect of Film Thickness on Electron Transport

In the preceding section 5.6, we have discussed electron transport in (Zn, Ti)O_x thin films with thickness ~ 200 nm. All the films showed 3D electron transport. It was observed that for both (Zn, Al)O_x and (Zn, Ti)O_x thin films, the samples which were grown with the cycle ratio of 1:50 (TiO_x or AlO_x :ZnO) showed enhanced metal-like conductivity (dρ/dT > 0) i.e., films were well inside the metallic side of MIT. Therefore, in the present case, we kept cycle ratio (TiO_x: ZnO) fixed at 1:50 and film thickness was varied from ~ 6 to 65 nm by varying the number of supercycles (s) from 1 to 7. The samples were named as S1, S2, S3, S4, S5, S6 and S7.

Fig.5.16 shows SIMS depth profiling spectra for few selected samples. The periodic oscillations in Ti counts closely followed the period of TiO_x insertion in the ZnO lattice as schematically shown in the inset of Fig.5.16.

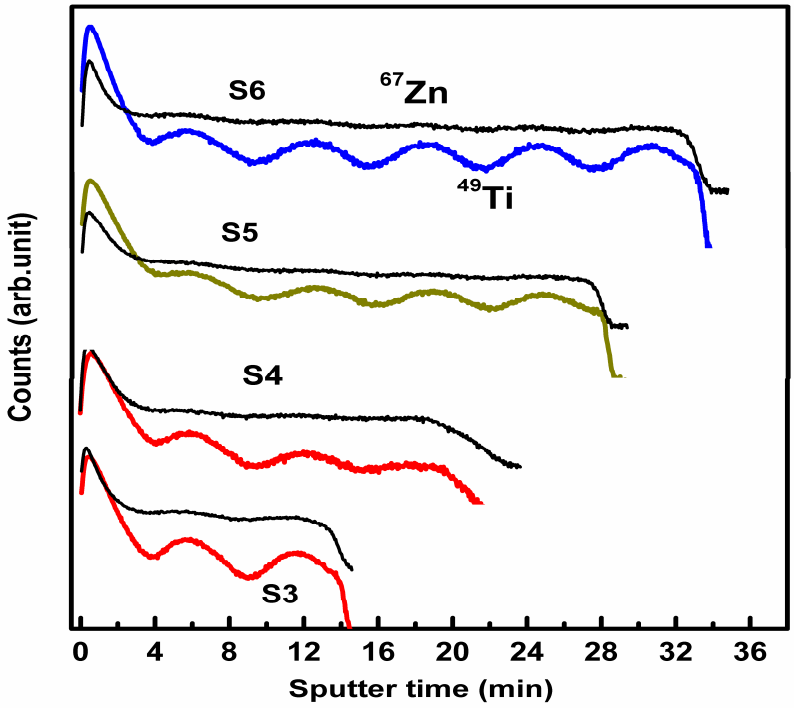

Fig. 5.16 SIMS depth profiling spectra of (Zn, Ti)O_x thin films with different number of 'supercycles'.

The optical transmittance spectra of ZnO/TiO_x stacked layers in the wavelength range of 200-900 nm are shown in Fig. 5.17. All the films were found to be optically transparent (~ 70%) in the visible spectral range. The optical absorption edge was found to be at ~ 360 nm below which optical transmittance was systematically decreased with increasing film thickness.

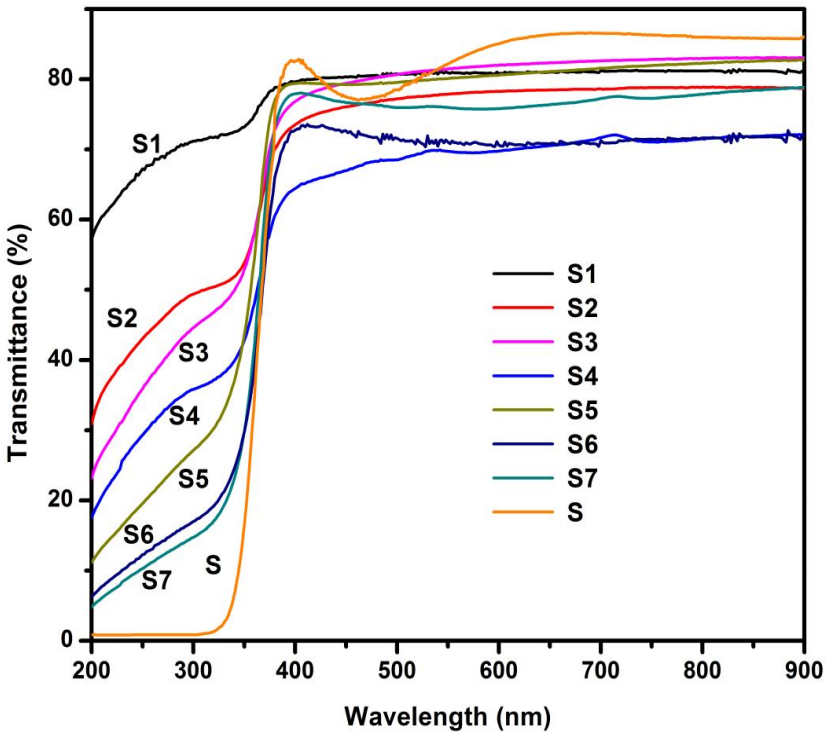

Fig.5.17 Optical transmittance spectra for all the ZnO/TiO_x stacked layers S1-S7 grown on (0001) sapphire substrates.

Fig. 5.18(a) and (b) shows cross sectional TEM images for the film S6 grown on Si substrate in bright-field and dark-field, respectively. Lee *et al.* in Al doped ZnO thin films grown by ALD observed nanolaminate structure of Al_2O_3/ZnO [132]. However, in the present case, columnar ZnO grains were observed and the growth of grains was found to be continious without being inhibited by the TiO_x cycle. This suggests incorporation of sub-monolayer of TiO_x in the host ZnO lattice [167]. The bright-field diffraction pattern (Fig. 5.18(a)) clearly shows polycrystalline nature of the (Zn, Ti)O_x films. AFM surface morphological images for the films S4, S5 and S7 in Fig. 5.18 (b), (c) and (d) show that film are composed of closely packed grains.

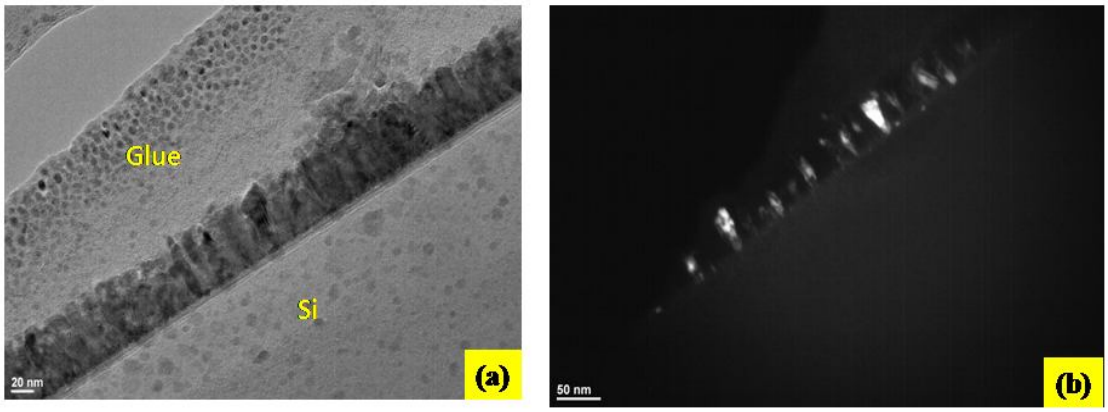

Fig. 5.18 Cross sectional TEM images for the film S6 in (a) bright field and (b) dark field

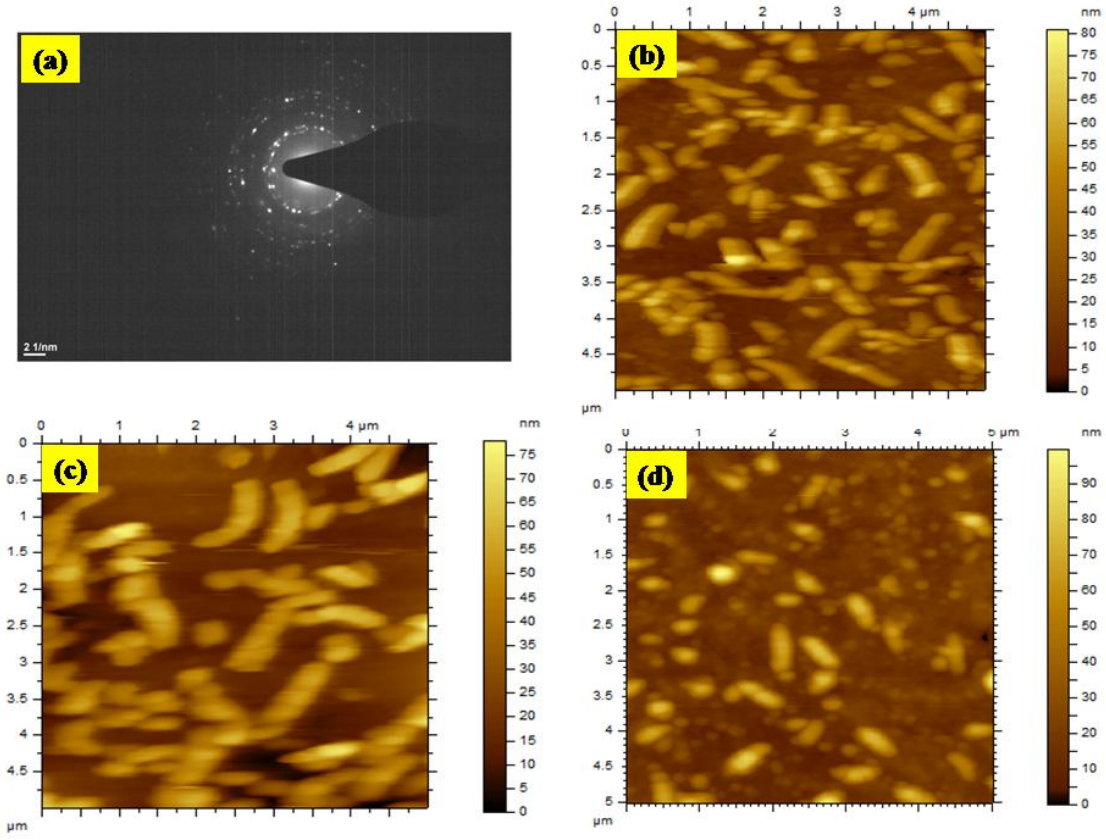

Fig. 5.19 (a) Bright filed TEM diffraction image for the sample S6. (b), (c) and (d) are the AFM micrographs for the films S4, S5 and S7 respectively.

The room temperature electrical resistivity (ρ), sheet resistance ($R_{\square} = \rho / t$), carrier density (N_e) and Hall mobility (μ) values of the films are listed in Table 5.2. The RT values of ρ, $R_{\square}$, N_e, μ of sample (say S) of thickness ~ 200 nm and $R_{Ti}(\%) \sim 2$ as mentioned in the earlier section are also given in the same table for comparison purpose. Electrical resistivity of S1 (n=1) was too high to be measured by our experimental setup. Such high electrical resistivity could be due to the formation of structurally and/or chemically disordered film-substrate interface at the initial stage of film growth, also called electrically insulating 'dead layer'[177]. Similar result was also observed in ultrathin Ga doped ZnO thin films and was attributed to the formation of 'dead layer' at the film-substrate interface [177].

Table 5.2 List of the values of room temperature electrical resistivity, carrier density, Hall mobility and sheet resistance of ZnO/TiO_x stacked layers grown by ALD. The films were named as S (m, 1: n) where 'm' denotes number of ZnO sub-cycles, followed by 1 sub-cycle of TiOx, making one complete supercycle, and 'n' represents total number of super-cycles.

Sample Name S(m, 1:n)	Thickness (nm)	Resistivity ($x10^{-3}$ Ω cm)	Carrier density ($x10^{20}$ cm^{-3})	Hall Mobility (cm^2/V s)	Sheet resistance (Ω/□)
S1(50, 1:1)	6	---	---	---	---
S2(50, 1:2)	12	80	---	---	$68x10^3$
S3(50, 1:3)	20	4	3.1	5.0	$2x10^3$
S4(50, 1:4)	30	1.4	4.1	10.6	480
S5(50, 1:5)	42	1.3	4.4	11.0	300
S6(50, 1:6)	54	1.4	4.0	11.2	250
S7(50, 1:7)	65	1.1	4.5	12.6	170
S(50, 1:20)	200	1.3	3.8	12.7	65

Room temperature electrical resistivity of S2 was measured to be ~ $82x10^{-3}$ Ω cm which is roughly two orders of magnitude higher than that of sample S (see Table 5.2). The carrier concentration of S2 could not be measured by using Hall measurement set up. This is plausibly due to the deteriorated crystalline quality of S2 which resulted in strengthened carrier scattering and consequently poor carrier mobility. However, further increment of one more staked layer i.e., for the sample S3 (n=3), resistivity was found to be drastically decreased to ~ $4x10^{-3}$ Ω cm. Carrier concentration and Hall mobility of S3 were found to be ~ $3x10^{20}$ cm^{-3} and ~ 5 cm^2/V s respectively. The measured carrier density of S3 is almost one order of magnitude higher than the intrinsic ZnO films grown by ALD. Therefore, incorporated Ti atoms start acting as efficient n-type dopant in ZnO from 3 stacking layers of ZnO/TiO_x. For the films S4-S7, resistivity and Hall mobility values were found to be almost comparable to that of sample S. This implies that above three stacking layers (n=3) of ZnO/TiO_x, the films grew uniformly as far as room temperature electrical properties are concerned. The huge difference between the electrical properties of the films (S1, S2) and the films (S3-S7 and S) instead of their same $R_{Ti}(\%)$ could be attributed to the poor crystalline quality and/or free carrier trapping by the chemisorbed O_2 and/or OH groups at the surface and at grain boundary defect sites of these ultra-thin films [178-180]. In order to investigate the role of such chemisorption phenomenon on the electrical properties, we have exposed all the samples under UV light (higher than the band gap of ZnO) for few minutes inside a high vacuum optical cryostat. Upon UV light exposure, the highly resistive film S1 did not show any decrement in its electrical resistance, which further confirmed the formation of an electrically insulating 'dead layer' [177]. On the contrary, resistivity of S2 was decreased to ~ $19x10^{-3}$ Ω cm as measured few hours after the UV illumination step. This conducting state remained almost intact for several weeks inside the optical cryostat chamber and slowly reverted to its initial highly-resistive state when exposed to open atmosphere. Such reversible

change in the electrical resistivity clearly implies defect states mediated adsorption (high resistive state) and desorption (low resistive state) of atmospheric O_2 and/OH groups [178-180]. The slow decrement of conductivity in air atmosphere after switching off the UV source clearly indicates the slow trapping process of conduction band electrons by the surface and grain boundary defect sites. The slow accumulation of electrons at the surface and grain boundaries also increases the height of the upward band bending which also prevents further trapping of free electrons. As a result, photoconductivity of the ultra-thin film tends to persist and few hours after the UV switching off step the original value of the dark conductivity is reached [178, 179]. However, the resistivity of UV light exposed S2 (inside the cryostat chamber) remained higher compared to the film S (~ 1.3×10^{-3} Ω cm). This difference in the electrical resistivity could be attributed to the higher crystalline disorder in S2 compared to S. The rest of the films (i.e., S3-S7 and S) showed only marginal decrement in the electrical resistivity upon UV light exposure. In order to further investigate the role of such chemisorption effects on the underlying electronic transport of the films, we have carried out temperature dependent electrical resistivity measurements. Results of these studies are discussed below.

Fig.5.20 shows temperature dependent electrical resistivity [ρ (T)] curves for the films S2 and S3 with and without UV treatment. As can be seen, UV unexposed film S2 exhibited a semiconductor like resistivity ($d\rho / dT < 0$) behaviour in the entire range of the measurement temperature. Its resistivity value on extrapolation to T→ 0 K was found to be diverged, implying S2 lies on the insulating side of the insulator-to-metal transition (IMT). However, the ρ (T) curve of the UV exposed film S2 showed a drastic change as evident from Fig. 5.20. The relative resistivity ratio [ρ_r = ρ(4.2 K)/ ρ(300 K)] value was found to be significantly decreased from 12.4 to 1.7. Interestingly, the UV exposed sample exhibited a finite resistivity at T→ 0 K i.e., upon UV treatment S2 moved to the metallic side of the IMT. In open

atmosphere, O_2 and/or OH groups get absorbed at the surface and grain boundary defect sites by trapping free electrons from the conduction band [$O_2(g) + e^- \rightarrow O_2^-(ad)$] [178-180].

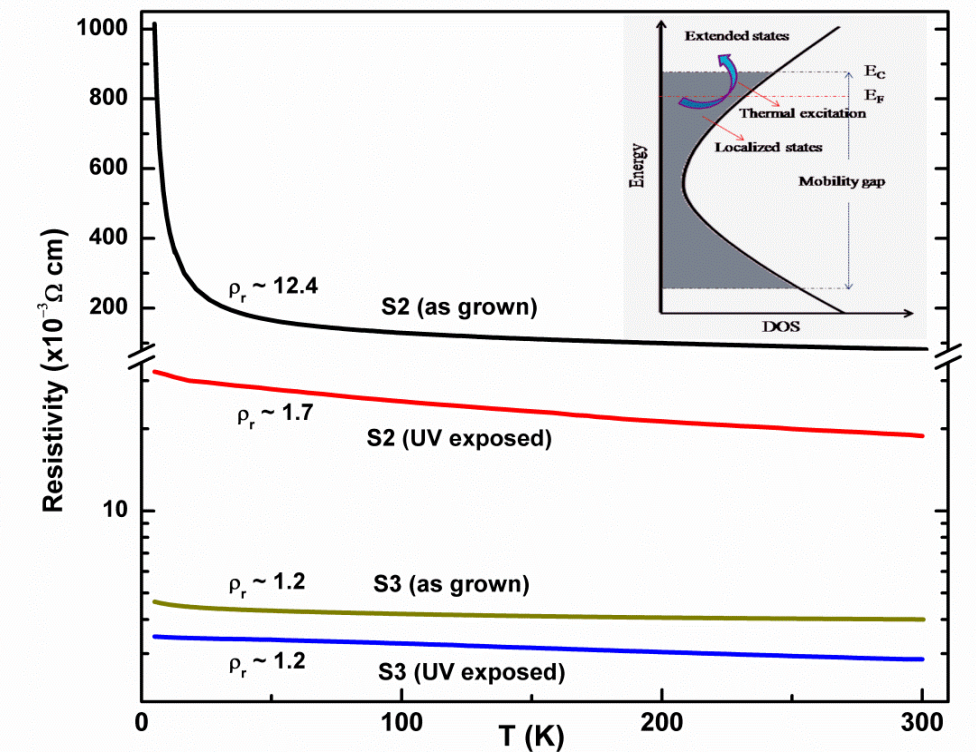

Fig. 5.20 Temperature dependent electrical resistivity curves for as grown and UV treated samples. Inset shows a schematic representation of density of states (DOS) vs energy. The shaded region represents localized states. The mobility edge (E_c) which is marked as the boundary between the localized and the non-localized states is also shown.

This leads to the free carrier depletion and concomitant upward band bending at film surface and at grain boundaries [178-180]. The effect of free carrier depletion from the surface and intra-grain regions was so pronounced that Fermi level (E_F) shifted below the mobility edge (E_c) i.e., electronic wave functions at E_F turned into localized and the sample exhibited insulating behaviour as schematically shown in the inset of Fig.5.20. However, upon UV light

treatment ($h\nu \rightarrow e^- + h^+$) inside the vacuum chamber, desorption of oxygen [$O_2^-(ad) + h^+ \rightarrow O_2(g)$] from the defect sites left behind free electrons into the conduction band [178-180]. As a result, E_F shifted above E_c i.e., electronic states at E_F changed into extended, which resulted in metallic conductivity. Thus, the observed IMT in S2 is purely reversible in nature and is induced by the movement of E_F across E_c. It is important to mention here that, in some cases IMT can also be induced by tuning the position of E_c with respect to E_F. This type of IMT has been observed in GeSbTe samples in which the position of E_c has been tuned by thermal annealing and free carrier density i.e., E_F was kept almost constant [82]. The rest of the samples (i.e., S3-S7 and S) exhibited metallic behaviour for both before and after UV light exposure (see Fig. 5.20 for the film S3). All these films showed only marginal or no change in the relative resistivity ratio value upon UV light exposure which further confirmed that O_2 and/or OH group's chemisorption effects have insignificant role on the underlying electronic transport in these films.

We are now interested to discuss the electrical resistivity curve of S2 in the insulating regime. In the insulating regime ($E_c > E_F$), the $\rho(T)$ curve of S2 as depicted in Fig. 5.21, could not be fitted by considering Arrhenius equation $\rho(T) = \rho_0 \exp(E_a / KT)$ with a single activation energy E_a. This simply implies the presence of different conduction channels with varying activation energies acting in parallel in the temperature range of 5-300 K. At relatively higher temperatures, both thermally activated carriers above E_c (see inset of Fig. 5.20) and phonon-assisted nearest neighbour hopping (NNH) of carriers below E_c can contribute to the electrical conductivity [71, 73]. However, at sufficiently low-temperatures, the number of empty sites among the nearest neighbours becomes too few, resulting in freezing of NNH conduction process. At this situation, variable range hopping (VRH) between localized states

with energies lying in the vicinity of the Fermi level ($E_F \pm \varepsilon$) may play a key role in charge transport below E_c i.e., without involving extended states contribution [71, 73].

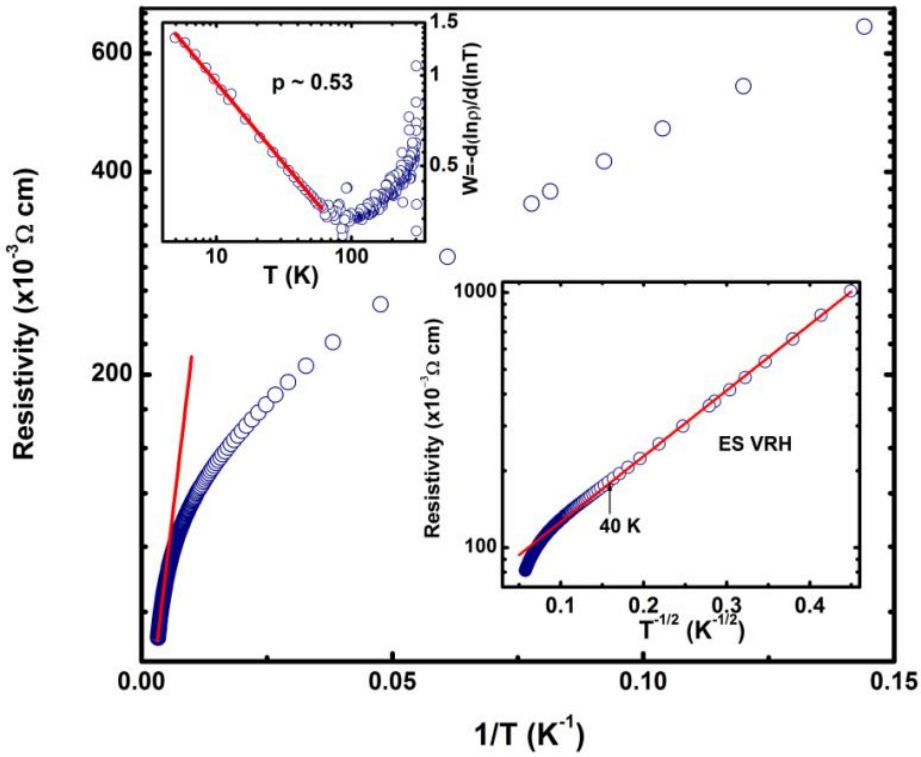

Fig. 5.21 Shows logarithm of resistivity as a function of $1/T(K^{-1})$. The straight solid line is the least-squares fit with Arrhenius equation. Upper inset shows log-log plot of reduced activation energy (W) with T (K) and the solid line is the least-squares fit with a straight line in the region $dw/dT < 0$. The lower inset shows logarithm of resistivity as a function of $(1/T)^{-1/2}$ and its least-squares fit with the ES VRH conduction law.

In order to unambiguously address the low-temperature VRH conduction process in ZnO/TiO_x film, we have plotted reduced activation energy w [$w = -d(\ln\rho)/d(\ln T)$] as a function of measurement temperature (T) in the upper inset of Fig. 5.21 [181]. Considering the general form of the temperature dependence of VRH[$\rho(T) = \rho_0 \exp(T_0/T)^p$], the

reduced activation energy can be written as $\ln w(T) = A - p \ln T$ with $A = p \ln T_0 + \ln p$ [181]. Negative slope of w $(dw/dT < 0)$ up to ~ 60 K further confirmed that the UV unexposed sample is in the insulating regime of IMT [181]. The least square fitting of the linear portion of $\ln w(T)$ vs $\ln T$ plot in the regime $dw/dT < 0$ provides p ~ 0.53 which points to Efros-Shklovskii (ES) type VRH mechanism $[\rho(T) = \rho_{ES0} \exp(T_{ES}/T)^{1/2}$, ρ_{ES0} is a resistivity parameter and T_{ES} is a characteristic temperature defined as $T_{ES} = \beta_1 e^2 / k\xi k_B$ where β_1 is a constant with a value ~ 2.8, e is the electronic charge, k is the static dielectric constant, ξ is the localization length and k_B is the Boltzmann constant] [71, 73]. Thus, in the lower inset of Fig. 5.21 we have plotted $\ln \rho(T)$ vs $T^{-1/2}$ which provided a linear behaviour up to ~ 40 K, implying ES VRH as the dominant conduction mechanism in ultra-thin ZnO/TiO_x film at lower temperatures. In order to get a deeper insight into the transport properties we have carried out temperature dependent magnetoresistance (MR) measurements on this film. Fig. 5.22 shows variation of MR as a function of applied magnetic field (Tesla) at different measurement temperatures. S2 shows negative MR similar to that of weakly localized (Zn, Al)O_x and ZnO/TiO_x stacked layers on the metallic side of the IMT. However, the appearance of negative MR in insulating S2 is not due to the suppression of weak localization effects as considered in our earlier reports. In the present case, the small value of ρ_r (~ 12) indicates that S2 is not deep into the insulating regime of IMT [181]. Disordered insulating systems which are close to IMT can also exhibit negative MR in the VRH regime due to magnetic field induced suppression of quantum interference between forward scattering events connecting the two sites of the hopping process [181-184]. According to this theory, the magnetic field dependence of resistivity is determined by the flux threading an area over which phase coherence is maintained. The area of such a coherent loop is an ellipse of length R_{hop} and width $(R_{hop}\xi)^{1/2}$ where R_{hop} is the average hopping length.

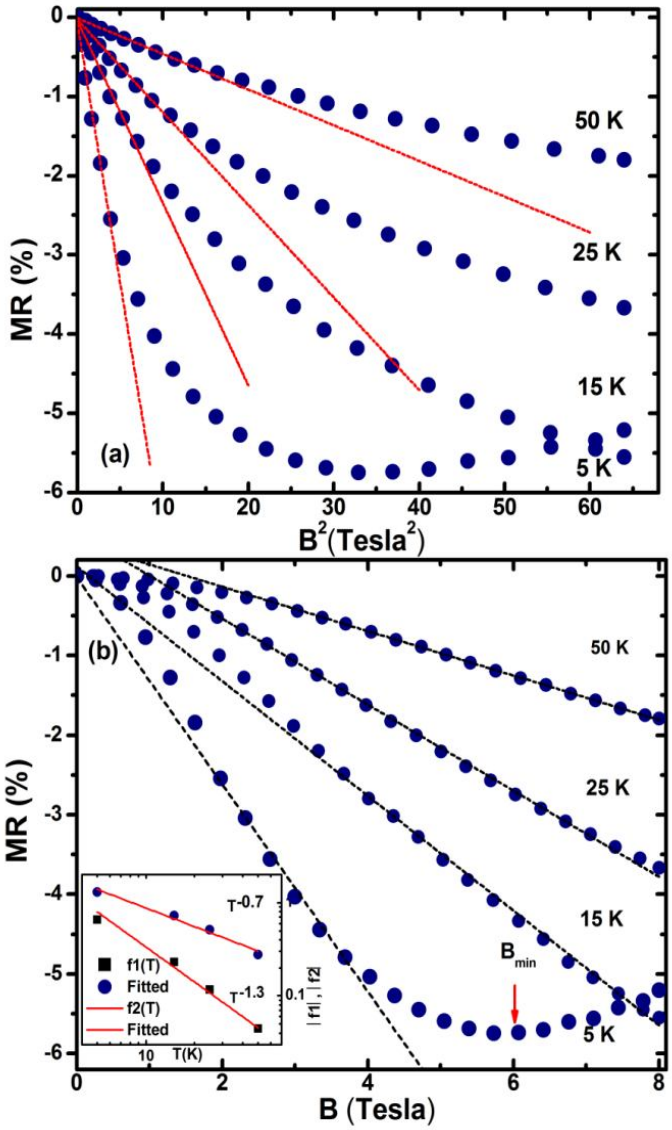

Fig. 5.22 (a) Shows magnetoresistance (MR) at different temperatures as a function of B^2. The straight dotted lines are the least-squares fits in the low magnetic field regime. (b) Shows MR as a function of B. The straight dotted lines are the least-squares fits in the high magnetic field regime. Inset shows log-log plot of $f1(T)$ and $f2(T)$ with T (K).

According to this theory, in low magnetic fields MR is given by [182-184]

$$-(\Delta\rho/\rho) \sim (R_{hop})^3 \xi(B) B^2 \sim f1(T)\xi(B)B^2 \qquad (5.7)$$

and in higher magnetic fields [182-184]

$$-(\Delta\rho/\rho) \sim (R_{hop})^{3/2}\xi^{1/2}(B)B \sim f2(T)\xi^{1/2}(B)B \quad (5.8)$$

As can be seen from Fig. 5.22(a), at low magnetic fields, MR is linear with B^2 as predicted by Eq. 1. However, at higher magnetic fields, MR exhibits a much weaker functional from of B. In Fig. 5(b), negative MR varies almost linearly with B. In ES VRH mechanism, $R_{hop} \sim T^{-1/2}$ and thus temperature dependence of $f1(T)$ and $f2(T)$ are $T^{-3/2}$ and $T^{-3/4}$ respectively (see Eq. 1 and 2). The inset of Fig. 5.22(b), shows that $f1(T)$ and $f2(T)$ are directly proportional to $T^{-1.3}$ and $T^{-0.7}$ respectively. This is in close agreement to the ES VRH mechanism in ZnO/TiO_x film at low temperatures. The positive upturn in MR at 5K was plausibly induced by the shrinkage of the impurity wave functions at higher magnetic fields [181].

The temperature dependent electrical resistivity curves for all the conducting films S2-S7 are shown in Fig. 5.23. The resistivity of sample S1 of thickness ~ 6 nm was too high to be measured and therefore, is not included in Fig. 5.23. The evolution of sheet resistance versus temperature curves with decreasing film thickness showed a metal to insulator transition.

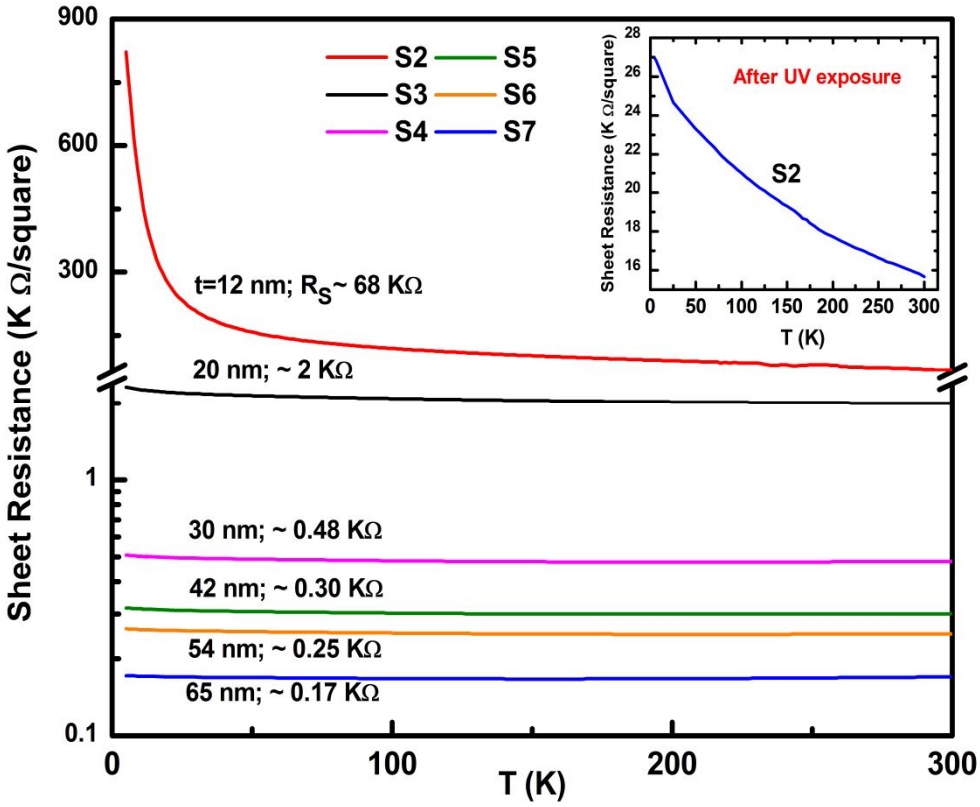

Fig. 5.23 Temperature dependent (5-300K) electrical resistivity of all the (Zn, Ti)O_x thin films. The inset shows ρ(T) curve for the film S2 as measured after 10 minutes of UV light exposure inside a high vacuum chamber.

As can be clearly seen, the films S2 is in the insulating regime and samples S3-S7 are metallic. We have already discussed, the electrical resistivity of S2 in the insulating side of MIT. We are now interested to explore the transport properties of the metallic films S3-S7 which showed quite stable electrical properties in air exposure and did not exhibited significant change in the RT resistivity under UV light exposure.

It is well established that on the metallic side of MIT, electronic transport in disordered 2D and 3D systems is driven by the effects of WL and EEIs [72, 76]. For 2D electronic system in the weakly localized regime the temperature dependence of electrical conductivity is given by [72, 185 and 186],

$$\sigma_{2D}(T) = \sigma_0 + p\frac{e^2}{\pi\hbar}\ln\left(T/T_0\right) \quad (5.9)$$

where σ_0 is the Drude conductivity and p the temperature exponent of the inelastic scattering length $l_{in}\alpha T^{-p/2}$. If the dominant scattering mechanism is electron-electron collision then p = 1, whereas for electron-phonon scattering p = 3 [185]. It is worthy to mention here that, WL effect in granular electronic systems can also provide logarithmic temperature dependence of conductivity [187]. In the present case, all the (Zn, Ti)O_x films are composed of densely packed grains. A representative AFM micrograph of these films is shown in the lower inset of Fig. 5.24. The very short electron mean free path values (l_e ~ 0.7-2 nm) indicate that grains are dirty enough due to the statistical distribution of the dopants and hence intragrain electron transport is in the diffusive transport regime ($D = v_F^2\tau / d$ where D is the diffusion constant, v_F is the Fermi velocity, τ is the elastic intragrain scattering time and d is the dimensionality of the grain). Moreover, heavily degenerate nature of these films also reduces grain barrier heights and depletion layer widths at grain boundaries. Therefore, intergrain tunneling will be a dominated phenomenon, and the condition for granular electron transport i.e., intergrain tunneling conductance (g_T) << intragrain conductance (g_0) will not be satisfied in these films [187]. After all, granular transport exhibits logarithmic T (K) dependence in conductivity for both two- and three-dimensional samples. In our earlier reports on 3D electron transport in polycrystalline ZnO and (Zn, Al)O_x thin films, we did not observe such ln(T) dependence. Therefore, the concept of granular electron transport is not applicable in these heavily degenerate (Zn, Ti)O_x thin films and Eq. 1 for 2D electron WL can reliably be employed. For the film S3, we have plotted sheet conductance versus ln(T) in Fig. 5.24. A linear fit to the curve yields a slope ~ 1.5×10^{-5} S up to T= 50 K i.e., p = 1.25. This indicates to the electron-electron collisions as the dominating scattering mechanism in the films [185]. The curve shows a deviation from the linear behaviour above 50 K. This could be due to the

cross over from the 2D to the 3D transport regime with increasing temperature [188]. Similar effect was also observed in other films S4-S7 in which the resistivity curves could not be explained by considering either 2D or 3D transport equations in the entire range of the measurement temperature. For instance, the film S7 had a resistivity minimum as shown in the lower inset of Fig. 5.24.

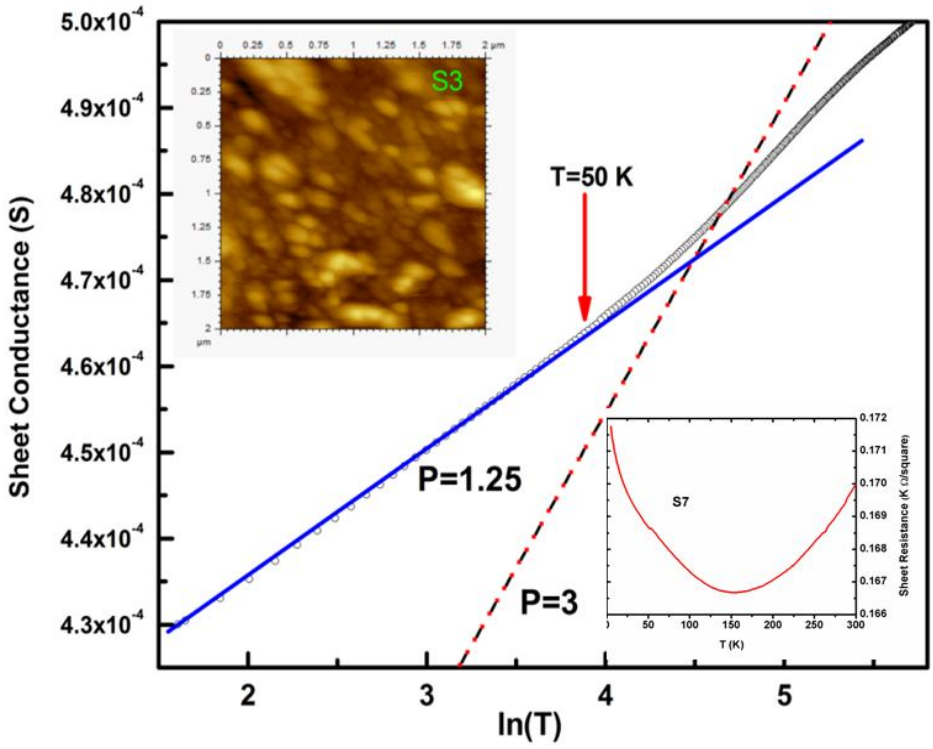

Fig. 5.24 The variation of sheet conductance for the film S3 with ln(T). The inset shows AFM micrograph for the sample.

The appearance of resistivity minimum in 2D and 3D disordered electronic systems could be attributed to the WL phenomena [185]. However, in the present case, the resistivity minimum could not be fitted by using 2D or 3D WL equation which points to a dimensional crossover of electron transport with increasing temperature [185, 188 and 189]. Nevertheless, the validity of this model needs further confirmation. For this purpose, we have carried out temperature dependent MR measurements in varying magnetic field of (0-8 T) for all the

samples. The results of MR measurements are shown in Fig. 5.25.

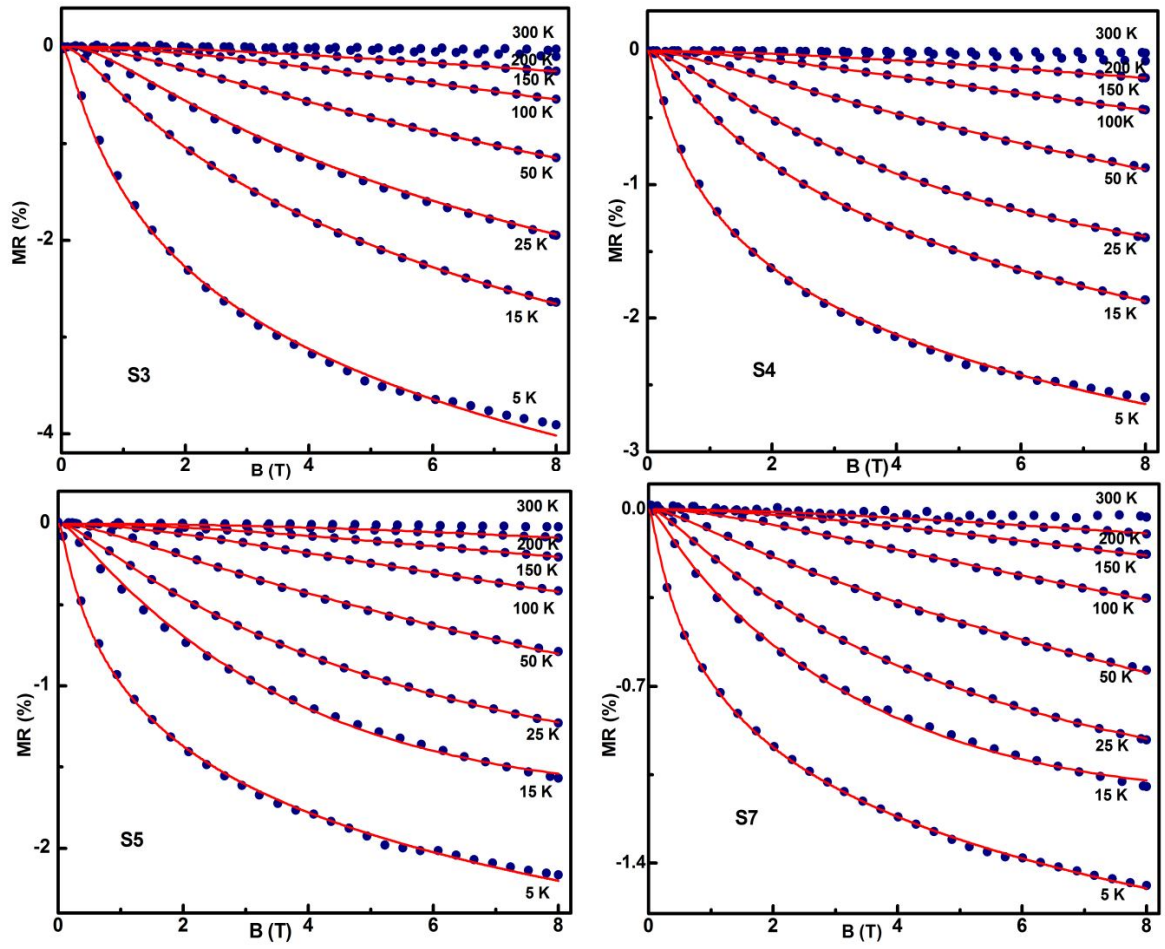

Fig. 5.25 Magnetic field (0-8 T) dependent MR for few selected samples at different temperatures in the range of 5-300K. The solid lines show theoretical fittings of the experimental data.

All the films showed small negative MR, characteristic of a disordered electronic system in the weakly localized regime [185, 188-190]. In case of 2D WL, MR can be written as [72, 185 and 188-190]

$$MR(\%) = -R_{\square}(0,T)\Delta\sigma_{\square}(H,T)X100(\%) = -R_{\square}(0,T)\frac{e^2}{\pi h}\left[\psi\left(\frac{1}{2}+\frac{1}{x}\right)+\ln(x)\right]X100(\%) \quad (5.10)$$

where $\Delta\sigma_{\square}(H,T)$ is called the magneto conductance and is defined as

$$\Delta\sigma_{\square}(H,T) = \sigma_{\square}(H,T) - \sigma_{\square}(0,T) = 1/R_{\square}(H,T) - 1/R_{\square}(0,T) \quad (5.11)$$

In Eq. 3, sheet conductance $\sigma_{\square} = \sigma t$ (S/□) and sheet resistance $R_{\square} = \rho / t$ (Ω/□) where t is the film thickness. In Eq. 5.8, ψ is the digamma function and $x = l_{in}^{\ 2} 4eB / \hbar$. Eq. 5.8 has only one fitting parameter, the inelastic scattering length l_{in}. The variation of l_{in} (nm) as a function of T (K) is shown in Fig. 5.26. As can be seen, negative MR was observed even when l_{in} value at 150 K reduced below the average grain size. This observation further confirmed the irrelevance of granular electron transport in these degenerately n-type doped ZnO films as discussed earlier [187]. The value of l_{in} at ~ 50 K was found to be comparable with the effective film thickness t_{eff} of the film S3. The effective films thickness of electron conduction is defined as $t_{eff} = t - t_d$ where t is the measured film thickness and t_d is the 'dead layer' thickness (~ 6 nm). Therefore, the film S3 can be considered as 2D disordered electronic system up to ~ 50 K as far as WL is concerned [185, 189]. The use of Eq. 2 above 50 K provided $l_{in} < t_{eff}$ i.e. 2D MR equation is invalid in this temperature range which points to a dimensional crossover of WL to 3D regime. This observation is highly consistent with our earlier discussion on the variation of zero field sheet conductance versus ln(T) plot (see Fig. 5.24) in which 2D WL equation (Eq. 1) showed good agreement up to ~ 50 K and a clear deviation above it. Thus, MR data above 50 K were fitted using 3D WL equation as has been used in our previous report on (Zn, Al)O_x thin films. The least square fitting of $l_{in}(T)$ up to T= 50 K (see Fig. 5.26) provided a temperature dependence of $T^{-0.56}$ i.e., 2D Nyquist e-e scattering $l_{in}\left(=\sqrt{D\tau_{in}} \sim T^{-p/2}\right)\ \alpha\ T^{-0.5}$ could be the dominant dephasing mechanism [189]. This is in close agreement with the temperature dependence of $l_{in}(T)$ as independently obtained from the $\sigma_{2D}(T)$ vs. ln(T) plot in Fig. 3. Above 50 K, $l_{in}(T)$ was found to be α $T^{-0.75}$ (dashed line in Fig. 5.26) which is usually observed in 3D dirty metallic systems. Therefore, MR results of the film S3 further confirmed a smooth crossover from 2D to 3D

WL regime with increasing temperature [189, 191]. However, the crossover temperature was found to be reduced with increasing film thickness [189, 191]. As can be seen, for the sample S7 (see Fig. 5.26), typical 3D temperature dependence of $l_{in}(T)\ \alpha\ T^{-0.72}$ was observed even up to 15 K. Similar observation has also been reported in n-type ZnO films in which the deviation of $l_{in}(T)$ from 3D behaviour was observed at ~10 K [191]. It is to be noted that in the present case, temperature dependence of $l_{in}(T)$ has been explained without considering any additional channel for electron dephasing due to inter sub-monolayer scattering (τ_{sm}) [176].

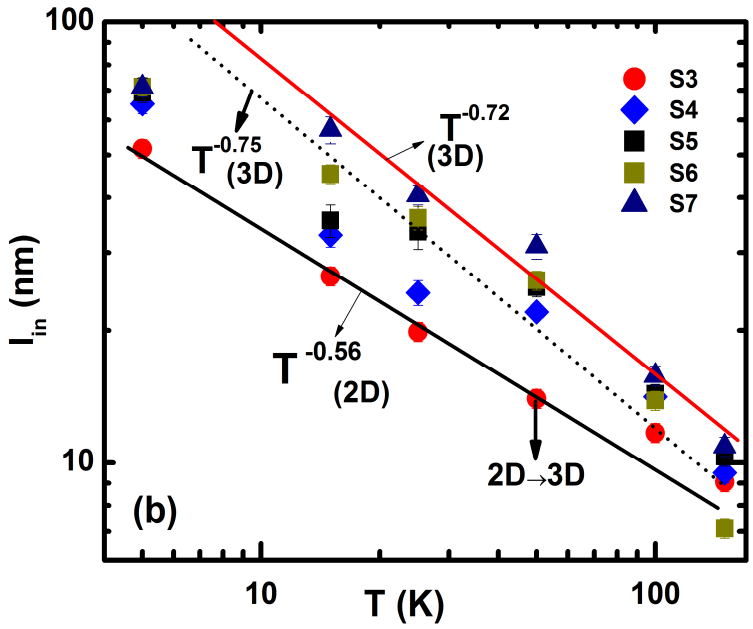

Fig. 5.26 shows variation of inelastic scattering length (l_{in}) as a function of temperature T (K). The solid lines are least square fittings of l_{in} versus T plots for the samples S3 (in 2D WL regime 5-50 K) and S7 (in 3D WL regime15-150 K). The dashed line shows a temperature dependence of $T^{-0.75}$ for the sample S3 above 50 K.

5.8 Correlation between Electrical and Optical Properties

After a detailed analysis of the electron transport mechanisms, we have carried out optical transmittance and temperature dependent (5-300 K) photoluminescence measurements for all the (Zn, Ti)O_x thin films as listed in Table 5.1. Optical properties were also found to be strongly dependent on the interplay of electron density and dopant induced static-disorder in the films – recall that similar effect was also observed in electron transport measurements. Therefore, electrical and optical characteristics of these films were found to be correlated with each other. The results of these studies are discussed below.

(I) Optical Transmittance Spectroscopy Measurements

Fig.5.27 shows the optical transmittance spectra for all the (Zn, Ti)O_x thin films with different Ti concentrations. The fundamental optical absorption edge (the minimum energy E_g^o needed to excite an electron from the valence band to the conduction band, Fig. 5.28 (a)) showed a systematic blue shift with increasing Ti concentration. For better clarity, see the inset of Fig. 5.27.

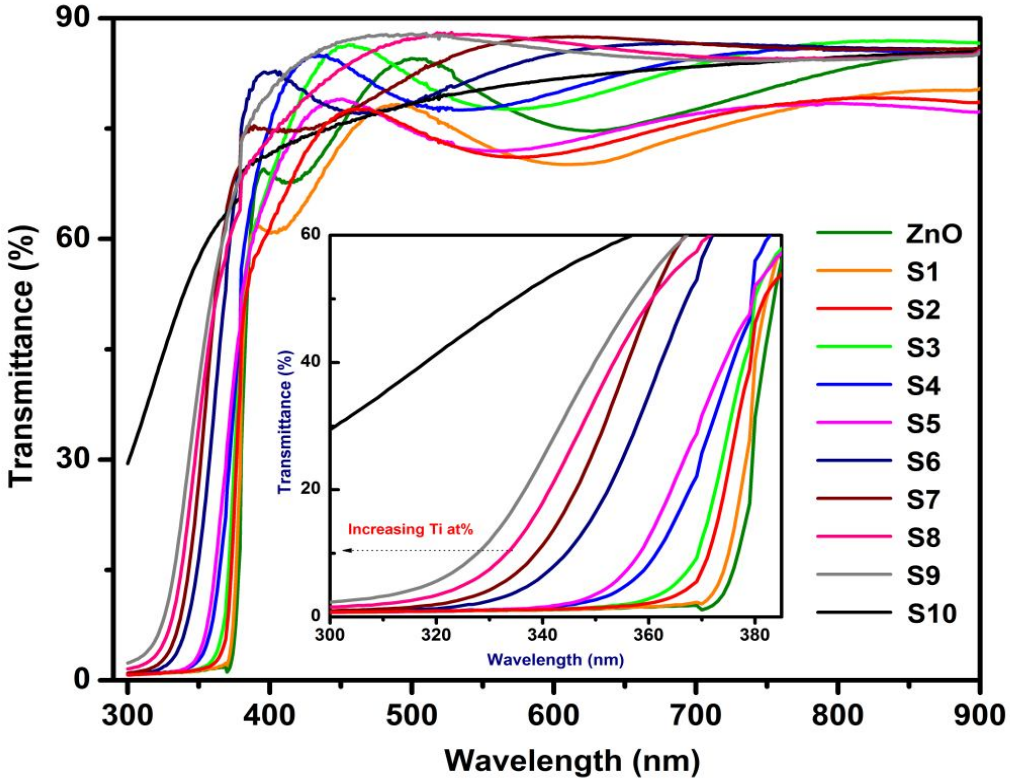

Fig. 5.27 Optical transmittance spectra of all the (Zn, Ti)O_x thin films with different Ti concentrations

Such increment in optical band-gap in these heavily degenerate semiconductors could be due to the Burstein-Moss (BM) band-filling effect as schematically shown in Fig. 5.28(b) [153]. However, as can be seen from Fig.5.9, electron concentration was decreased with increasing Ti concentration beyond sample S5 i.e., for the samples in zone-II. Therefore, in zone-II, the increase in optical band-gap could not be entirely due to the BM effect. These samples exhibited pronounced structural disorder due to higher dopant incorporation as discussed earlier. Moreover, Hall mobility (see Fig.5.11) and doping-efficiency (see inset of Fig.5.11) were also found to be drastically decreased in zone-II. All these observations clearly suggest intra-grain congregation and/or grain boundary segregation of Ti impurities, formation of phase separated TiO_x sub-oxides and/or Zn_2TiO_4 cubic spinel-type, hexagonal $ZnTiO_3$ phases

in these heavily doped (Zn, Ti)O_x samples. However, synchrotron XRD spectra did not show peaks corresponding to these phases, plausibly due to the presence of trace amount of these crystalline phases which is beyond the detection limit of XRD. The sample with the highest Ti concentration was found to be X-ray amorphous. The sharpness of optical absorption was also found to be significantly deteriorated with increasing doping concentration in zone-II. These samples showed longer Urbach tails below the free excitonic absorption due to increased structural disorder [192]. As can be seen from Fig. 5.27, for the sample S10 with the highest Ti concentration, the fundamental optical absorption edge corresponding to ZnO lattice did not appear. Such optical transmittance spectrum clearly indicates significant deterioration in the crystalline structure of the host ZnO lattice, which is indeed reflected by the X-ray amorphous nature of this sample. Therefore, the increment in the optical band-gap for the samples in zone-II plausibly arises due to the combinatorial effect of BM effect and significant modification in the band structure of ZnO. Similar results were also reported in Al doped ZnO thin films grown by ALD and other thin film deposition techniques [58, 64].

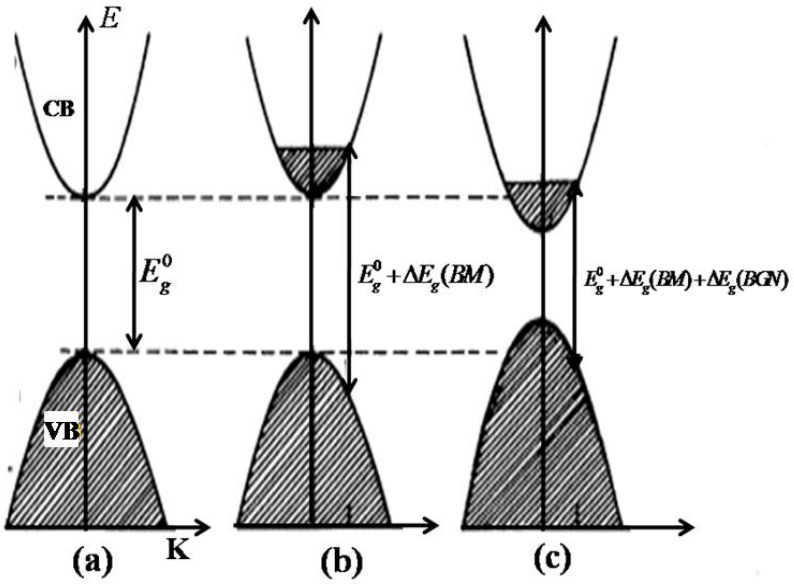

Fig. 5.28 Schematic representations of (a) the fundamental optical band-gap, (b) the Burstein-Moss band filling effect and (c) band gap narrowing effect due to many body interactions.

In zone-I, the variation of optical band-gap with electron density is shown in Fig. 5.29. In heavily doped n-type semiconductors, as the donor electrons occupy states at the bottom of the conduction band, optical transitions from top of the valance band to the bottom of the conduction band are forbidden due to Pauli blocking [153]. As a result, the fundamental optical band gap is increased which is known as the Burstein-Moss (BM) band-filling effect [58, 64]. The expression for BM shift is given by [193],

$$\Delta E_g(BM) = \left(E_c^o(K_F) - E_v^o(K_F)\right) - E_g^0 \tag{5.12}$$

$$= \frac{\hbar^2 K_F^2}{2m_c^*} + \frac{\hbar^2 K_F^2}{2m_v^*}$$

$$= \frac{\hbar^2 K_F^2}{2m_{vc}^*} \tag{5.13}$$

where $m_{vc}^* = \left(\frac{1}{m_c^*} + \frac{1}{m_v^*}\right)^{-1}$ is the reduced effective mass with m_c^* and m_v^* are the effective masses of carriers in the conduction and valance bands respectively. The expression for the Fermi wave vector is given by $K_F = \left(3\pi^2 n_e\right)^{1/3}$ where n_e is the electron density. Therefore, Eq. 5.13 becomes

$$\Delta E_g(BM) = \frac{\hbar^2 (3\pi^2 n_e)^{2/3}}{2m_{vc}^*} \tag{5.14}$$

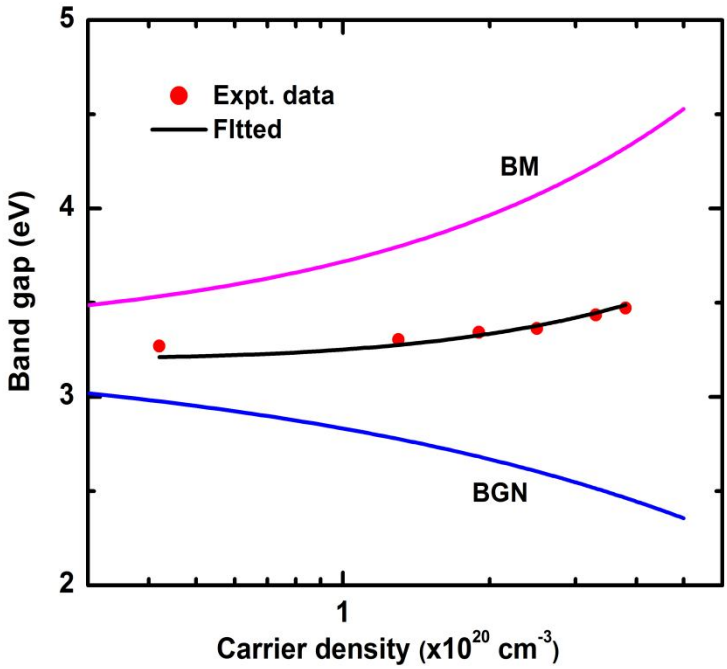

Fig. 5.29 Variation of optical band-gap of (Zn, Ti) O_x thin films with electron density. The solid black line shows theoretical fitting considering the combined effects of BM and BGN as given by Eq. 5.16.

Therefore according to BM effect the optical band-gap of a degenerate semiconductor is given by

$$E = E_g^0 + \Delta E_g(BM) \tag{5.15}$$

However, as can be seen form Fig. 5.29, measured band-gap values were significantly lower compared to that predicted by BM shift [193]. This could be due to the effect of band-gap narrowing (BGN) [193-195]. As the electron concentration is well above the Mott's critical value of ZnO ($n_c \sim 1x10^{19}$ cm^{-3}), the modification of electronic states begins to appear in the crystal because of the correlated motion of conduction electrons and their scattering against ionized impurities [193-195]. Thus, the effect of band-gap renormalization due to many-body interactions leads to band-gap narrowing as schematically shown in Fig. 5.28 (c) [193-195]. This negative effect of BGN is competitive with the positive BM shift. Therefore, we have

fitted the data in Fig. 5.29 by considering the combined effects of BM shift and BGN effect by using the following equation [193-195],

$$E = E_g^0 + \Delta E_g(BM) + \Delta E_g(BGN)$$

$$E = E_{go} + \Delta E_g^{BM} - 1.83\frac{\Lambda}{N_b^{1/3}}\frac{R}{r_s} - \frac{0.95R}{r_s^{3/4}} - \left(1 + \frac{m_{\min}}{m_{maj}}\right)\frac{1.57R}{N_b r_s^{3/2}} \quad (5.16)$$

Here Λ is the correction factor due to anisotropy in the conduction band. It is usually in the range from 0.75 to 1. In our case the effect of band anisotropy was ignored by assuming Λ =1 in accordance with the available literatures. N_b is the number of equivalent valleys in the conduction band for n-type semiconductors and its value can be taken to be 1. $R = \frac{13.6 m_r}{\varepsilon_r^2}$ eV where m_r =0.28 and ε_r =8.65. The value of r_s is calculated by using $r_s = \frac{r_a}{a_B^*}$ where $r_a = \left(\frac{3}{4\pi N_e}\right)^{1/3}$ and the effective Bohr radius a_B^* is given by $a_B^* = \left(\frac{0.53\varepsilon_r}{m_r}\right) X 10^{-8}$ cm. $m_{\min}$ and m_{maj} are the minority and majority carrier effective masses respectively. Experimental data in Fig. 5.29 was found to be in good agreement with Eq. 5.16.

(II) Photoluminescence Spectroscopy Measurements

Fig. 5.30 shows the room temperature (RT) photoluminescence (PL) spectra for all the degenerately n-type doped (Zn, Ti)O_x thin films with Ti concentration varying from ~ 0-10.4 at.%. Earlier PL measurements have been carried out on various degenerately doped semiconductors [196-204]. The intrinsic ZnO film and the samples in zone-I i.e., S1-S5 showed near band edge (NBE) PL in UV spectral range. However, the UV PL intensity was found to be significantly deteriorated for the film S5 at ~ 0.78 at% and completely diminished beyond it i.e., for the films grown in zone-II. This is plausibly due to the poor crystalline quality and increased non radiative decay centres (deep level luminescence killers) in the

films. Similar observations have also been reported by Makino *et al.* in heavily Ga doped ZnO thin films [196]. As can be seen from the inset of Fig. 5.30, the NBE peak position is monotonically shifted to the higher energy with increasing electron concentration. This is plausibly attributed to the combinatorial effect of compressive lattice strain and Burstein-Moss band filling effects [198, 204]. However, a maximum band gap shift of ~ 8 meV was calculated due to residual strain in the films [3]. The variation of FWHM of NBE emission with electron concentration, shown in the inset of Fig. 5.30, could not be explained by considering the equation

$$\Delta E_{FWHM} = \frac{2e^2}{3\pi\varepsilon}\sqrt{(N_D + N_A)\frac{\pi r_s}{3}}\exp(-3/4)2\sqrt{2\ln 2} \qquad (5.17)$$

in which only the effect of dopant induced potential fluctuations is considered [197]. In Eq. 5.17 ε is the dielectric constant, N_D and N_A are the donor and acceptor concentrations respectively and r_s is the Debye or Thomas-Fermi screening radius [197]. The failurity of Eq. 5.17 in explaining the FWHM vs N_e curve is plausibly due to the heavily degenerate nature of the (Zn, Ti)O_x thin films which had an estimated N_e higher than Mott's limit in ZnO [195].

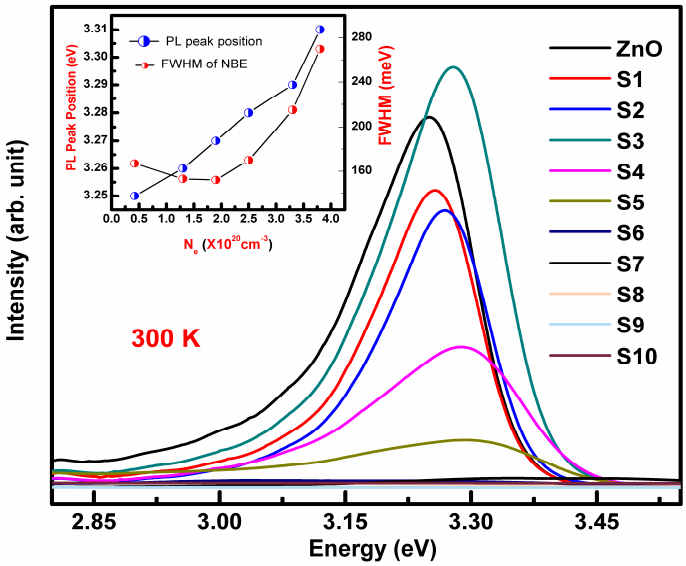

Fig. 5.30 PL spectra of (Zn, Ti)O_x films with different Ti concentrations. The inset shows variation of NBE PL peak position and FWHM as a function of carrier concentration.

The room temperature optical absorption spectra of the films along with their PL spectra are shown in Fig. 5.31. As can be seen for all the films PL is red shifted with respect to its absorption edge as marked by the vertical arrow in Fig. 5.31. This is because optical absorption take place only at K_F^C, the Fermi wave vector, since all the CB states are filled up to that point. However, most luminescence will occur below K_F^C, because as the excited holes percolate from K= K_F^V up to K = 0, they can recombine at any point along the way, since the states directly above them (in K space) are always filled with electrons. Therefore, in degenerate materials such as Ti-doped ZnO, PL is always red shifted with respect to its absorption onset.

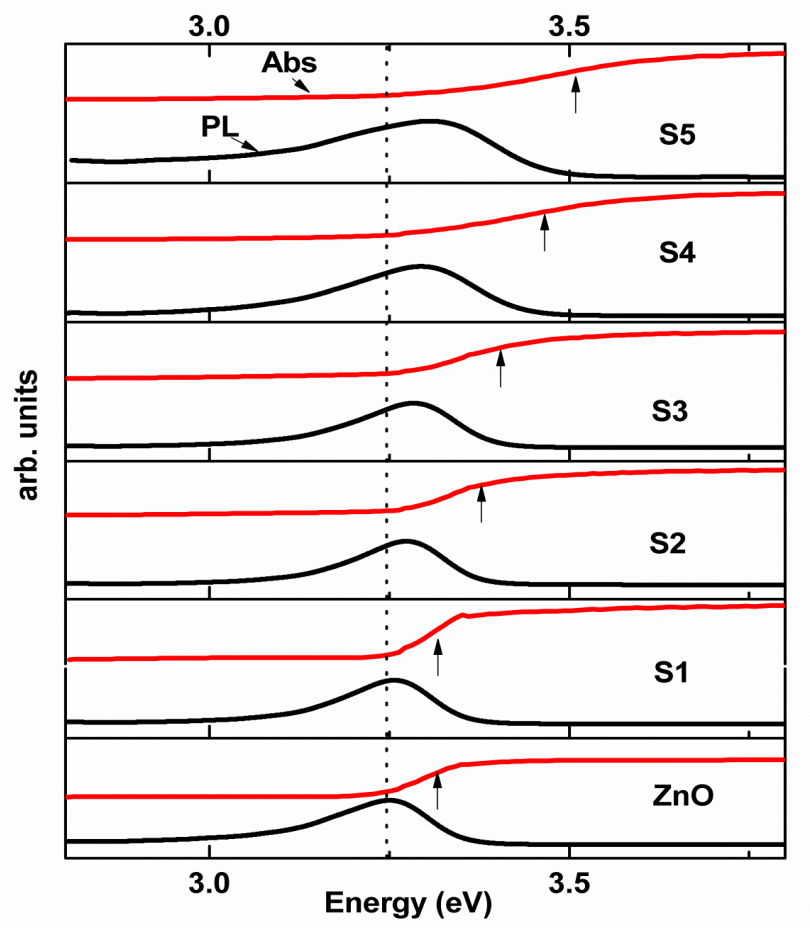

Fig. 5.31 Room temperature PL and absorption spectra for all the (Zn, Ti)O_x thin films.

Fig. 5.32 shows variation of Stokes shift with doping concentration. As can be seen, Stokes shift increases very rapidly with increasing doping concentration above 0.2 at.%. This could be attributed to the increased localization of the photo generated carriers due to the enhanced potential fluctuations [195].

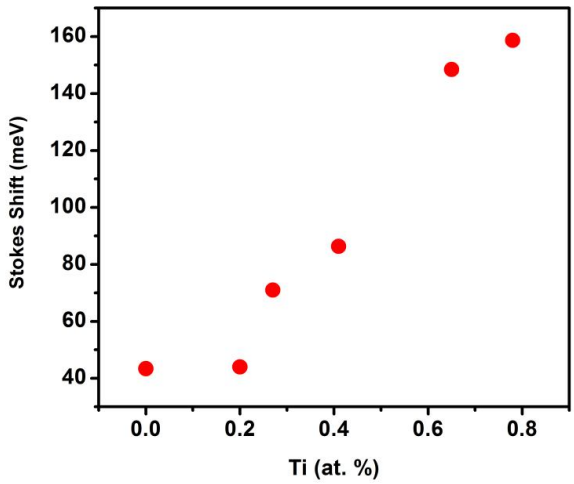

Fig. 5.32 Variation of Stokes shift with Ti concentration in (Zn, Ti)O_x thin films.

In order to further investigate the effect of free carrier density and dopant induced static-disorder in the PL spectra; we have carried out temperature dependent PL measurements in the range of ~ 5 to 300 K as shown in Fig. 5.32. At low temperatures, all the films showed typical line shape of a degenerate semiconductor: the high-energy edge is given by the sharp cut off of the Fermi occupation function and the low-energy edge of the spectrum is determined by the combined density of states washed out by the conduction band tail arising due to heavy doping induced disorder in the films [198]. In doped semiconductors, the Coulomb interaction between electron-hole pairs in an exciton is screened by the free carriers and dissociation of excitons occur when electron concentration reaches Mott's critical limit [199]. This phenomenon is usually referred to as the excitonic Mott transition [199, 200]. In the present case, all the films had an estimated electron density higher than the Mott's critical

limit of ZnO. However, surprisingly enough, the films (0-0.4 at%) exhibited distinct NBE peak due to free exciton (F_x) recombinations at lower temperatures (at and below 100 K). The peak position decreases monotonically with increasing temperature. Such variation of peak position with T (K) can be well explained by considering Varshini's empirical relation given by

$$E_g(T) = E_g(0) - \frac{aT^2}{(T + \Theta_D)} \tag{5.18}$$

where $E_g(0)$ is the peak position at T=0K, a is fitting parameter and Θ_D is the Debye temperature of ZnO which is about 920 K.

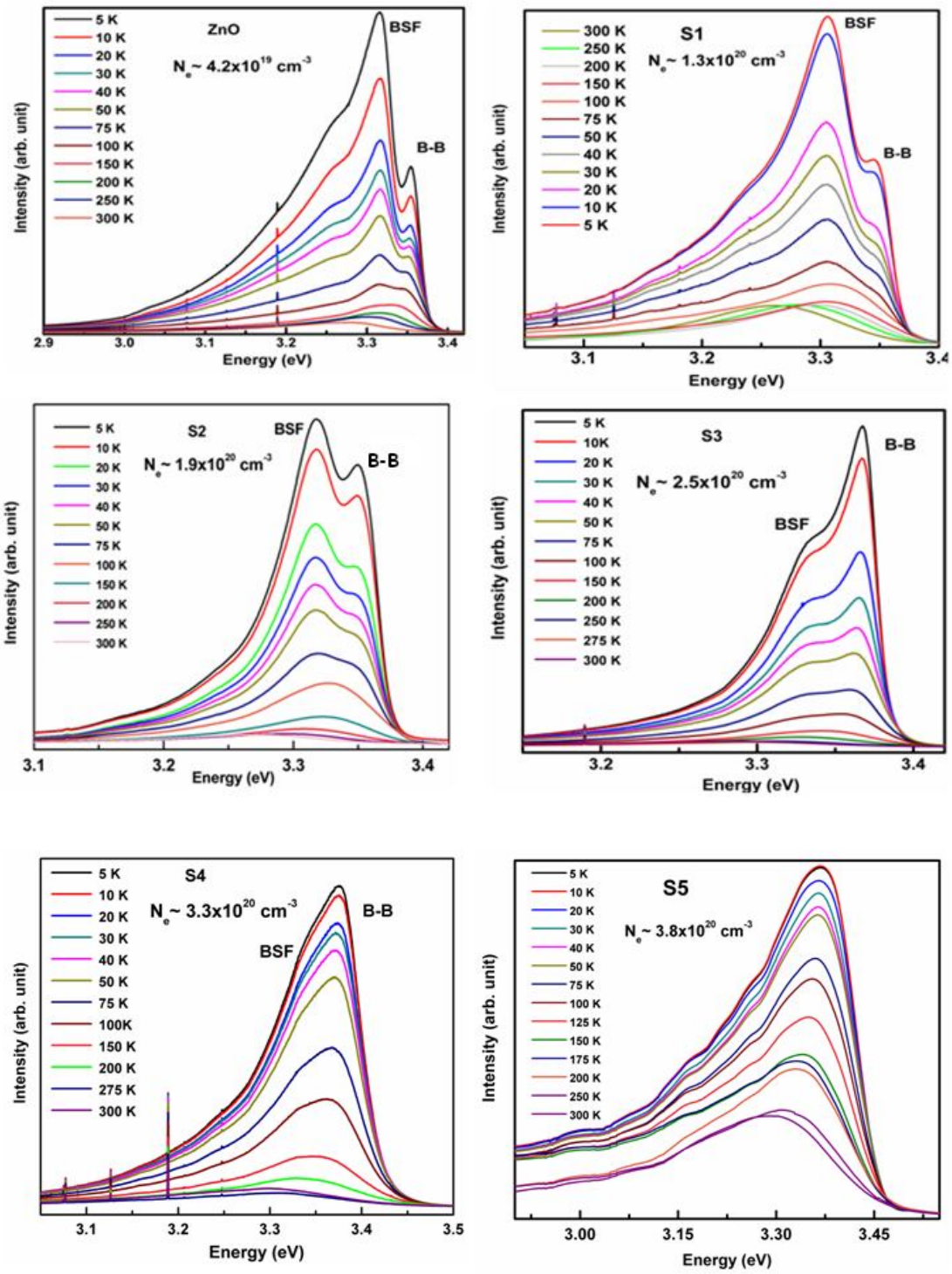

Fig. 5.33 Temperature dependent (5-300 K) PL spectra for (Zn, Ti)O_x thin films with Ti concentration in the range of 0-0.78 at.%.

In addition to F_x two other well-resolved peaks corresponding to electron-acceptor (e-A^0) recombination (at ~ 3.31 eV) and 1-LO phonon replica of F_x were also observed [201]. In literature the PL peak at ~ 3.31 eV has also been assigned to the donor acceptor pair transition (DAP) [46, 47]. In order to exclude the origin of DAP transition in the present case, we have carried out intensity dependent PL measurement for all the films at 5 K in which the PL peak at ~3.31 eV did not show any shift (see Fig. 5.33). This is in contrary to the DAP transition which shows a blue shift with increasing incident laser beam intensity [201].

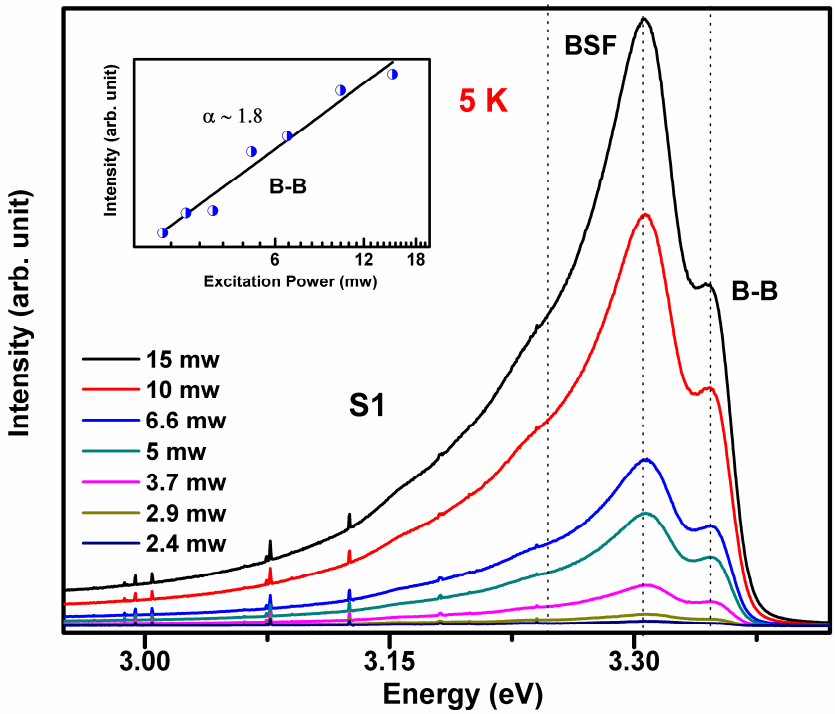

Fig. 5.34 The power dependent PL spectra for S1 at 5 K. The upper inset shows emission intensity versus the excitation power for the B-B emission.

In the literature, the appearance of ZnO PL peak at ~ 3.31 eV is much debated and has also been assigned to the basal plane stacking faults (BSFs) related microstructural defects [202, 203]. Yang *et al.* has observed high density (~ $1x10^6$ cm^{-1}) of BSFs in ALD grown ZnO films on c-plane sapphire substrates [203]. They have attributed the PL peak at ~ 3.31 eV to the

recombination of the confined indirect excitons in type-II quantum well BSFs [203]. Schirra *et al.* have carried out a detailed investigation on the electronic nature and structural origin of the omnipresent PL peak at ~ 3.31 eV for epitaxial ZnO layers [202]. They concluded that the PL peak at ~ 3.31 eV plausibly arises due to the free-to-bound (e, A^0) transition of electrons from the conduction band to the acceptor like defects located in the BSFs [202]. As can be seen from the inset of Fig. 5.33, the plot of PL intensities for both the NBE and (e, A^0) emission at 5 K with excitation power show a power law dependence: $I \propto P^{\alpha}$ with $\alpha = 1.8$ and 1.9, respectively. For free or bound excitonic emissions, the value of the exponent 'α' lies in the range of $1 \leq \alpha \leq 2$ [203]. On the contrary, for DAP emission, α should be less than 1 [203]. Therefore, the absence of PL peak shift and excitation power dependence of the PL peak at ~ 3.31 eV, clearly eliminates the origin of DAP transition. In literature, the observation of free excitonic absorption and photoluminescence were reported in ZnO, GaN and InN thin films above the Mott's critical limit [198, 199 and 204]. In these heavily degenerate semiconductors, photo excited electron-hole pairs which interacts with the Fermi sea in the conduction band, still forms a bound state, the so-called Mahan exciton [200]. Therefore, the observed excitonic emission could be due to the formation of Mahan excitons in these films [200]. However, the spectral features were broadened and merged together for the film with Ti concentration of ~ 0.65 at% having carrier density ~ 3.3×10^{20} cm^{-3}. With further increment in electron density, i.e. ~ 3.8×10^{20} cm^{-3} for the film S5 with ~ 0.78 at% of Ti, only momentum non conserving band-to-band transitions prevailed. Therefore, excitonic Mott transition occurs at much higher electron density which lies deep into the metallic side of MIT. Similar results have also been obtained by Feneberg *et al.* in n-type doped GaN thin films [196]. A more detail investigation of the PL characteristics and their correlation with the microstructural defects in heavily degenerate (Zn, Ti)O_x films is underway.

5.9 Conclusions

Therefore, we have studied temperature dependent electron transport in (Zn, Ti)O_x thin films by measuring their temperature dependent (5-300K) electrical resistivity and magnetoresistance. Electron transport in these films was found to be intricately dependent on the interplay of screening and strength of static-disorder. The evolution of electron transport with film thickness was also studied which showed dimensional crossover of weak localization from 2D to 3D regime with increasing temperature. Finally, a correlation has been established between the electrical and optical properties of the films by measuring their optical transmittance and temperature dependent photoluminescence spectra.

Chapter 6: Conclusions and Scope for Future Work

The main motivation of the present research work is to grow highly conducting intrinsically and/or extrinsically n-type doped ZnO thin films which are suitable for transparent conducting electrode applications and to investigate the underlying electron transport mechanisms in these films. For this purpose, we have successfully grown heavily degenerate intrinsic ZnO and its multi-component oxide thin films such as (Zn, Al)O_x and (Zn, Ti)O_x on (0001) Sapphire substrates using a flow-type thermal ALD reactor (Beneq TFS 200). Our main achievements and scope for future work are summarized below.

First, we have studied the effect of various process parameters on the electrical, structural and optical properties of intrinsic ZnO thin films. The 'ALD window' for the self-limiting growth of ZnO was achieved in the temperature range of ~ 140-200^{0}C with a constant growth rate of ~0.2 nm per cycle. The optimum optical and crystalline quality ZnO films with lowest value of room temperature electrical resistivity ~ 3.6x10^{-3} Ω cm was achieved at ~ 200^{0}C. X-ray diffraction and photoluminescence spectra showed that crystalline and compositional native defects were strongly dependent on the substrate temperature. The effect of disorder on the underlying electron transport mechanisms were investigated by temperature dependent electrical resistivity measurements. The films grown at ~ 150, 300 and 350^{0}C showed only semiconductor-like ($d\rho/dT<0$) resistivity behaviour in the entire range of the measurement temperature due to strengthened disorder in these films. However, a transition from metal-like ($d\rho/dT>0$) to semiconductor-like ($d\rho/dT<0$) transport behaviour giving rise to a resistivity minimum at lower temperature was observed for the films grown at ~ 200 and 250^{0}C plausibly due to reduced defects and improved crystalline quality of the films. The observed resistivity up turn below the transition temperature could be well explained by considering quantum corrections to the Boltzmann conductivity which includes the effect of disorder induced weak localization and coulomb electron-electron interactions.

In order to enhance the electrical conductivity of intrinsic ZnO films, we have used Al as an n-type dopant in ZnO. However, realizing higher doping-efficiency in ALD grown films is a difficult task due to its self-limiting and layer-by-layer growth methodology. We have alleviated this problem by using in-situ sub-saturating dopant exposure on the growing film surface. (Zn, Al)O_x thin films were grown with Al concentration in the range of ~ 1.6-12.4 at.%. Minimum electrical resistivity of ~ $0.86 \times 10^{-3} \Omega$ cm with comparatively good Hall mobility ~ 18 cm^2/Vs was achieved for Al concentration of ~ 2.2 at.%. Temperature dependent electrical resistivity and magnetoresistance measurements showed disorder induced quantum-interference phenomena which resulted in phase-coherent electron transport in these films up to 200 K. With increasing Al concentration, a crossover from good metallic to incipient non-metallic resistivity behaviour was observed at ~ 5.5 at.% of Al. The film with the highest static disorder ($K_F l_e$~0.6) showed enhanced electron-electron interactions due to reduced screening effect. It was observed that instead of periodic incorporation of insulating AlO_x sub-monolayer into the conducting ZnO matrix, the electron transport in these films was effectively three-dimensional. The temperature dependence of phase-coherence length ($l_\varphi \propto T^{-3/4}$) as extracted from the magnetoresistance measurements, indicated inelastic electron-electron scattering as the dominant dephasing mechanism in these films.

Later we have studied the possibility of obtaining heavily degenerate ZnO thin films using Ti as an n-type dopant. In our preceding work on (Zn, Al)O_x thin films, the degree of static-disorder in these multi-component oxides could not be tuned systematically due to the low vapor pressure of $AlCl_3$ precursor which was pulsed into the reactor using carrier gas assisted booster option. On the contrary, metal halide $TiCl_4$ exhibits higher vapor pressure and therefore, could be easily pulsed into the reactor to tune the degree of disorder in (Zn, Ti)O_x films. The strength of static-disorder as measured by the dimensionless parameter $K_F l_e$ was tuned in a wide range from good metallic ($K_F l_e$ ~ 4.2) to the incipient non-metallic ($K_F l_e$ ~

0.2) regime with controlled incorporation of Ti. Heavily degenerate (Zn, Ti)O_x thin films were grown by periodic in-situ incorporation of sub-monolayer TiO_x i.e., through sub-saturating exposure of $TiCl_4$ precursor on the growing ZnO film surface. We have achieved enhanced doping-efficiency as high as ~ 130% and minimum resistivity of ~ $1x10^{-3}\Omega$ cm by following this over-simple approach of dopant incorporation. Analysis of the temperature dependent electron transport data for the films with homogeneous and inhomogeneous dopant profiles revealed that formation of spatially dispersed and homogeneous dopant profile is not the adequate criterion to improve the doping-efficiency. The combined effects of degree of static-disorder as induced by the dopants and screening of the potential fluctuations plays a crucial role in controlling the electrical properties. The observation of three dimensional electron transport in (Zn, Ti)O_x films with spatially localized dopant profiles revealed that dopant atoms are not mirror-imaged by the conduction electrons.

We have also studied the evolution of sheet resistance versus temperature curve with (Zn, Ti)O_x film thickness. We have varied film thickness by stacking different numbers (n=1-7) of ZnO/TiO_x layers on (0001) sapphire substrates. R_{Ti} (%) was kept fixed at ~ 2 with which we obtained maximum electron density in our earlier work. Metal to insulator transition was observed at a film thickness of 12 nm (n=2). It was observed that above a critical thickness of 2 stacking layers (n=2), incorporated Ti atoms starts acting as efficient electron donors in ZnO. Below this critical thickness, resistivity of the film S1 (n=1) was too high to be measured, plausibly due to the formation of an electrically insulating ‘dead layer’. Exposure of atmospheric O_2 did not show any effect on the electrical properties of S1. On the contrary, the film S2 with the critical thickness of 2 stacking layers (n=2) showed highly air sensitive electrical resistivity. It exhibited UV light induced insulator-metal transition which is plausibly induced by the de-trapping of conduction electrons from the surface and grain boundary defect sites. The films with n≥2 showed quite stable electrical properties in air

exposure. A clear signature of dimensional crossover (2D→3D) of weak localization was observed for all these films (S3-S7) through a combined study of temperature dependent zero filed sheet resistance and magnetoresistance measurements. However, crossover temperature was found to be reduced with increasing film thickness. The insignificant role of inter sub-monolayer scattering as an additional channel for electron dephasing implied that, despite spatially localized dopant-profiles, ZnO/TiO_x stacked layers can be considered as homogeneously disordered electronic systems as far as WL is concerned.

Later we have carried out room temperature optical transmission and temperature dependent (5-300 K) photoluminescence measurements on all the (Zn, Ti)O_x films. The optical properties of these films were found to be highly correlated with their electrical properties. The optical absorption and photoluminescence spectra of these films were found to be strongly dependent on free electron concentration and dopant induced disorder incorporation. The increase in optical band-gap with increasing electron density up to ~ 0.78 at% of Ti was found to be in good agreement with the combined effects of Burstein-Moss band filling and many body interactions induced band-gap narrowing. Surprisingly enough, the films (0-0.4 at% of Ti) with net electron density above the excitonic Mott transition, exhibited distinct free excitonic recombination at lower temperatures.

Though we have carried out detailed study on the electron transport in degenerately n-type doped ZnO thin films, there are enough scope for future work pertinent to this research field.

First of all, we have not given much effort to control the unintentional background n-type conductivity in as grown ZnO films. Such high level of electron density is indeed very useful for some particular applications, such as TCEs in optoelectronic devices. However, it is highly desirable to obtain better control over the n-type conductivity to realize stable and reproducible p-type doping for the successful fabrication of ZnO based light-emitting diodes and laser diodes in particular. In the present case, we observed a sharp transition in electrical

conductivity of intrinsic ZnO thin films from highly conducting to the highly resistive state at deposition temperature of ~ 150^0C. The highly resistive nature plausibly arises due to the presence of hydroxyl groups and/or oxygen interstitials due to incomplete chemical reactions between the surface hydroxyl groups and the Zn precursor molecules. Therefore, there is a possibility to obtain lower n-type conductivity in as grown ZnO films by choosing a very narrow temperature window around 150^0C and optimization of all the relevant process parameters, specially purging time after the water pulse in a very systematic way. Plasma enhanced ALD (PEALD) or ozone based ALD would be a better option in this case. Because of the high reactivity of the plasma species, PEALD grown films were found to have higher compositional stoichiometry compared to that grown in a thermal ALD reactor at lower temperatures. Moreover, in PEALD, the use of oxygen plasma as a co-reactant eliminates hydroxyl groups related issues on the electrical properties.

Growth of resistive ZnO thin films with reduced n-type intrinsic defects and without any self compensation effect is required to achieve highly confined two-dimensional electron gas (2DEG) through δ-doping scheme. Moreover, vertically stacked multiple 2DEG systems can be fabricated by following almost the same growth methodology as we have adopted to grow (Zn, Al)O_x and (Zn, Ti)O_x thin films. Optimized growth of such structures will be highly useful to investigate various electron transport phenomena in quantum confined regime.

ALD grown ZnO films are generally found to be in polycrystalline or in amorphous form. Growth of high quality epitaxial layers of ZnO thin films using ALD has not been reported yet. In literature, it is found that basal plane stacking faults are the majority structural defects in ALD grown c-ZnO films on sapphire substrates. Therefore, homo epitaxial growth of ZnO thin films using single crystal ZnO substrates could be an excellent research problem to alleviate these issues.

References

1. D.C. Look, Materials Science and Engineering: B 80, 381 (2001).

2. D. C. Reynolds, D. C. Look, B. Jogai, C. W. Litton, G. Cantwell, and W. C. Harsch, Physical Review B: Condensed Matter 60, 2340 (1999).

3. Ü. Özgür, Ya. I. Alivov, C. Liu, A. Teke, M. A. Reshchikov, S. Doğan, V. Avrutin, S.J. Cho and H. Morkoç, J. Appl. Phys. 98, 041301 (2005).

4. Ümit Özgür, Daniel Hofstetter, and Hadis Morkoc, Proceedings of the IEEE 98, 7, 1255-1268 (2010).

5. Anderson Janotti and Chris G Van de Walle, Rep. Prog. Phys. 72, 126501(2009).

6. C. Jagadish and S. J. Pearton, Zinc Oxide Bulk, Thin Films, and Nanostructures (New York: Elsevier, 2006)

7. Hadis Morkoç and Ümit Özgür, Zinc OxideFundamentals, Materials and Device Technology (Wiley-VCH Verlag GmbH and Co. KGaA, 2007).

8. S. Nakamura and S. F. Chichibu, Nitride Semiconductor Blue Lasers and Light Emitting Diodes (Boca Raton, FL: CRC Press, 2000).

9. A. Janotti and C. G. Van de Walle, Phys. Rev. B 76, 165202 (2007).

10. D. C. Look, D. C. Reynolds, C. W. Litton, R. L. Jones, D. B. Eason and G. Cantwell, Appl. Phys. Lett. 81, 1830 (2002).

11. T. Aoki, Y. Hatanaka and D. C. Look, Appl. Phys. Lett.76, 3257 (2000).

12. K. K. Kim, H. S. Kim, D. K. Hwang, J. H. Lim and S. J. Park, Appl. Phys. Lett. 83, 63 (2003).

13. F. Oba, A. Togo, I. Tanaka, J. Paier and G. Kresse, Phys. Rev. B 77, 245202 (2008).

14. A. R. Hutson, Phys. Rev. 108, 222 (1957).

15. F. Tuomisto, K. Saarinen, D. C. Look and G. C. Farlow, Phys. Rev.B 72, 085206 (2005).

16. F. Tuomisto, V. Ranki, K. Saarinen and D. C. Look, Phys. Rev. Lett.91, 205502 (2003).

17. C. G. Van de Walle, Phys. Rev. Lett.85, 1012 (2000).

18. J. Hu and R. G. Gordon, J. Appl. Phys. 71, 880 (1992).

19. H. J. Ko, Y. F. Chen, S. K. Hong, H. Wenisch, T. Yao and D. C. Look, Appl. Phys. Lett. 77, 3761 (2000).

20. J. Hu and R. G. Gordon, J. Appl. Phys. 72, 5381 (1992).

21. J. Hu and R. G. Gordon, Mater. Res. Soc. Symp. Proc. 283, 891 (1993).

22. A. Valentini, F. Quaranta, M. Rossi, and G. Battaglin, J. Vac. Sci. Technol.A 9, 286 (1991).

23. A. Kobayashi, O. F. Sankey, and J. D. Dow, Phys. Rev. B 28, 946 (1983).

24. A. B. M. A. Ashrafi, I. Suemune, H. Kumano, and S. Tanaka, Jpn. J. Appl. Phys., Part 2 41, L1281 (2002).

25. T. Aoki, Y. Hatanaka, and D. C. Look, Appl. Phys. Lett. 76, 3257 (2000).

26. Y. R. Ryu, S. Zhu, D. C. Look, J. M. Wrobel, H. M. Jeong, and H. W. White, J. Cryst. Growth 216, 330 (2000).

27. C. H. Park, S. B. Zhang, and S. H. Wei, Phys. Rev. B 66, 073202 (2002).

28. D. C. Look, R. L. Jones, J. R. Sizelove, N. Y. Garces, N. C. Giles, and L.E. Halliburton, Phys. Status Solidi A 195, 171 (2004).

29. D. Vogel, P. Kruger, J. Pollmann, Phys. Rev. B 52, R14316 (1995).

30. D. W. Langer and C. J. Vesely, Phys. Rev. B 2, 4885 (1970).

31. R. A. Powell, W. E. Spicer, and J. C. McMenamin, Phys. Rev. B 6, 3056 (1972).

32. L. Ley, R. A. Pollak, F. R. McFeely, S. P. Kowalezyk, and D. A. Shirley, Phys. Rev. B 9, 600 (1974).

33. W. Y. Liang and A. D. Yoffe, Phys. Rev. Lett. 20, 59 (1968).

34. V. Srikant and D. R. Clark, J. Appl. Phys. 81, 6357 (1997).

35. T. Makino, T. Yasuda, Y. Segawa, A. Ohtomo, K. Tamura, M. Kawasaki and H.

Koinuma , Appl. Phys. Lett. 79, 1282 (2001).

36. H. C. Ong, A. X. E. Zhu and G. T. Du, Appl. Phys. Lett. 80, 942 (2002).

37. S. Barik, A. K. Srivastava, P. Misra, R.V. Nandedkar and L. M. Kukreja, Solid State Commun.127, 463 (2003).

38. P. Misra, T. K. Sharma, S. Porwal and L. M. Kukreja, Appl. Phys.Lett. 89, 161912: 1 - 3 (2006).

39. K. Vanheusden, C. H. Seager, W. L. Warren, D. R. Tallant, and J. A.Voigt, Appl. Phys. Lett. 68, 403 (1996).

40. K. Vanheusden, W. L. Warren,C. H. Seager, D. R. Tallant, J. A. Voigt, and B. E. Gnade, J. Appl. Phys.79, 7983 (1996).

41. C. Klingshirn, Semiconductor Optics, (3rd ed., Springer, Heidelberg 2006).

42. J. I. Pankove, Optical processes in semiconductors, (Dover Publications. New York 1971).

43. D. C. Reynolds, D. C. Look, B. Jogai, C. W. Litton, T. C. Collins, W. Harsch and G. Cantwell, Phys. Rev. B 57, 12151 (1998).

44. K. Thonke, T. Gruber, N. Teofilov, R. Schönfelder, A. Waag, and R. Sauer, Physica B 308–310, 945 (2001).

45. C. Klingshirn, Chem. Phys. Chem. 8, 782, (2007).

46. Z. Yang and J. L. Liu, J. Vac. Sci. Technol. B 28 (3), C3D6 (2010).

47. Z. Yang,D. C. Look,and J. L. Liu, App. Phys. Lett. 94, 072101 (2009).

48. K. Thonke, T. Gruber, N. Teofilov, R. Schönfelder, A. Waag, and R. Sauer, Physica B 308–310, 945 (2001).

49. A. F. Kohan, G. Ceder, D. Morgan, and C. G. Van de Walle, Phys. Rev. B 61, 15019 (2000).

50. S. A. Studenikin and M. Cocivera, J. Appl. Phys. 91, 5060 (2002).

51. M. Liu, A. H. Kitai and P. Mascher, J. Lumin. 54, 35 (1992).

52. Z. W. Liu and C. K. Ong, Appl. Phys. Lett. 88, 053110(2006).

53. Hideo Hosono and David C. Paine, Handbook of Transparent Conductors (Springer Science + Business Media, LLC 2010).

54. V. Bhosle, A. Tiwari, and J. Narayan, J. Appl. Phys. 100, 033713 (2006).

55. Amit K. Das, P. Misra, R. S. Ajimsha, A. Bose, S. C. Joshi, D. M. Phase, and L. M. Kukreja, J. Appl. Phys. 112, 103706 (2012).

56.Tadatsugu Minami, *Semicond. Sci. Technol.*20, S35 (2005).

57. O. Nakagawara, Y. Kishimoto, H. Seto, Y. Koshido and T. Makino, Appl. Phys. Lett. 89, 91904 (2006).

58. Parag Banerjee, Won-Jae Lee, Ki-Ryeol Bae, Sang Bok Lee, andGary W. Rubloff, J. App. Phys. 108, 043504 (2010).

59. D. H. Zhang, H. L. Ma, App. Phys. A 62, 487 (1996).

60. H. Y. Liu, V. Avrutin, N. Izyumskaya, U. Ozgur, A. B. Yankovich, A. V. Kvit, p. M. Voyles and H. Morkoc, J. App.Phys. 111, 103713 (2012).

61. Klaus Ellmer, Rainald Mientus, Thin Solid Films 516, 4620 (2008).

62.K Ellmer, J. Phys. D:Appl. Phys. 34, 3097 (2001).

63.K. Ellmer, Nature Photonics 6, 809 (2012).

64.J. G. Lu, Z. Z. Ye, Y. J. Zeng, L. P. Zhu, L. Wang, J. Yuan, B. H. Zhao, and Q. L. Liang, J. App. Phys. 100, 073714 (2006).

65. Klaus Ellmer, Gotz Vollweiler, Thin Solid films 496, 104 (2006).

66. J. Steinhauser, S. Fay, N. Oliveira, e. Vallat-Sauvain, and C. Ballif, App. Phys. Lett.90, 1 (2007).

67. J. Y. Seto, J. App. Phys. 46, 5247 (1975).

68. C. Y. Wu, W. B. Jian, and J. J. Lin, Phys. Rev. B 57, 11232 (1998).

69. J. J. Lin, tsang-Jou Li, and T. M. Wu, Phys Rev. B 61, 3170 (2000).

70. K. Makise, M. Funaki, b. Shinozaki, K. Yano, Y.Shimane, K. Inoue and H. Nakamura, Thin Solid Films 516, 5805 (2008).

71. V. F. Gantmakher, Electrons and Disorder in solids (Clarendon Press, Oxford, 2005).

72. P. A. Lee and T. V. Ramakrishnan, Rev. Mod. Phys. 57, 287 (1985).

73. N. F. Mott, Conduction in Non-Crystalline Materials (Clarendon Press, Oxford, 1993).

74.E. F. Schubert, Doping in III-V Semiconductors (Cambridge University Press, 1993).

75. Peter Phillip Edwards and Michell J.Sienko, Phys. Rev. B 17, 2575 (1978).

76. Peihua Dai, Youzhu Zhang, and M. P. Sarachik, Phys. Rev. B 45, 3984 (1992).

77. G. A. Thomas, A. Kawabata, Y. Ootuka, S. Katsumoto, S. Kobayashi, and W. Sasaki, Phys. Rev. B26, 2113 (1982).

78. T. F. Rosenbaum, R. F. Milligan, M. A. Paalanen, G. A. Thomas, and R. N. Bhatt and W. Lin, Phys. Rev. B 27, 7509 (1983).

79. C. Leighton and I. Terry and P. Becla, Phys. Rev. B, 58 9773, (1998).

80. E. Abrahams, P. W. Anderson, D. C. Licciardello, and T. V. Ramakrishnan. Phys. Rev. Lett. 42, 673 (1979).

81.P. W. Anderson, Phys. Rev. 109, 1492 (1958).

82.T. Siegrist, P. Jost, H. Volker, M. Woda, P. Merkelbach, C. Schlockermann and M. Wuttig, Nature Mater. 10, 201 (2011).

83. R. C. Dynes and P. A. Lee, Science 223, 355 (1984).

84. G. Herranz, F. Sanchez, B. Martinez, J. Fontcuberta, m. V. Garcia-cuenca, c. Ferrater, M.Varela, and P. Levy, The European Phys. J. B 40, 49 (2004).

85. G. Herranz, B. Martinez, J. Fontcuberta, F. Sanchez, C. Ferrater, M. V. Garcia-cuenca, and M.Varela, Phys. Rev. B 67, 174423 (2003).

86. B. L. Altshuler and A. G. Aronov, Solid State Commun. 30, 115 (1979).

87. J. J. Linand J P Bird, J. Phys.: Condens. Matter.14, R501 (2002).

88. R. L. Puurunen, J. App. Phys. 97, 121301 (2005).

89. S. M. George, Chem. Rev. 110, 111 (2010).

90. V. Miikkulainen,M. Leskel,M. Ritala,and R. L. Puurunen, J. App. Phys. 113, 021301 (2013).

91. W.M.M. (Erwin) Kessels and Matti Putkonen, MRS BULLETIN 36, 907 (2011).

92. M. Godlewski, E. Guziewicz, G. Łuka, T. Krajewski, M. Łukasiewicz, Ł. Wachnicki, A. Wachnicka, K. Kopalko, A. Sarem, B. Dalati, Thin Solid Films 518, 1145 (2009).

93. E. Guziewicz, M. Godlewski, T. Krajewski, Ł.Wachnicki, A. Szczepanik,K. Kopalko, A.Wójcik-Głodowska, E. Przeździecka, W. Paszkowicz, E. Łusakowska, P. Kruszewski, N. Huby, G. Tallarida, and S. Ferrari, J. Appl. Phys. 105, 122413 (2009).

94. N. Huby, S. Ferrari, E. Guziewicz, M. Godlewski and V. Osinniy, Appl. Phys. Lett. 92, 023502 (2008).

95. D. Saha, V. K. Sahu, Amit K. Das, R. S. Ajimsha, P. Misra, L. M. Kukreja,Phys. Express (2013) 3:9.

96. D. Saha,Amit. K. Das, R. S. Ajimsha, P. Misra, and L. M. Kukreja, J. App. Phys. 114, 043703 (2013).

97. E Przezdziecka, Ł Wachnicki, W Paszkowicz, E Łusakowska, T Krajewski, G Łuka, E Guziewicz and M Godlewski, Semicond. Sci. Technol. 24, 105014 (2009).

98. Swee-Yong Pung, Kwang-Leong Choy, Xianghui Hou and Chongxin Shan, Nanotechnology 19, 435609 (2008).

99. A. Wojick, M. Godlewski, E. Guziewicz, R. Minikayev, W. Paszkowicz, J. Cryst. Growth.310, 284 (2008).

100. M. Tammenmaa, T. Koskinen, L. Hiltunen and L. Niinist, Thin Solid Films 124, 125(1985).

101. Jari Malm, Elina Sahramo, Juho Perälä, Timo Sajavaara, Maarit Karppinen, Thin Solid Films 519, 5319(2011).

102. Jukka T. Tanskanen, Jonathan R. Bakke, Tapani A. Pakkanen and Stacey F. Bent, J. Vac. Sci. Technol.A 29, 031507-1 (2011).

103. K. Kopalko, A. W´ojcik, M. Godlewski, E. Łusakowska, W. Paszkowicz, J. Z. Domagała, M. M. Godlewski, A. Szczerbakow, K. ´Swiatek and K. Dybko, Phys.Status Solidi 2, 1125 (2005).

104. E. B. Yousfi, J. Fouache and D. Lincot, Appl. Surf. Sci. 153, 223 (2000).

105. J. Lim and C. Lee, Thin Solid Films 515, 3335 (2007).

106. E. Guziewicz, I. A. Kowalik, M. Godlewski, K. Kopalko, V. Osinniy, A. W´ojcik, S. Yatsunenko, E. Łusakowska, W. Paszkowicz and M. Guziewicz, J. Appl. Phys. 103, 033515 (2008).

107. K. Tapily, D. Gu, H. Baumgart, G. Namkoong, D. Stegall and A. A. Elmustafa Semicond. Sci. Technol. 26, 115005 (2011).

108. Y-TLin, P-H Chung, H-W Lai, H-L Su, D-Y Lyu, K-Y Yen, T-Y Lin, C-Y Kung and J-R Gong, Appl. Surf. Sci. 256, 819 (2009).

109. S K Kim, C S Hwang, S-H K Park and S J Yun, Thin Solid Films 478, 103 (2005).

110. S-K Kwon, D-W Kim, Y-H Jung and B-J Lee, J. Korean Phys. Soc.55, 999 (2009).

111. D. Kim, H. Kang, J-M Kim and H. Kim, Appl. Surf. Sci. 257, 3776 (2011).

112. T. Suntola and J. Antson, U.S. Patent No. 4,058,430 (15 November1977).

113. M. B. M Mousa, C. J. Oldham, J. S. Jur and G. N. Parsons, J. Vac. Sci. Technol. A 30, 01A155 (2012).

114. N. Y. Yuan, S. Y. Wang, C. B. Tan, X. Q. Wang, G. G. Chen and J. N. Ding, J. Cryst. Growth 366, 43 (2013).

115. Z. Baji, Z. L´abadi, Z. E. Horv´ath, G. Moln´ar, J. Volk, I. B´arsony and P. Barna, Cryst. Growth Des.12, 5615 (2012).

116. K. Kopalko, M. Godlewski, J. Z. Domagala, E. Lusakowska, R. Minikayev, W.

Paszkowicz, and A. Szczerbakow, Chem. Mater. 16, 1447 (2004).

117. Ł. Wachnicki, T. Krajewski, G. Łuka, B. Witkowski, B. Kowalski, K. Kopalko, J. Z. Domagala, M. Guziewicz,M. Godlewski and E. Guziewicz, Thin Solid Films 518, 4556 (2010).

118. Ching-Shun Ku, Hsin-Yi Lee, Jheng-Ming Huang, Chih-Ming Lin, Materials Chemistry and Physics120, 236 (2010).

119. H.C. Chen, M.J. Chen, T.C. Liu, J.R. Yang, M. Shiojiri, Thin Solid Films 519, 536 (2010).

120. S.Lee,Y.H.Im,S.H.Kim,Y.B.Hahn, Superlattices and Microstructures 39, 24 (2006).

121. S. Yang, B. H. Lin, W-R Liu, J-H Lin, C-S Chang, C-H Hsu and W. F. Hsieh, Cryst. Growth & Des.9, 5184 (2009).

122. B. Sang and M. Konagai, Japan. J. Appl. Phys. 35, L602 (1996).

123. T. Krajewski, E. Guziewicz, M. Godlewski, L. Wachnicki, I.A. Kowalik, A. Wojcik-Glodowska,M. Lukasiewicz, K. Kopalko, V. Osinniy, M. Guziewicz, Microelectronics Journal 40, 293 (2009).

124. Sunyeol Jeon,Seokhwan Bang,Seungjun Lee,Semyung Kwon,Wooho Jeong,Hyeongtag Jeon,Ho Jung Chang,and Hyung-Ho Par, J. Electrochem.Soc. 155, H738 (2008).

125. S.J. Lim, Soonju Kwon, H. Kim, Thin Solid Films 516, 1523 (2008).

126. Jeong-Seok Na, Giovanna Scarel, and Gregory N. Parsons, J. Phys. Chem. C 114, 383 (2010).

127. J. D. Ferguson, A. W. Weimer, and S. M. George, J. Vac. Sci. Technol. A 23(1), 118 (2005).

128. Akira Yamada, Baosheng Sang, Makoto Konagai, App. Suf. Sci. 112, 216 (1997).

129. Koki Saito, Yuki Watanabe, Kiyoshi Takahashi, Takeo Matsuzawa, Baosheng Sang, Makoto Konagai, Solar Energy Materials and Solar Cells 49, 187 (1997).

130. Doyoung Kim, Hyemin Kang, Jae-Min Kim, Hyungjun Kim, App. Suf. Sci.257, 3776(2011).

131. M. Schuisky and J. W. Elam, and S. M. George, App. Phys. Lett. 81, 180 (2002).

132. D-J Lee, H-M Kim, J-Y Kwon, H Choi, S-HKim and K-B Kim, Adv. Funct. Mater.21 448, (2011).

133. Y. Geng, Z-Y Xie, S-S Xu, Q-Q Sun, S-J Ding, H-L Lu, and D. W. Zhang ECS J. Solid State Sci. Technol.1 N45 (2012).

134. S. J. Kwon, Japan. J. Appl. Phys. 44, 1062 (2005).

135. C. H. Ahn, H. Kim and H. K. Cho, Thin Solid Films 519, 747 (2010).

136. H. Yuan, B. Luo, D. Yu, A-J Cheng, S. A. Campbell and W. L. Gladfelter J. Vac. Sci. Technol.A 30, 01A138 (2012).

137. Z-Y Ye, H-L Lu, Y Geng, Y-Z Gu, Z-Y Xie, Y Zhang, Q-Q Sun, S-J Ding and D W Zhang, Nanoscale Res. Lett. 8, 108 (2013).

138. H J Yuan, Mater. Sci. Mater. Electron.23 2075 (2012).

139. K. Saito, Y. Hiratsuka, A. Omata, H. Makino, S. Kishimoto, T. Yamamoto, N. Horiuchi and H. Hirayama, Superlattices Microstruct. 42, 172 (2007).

140. Jeong-Seok Na, Qing Peng, Giovanna Scarel, and Gregory N. Parsons, Chem. Mater. 21, 5585 (2009).

141. A. Y. Gil, K. E. Peterson, and J. W. Elam, Chem. Mat. 23, 4295 (2011).

142. Y. Wu, S. E. Potts, P. M. Hermkens, H. C. M. Knoops, F. Roozeboom, and W. M. M. Kessels, Chem. Mater, 25, 4619 (2013).

143. A. Illiberi, R. Scherpenborg, Y. Wu, F. Roozeboom, and P. Poodt, App. Mater. & Interfaces, 5, 13124 (2013).

144. Tommi Tynell and Maarit Karppinen, Semicond. Sci. Technol. 29, 043001(2014).

145. Vennesa O. Williams,Nak Cheon Jeong,Chaiya Prasittichai,Omar K. Farha,Michael J.

Pellin, and Joseph T. Hupp, ACS Nano 6, 6185 (2012).

146. Alex B. F. Martinson, Ma´rcio S. Go´es,Francisco Fabregat-Santiago, Juan Bisquert, Michael J. Pellin, and Joseph T. Hupp, J. Phys. Chem.A, 113, 4015 (2009).

147. Matt Law,Lori E. Greene,Aleksandra Radenovic,Tevye Kuykendall,Jan Liphardt,and Peidong Yang, J. Phys. Chem. B, 110, 22652 (2006).

148. J. Zhang, H. Yang, Qi-Long Zhang, S. Dong and j. K. Luo, App. Phys. Lett.102, 012113 (2013).

149. V. B. Aleskovskii, Zh. Prikl. Khim.J. Appl. Chem. USSR 47, 2207 (1974).

150. H. B. Profijt, S. E. Potts, M. C. M. van de Sanden, and W. M. M. Kessels, J. Vac. Sci. Technol. A 29(5), 050801-1 (2011).

151. Nicola Pinna and Mato Knez, Atomic Layer Deposition of Nanostructured Materials (Wiley-VCHVerlag GmbH and Co. KGaA, 2012).

152. S. V. Andersen, V. Vandalon, R. H. E. C. Bosch, B. W. H. Van de Loo, K. Pedersen, and W. M. M. Kessels, App. Phys. Lett. 104, 051602 (2014).

153. Henry Hung-Chun Lai,Tahseen Basheer,Vladimir L. Kuznetsov,Russell G. Egdell,Robert M. J. Jacobs,Michael Pepper,and Peter P. Edwards, J. App. Phys. 112, 083708 (2012).

154.S. T. Tan, B. J. Chen, X. W. Sun, W. J. Fan, H. S. Kwok, X. H. Zhang, and S. J. Chua, J. App. Phys. 98, 013505 (2005).

155. V. Srikant and D. R. Clarke,J. Appl. Phys. 81, 6357 (1997).

156. Ashutosh Tiwari, C. Jin, J. Narayan, and M. Park, J. Appl. Phys. 96, 3827 (2004).

157. J. G. Lu, S. Fujita, T. Kawaharamura, H. Nishinaka, Y. Kamada, and T. Ohshima, Z. Z. Ye,Y. J. Zeng, Y. Z. Zhang, L. P. Zhu, H. P. He, and B. H. Zhao, J. App. Phys. 101, 083705 (2007).

158. J. G. Lu, Z. Z. Ye, Y. J. Zeng, L. P. Zhu, L. Wang, J. Yuan, B. H. Zhao, and Q. L. Liang,

J. App. Phys. 100, 073714 (2006).

159. D. Saha, P. Misra, R. S. Ajimsha, M. P. Joshi, and L. M. Kukreja, App. Phys. Lett. 105, 212102 (2014).

160. A. Kawabata, J. Phys. Soc. Jpn. 49, 628 (1980).

161. D. Saha, R.S. Ajimsha, K. Rajiv, C. Mukherjee, M. Gupta, P. Misra, L. M. Kukreja, App. Surf. Sci. 315, 116 (2014).

162. Jaan Aarik, Aleks Aidla, Alma-Asta Kiisler, Teet Uustare, Vaino Sammelselg, Thin Solid Films 305 (1997) 270.

163. J. Aarik, A. Aidla, H. MaÈ ndar, T. Uustare, Appl. Surf.Sci. 172 (2001)148.

164. Jaan Aarik, Aleks Aidla, Hugo M.andar, Teet Uustare, Mikael Schuisky, Anders Harsta, J. Cryst. Growth 242 (2002)189.

165. Mikko Ritala, Markku Leskela, Leena-Sisko Johansson, Lauri Niinisto, Thin Solid Films 228 (1993) 32.

166. E. F. Schubert, Delta-doping of semiconductors (Cambridge University Press, 1996).

167. Do-Joong Lee, Ki-Ju Kim, Soo-hyun Kim, jang-yeon kwon, jimmy Xu and Ki-Bum Kim, J. Mater. Chem. C 1, 4761 (2013).

168. Yang Geng, Li Guo, Sai-Sheng Xu, Qing-Qing Sun, Shi-Jin Ding, Hong-Liang Lu, and David Wei Zhang, J. Phys. Chem. C 115, 12317 (2011).

169. J. T. Thienprasert, S. Rujirawat, W. Klysubun, J. N. Duenow, T. J. Coutts, S. B. Zhang, D. C. Look, and S. Limpijumnong, Phys. Rev. Lett.110, 055502 (2013).

170. J. Y. Noh, H. Kim, Y. S. Kim, and C. H. Park,J. App. Phys. 113, 153703 (2013).

171. M. Ahlskog, Reghu Menon, A. J. Heeger, T. Noguchi, and T. Ohnoshi, Phys. Rev. B 55, 6777 (1997).

172. Qingyu Xu, Lars Hartmann, Heidemarie Schmidt, Holger Hochmuth, Michael Lorenz,Rüdiger Schmidt-Grund, Daniel Spemann, Andreas Rahm, and Marius Grundmann,

Thin Solid Films 515, 2549 (2006).

173. J. M. Monsterleet, B. Capoen and G. Biskupski, J. Phys.: Condens. Matter 9 8657 (1997).

174. Qingyu Xu,Lars Hartmann, and Heidemarie Schmidt, Holger Hochmuth, Michael Lorenz, Daniel Spemann, and Marius Grundmann, Phys. Rev. B 76, 134417 (2007).

175. Qingyu Xu, Lars Hartmann, Heidemarie Schmidt, Holger Hochmuth, Michael Lorenz, Rüdiger Schmidt-Grund, Chris Sturm, Daniel Spemann, and Marius Grundmann, Phys Rev. B **73**, 205342 (2006).

176. G. Scappucci, W. M. Klesse, A. R. Hamilton, G. Capellini, D. L. Jaeger, M. R. Bischof, R. F. Reidy, B. P. Gorman, and M. Y. Simmons, Nano. Lett.12, 4953 (2012).

177. David C. Look, Kevin D. Leedy, Darren B. Thomson, and Buguo Wang, Japanese Journal of Appl. Phys. 53, 05FJ01 (2014).

178. Davide Cammi and Carsten Ronning, Advances in Condensed Matter Physics (available at: http://dx.doi.org/10.1155/2014/184120)

179. O. Lupan, G. Chai, L. Chow, G. A. Emelchenko, H. Heinrich, V. V. Ursaki, A. N. Gruzintsev, I. M. Tiginyanu, and A. N. Redkin, Phys. Status Solidi A, 1–6 (2010) (available at: DOI 10.1002/pssa.200983706)

180. Y. Muraoka, N. Takubo, and Z. Hiroi, J. App. Phys. 105, 103702 (2009).

181. J. Vavro, J. M. Kikkawa, and J. E. Fischer, Phys. Rev. B 71 (2005) 155410.

182. Lahcen Essaleh, Syed M. Wasim, Jean Galibert, Mater. Lett. 60 (2006) 1947.

183. S. Ishida, S. Takaoka, K. Oto, K. Murase, S. Shirai, T. Serikawa, Appl. Surf. Sci. 113/114 (1997) 685.

184. U. Sivan, O. Entin-Wohlman and Y. Imry, Phy. Rev. Lett. 60 (1988) 1566.

185. R. Scherwitzl, S. Gariglio, M. Gabay, P. Zubko, M. Gibert, and J.-M. Triscone, Phys. Rev. Lett. 106, 246403 (2011).

186. A. Goldenblum, V. Bogatu, and T. Stoica, Y. Goldstein and A. Many, Phys. Rev. B 60, 5832 (1999).

187. I. S. Beloborodov, A. V. Lopatin, and V. M. Vinokur, and K. B. Efetov, Rev. Mod. Phys. 79, 469 (2007).

188. Z. Ovadyahu, S. Moehlecke, and Yoseph Imry, Surface Science 113, 544 (1982).

189. A. M. Gilbertson, A. K. M. Newaz, Woo-Jin Chang, R. Bashir, S. A. Solin, and L. F. Cohen, App. Phys. Lett. 95, 012113 (2009).

190. B. Shinozaki, S. Ezaki, K. Hidaka,K. Makise, T. Asano,1 K. Yano, and H. Nakamura, AIP. Adv. 1, 032149 (2011).

191. T. Andrearczyk, J. Jaroszynski, G. Grabecki, T. Dietl, T. Fukumura, and M. Kawasaki, Phys. Rev. B 72, 121309(R) (2005).

192. R. C. Rai, J. App. Phys. 113, 153508 (2013).

193. A K Das, P Misra and L M Kukreja, J. Phys. D: Appl. Phys 42, 165405 (2009).

194. S. C. Jain and D. J. Roulston, Solid-State electronics 34, 453 (1991).

195. J. G. Lu, S. Fujita, T. Kawaharamura, H. Nishinaka, Y. Kamada, T. Ohshima, Z. Z. Ye,Y. J. Zeng, Y. Z. Zhang, L. P. Zhu, H. P. He, and B. H. Zhao, J. App. Phys. 101, 083705 (2007).

196. T. Makino, Y. Segawa, S. Yoshida, A. Tsukazaki, A. Ohtomo, and M. Kawasaki, App. Phys. Lett. 85, 759 (2004).

197. E. F. Schubert, I. D. Goepfert, W. Grieshaber, and J. M. Redwing, Appl. Phys. Lett. 71, 921 (1997).

198. Martin Feneberg, Jürgen Däubler, Klaus Thonke, and Rolf Sauer, Phys. Rev. B 77, 245207 (2008).

199. Andre´ Schleife, Claudia Ro¨dl, Frank Fuchs, Karsten Hannewald, and Friedhelm Bechstedt, Phys. Rev. Lett. 107, 236405 (2011).

200. G. D. Mahan, Phys. Rev. 153, 882 (1966).

201. Xiangdong Meng, Zhiming Shi, Xiaobing Chen, Xianghua Zeng, and Zhuxi Fu, J. App. Phys. 107, 023501 (2010).

202. M. Schirra, R. Schneider, A. Reiser, G. M. Prinz, M. Feneberg, J. Biskupek, U. Kaiser, C. E. Krill, K. Thonke, and R. Sauer, Phys. Rev. B 77, 125215 (2008).

203. S. Yang, C. C. Kuo, W. R. Liu, B. H. Lin, H. C. Hsu, C, H, Hsu, and W. F. Hsieh, App. Phys. Lett. 100, 101907 (2012).

204. Martin Feneberg, Sarah Osterburg, Karsten Lange, Christian Lidig, Bernd Garke, and R¨udiger Goldhahn, Eberhard Richter and Carsten Netzel, Maciej D. Neumann and Norbert Esser, Stephanie Fritze, Hartmut Witte, J¨urgen Bl¨asing, Armin Dadgar, and Alois Krost, Phys. Rev. B 90, 075203 (2014).

Appendix

(I) Process Recipe for the Growth of ZnO Thin Films

*Recipe (BHU) ZnO at 150C
*Recipe for ZnO
*Precursors DEZn and Water by own vapor pressures
*Mim , 2008 1 July
*Based on flow chart N500749
*DEZn at liquid source 2
*Water at liquid source 1
*Source needle valves (NV-PL1 open 1 turn, NV-PL2 open 1.5 turns)
*reactor temperature 150
*Liquid source temp 20^{o}C

*Program start
SPROG

*Open the N2 main valve and chamber flow valve and make sure filling valve is closed
OPEN DV-SN1,DV-NV2
CLOSE DV-NV1

*Open main vacuum valve
OPEN DV-VP1

*Set process gas flows
FLOW MFC-NOVS=200
FLOW MFC-NOPS=300

*Close pulse valves
CLOSE DV-PL1,DV-BL1,DV-AL1
CLOSE DV-PL2,DV-BL2,DV-AL2
CLOSE DV-PL3,DV-BL3,DV-AL3
CLOSE DV-PH1,DV-BH1,DV-BHA1
CLOSE DV-AE,DV-AF

*Close process gas valves
CLOSE DV-SG1,DV-PG1,DV-PG2

*Check the vacuum level
WUNTIL PT-P1<10 10s

*Set temperatures
TEMP TE-R1S=150

*wait until temperature is ok
WUNTIL TE-R1>TE-R1S 5h

*Are temperatures ok to start the process ?
WRITE M5
WUSER YES

*Make sure that holder lifter is up
WRITE M38
WUSER YES

*open precursor hand valves
WRITE M6
WUSER YES

*Pulsing DEZn and Water 1000 cycles, appr. 200 nm

REPEAT 1000

Pulse DV-PL2 200ms
Purge 1s

Pulse DV-PL1 200ms
Purge 1s

REND

*Set temperatures
*TEMP TE-R1S=20

*Close pulse valves
CLOSE DV-PL1,DV-BL1,DV-AL1
CLOSE DV-PL2,DV-BL2,DV-AL2
CLOSE DV-PL3,DV-BL3,DV-AL3
CLOSE DV-PH1,DV-BH1,DV-BHA1
CLOSE DV-AE,DV-AF

*Close process gas valves
CLOSE DV-SG1,DV-PG1,DV-PG2

*close precursor hand valves

WRITE M7
WUSER YES

*confirm that all precursor hand valves are closed
WRITE M22
WUSER YES

*Start DEZ line purge
WRITE M25
WUSER YES

PULSE DV-PL2 3min

*end program
EPROG

*----------

(II) Process Recipe for the Growth of TiO_2 Thin Films

*Recipe TiO2 Optimis 250^{o}C
*Recipe for 200 nm of TiO_2
*Precursors TiCl4 and Water by own vapor pressures
*Mim , 2012 sept
*Based on flow chart N500749
*TiO2 at liquid source 3
*Water at liquid source 1
*Source needle valves (NV-PL1 open 1 turn, NV-PL3 open 1.5 turn)
*reactor temperature 200

*Program start
SPROG

*Open the N2 main valve and chamber flow valve and make sure filling valve is closed
OPEN DV-SN1,DV-NV2
CLOSE DV-NV1

*Check the vacuum level
WUNTIL PT-P1<10 10s

*Open main vacuum valve
OPEN DV-VP1

*Set flows
FLOW MFC-NOVS=200
FLOW MFC-NOPS=300

*Close pulse valves
CLOSE DV-PL1,DV-BL1,DV-AL1
CLOSE DV-PL2,DV-BL2,DV-AL2
CLOSE DV-PL3,DV-BL3,DV-AL3
CLOSE DV-PH1,DV-BH1,DV-BHA1
CLOSE DV-AE,DV-AF

*Close process gas valves
CLOSE DV-SG1,DV-PG1,DV-PG2

*Set temperatures
TEMP TE-R1S=200

*wait until temperature is ok
WUNTIL TE-R1>TE-R1S 5h

*Are temperatures ok to start the process ?
*WRITE M5
*WUSER YES

*Make sure that holder lifter is up
WRITE M38
WUSER YES

*open precursor hand valves
*WRITE M6
*WUSER YES

*Pulsing TiCl4 and Water 1000 cycles

REPEAT 1000

Pulse DV-PL3 500ms
Purge 1s

Pulse DV-PL1 500ms
Purge 1s

REND

*Set temperatures
TEMP TE-R1S=20

*Close pulse valves
CLOSE DV-PL1,DV-BL1,DV-AL1
CLOSE DV-PL2,DV-BL2,DV-AL2
CLOSE DV-PL3,DV-BL3,DV-AL3
CLOSE DV-PH1,DV-BH1,DV-BHA1
CLOSE DV-AE,DV-AF

*Close process gas valves
CLOSE DV-SG1,DV-PG1,DV-PG2

*close precursor hand valves
WRITE M7
WUSER YES

*confirm that all precursor hand valves are closed
WRITE M22
WUSER YES

*Start TMA line purge
WRITE M37
WUSER YES

PULSE DV-PL3 2min

*end program
EPROG

*----------

(III) Process Recipe for the Growth of Al_2O_3 Thin films

*Recipe Hot Source Al2O3 deposition at 300C with Booster Option
*Recipe for Hot Source 1
*Precursors at Hot Source 1
*Mim, 2008 1 July
*Based on flow chart N500749
*reactor temperature 200

*Program start

SPROG

*Open the N2 main valve and chamber flow valve and make sure filling valve is closed
OPEN DV-SN1,DV-NV2
CLOSE DV-NV1

*Open main vacuum valve
OPEN DV-VP1

*Set flows
FLOW MFC-NOVS=200
FLOW MFC-NOPS=300

*Close pulse valves
CLOSE DV-PL1,DV-BL1,DV-AL1
CLOSE DV-PL2,DV-BL2,DV-AL2
CLOSE DV-PL3,DV-BL3,DV-AL3
CLOSE DV-PH1,DV-BH1,DV-BHA1
CLOSE DV-AE,DV-AF

*Close process gas valves
CLOSE DV-SG1,DV-PG1,DV-PG2

*Check the vacuum level
WUNTIL PT-P1<10 10s

*Set temperature
TEMP TE-R1S=300

*Set temperature for HotSource 1
TEMP TE-HS1S=100

*wait until temperature is ok
WUNTIL TE-R1>TE-R1S 5h

*Are temperatures ok to start the process ?
WRITE M5
WUSER YES

*Make sure that holder lifter is up
WRITE M38
WUSER YES

*open precursor hand valves
WRITE M6
WUSER YES

*Pulsing H20 and HS1

REPEAT 1000

Pulse DV-PL1 200ms
Purge 1s

Pulse DV-BHA1,DV-BH1 500ms
WTIME 50ms
Pulse DV-PH1 500ms
Purge 1s

REND

*Set reactor temperature
TEMP TE-R1S=20

*Set HotSource1 temperature
TEMP TE-HS1S=20

*Close pulse valves
CLOSE DV-PL1,DV-BL1,DV-AL1
CLOSE DV-PL2,DV-BL2,DV-AL2
CLOSE DV-PL3,DV-BL3,DV-AL3
CLOSE DV-PH1,DV-BH1,DV-BHA1
CLOSE DV-AE,DV-AF

*Close process gas valves
CLOSE DV-SG1,DV-PG1,DV-PG2

*close precursor hand valves
WRITE M7
WUSER YES

*confirm that all precursor hand valves are closed
WRITE M22
WUSER YES

*Start TMA line purge
WRITE M25

WUSER YES

PULSE DV-PL2 2min

*end program
EPROG

*--

(IV) Process Recipe for the Growth of (Zn, Al)O_x Thin films

*Recipe Al doped ZnO 1:70
*Recipe for HotSource 1
*Precursors at HotSource 1
*Mim , 2008 1 July
*Based on flow chart N500749
*reactor temperature 200

*Program start
SPROG

*Open the N2 main valve and chamber flow valve and make sure filling valve is closed
OPEN DV-SN1,DV-NV2
CLOSE DV-NV1

*Open main vacuum valve
OPEN DV-VP1

*Set flows
FLOW MFC-NOVS=200
FLOW MFC-NOPS=300

*Close pulse valves
CLOSE DV-PL1,DV-BL1,DV-AL1
CLOSE DV-PL2,DV-BL2,DV-AL2
CLOSE DV-PL3,DV-BL3,DV-AL3
CLOSE DV-PH1,DV-BH1,DV-BHA1
CLOSE DV-AE,DV-AF

*Close process gas valves
CLOSE DV-SG1,DV-PG1,DV-PG2

*Check the vacuum level
WUNTIL PT-P1<10 10s

*Set temperature
TEMP TE-R1S=300

*Set temperature for HotSource 1
TEMP TE-HS1S=100

*wait until temperature is ok
WUNTIL TE-R1>TE-R1S 5h

*Are temperatures ok to start the process ?
WRITE M5
WUSER YES

*Make sure that holder lifter is up
WRITE M38
WUSER YES

*open precursor hand valves
WRITE M6
WUSER YES

*Pulsing H20 and HS1

REPEAT 14
REPEAT 70

Pulse DV-PL2 200ms
Purge 1s

Pulse DV-PL1 200ms
Purge 1s

REND

REPEAT 1
Pulse DV-BHA1, DV-BH1 500ms
WTIME 50ms
Pulse DV-PH1 25ms
Purge 1s

Pulse DV-PL1 200ms
Purge 1s

REND
REND

*Set reactor temperature
TEMP TE-R1S=20

*Set HotSource1 temperature
TEMP TE-HS1S=20

*Close pulse valves
CLOSE DV-PL1,DV-BL1,DV-AL1
CLOSE DV-PL2,DV-BL2,DV-AL2
CLOSE DV-PL3,DV-BL3,DV-AL3
CLOSE DV-PH1,DV-BH1,DV-BHA1
CLOSE DV-AE,DV-AF

*Close process gas valves
CLOSE DV-SG1,DV-PG1,DV-PG2

*close precursor hand valves
WRITE M7
WUSER YES

*confirm that all precursor hand valves are closed
WRITE M22
WUSER YES

*Start TMA line purge
WRITE M25
WUSER YES

PULSE DV-PL2 2min

*end program
EPROG

*----------

(V) Process Recipe for the Growth of (Zn, Ti)O_x Thin films

*Recipe Ti doped ZnO 1:150
*Recipe for TZO
*Precursors at Liquid Source
*Mim , 2008 1 July
*Based on flow chart N500749
*reactor temperature 200

```
*Program start
SPROG

*Open the N2 main valve and chamber flow valve and make sure filling valve is closed
OPEN DV-SN1,DV-NV2
CLOSE DV-NV1

*Open main vacuum valve
OPEN DV-VP1

*Set flows
FLOW MFC-NOVS=200
FLOW MFC-NOPS=300


*Close pulse valves
CLOSE DV-PL1,DV-BL1,DV-AL1
CLOSE DV-PL2,DV-BL2,DV-AL2
CLOSE DV-PL3,DV-BL3,DV-AL3
CLOSE DV-PH1,DV-BH1,DV-BHA1
CLOSE DV-AE,DV-AF

*Close process gas valves
CLOSE DV-SG1,DV-PG1,DV-PG2


*Check the vacuum level
WUNTIL PT-P1<10 10s

*Set temperature
TEMP TE-R1S=300

*Set temperature for Hot Source 1
TEMP TE-HS1S=100

*wait until temperature is ok
WUNTIL TE-R1>TE-R1S 5h

*Are temperatures ok to start the process?
WRITE M5
WUSER YES

*Make sure that holder lifter is up
WRITE M38
WUSER YES


*open precursor hand valves
WRITE M6
```

WUSER YES

*Pulsing H20 and HS1

REPEAT 7
REPEAT 150

Pulse DV-PL2 200ms
Purge 1s

Pulse DV-PL1 200ms
Purge 1s

REND

REPEAT 1

Pulse DV-PL3 25ms
Purge 1s

Pulse DV-PL1 200ms
Purge 1s

REND
REND

*Set reactor temperature
TEMP TE-R1S=20

*Set HotSource1 temperature
TEMP TE-HS1S=20

*Close pulse valves
CLOSE DV-PL1,DV-BL1,DV-AL1
CLOSE DV-PL2,DV-BL2,DV-AL2
CLOSE DV-PL3,DV-BL3,DV-AL3
CLOSE DV-PH1,DV-BH1,DV-BHA1
CLOSE DV-AE,DV-AF

*Close process gas valves
CLOSE DV-SG1,DV-PG1,DV-PG2

*close precursor hand valves
WRITE M7
WUSER YES

*confirm that all precursor hand valves are closed
WRITE M22
WUSER YES

*Start TMA line purge
WRITE M25
WUSER YES

PULSE DV-PL2 2min

*end program
EPROG

*----------